Precision measurement of the e+e− → π + π−(γ) cross-section with ISR method

L.-L. Wang

Precision measurement of the $e^+e^- \to \pi^+\pi^-(\gamma)$ cross-section with ISR method

Liang-Liang WANG

Supervisors:

Prof. Michel DAVIER

Prof. Chang-Zheng YUAN

Paris-Sud University

and

Institute of High Energy Physics

Chinese Academy of Sciences

May, 2009

Submitted in total fulfilment of the requirements for the degree of Ph.D. in Particle Physics and Nuclear Physics

Abstract

Vacuum polarization integral involves the vector spectral functions which can be experimentally determined. As the dominant uncertainty source to the integral, the precision measurement of the cross section of $e^+e^- \to \pi^+\pi^-(\gamma)$ as a function of energy from 2π threshold to 3GeV is performed by taking the ratio of $e^+e^- \to \pi^+\pi^-(\gamma)$ cross section to $e^+e^- \to \mu^+\mu^-(\gamma)$ cross section which are both measured with *BABAR* data using ISR method in one analysis. Besides that taking the ratio of the cross sections of the two processes can cancel several systematic uncertainties, the acceptance differences between data and MC are measured using the same data, and the corresponding corrections are applied on the efficiencies predicted by MC which can control the uncertainties. The achieved final uncertainty of the born cross section of $e^+e^- \to \pi^+\pi^-(\gamma)$ in ρ mass region ($0.6 \sim 0.9$GeV) is 0.54%. As a consequence of the new vacuum polarization calculation using the new precision result of the $e^+e^- \to \pi^+\pi^-(\gamma)$ cross section, the impact on the SM prediction of muon anomalous magnetic moment $g-2$ is presented, which is also compared with other data based predictions and direct measurement.

Keywords: $e^+e^- \to \mu^+\mu^-(\gamma)$ cross section, $e^+e^- \to \pi^+\pi^-(\gamma)$ cross section, ISR, FSR, muon anomalous magnetic moment $g-2$, vacuum polarization

Contents

List of tables

List of figures

Chapter 1

Introduction

1.1 The Standard Model

The basic composing of matter and the interactions between them make human curious and it is still the main theme of modern physics. Electromagnetic, weak, strong and gravitational interactions are the already known four fundamental interactions. Except gravitational interaction, they can be described successfully by the so-called *Standard Model* (SM). According to this model, matter are made up by a few fundamental spin $\frac{1}{2}$ particles called fermions: six quarks, six leptons (Table 1.1) and their antiparticles. The interactions between the fundamental constituents are mediated by spin 1 particles (Table 1.2). It should not be doubted that the SM is really a very successful and effective theoretical model for the fundamental constitutes and three fundamental interactions between them, which can account for a huge amount of experimental data. But one should also notice that at least the current Standard Model is not the final ultimate model, because gravitational interaction is not included, this model has 17 arbitrary parameters the origin of the values of which is not understood, and some features of our universe like the dominant 'dark matter' and the large matter-antimatter asymmetry indicate something unknown beyond the SM. At this moment, concerning experiments, people try to look for something not observed yet like the famous Higgs boson or improve the precision of the measurements to test if there is some real deviation from the SM.

1.2 Motivation

1.2.1 Hadronic vacuum polarization

Hadronic vacuum polarization (Figure 1.1) in the photon propagator plays an important role in the precision tests of the SM.

Table 1.1: The fundamental fermions

Particle	Flavor			$Q/\|e\|$
lepton	e	μ	τ	-1
	ν_e	ν_μ	ν_τ	0
quark	u	c	t	$+\frac{2}{3}$
	d	s	b	$-\frac{1}{3}$

Table 1.2: The boson mediators

Interaction	Mediator	Spin/parity
strong	G(gluon)	1^-
electromagnetic	γ(photon)	1^-
weak	$W^\pm$,Z^0	1^-,1^+

One case is for the evaluation of the electromagnetic coupling at the Z mass scale,

$$\alpha(M_Z^2) = \frac{\alpha}{1 - \Delta\alpha(M_Z^2)}, \tag{1.1}$$

where $\alpha = \frac{e}{4\pi}$ is the QED fine structure constant, the correction at the Z mass scale $\Delta\alpha(M_Z^2)$ originates from the vacuum polarization in the photon propagator, among which the hadronic contribution $\Delta\alpha_{had}(M_Z^2)$ is of the order of 2.8×10^{-2} that must be known better than 1% so that it will not limit the accuracy on the indirect extraction of the Higgs boson mass from the measurements of $\sin^2\theta_{\mathrm{W}}$ (θ_{W} is the weak mixing angle).

Another case is for the theoretical prediction for the anomalous magnetic moment of muon, which is generally divided into three contributions by the SM (see Figure 1.2):

$$a_\mu^{\mathrm{SM}} = a_\mu^{\mathrm{QED}} + a_\mu^{\mathrm{weak}} + a_\mu^{\mathrm{had}}. \tag{1.2}$$

The theoretical calculation of the QED part a_μ^{QED} including all photonic and leptonic loops is performed up to 4-loop level and estimated to 5-loop level [1], which gives:

$$a_\mu^{\mathrm{QED}} = (116\,584\,718.10 \pm 0.16) \times 10^{-11}, \tag{1.3}$$

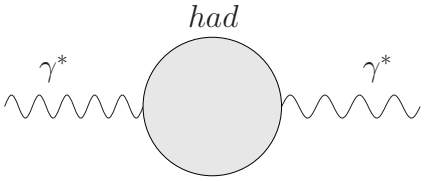

Figure 1.1: Feynman diagram for the hadronic vacuum polarization.

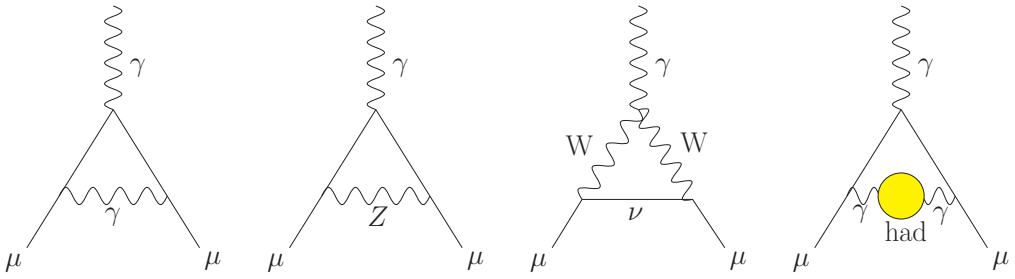

Figure 1.2: Feynman diagrams contributing to a_μ^{SM}. From left to right: first order QED, lowest order weak involving Z, lowest order weak involving W, lowest order hadronic.

The weak term a_μ^{weak} includes Z, $W^\pm$ and Higgs loop contributions, and is suppressed by the heaviness of their masses. As the 3-loop level correction to it is negligible, the prediction considering the corrections up to 2-loop level for it is [2, 3]:

$$a_\mu^{\mathrm{weak}} = (154 \pm 1 \pm 2) \times 10^{-11}, \tag{1.4}$$

So far, the hadronic contributions (a_μ^{had}) to a_μ^{SM} can not be calculated from first principles. For convenience, they are separated into three terms too:

$$a_\mu^{\mathrm{had}} = a_\mu^{\mathrm{had,LO}} + a_\mu^{\mathrm{had,HO}} + a^{\mathrm{had,LBL}}, \tag{1.5}$$

where $a_\mu^{\mathrm{had,LO}}$ is the lowest order hadronic vacuum polarization contribution, $a_\mu^{\mathrm{had,HO}}$ is the higher order hadronic vacuum polarization contribution, and $a^{\mathrm{had,LBL}}$ is the hadronic light-by-light scattering contribution (see Figure 1.3).

Instead of the direct calculation from first principles, the contribution of the hadronic vacuum polarization to $a_\mu^{\mathrm{had,LO}}$ can be calculated via the dispersion integral [8]:

$$a_\mu^{\mathrm{had,LO}} = \frac{\alpha^2(0)}{3\pi^2} \int_{4m_\pi^2}^{\infty} ds \frac{K(s)}{s} R(s), \tag{1.6}$$

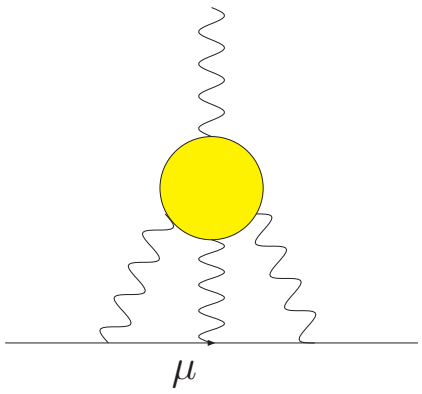

Figure 1.3: One example of the Feynman diagrams for the hadronic light-by-light scattering contribution to $a_\mu^{\rm SM}$.

where K(s) is the QED kernel [9],

$$K(s) = x^2\left(1-\frac{x^2}{2}\right) + (1+x)^2\left(1+\frac{1}{x^2}\right)\left[\ln(1+x) - x + \frac{x^2}{2}\right] + x^2 \ln x \frac{1+x}{1-x}\,, \tag{1.7}$$

with $x = (1-\beta_\mu)/(1+\beta_\mu)$ and $\beta_\mu = (1-4m_\mu^2/s)^{1/2}$. In (1.6), $R(s) \equiv R^{(0)}(s)$ denotes the ratio of the 'bare' cross section for e^+e^- annihilation into hadrons to the point-like muon-pair cross section. The 'bare' cross section is defined as the measured cross section, corrected for initial state radiation, electron-vertex loop contributions and vacuum polarization effects in the photon propagator. The function $K(s) \sim 1/s$ decreases monotonically with increasing s. It gives a strong weight to the low energy part of the integral (1.6). About 91% of the total contribution to $a_\mu^{\rm had,LO}$ is accumulated at center-of-mass energies $\sqrt{s} < 1.8$GeV and 73% of $a_\mu^{\rm had,LO}$ is covered by the two-pion final state which is dominated by the $\rho(770)$ resonance. In other words, $a_\mu^{\rm had,LO}$ is dominated by the $\rho(770)$ resonance.

The higher order of hadronic contribution can be obtained in the similar way using also $e^+e^- \to$ hadrons data [7, 10]:

$$a_\mu^{\rm had,HO} = (-98 \pm 1) \times 10^{-11} \tag{1.8}$$

For hadronic light-by-light scattering contribution, one can get the estima-

tion following [11]:

$$a_\mu^{\mathrm{had,LBL}} = (105 \pm 26) \times 10^{-11}. \tag{1.9}$$

1.2.2 Status of the relevant results about a_μ

On the prediction side, $e^+e^- \to$ hadrons data is used to estimate $a_\mu^{\mathrm{had,LO}}$ as shown in Eq. 1.6, which gives [7]:

$$a_\mu^{\mathrm{had,LO}} = (6894 \pm 42 \pm 18) \times 10^{-11} \quad (e^+e^- \text{ based}), \tag{1.10}$$

where the first error is experimental (dominated by systematic uncertainties), and the second is the uncertainty because of QED radiative corrections to the data.

From hadronic τ decay ($\tau \to \nu_\tau +$ hadrons), one can get vector spectral functions which can be related to isovector $e^+e^- \to$ hadrons cross sections by isospin rotation. After isospin-breaking corrections, one can find [5, 6]:

$$a_\mu^{\mathrm{had,LO}} = (7103 \pm 50 \pm 7 \pm 28) \times 10^{-11} \quad (\tau \text{ based}), \tag{1.11}$$

where the errors are statistical, systematic and the uncertainty due to isospin-breaking corrections.

If one sums all the predicted parts of a_μ as given above, one gets:

$$a_\mu^{\mathrm{SM}} = (116\,591\,773 \pm 53) \times 10^{-11} \quad (e^+e^- \text{ based}), \tag{1.12}$$

$$a_\mu^{\mathrm{SM}} = (116\,591\,982 \pm 63) \times 10^{-11} \quad (\tau \text{ based}), \tag{1.13}$$

where 2.8σ deviation is found between the e^+e^- data based result and the τ data based result.

On the side of direct measurements, a_μ was already measured in 1970's at CERN [12]. And the results were improved by a factor of 14 after the E821 experiment at Brookhaven National Lab (BNL) which studied the precession of μ^+ and μ^- in a constant external magnetic field as they circulated in a confining storage ring. The present average experimental result of $a_{\mu^+}^{\mathrm{exp}}$ and $a_{\mu^-}^{\mathrm{exp}}$ is [13]:

$$a_\mu^{\mathrm{exp}} = (116\,592\,080 \pm 54 \pm 33) \times 10^{-11}, \tag{1.14}$$

where the first error is statistical and the second systematic.

Now one can compare the direct measurement and the prediction from the SM for a_μ:

$$\Delta a_\mu = a_\mu^{\rm exp} - a_\mu^{\rm SM} = \quad (307 \pm 82) \times 10^{-11} \qquad (e^+e^- \text{ based}) \tag{1.15}$$

$$\Delta a_\mu = a_\mu^{\rm exp} - a_\mu^{\rm SM} = \quad (98 \pm 90) \times 10^{-11} \qquad (\tau \text{ based}) \tag{1.16}$$

For the e^+e^- data based prediction, there is 3.7σ deviation from the measured result. For the τ data based prediction, there is 1.1σ deviation which is smaller.

As already shown, the biggest uncertainty of the prediction for a_μ comes from the contribution of the hadronic vacuum polarization and is dominated by $\rho(770) \to \pi^+\pi^-$. And concerning the differences between the e^+e^- data based prediction, τ data based prediction and direct measurement for a_μ, more precision measurement of the $e^+e^- \to \pi^+\pi^-(\gamma)$ cross-section is really interesting and demanded.

1.3 Measure $\sigma(e^+e^- \to \text{hadrons})$ with ISR method

The traditional method to measure the cross sections of $e^+e^- \to$ hadrons is using energy scan techniques that data is gathered for different collision energies. The exclusive low energy e^+e^- cross sections have been measured mainly by experiments running at e^+e^- colliders in Novosibirsk and Orsay. Due to the high hadron multiplicity at energies above ~ 2.5 GeV, the exclusive measurement of the respective hadronic final states is not practicable. Consequently, the experiments at the high energy colliders ADONE, SPEAR, DORIS, PETRA, PEP, VEPP-4, CESR and BEPC have measured the total inclusive cross section ratio R. Recent examples include the measurements of R near the ρ peak by the CMD-2 collaboration [14] and the measurement by BES over the range $\sqrt{s} = 2 \sim 5$GeV [15].

However this method has several limitations:

- Colliders perform optimally only in a limited range of beam energies. It is therefore necessary to combine data from several experiments in order

to measure R over a large energy range, which can cause problems if the conditions of the data-taking were different.

- Even within the dataset of a single dataset, the changes in the beam energy can alter the machine environment, leading to 'point-to-point systematics' between data taken at different energy values.

- There are 2 main sources of systematics inherent to the low-energy measurements: first the presence of beam backgrounds which can fake hadronic events, and second the dependence on the details of the hadronic model, in particular to measure detection efficiency.

Another method raised long ago is utilizing initial state radiation (ISR) to study e^+e^- annihilation at a lower effective energy than the nominal collision energy [16]. And the implements at the high luminosity ϕ and B factories were discussed in Refs. [17, 18].

The ISR process is shown in Fig. 1.4, in which an energetic photon is emitted from one of the incoming e^+e^- pair, with the remained lower 'effective' collision energy $\sqrt{s'}$, a hadronic (or leptonic) event is produced. The total cross section for this kind of processes can be written as:

$$\frac{d\sigma(s,x,\theta_\gamma^*)}{dx\ d\cos\theta_\gamma^*} = W(s,x,\theta_\gamma^*)\sigma_0(s(1-x)), \tag{1.17}$$

where $\sqrt{s}$ is the e^+e^- center-of-mass (C.M.) energy, $x \equiv 2E_\gamma^*/\sqrt{s}$, E_γ^* and θ_γ^* are the energy and polar angle in the c.m frame for the photon from ISR, $s(1-x) = s'$ is the effective center-of-mass energy after ISR and σ_0 is defined as the Born cross section for $e^+e^- \to$ hadrons. The function (for example, see [18])

$$W(s,x,\theta_\gamma^*) = \frac{\alpha}{\pi x}\left(\frac{2-2x+x^2}{\sin^2\theta_\gamma^*} - \frac{x^2}{2}\right), \tag{1.18}$$

describes the possibility of the ISR photon emission for $\theta_\gamma^* \gg m_e/\sqrt{s}$, where α is the fine structure constant and m_e is the rest mass of electron. From this function, one can find that the ISR photon dominates at small angle with respect to either of the beams, and about 10% of them can be in $30^\circ < \theta_\gamma^* < 150^\circ$ (i.e.

can be detected by *BABAR*). Obviously, by using ISR method, the cross section of $e^+e^- \to$ hadrons can be studied over a rather large range of energy from threshold ($2m_\pi$) to the nominal collision energy s in one experiment.

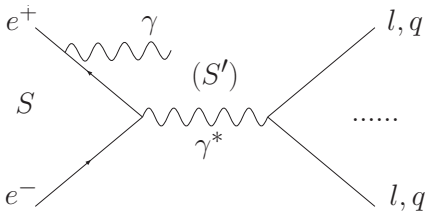

Figure 1.4: Feynman diagram for ISR events.

As a high luminosity B factory (see Chapter 2 for details), *BABAR* is an appropriate place to study $e^+e^- \to$ hadrons using ISR method. A program was planned to achieve a precision measurement of $R = \sigma(e^+e^- \to \text{hadrons})/\sigma_{pt}$ at low energy range ($2m_\pi \sim 5$GeV) which is well covered by ISR events gathered by BaBar, and actually some exclusive ISR processes have already studied with BaBar data (see [19]-[26]).

The precision required on the integrals involving R needed in these vacuum polarization calculations should be better than 1%, so that systematic uncertainties on R which are correlated over the relevant mass range have to be kept well below this level.

1.4 Principle of the measurements of the $e^+e^- \to \pi^+\pi^-(\gamma)$ cross section

This thesis will focus on the study of the cross sections of the two processes $e^+e^- \to \gamma^* \to \mu^+\mu^-(\gamma)$ and $e^+e^- \to \gamma^* \to \pi^+\pi^-(\gamma)$ with ISR method. The cross section ratio $R_{\pi\pi(\gamma)}$ is the dominant contribution to the hadronic vacuum polarization integral needed to compute the SM prediction to the muon magnetic moment anomaly.

In real data, the processes include not only the lowest order ISR (Fig. 1.5) but also the lowest order FSR, additional ISR, additional FSR which are shown in Fig. 1.6 and even higher order radiations. In the lower mass region (<3 GeV),

ISR strongly dominates. The interference between ISR and FSR amplitudes vanishes when integrating over a charge-symmetric acceptance. Since the lowest-order $\mu\mu$ process should be well described by QED calculations (even including additional ISR and FSR radiation), one can use the Monte Carlo (MC) generator (AfkQed) to predict the relative amount of the remaining $|FSR|^2$ contribution as a function of mass:

$$\delta_{FSR}^{\mu\mu} = \frac{|FSR|^2}{|ISR|^2} \ . \tag{1.19}$$

Here the lowest order FSR for $\gamma\pi\pi$ is negligible as expectation, because of the π structure and the subsequent smallness of the pion form factor at $\sqrt{s} = 10.58$ GeV.

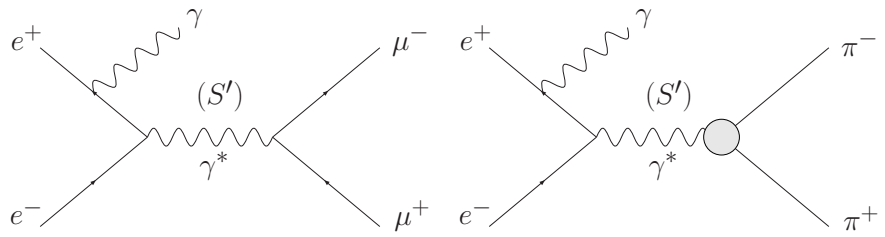

Figure 1.5: Feynman diagrams for the lowest ISR processes $e^+e^- \to \gamma\gamma^* \to \gamma\mu^+\mu^-$ (left) and $\gamma\pi^+\pi^-$ (right).

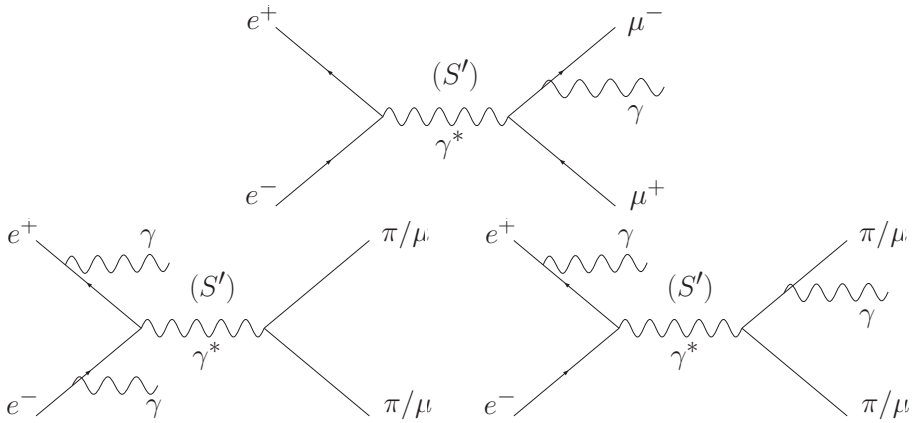

Figure 1.6: Feynman diagrams for the FSR process $e^+e^- \to \gamma\mu^+\mu^-$ (top), additional ISR process (bottom left) and additional FSR process (bottom right).

In our analysis, the events with one additional photon are also selected to

gain higher efficiency and better precision. In practice the next-to-leading-order is sufficient to reach accuracies of 10^{-3}, so the selection keeps $\mu\mu\gamma$ ($\pi\pi\gamma$) as well as $\mu\mu\gamma\gamma$ ($\pi\pi\gamma\gamma$) as final states, where the additional photon can be either ISR or FSR. It should be noted that, since we are interested in $\mu\mu(\gamma)$ ($\pi\pi(\gamma)$) produced by ISR, the relevant final state mass is $\sqrt{s'}$, i.e. $m_{\mu\mu}$ ($m_{\pi\pi}$) when there is no additional radiation or additional ISR, and $m_{\mu\mu\gamma}$ ($m_{\pi\pi\gamma}$) in the case of additional FSR. In all cases the main ISR photon is assumed to be the photon with the highest energy in the e^+e^- center-of-mass.

In these conditions the observed mass spectrum of $\mu\mu\gamma(\gamma)$ events is given by

$$\frac{dN_{\mu\mu\gamma(\gamma)}}{d\sqrt{s'}} = \frac{dL^{eff}_{ISR}}{d\sqrt{s'}}\,\sigma_{\mu\mu(\gamma)}(\sqrt{s'})\,(1+\delta^{\mu\mu}_{FSR})\,\epsilon_{\mu\mu\gamma(\gamma)}(\sqrt{s'}), \tag{1.20}$$

where $\epsilon_{\mu\mu\gamma(\gamma)}$ is the full efficiency for the event sample, determined by MC with suitable corrections, and $\sigma_{\mu\mu(\gamma)}$ is the cross section for the process $e^+e^- \to \gamma^* \to \mu^+\mu^-(\gamma)$. The effective ISR luminosity function,

$$\frac{dL^{eff}_{ISR}}{d\sqrt{s'}} = L_{ee}\,\frac{dW}{d\sqrt{s'}}\left(\frac{\alpha(s')}{\alpha(0)}\right)^2\frac{\epsilon_{ISR\gamma}(\sqrt{s'})}{\epsilon^{MC}_{ISR\gamma}(\sqrt{s'})}\,, \tag{1.21}$$

takes into account the e^+e^- luminosity (L_{ee}), the probability to radiate an ISR photon (with possibly additional ISR photons) ($\frac{dW}{d\sqrt{s'}}$) so that the produced final state (excluding ISR photons) has a mass $\sqrt{s'}$, the vacuum polarization in the photon propagator γ^*, and the ratio of $\epsilon_{ISR\gamma}$, the efficiency to detect the main ISR photon, to the same quantity, $\epsilon^{MC}_{ISR\gamma}$, in simulation. The effective ISR luminosity function can be directly deduced from the observed mass spectrum of $\mu\mu\gamma(\gamma)$ events following Eq. (1.20), inserting for $\sigma_{\mu\mu(\gamma)}(\sqrt{s'})$ the cross section computed with QED.

The cross section σ_X for any annihilation reaction $e^+e^- \to X$ can be obtained from the $\sqrt{s'}$ spectrum from the ISR $e^+e^- \to X\gamma$ process, corrected by the acceptance $\epsilon_{X\gamma}$:

$$\sigma_X(\sqrt{s'}) = \frac{\frac{dN_{X\gamma}}{d\sqrt{s'}}}{\epsilon_{X\gamma}\,\frac{dL^{eff}_{ISR}}{d\sqrt{s'}}}\,, \tag{1.22}$$

using the effective ISR luminosity derived from the $\mu\mu\gamma(\gamma)$ cross section as above. Many advantages follow from proceeding in this way:

- the result is independent of the BaBar luminosity L_{ee};
- the ISR photon efficiency cancels out;
- the result is independent of the presence of additional ISR photons;
- vacuum polarization also cancels out;
- AfkQed MC is only used to compute the acceptance of the studied $X\gamma$ process.

As one specific example of the $e^+e^- \to X$ reactions, the observed mass spectrum ($\sqrt{s'} = m^2_{\pi\pi(\gamma)}$) of $\pi\pi\gamma(\gamma)$ events is given by

$$\frac{dN_{\pi\pi\gamma(\gamma)}}{d\sqrt{s'}} = \frac{dL^{eff}_{ISR}}{d\sqrt{s'}}\,\varepsilon_{\pi\pi\gamma(\gamma)}(\sqrt{s'})\,\sigma_{\pi\pi(\gamma)}(\sqrt{s'})\,, \tag{1.23}$$

similarly, where $\varepsilon_{\pi\pi\gamma(\gamma)}$ is the full acceptance for the event sample, determined by MC with suitable corrections, and $\sigma_{\pi\pi(\gamma)}$ is the cross section for the process $e^+e^- \to \gamma^* \to \pi^+\pi^-(\gamma)$.

From Eqs. 1.20 and 1.23, one can get the ratio $R_{\rm exp}(\sqrt{s'})$ of the observed $\pi\pi\gamma(\gamma)$ and $\mu\mu\gamma(\gamma)$ events as a function of $\sqrt{s'}$:

$$\begin{aligned}
R_{\rm exp}(\sqrt{s'}) &= \frac{dN_{\pi\pi\gamma(\gamma)}/d\sqrt{s'}}{dN_{\mu\mu\gamma(\gamma)}/d\sqrt{s'}} \\
&= \frac{\sigma_{\pi\pi(\gamma)}(\sqrt{s'})\,\varepsilon_{\pi\pi\gamma(\gamma)}(\sqrt{s'})}{\sigma_{\mu\mu(\gamma)}(\sqrt{s'})\,(1+\delta^{\mu\mu}_{FSR})\,\varepsilon_{\mu\mu\gamma(\gamma)}(\sqrt{s'})} \\
&= \frac{\sigma_{\pi\pi(\gamma)}(\sqrt{s'})\,\varepsilon_{\pi\pi\gamma(\gamma)}(\sqrt{s'})}{\sigma_{pt}(\sqrt{s'})\,(1+\delta^{\mu\mu}_{add\ FSR})\,(1+\delta^{\mu\mu}_{FSR})\,\varepsilon_{\mu\mu\gamma(\gamma)}(\sqrt{s'})} \\
&= R_{\pi\pi(\gamma)}(\sqrt{s'})\,\frac{\varepsilon_{\pi\pi\gamma(\gamma)}(\sqrt{s'})}{(1+\delta^{\mu\mu}_{add\ FSR})\,(1+\delta^{\mu\mu}_{FSR})\,\varepsilon_{\mu\mu\gamma(\gamma)}(\sqrt{s'})}\,,
\end{aligned} \tag{1.24}$$

where $\sigma_{pt}(\sqrt{s'}) = 4\pi\alpha^2/3s'$ is the cross section for point-like charged fermions and the definition $R_{\pi\pi(\gamma)}(\sqrt{s'}) = \frac{\sigma_{\pi\pi(\gamma)}(\sqrt{s'})}{\sigma_{pt}(\sqrt{s'})}$ is used. The factors $(1+\delta^{\mu\mu}_{FSR})$ and $(1+\delta^{\mu\mu}_{add\ FSR})$ correct for the lowest-order $|FSR|^2$ contribution in $ee \to \mu\mu\gamma$ and additional FSR in $ee \to \mu\mu$ processes. In this procedure, $R_{\pi\pi(\gamma)}(\sqrt{s'})$ can be extracted from the measured ratio $R_{\rm exp}(\sqrt{s'})$ according to Eq. 1.24. And

besides the advantages mentioned above for ISR method, the overall systematic uncertainty on the $\pi\pi$ cross section is reduced, as some individual uncertainties cancels between the pions and muons because of the close kinematics and most of selection conditions in common.

Chapter 2

BABAR experiment

BABAR experiment locates at SLAC, where the *BABAR* detector was built to study the millions of B mesons produced by the PEP-II storage ring. Because of the high luminosity, the PEP-II collider is also called B-factory. This chapter will give a brief introduction to the PEP-II and *BABAR* detector according to the Ref. [27, 28, 29]. More detailed information about the PEP-II, the *BABAR* detector and physics at *BABAR* can found therein.

2.1 The PEP-II Asymmetric Collider

The PEP-II facility is composed by the electron gun, the linear accelerator (linac) and the e^+e^- storage rings, as shown in Fig. 2.1.

The electron beam is produced in the electron gun at the source end of the linac, accelerated by the electric field and pushed into the linac. The electron bunches are accelerated in the linac with synchronized radio-frequency (RF) electromagnetic pulses. When reaching an energy of about 1 GeV, the electron beam is directed into a damping ring, where it circles for some time, during which it losses energy due to synchrotron radiation and is continuously re-accelerated by RF cavities. In this step, spatial and momentum spread of the beam will be reduced. The "damped" beam is then re-directed to the linac and accelerated to 8.9 GeV.

Half of the generated electron bunches are accelerated to approximately 30 GeV, extracted from the linac, and directed onto a tungsten target to generate of the positron beam. After the positron bunches being gathered, they are accelerated, and sent through the return line to the source end of the linac. The positron beam is then accelerated and shaped like the electron beam through the linac and its own damping ring, and finally reach an energy of 3.1 GeV.

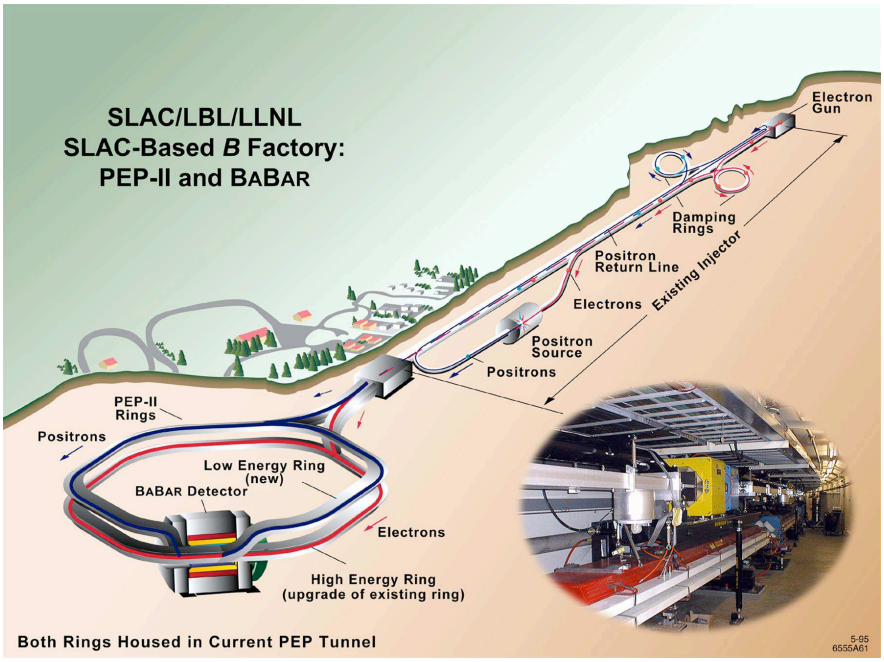

Figure 2.1: A schematic depiction of the B factory accelerator complex at SLAC.

When the respective nominal energies are reached, the electron and positron beams are rejected into the PEP-II storage rings from the linac. The high energy ring is for the electron beam, and the low energy ring is for the positron beam. The beams circle in the rings, being focused further by a complex of magnets and accelerated by RF cavities to compensate the synchrotron-radiation losses. In the interaction region where the *BABAR* detector is located, the electron beam collides head-on with the positron beam. The asymmetric collision of the electron and positron results in a center-of-mass energy $\sqrt{s} = 10.58\text{GeV}$, the mass of $\Upsilon(4S)$ resonance, with a Lorentz boost to the final states of $\beta\gamma = 0.56$ with respect to the *BABAR* detector. As the lightest $b\bar{b}$ state above the $B\bar{B}$ production mass threshold, $\Upsilon(4S)$ decays into $B\bar{B}$ dominantly. The boost is designed to make it possible to measure the decay vertices of B mesons, from which one can determine their relative decay length, and thus extract the time dependence of their decay rates.

The designed instantaneous luminosity of $3 \times 10^{33}\text{cm}^{-2}\text{sec}^{-1}$ for PEP-II has been improved by a factor of four, $12 \times 10^{33}\text{cm}^{-2}\text{sec}^{-1}$, a peak-luminosity record

achieved in August 2006. From the start of the operation in October 1999 to the turnoff in April 2008, the PEP-II has delivered a integrated luminosicy 553.48fb^{-1} in total (Fig. 2.2).

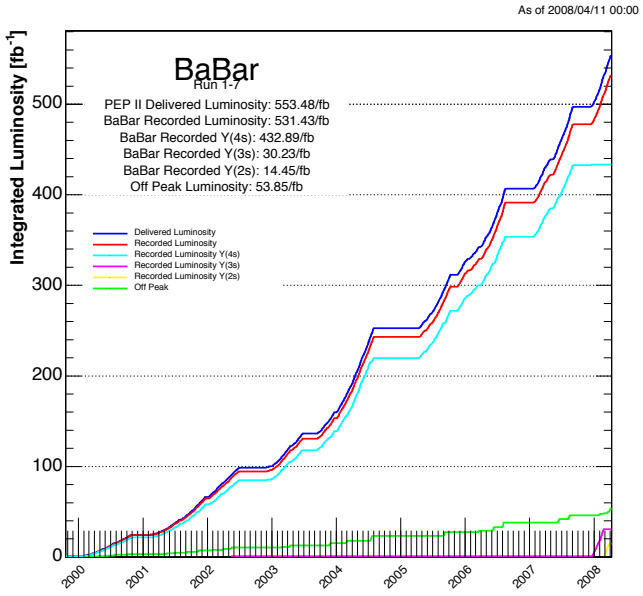

Figure 2.2: The integrated luminosities delivered by the PEP-II and recorded by *BABAR* .

2.2 The *BABAR* Detector

The *BABAR* detector is a large, multi-purpose hermetic detector with several components as shown in Fig. 2.3. The right-handed coordinate system of the *BABAR* detector is defined with z axis pointing to the higher energy (electron) beam running direction (called *forward* direction as well) with a small offset (about 20 mrad) relative to the beam in the horizontal plane, y axis pointing upwards vertically and x axis pointing horizontally away from the center of the PEP-II rings as a consequence. The geometric center of the whole detector is offset relative to the beam-beam interaction point (IP) by 0.37m in the direction of the electron beam in order to maximize the geometric acceptance for the boosted $\Upsilon(4S)$ decays. The inner detector consists of a silicon vertex tracker

(SVT), a drift chamber (DCH), a ring-imaging Cherenkov detector (DIRC), and a CsI calorimeter (EMC). These detector systems are surrounded by a superconducting solenoid that is designed for a field of 1.5T. The steel flux return is instrumented for muon and neutral hadron detection. The polar angle coverage extends to 350mrad in the forward direction and 400 mrad in the backward direction. In order to reduce the effects from multiple Coulomb scattering on tracks, the material in the active volume of the detector is kept to a minimum carefully. The distribution of material in the various detector systems in units of radiation lengths is shown in Fig. 2.4. Each curve indicates the material that a high energy particle traverses before it reaches the first active element of a specific detector system.

2.2.1 The Silicon Vertex Tracker

The tracking system of *BABAR* constituted by the SVT and DCH, is designed to detect charged tracks and measure their vertices, momenta, dE/dx (used for charged particle identification) with high precision. Figure 2.5 shows the longitudinal and transverse sections of the SVT which is specifically optimized for the reconstruction of the primary and secondary decay vertices. It consists of five layer of double-sided silicon strip sensors, which have 6, 6, 6, 16 and 18 modules respectively and cover 90% of the solid angle in the c.m system. The two trips, ϕ trip and z trip, on the opposite sides of each sensor are oriented orthogonally to each other in order to measure the position precisely in both ϕ and z directions. The inner 3 layers are straight and the outer 2 layers have arch shapes which can minimize the amount of silicon to satisfying the coverage angle and increase the crossing angle for the tracks near the edges (see Fig. 2.5 (a)). The inner 3 layers are placed as closely as practically possible to the beam pipe to minimize the influence from multiple scattering. And their modules have a overlap between neighbor modules, which give a full azimuthal coverage. The outer 2 layers have two sub-layers each and are placed at slightly different radii to avoid gap and provide suitable overlaps in ϕ (see Fig. 2.5 (b)), and are mainly used to match SVT tracks with DCH tracks.

The performance of the SVT have been checked that the hit reconstruction

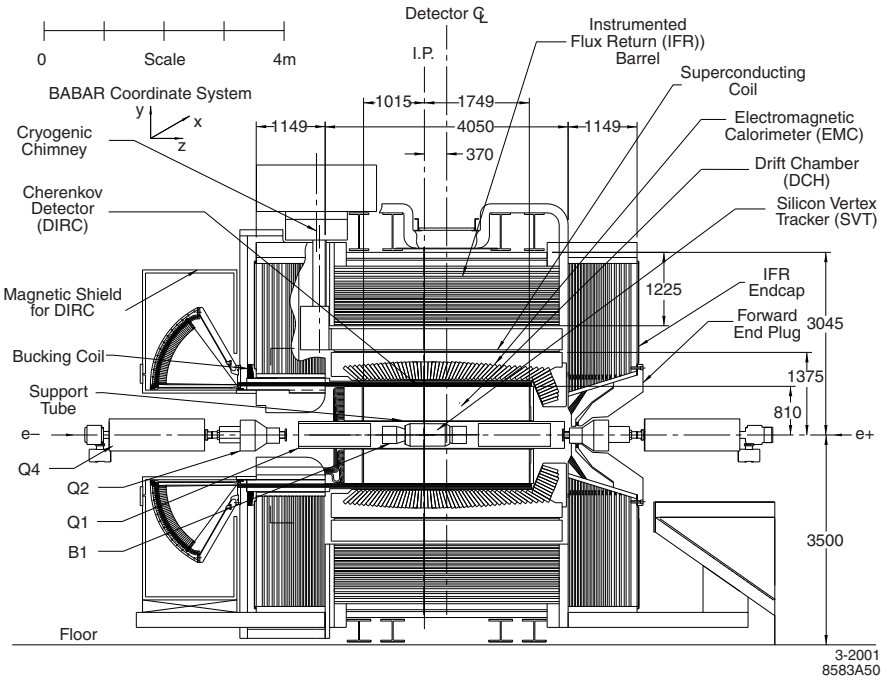

(a) The longitudinal section

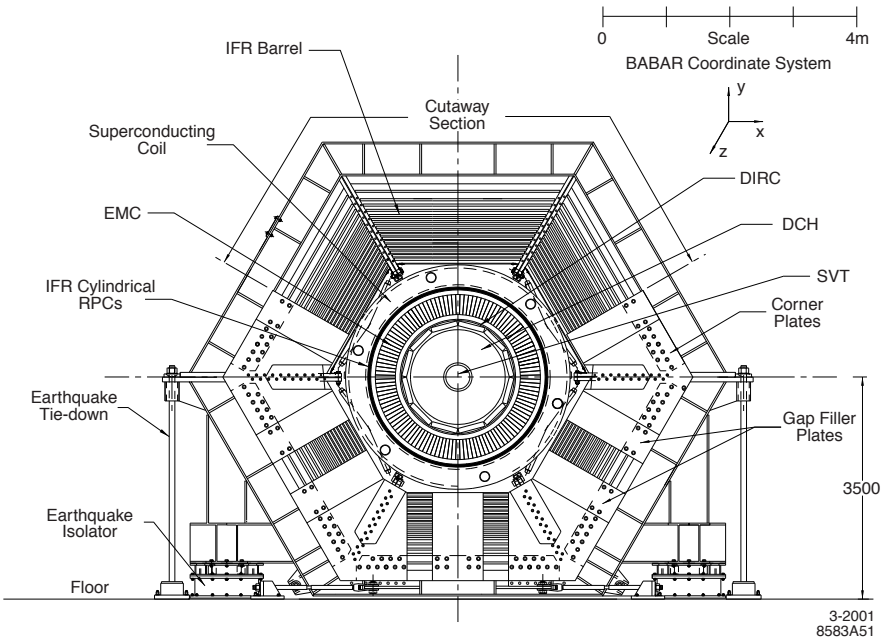

(b) The transverse section

Figure 2.3: The *BABAR* detector.

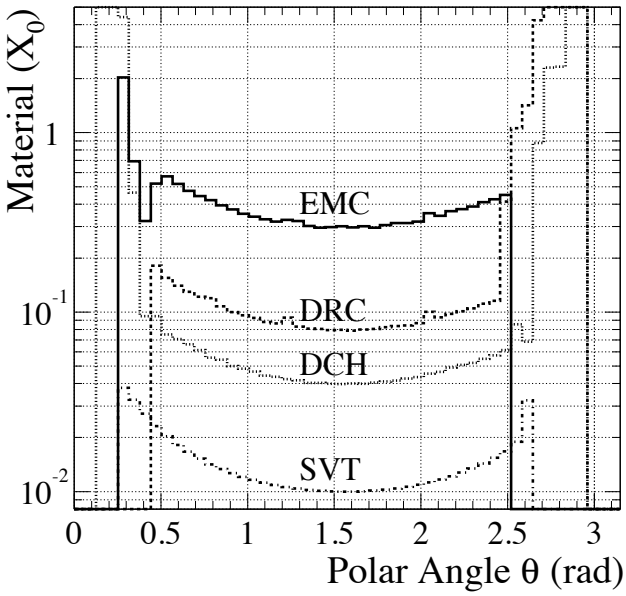

Figure 2.4: Amount of material (in units of radiation lengths) which a high energy particle, originating from the center of the coordinate system at a polar angle θ, traverses before it reaches the first active element of a specific detector system.

efficiency is $\sim 97\%$, the spatial resolution of SVT hits is 10μm $\sim 50\mu$m depending on the orientation of the strip (ϕ or z) and the layer, and the resolution of the dE/dx from the ten measurements per track is $\sim 14\%$.

2.2.2 The Drift Chamber

As the other sub-detector of the tracking system, the multi-wire DCH is designed to measure the momenta and dE/dx for charged tracks. The DCH is built with an inner radius of 26.6 cm, an outer one of 80.9 cm and a length of 280 cm as shown in Fig. 2.6. It has 7104 hexagonal drift cells making ten super-layers of four layers each, thus providing up to 40 position and ionization loss measurements per trajectory. The cells are formed by one gold-coated tungsten-rhenium sense wire, 20μm in diameter, surrounded by six gold-coated aluminum field wires with a diameter of 120μm. To allow position measurements along the beam axis, six super layers are stereo layers with alternating tilts of $\pm(45 \sim 76)$ mrad. The other four super layers are axial. The DCH is filled with a 80:20 gas

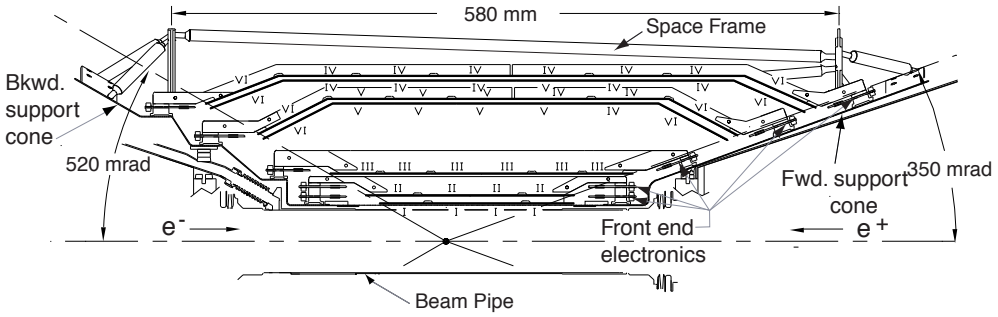

(a) The longitudinal section

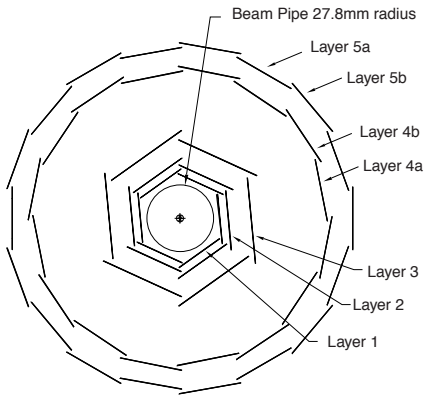

(b) The transverse section

Figure 2.5: The Silicon Vertex Tracker.

mixture of helium and isobutane and operates typically at +1960V, applied to the sense wires.

At the design voltage of 1960V, the DCH tracking efficiency averages $(98 \pm 1)\%$ per track above 200MeV/c and polar angle larger than 500mrad. The position and angle measurements near the IP are dominated by the SVT measurements, the DCH contributes primarily to the pt measurement with a relative resolution

$$\frac{\sigma_{p_t}}{p_t} = (0.13 \pm 0.01)\% \cdot p_t + (0.45 \pm 0.03)\%, \tag{2.1}$$

where the transverse momentum p_t is in GeV/c. The resolution of dE/dx achieved to date is typically 7.5%, which is close to the expected resolution of 7%

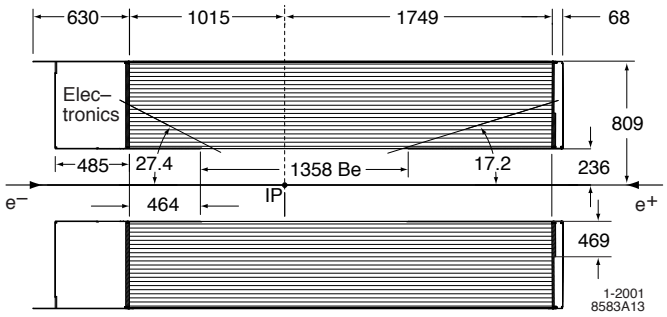

Figure 2.6: Longitudinal section of the DCH with principal dimensions.

and allows the K/π separation for low momenta tracks ($<\sim$ 700GeV/c). The measured dE/dx as a function of track momenta for different charged particles are shown in Fig. 2.7. For the high momenta tracks in the barrel region, the DIRC can complement the PID capability.

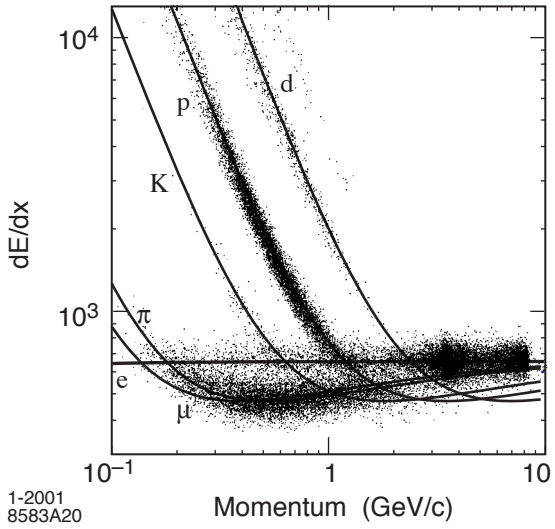

Figure 2.7: The specific energy loss, dE/dx, as a function of track momenta for charged particles, superimposed with Bethe-Bloch predictions.

2.2.3 The Cherenkov Detector

In order to provide good π/K separation, a new of ring-imaging Cherenkov detector called the DIRC (Detector of Internally Reflected Cherenkov light) is used by *BABAR* , which can work for all tracks from the pion Cherenkov threshold

up to 4.2 GeV/c. To minimize the impact on the EMC, the 144 DIRC bars are long but thin and light, which are made of synthetic, fused silica, and arranged in a 12-sided polygonal barrel with 12 bars per side (see Fig. 2.8(b)). The radiator bars cover about 94% of the azimuthal angle and 83% of the polar angle in the CM system. The DIRC photon detector is placed at the backward end to minimize the interference with other sub detector in the forward region. Mirrors are placed at the forward end of the bars to reflect incident photons to the backward end. As shown in Fig. 2.8(a), when a particle which moves faster than the light in the same medium, passes the radiator bars, the Cherenkov radiation happens on a cone with a Cherenkov angle θ_C the value of which can be given by

$$\cos\theta_C = \frac{1}{n\,\beta}, \tag{2.2}$$

where n represents the mean index of refraction of fused silica ($n = 1.473$), $\beta = v/c$, v = velocity of the particle, c = velocity of light in vacuum. Then, these produced photons reflect in the radiator bars, transport to the backward end of the bars, enter the standoff box filled with purified water that has a similar refractive index of $n = 1.346$, and are detected by the PMTs (photo multiplier tubes). The PMTs are at the rear of the standoff box, about 1.2m away from the bar end, arranged into 12 sectors of 896 PMTs each. The magnitudes of angles are maintained upon reflection from a flat surface, so the expected Cherenkov light pattern at this surface where PMTs locate, is essentially a conic section. After a small modification for the refraction at the interface between the bar end and the water, the Cherenkov production angle can be obtained from the cone opening angle and the timing information measured by the PMTs.

From the measured Cherenkov θ_C, one can obtain the velocity of the charged particle, together with the momentum of the matched track, the mass of the particle can be determined or the particle can be identified. The measured Cherenkov θ_C as a function of track momenta for different types of particles are shown in Fig. 2.9(a). Figure 2.9(b) show that the DIRC has an excellent π/K separation, about 8σ at 2GeV/c, still above 4σ at 3GeV/c and about 2.5σ at 4.1GeV/c.

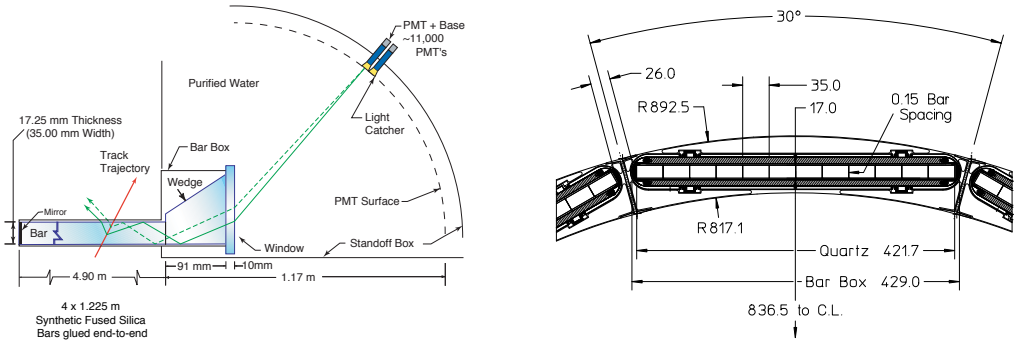

(a) Schematic layout of the DIRC.

(b) Transverse section of the DIRC bar box (mm).

Figure 2.8: The DIRC detector.

2.2.4 The Electromagnetic Calorimeter

In order to measure electromagnetic showers from photons and electrons (positrons) with excellent efficiency, and energy and angular resolution over the energy range from 20MeV to 9GeV, the electromagnetic calorimeter (EMC) of *BABAR* is designed as a hermetic, total-absorption calorimeter, composed of a finely segmented array of thallium-doped cesium iodide (CsI(Tl)) crystals (see Fig. 2.10(a)). The EMC consists of a cylindrical barrel of 48 rings with 120 identical crystals each and a conical forward endcap of 8 rings with 820 crystals in total, which has a full coverage in azimuth and one from 15.8° to 141.8° in polar angle corresponding to a solid-angle coverage of 90% in the center-of-mass system (see Fig. 2.10(b)).

A typical electromagnetic shower spreads over many adjacent crystals, forming a cluster of energy deposits. The clusters should be identified by the reconstruction algorithm. The single cluster with only one local energy maximum is regard as one bump, the merged cluster with more than one local energy maximum should be divided into bumps, and all the bumps should be determined whether come from a charged or a neutral particle with the help of the extrapolation of the tracking information. The achieved energy and angular resolutions

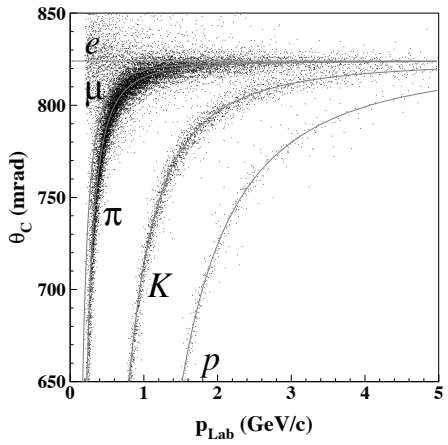

(a) The measured Cherenkov angle θ_c vs track momentum pLab for different charged particles

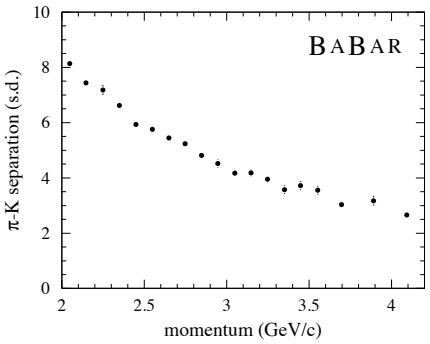

(b) The π/K separation in units of standard deviations.

Figure 2.9: The PID capability of DIRC.

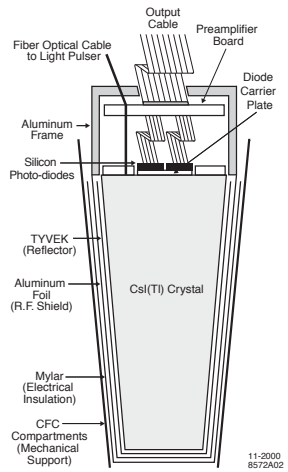

(a) A schematic view of the EMC crystal.

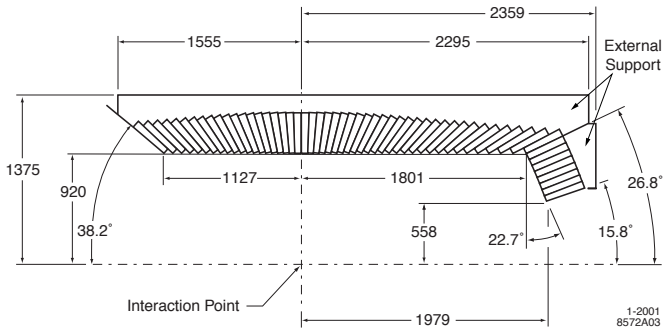

(b) Longitudinal section of the EMC.

Figure 2.10: The plots for EMC.

are given by

$$\frac{\sigma_E}{E} = \frac{(2.32 \pm 0.30)\%}{\sqrt[4]{E(\mathrm{GeV})}} \oplus (1.85 \pm 0.12)\%, \quad (2.3)$$

$$\sigma_\theta = \sigma_\phi = (\frac{3.87 \pm 0.07}{\sqrt{E(\mathrm{GeV})}} + 0.00 \pm 0.04)\ \mathrm{mrad}, \quad (2.4)$$

In both cases, the first term is due to fluctuations in the number of photons and to electronic noise of the photon detector and electronics, while the second term arises from the non-uniformity of light collection, leakage and absorption due to materials between and in front of the crystals, and calibration uncertainties. The most important variable for the discrimination of hadrons from electrons is the ratio of the shower energy to the track momentum (E/p).

2.2.5 The Detector for Muons and Neutral Hadrons

The Instrumented Flux Return (IFR) was designed to identify muons with large solid angle coverage, high efficiency and good purity, and to detect neutral hadrons (primarily K_L^0 and neutrons) over a wide range of momenta and angles with good resolution. The IFR uses the steel flux return of the magnet as a muon filter and hadron absorber, and single gap resistive plate chambers (RPCs) as detectors.

As shown schematically in Fig. 2.11(a), a planar RPC consist of two 2mm-thick bakelite (phenolic polymer) sheets which have large resistivity of $10^{11} \sim 10^{12}\Omega$ cm and a gap of 2 mm between them. The gap is enclosed at the edge by a 7mm wide frame and filled with a non-flammable gas mixture of 56.7% argon, 38.8% freon 134a (CH2F-CF3), and 4.5% isobutane. The inside surfaces of the bakelite sheets are smoothed with a linseed-oil coating so that the electric field is uniform, thus preventing discharges in the gas and large dark currents. The external surfaces of the bakelite sheets are coated with graphite to achieve a surface resistivity of 100KΩ/square, connected to high voltage ($\sim$ 8 KV) and ground, and protected by an insulating mylar film. The RPCs are operated in limited streamer mode and the signals are read out capacitively, on both sides of the gap, by external electrodes made of aluminum strips on a mylar substrate, in two orthogonal directions.

The RPCs are installed in the gaps of the finely segmented steel of the barrel and the end doors of the flux return, as illustrated in Fig. 2.11(b). There are 19 RPC layers in the barrel and 18 in the endcaps. In addition, two layers of cylindrical RPCs are installed between the EMC and the magnet cryostat to detect particles exiting the EMC. The IFR detectors cover a total active area of about $2,000\text{m}^2$.

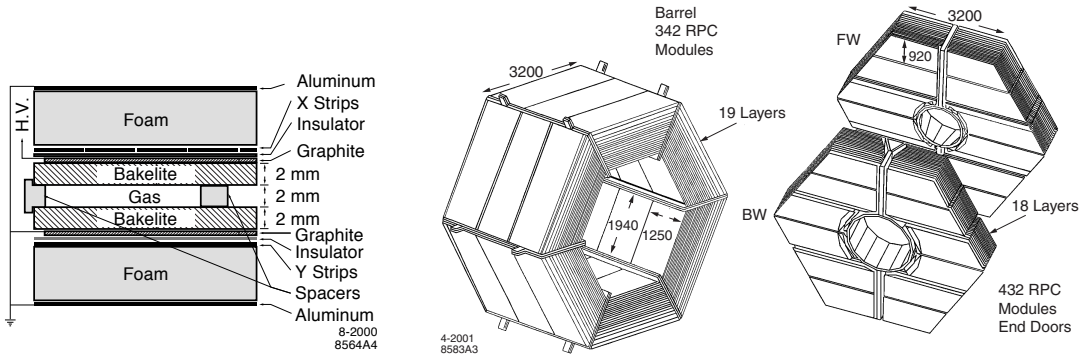

(a) A schematic view of an RPC.

(b) Overview of the IFR: Barrel sectors and forward (FW) and backward (BW) end doors.

Figure 2.11: The plots for IFR.

The results of testing the all RPC modules show that, of the active RPC modules, 75% exceed an detection efficiency of 90%. If the clusters detected by the RPCs are within a predefined distance from the predicted intersection of a charged track and RPCs, which is determined from the extrapolation of the track reconstructed in the SVT and the DCH, consequently they are associated with the track. The information from IFR is almost the only one to identify muon tracks. As illustrated in Fig. 2.12, a muon identification efficiency of close to 90% has been achieved in the momentum range of $1.5 < p < 3.0\text{GeV/c}$ with a fake rate for pions of about $6 \sim 8\%$. The clusters not associated with a charged track, will be regarded to be from neutral hadrons. The directions of the neutral hadrons can be determined from the event vertex and the centroid of the neutral cluster in the IFR.

Not long after the start of data-tacking with *BABAR* , some problems came out with the linseed oil used in the manufacturing of the RPCs which led a

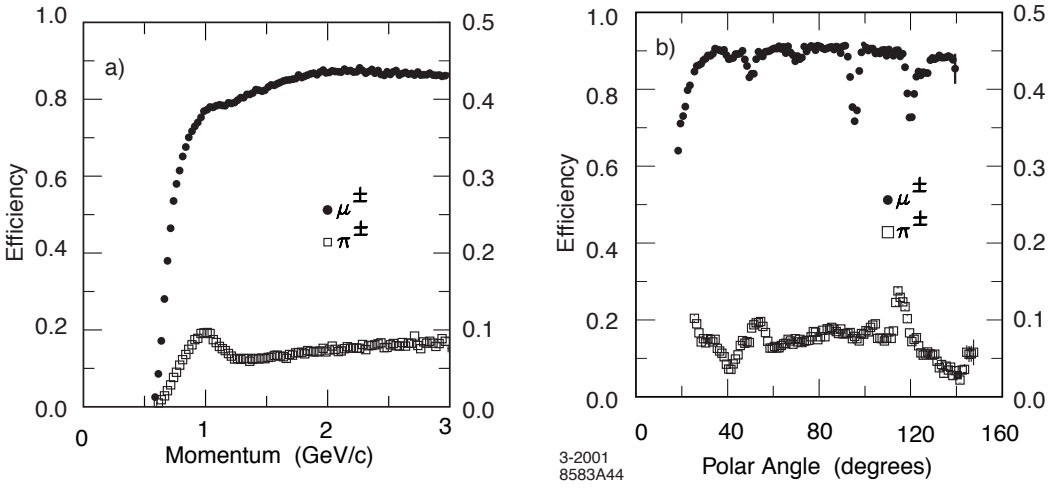

(a) (b)

Figure 2.12: Muon identification efficiency (left scale) and pion misidentification probability (right scale) as a function of (a) the laboratory track momentum, and (b) the polar angle (for $1.5 < p < 3.0$GeV/c momentum), obtained with loose selection criteria (defined in Table 6.2).

continuous significant reduction of the detection efficiency. To avoid losing muon ID capability, the forward endcap was replaced with new improved RPCs in 2002 and the barrel was replaced with Limited Streamer Tubes (LSTs) [30]. But the analysis in this thesis uses the data recorded before the installation of the LSTs exclusively, as μ identification performance is different for different μ detectors, and the systematic error in the analysis dominates, not the statistical one.

2.3 The Trigger System

The trigger system is designed to select events of interest with a high, stable, and well-understood efficiency while rejecting background events and keeping the total event rate under a certain value. The two-level hierarchy trigger system of *BABAR* consists of the Level 1 (L1) in hardware followed by the Level 3 (L3) in software.

The L1 trigger decision is based on charged tracks in the DCH above a preset transverse momentum, showers in the EMC, and tracks detected in the

IFR. These trigger data are processed by three specialized hardware processors, the DCH trigger (DCT), EMC trigger (EMT), and the IFR trigger (IFT). Then the summary data on the position and energy of particles are sent to the global trigger (GLT). The GLT processes all basic trigger information to form specific triggers and then delivers them to the Fast Control and Timing System (FCTS). If the FCTS gives a valid trigger finally, a L1 Accept is issued to initiate event readout. And the trigger definition logic, masks, and pre-scale values are all configurable on a per run basis. The L1 trigger has greater than 99.5% efficiency for $B\bar{B}$ processes.

The L3 trigger software which runs on the online computer farm, comprises event reconstruction and classification, a set of event selection filters, and monitoring. Because the complete event data including the output of L1 trigger can be accessed by the filters at this level, the L3 trigger system can refine and augment the selection methods used in L1. It maintains the $B\bar{B}$ selection efficiency at more than 99% while reducing the data rate to about 200Hz.

Chapter 3

Samples and Event Selection

3.1 Data and Monte Carlo simulated Samples

3.1.1 Data Sample

The analysis is based on the data collected by the *BABAR* detector, in runs 1 through 4. Run 2 is split into 3 parts (a, b, c), reflecting different operating performances of the IFR detector. Data in run 2c are actually removed from this analysis and the determination of R, because of the very poor IFR condition in this period. Measurements are performed separately for all runs, but are generally regrouped into runs 1-2 and runs 3-4 because of important differences in muon ID performances in these two periods.

The data actually used correspond to a total integrated luminosity of

$$\mathcal{L} = 230.81 \text{ fb}^{-1}, \tag{3.1}$$

the details of which are shown in Table 3.1. The systematic uncertainty given is 0.94% (Refs. [39, 40]). Reconstruction releases used are 12.xx for runs 1-2 and 14.xx for runs 3-4.

3.1.2 Monte Carlo Simulated Samples

Simulated events are produced using Monte Carlo (MC) methods. They are used to understand the signal better, develop the event selection criteria, calculate the selection efficiencies and estimate the background contributions.

The corresponding samples of simulated events have been generated with the AfkQED generator with a statistics ~ 5 times larger than data for $\mu\mu\gamma(\gamma)$ and ~ 10 times for $\pi\pi\gamma(\gamma)$. Unlike data, MC generation has been performed requiring that the ISR photon polar angle in center-of-mass is in the range $20^\circ \sim 160^\circ$

Table 3.1: Summary of luminosities (fb^{-1}) for all data sets (taken from Refs. [39, 40]). The splitting of run 2 into (a, b, c) parts is made necessary because of different IFR conditions. *Data from run 2c are not used in this analysis.*

	On peak	Off peak	Total
run 1 (9932-17106)	20.46	2.62	23.07
run 2a (18184-25797)	36.65	4.67	41.32
run 2b (26222-29435)	20.31	2.22	22.52
run 2c (25804-26080)	1.32	0.0	1.32
run 3 (32955-39320)	31.09	2.40	33.49
run 4 (40055-50635)	100.34	10.06	110.41
Sum			232.14

(larger than the detector acceptance), and the energy in the center-of-mass (E^*_γ) is larger than 3 GeV. Thus only $\mu\mu$ or $\pi\pi$ masses less than about 7 GeV are available in the simulation which already cover the low mass range quite well where we want to study.

3.2 Event selection

There are two charged tracks and one hard photon in the final states of $e^+e^- \to \mu\mu\gamma(\gamma)$ and $e^+e^- \to \pi\pi\gamma(\gamma)$. The event selection criteria are:

- any L1 and L3 trigger fired and BGFilter satisfied
- 2 and only 2 good tracks identified as muons or pions, and in the DIRC and IFR active areas
- a photon with the CM energy larger than 3 GeV and in the *BABAR* angular range 0.35-2.4 rad
- an overlap cut in the IFR is applied for runs 1-2 on the two projections (dv_1, dv_2) of the distance between the impact points of the two tracks(see Section 6.1.3 for details); no cut is required in runs 3-4.

Here the 'Good' tracks must satisfy the following requirements:

- $0.4 < \theta < 2.45$ rad
- distance of closest approach to beam axis in xy plane $docaxy < 0.5$ cm
- distance to beam spot along the z axis such that $|dz| < 6$ cm
- momentum $p > 1$ GeV
- number of DCH hits $N_{DCH} \geq 15$
- electron veto $((E_{cal}/p - 1)/0.15)^2 + ((dE/dx_{DCH} - 690)/150)^2 > 1$, E_{cal} is the deposited energy in EMC which is associated to the track.

There is a pre-selection for ISR candidates in order to make relevant analyses more efficient. In pre-section, track definition say 'standard' tracks are used with more relaxed criteria: $docaxy < 2.5$ cm, no cut on the number of DCH hits and momentum only limited by $p_T > 0.1$ GeV.

All types of ISR events are pre-selected requiring an OR of three conditions:

- at least two standard tracks with zero total charge total, and the angle between the missing momentum vector (including photons, but excluding the highest energy in the e^+e^- center-of-mass system, called ISR photon) and the ISR photon less than 0.3 rad;
- any odd number of standard tracks (for the study of tracking efficiency) 0;
- at least one K_s^0 candidate (2 tracks with secondary vertex and mass in a window around K_s^0 mass).

The large majority of $\mu\mu\gamma$ (and $\pi\pi\gamma$) events are selected by the first condition, the second accounting for only 2% of the final sample and the third being negligible (6×10^{-5}).

3.3 Data-MC corrections for the efficiency difference

The goal of the analysis is to measure the amount of the produced signals with high precision, where the absolute overall efficiencies are really important

and dominate the systematic errors. As we know, the generation and simulation of MC sample are not perfect, there are always some differences between data and MC. This analysis uses as a starting point the MC simulation for acceptance, trigger, tracking, particle ID, kinematic fit constraint and so on. Through specific studies we can determine the ratios of efficiencies obtained in data and simulation, and apply them as corrections to the MC global efficiency. Thus, the corrected acceptance is

$$\varepsilon = \varepsilon_{\rm MC} \left(\frac{\varepsilon^{\rm data}_{trigger}}{\varepsilon^{\rm MC}_{trigger}}\right) \left(\frac{\varepsilon^{\rm data}_{tracking}}{\varepsilon^{\rm MC}_{tracking}}\right) \left(\frac{\varepsilon^{\rm data}_{PID}}{\varepsilon^{\rm MC}_{PID}}\right) \cdots . \tag{3.2}$$

Generally, to make all the corrections multipliable, one correction for a certain selection cut should be studied using the sample satisfying the cuts studied already, except in the case that there is little correlation between them. These corrections are reviewed in turn in the next chapters.

Chapter 4

Trigger and Filter Efficiencies

4.1 General method

No specific trigger configuration is required at analysis level, in fact the OR of all lines at a given trigger level is set. Trigger efficiencies are measured after applying the exact same selections on data and simulation samples. Efficiencies are computed by crossing the response of trigger lines, after choosing lines as orthogonal and as efficient as possible.

The method is best explained for L3 trigger where two lines dominate the overall efficiency: one-track trigger (T_1) and calorimetric trigger (EM). On both data and Monte-Carlo the efficiency of T_1 can be determined by selecting the samples satisfying the EM condition. The overall efficiency is given by the OR of the two conditions. This is only true in the absence of correlations between the two trigger lines. Although this may apparently be true due to the nature of the requirements, it is in fact not the case. Both trigger efficiencies are affected by the spatial topology of the event. Indeed T_1 has a lower efficiency when the two tracks overlap in the tracking system, while EM is more easily satisfied when the two overlap in the EMC. Since these two effects occur for similar $\mu\mu$ or $\pi\pi$ masses (around 0.4-0.5 GeV), a clear anti-correlation is expected and found. This leads to a bias between the efficiency determined by the method and the true one.

Two points need to be emphasized. First, background is subtracted in data (mainly for $\pi\pi$ channel) using MC, for the direct efficiency determination. Second, biases are determined with simulation. However once the origin of the bias has been identified, an indirect assessment of the data/MC consistency is performed.

The method has been applied to the determination of L1, L3, and BGFilter efficiencies. The difficulty in this analysis is that trigger efficiencies have to be

determined for a sample unbiased with respect to the number of tracks actually reconstructed. In practice, one and two-track samples are sufficient, but the former sample contains more non-$\mu\mu\gamma$ background which has to be studied and subtracted out. For all details, see Ref. [31].

4.2 Trigger efficiency correction to the $\mu^+\mu^-\gamma$ cross section

L_1 data/MC corrections for the $\mu^+\mu^-\gamma$ cross section are found to be smaller than 2×10^{-4} in runs 2-4 and a conservative systematic error of 1×10^{-4} is assigned. The situation is different in run 1: a correction up to $\sim (3 \pm 2) \times 10^{-3}$ needs to be applied at low mass ($m_{\mu\mu} \sim 0.4 - 0.6$ GeV), decreasing to $\sim 10^{-3}$ at 1 GeV.

The L_3 efficiency for $\mu^+\mu^-\gamma$ is dominated by the track trigger T_1, as the EM trigger is only satisfied at the 10% level for $\mu^+\mu^-\gamma$. This fact limits the precision of the measurement as EM should be required to determine the T_1 efficiency. The latter is controlled by track overlap in the DCH with a relevant variable as the difference $\Delta\phi$ of the azimuthal angles of μ^+ and μ^-. The bias between the measured and the true efficiency is also studied through $\Delta\phi$ distributions. Its origin in terms of simultaneous overlap in the DCH and the EMC has been clearly demonstrated. The global correction to the MC L_3 efficiency is given in Fig. 4.1. To illustrate the statistical power of the full data set, each efficiency and bias in data and MC is adjusted by a fit as a function of $m_{\mu\mu}$, resulting in the shaded band in Fig. 4.1. However, the individual results in each mass bin, with errors dominated by statistics, hence uncorrelated, are used for correcting the $\mu\mu$ mass spectrum. Above 2.5 GeV the correction is set to 1 with a decreasing uncertainty. The L_3 correction is rather large, about 1% at 0.7 GeV, and known to a precision of 3×10^{-3}, increasing to 5×10^{-3} for $m_{\mu\mu} < 0.5$ GeV.

BGFilter inefficiency has been found to be $< 10^{-4}$ in both data and MC for $\mu^+\mu^-\gamma$.

4.3 Trigger efficiency correction to the $\pi^+\pi^-\gamma$ cross section

L1 data/MC corrections for the $\pi^+\pi^-\gamma$ cross section through the R ratio are found conservatively below 5×10^{-4}.

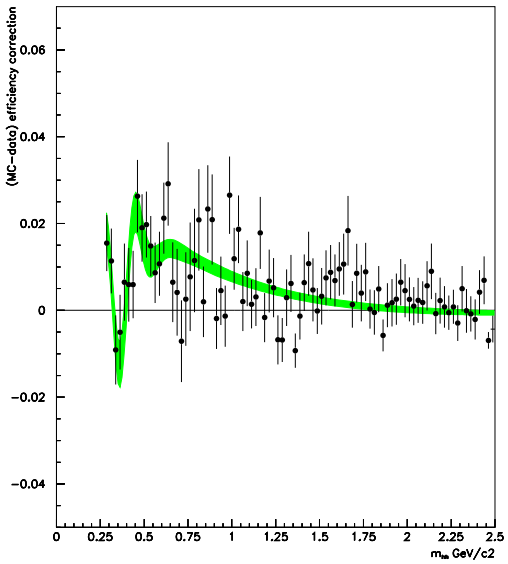

Figure 4.1: Global data/MC correction for $\mu^+\mu^-\gamma$ to be applied to the MC efficiency of the L_3 trigger as a function of $m_{\mu\mu}$, including the bias in the measurement method. The band is the result of fit and represents the correction with its systematic uncertainty. Runs 1-4.

As already mentioned, the L3 level involves the track trigger T_1 and the EM trigger. Both of them are efficient for $\pi^+\pi^-\gamma$ events. Similarly, the T_1 efficiency is controlled by track overlap in the DCH conveniently parameterized by the difference $\Delta\phi$ of the azimuthal angles of π^+ and π^- tracks. The bias between the measured and the true efficiency is also studied through $\Delta\phi$ distributions. Its origin in terms of simultaneous overlap in the DCH and the EMC has been clearly demonstrated. The global correction to the MC L3 efficiency is given in Fig. 4.2 as a function of $m_{\pi\pi}$. The L3 correction is small, about 2×10^{-3} at the ρ peak, and known to a precision better than 10^{-3}.

Unlike for muons, the BGFilter inefficiency for $\pi^+\pi^-\gamma$ events has been found to be quite significant in data, at least at low mass. The pion tagging is tightened respect to the standard pi-ID to reduce backgrounds. As seen in Fig. 4.2 the

correction with respect to simulation amounts to 4% at threshold, decreasing to 1.5% at 0.4 GeV and 2.6×10^{-3} at the ρ peak (see Ref. [31] for details). Systematic uncertainties are 1.0×10^{-3} in the ρ region, estimated from the study of the measurement bias on the BGFilter efficiency, but significantly increased to 0.5% at 0.5 GeV and 3% below 0.35 GeV.

Above 1.4 GeV the determinations are limited by the smaller statistics of pions and the larger background. The correction is expected to go to zero at larger masses because overlap effects vanish. A value of 0 is assumed with a conservative error of 0.4%.

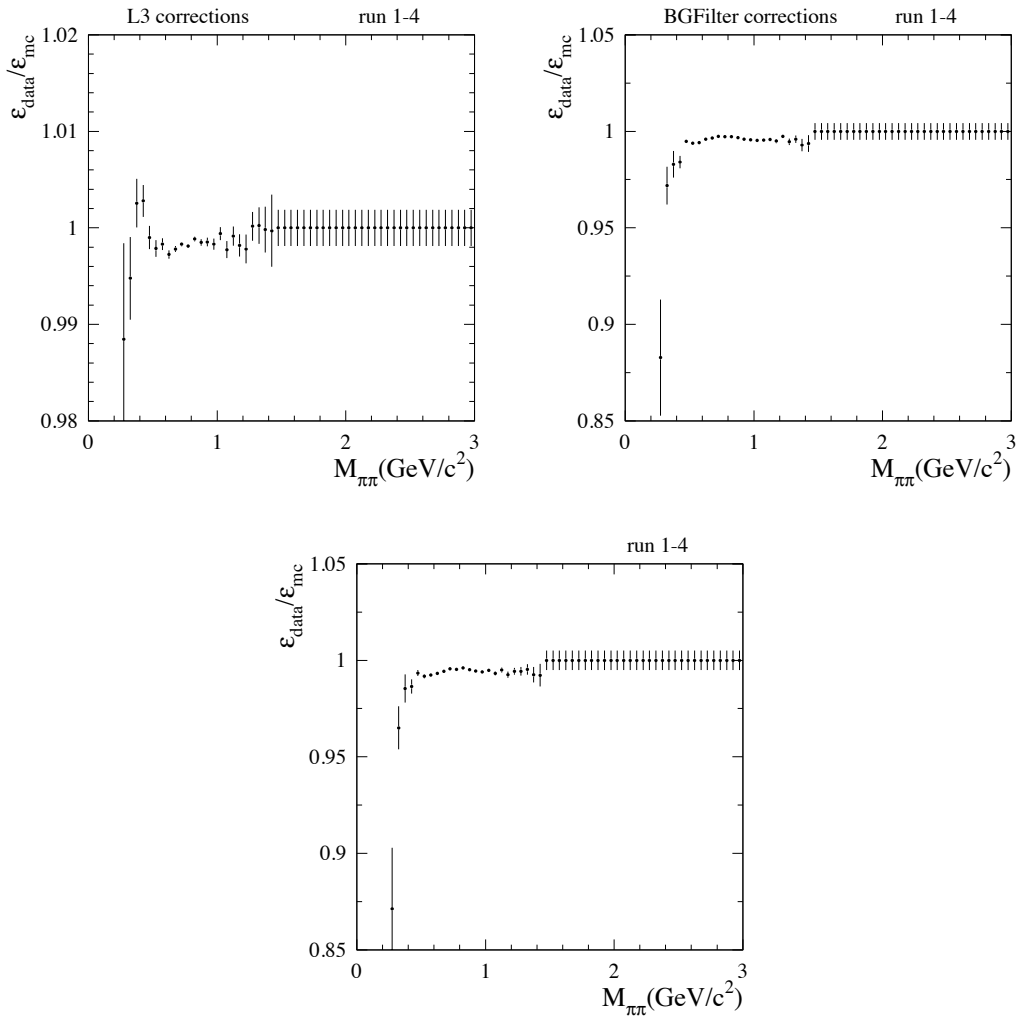

Figure 4.2: Global data/MC correction to the $\pi^+\pi^-\gamma$ cross section, applied to the MC efficiency of the L3 trigger (top left) and the BGFiflter (top right) as a function of $m_{\pi\pi}$ in GeV. The bottom plot gives the total trigger+BGFilter correction. Runs 1-4.

Chapter 5

Tracking Efficiency

5.1 Principle of measurement

A 1C kinematic fit (defined bellow) is used to select $\mu^+\mu^-\gamma$ and $\pi^+\pi^-\gamma$ events for tracking efficiency studies. The fit is performed using as input only one muon or pion track (called 'primary') and a photon, and the momentum vector of the second muon or pion is predicted. Testing whether the predicted track has been actually reconstructed in the tracking system, with a charge opposite to that of the primary track, yields over a finite track sample the tracking efficiency.

Conditions must be satisfied to ensure the validity of the measurement:

- the event must be triggered on and selected without specific requirements on the second track,
- a pure $\mu^+\mu^-\gamma$ and $\pi^+\pi^-\gamma$ samples are selected, with additional cuts to enhance the purity, in addition to the kinematic fit,
- attention is given to the angular and momentum resolution of the predicted track since it must fulfill the tracking acceptance.

The determination of the tracking efficiency is based on the assumption that the efficiencies of the two tracks are uncorrelated. However, a very sharp increase of the tracking inefficiency is observed for overlapping tracks in the DCH. Not only the individual track efficiency is locally reduced, but a correlated loss of the 2 muon or pion tracks can occur. These effects have been studied in details [32].

It should be emphasized that the method determines the efficiency to reconstruct a given track in the SVT+DCH system somewhere in a specified geometrical acceptance, no matter how close or distant this track is with respect to the

real one. However, the possible mismatch in momentum and/or angles will affect the full kinematic reconstruction of the event and its effect will be included in the efficiency of the corresponding χ^2 cuts used for the physics sample.

The final physics sample is required to have 2 and only 2 good tracks (good track is defined in Section 3.2) with opposite charges, so that the understanding of the tracking involves not only track losses, but also the probability to reconstruct extra tracks as a result of secondary interactions with the detector material or the presence of beam-background tracks. This effect is very small for muons, but not for pions.

A lot of attention has been paid to biases affecting the tracking efficiency measurement as a result of the selection of the primary track and of the event-level background cuts. All components are evaluated and included in the results.

Because of backgrounds, the pion tracking efficiency can be obtained directly for data only in the ρ peak region, 0.6 to 0.9 GeV. Below and above this region, the results are too sensitive to the background subtraction. However the two main sources of track loss have been identified —the track overlap in the DCH and the secondary interactions. Since both effects can be separated looking at the $\Delta\phi$ distribution of the tracking inefficiency in the clean ρ peak region, it is possible to extrapolate this behavior in other regions with this "two-component" model.

The event correction C_{track} to be applied to the MC tracking acceptance involves all effects studied above: it is the product of the ratios in data over MC of (1) the square of the tracking efficiencies, (2) the probability for not loosing the two tracks in a correlated way (loss probability = f_0), and (3) the probability for not having an extra reconstructed track (loss probability = f_3). Therefore:

$$C_{track} = \left(\frac{\epsilon_{track}^{data}}{\epsilon_{track}^{MC}}\right)^2 \frac{(1-f_0-f_3)^{data}}{(1-f_0-f_3)^{MC}}. \tag{5.1}$$

For all details, see [32].

5.2 Tracking efficiency correction to the $\mu^+\mu^-\gamma$ cross section

Figs. 5.1 and 5.2 summarize the three corrections as a function of the $\mu\mu$ mass and the overall correction $C^{\mu\mu}_{track}$ for runs 1-2 and 3-4, respectively, where for reading convenience the quantity plotted is $1 - C^{\mu\mu}_{track}$. The latter amounts to $1.0 \sim 1.5\%$ at threshold and $0.4 \sim 0.5\%$ above 2 GeV, with a uniform decrease in between. Since all the bins have uncorrelated statistics and all the bias sources are smooth, it is possible to parameterize the mass dependence of the correction and obtain the band shown on the figures. The results of the fits show that the tracking corrections to the $\mu^+\mu^-\gamma$ MC efficiency are obtained with a statistical precision of 0.6×10^{-3} for runs 1-4, fully correlated over the complete mass spectrum. However the point-to-point results with their individual errors are used to correct the mass spectrum.

In principle, all systematic effects (in the sense of differences between the *BABAR* simulation and the actual detector performance) are contained in the ratio of tracking efficiency measurements between data and MC. However, additional systematic uncertainties, not included in the statistical errors of the measurements, originate at different steps in the analysis when, for very small components of the tracking loss, no direct data/simulation comparison could be performed. For those components, the ratio data/MC was assumed to be one and a 100% systematic error was assigned to this part, when no additional information was available.

Table. 5.1 shows the summary of the systematic uncertainties on the tracking efficiency correction measurement for $\mu^+\mu^-\gamma$. The different contributions are added quadratically for a total uncertainty of 0.8×10^{-3} from 0.4 to 1 GeV, completely correlated over the $\mu\mu$ mass spectrum.

5.3 Tracking efficiency correction to the $\pi^+\pi^-\gamma$ cross section

Figs. 5.3 and 5.4 summarize the three sources of inefficiency as a function of the $\pi\pi$ mass and the overall inefficiency on the cross section. The direct mea-

Table 5.1: Systematic uncertainties ($\times 10^{-3}$) on the $\mu^+\mu^-\gamma$ cross section determination from the tracking measurements in 3 mass ranges. The first three groups of rows refer to the track inefficiency, the 2-track correlated loss, and the probability to reconstruct an extra track. The last row gives results from a global test performed on the simulation where the true tracking efficiency is known. For the total uncertainty, all components have been added in quadrature, with the track inefficiency uncertainties counted twice.

source \ mass ranges	$0.4 - 1$ GeV	< 0.4 GeV	> 1 GeV
limited θ range	0.2	0.2	0.2
predicted track resolution	0.1	0.1	0.1
χ^2 and additional radiation	0.2	0.2	0.2
docaxy cut	0.2	0.2	0.2
0-good 2-standard tracks	0.3	0.3	0.3
only 1 extra good track	< 0.1	< 0.1	< 0.1
MC test true/measured	0.3	1.5	1.0
total	0.8	1.7	1.3

surement of the tracking efficiency is only done in the ρ region and it is extended outside using the two-component model. The fraction f_0 of correlated 2-track loss is measured with events containing two standard *BABAR* tracks (standard track is defined in Section 3.2) not satisfying the stricter definition of good tracks used in this analysis. With the good track definition, few tracks from secondary interactions are included in the physics sample, and so the probability to register more than two good tracks (f_3) is very small, 1.7×10^{-3} in the simulation and 3 times less in data. Since no mass dependence is observed in the MC, the same behavior is assumed for the data.

The final correction $C^{\pi\pi}_{track}$ to the $\pi^+\pi^-\gamma$ cross section is given in Fig. 5.5 for runs 1-2 and 3-4. The correction amounts to about $2.5 \sim 3.5\%$ at threshold and $1.5 \sim 2\%$ on the ρ peak.

The point-to-point errors in Fig. 5.5 are correlated as the result of using the two-component model. Therefore they are introduced as systematic uncertainty: 1.9×10^{-3} and 1.4×10^{-3} for runs 1-2 and 3-4, respectively, both at the ρ peak. All

the values are given in Table 5.2, they are uncorrelated between the two running periods.

Table 5.2: Systematic uncertainties ($\times 10^{-3}$) on the $\pi\pi\gamma$ cross section determination from the tracking measurements in 5 mass ranges (in GeV).

runs \ mass ranges	< 0.4 GeV	$0.4 - 0.6$ GeV	$0.6 - 0.9$ GeV	$0.9 - 1.2$ GeV	>1.2 GeV
$1 - 2$	6.	3.	1.9	3.	5.
$3 - 4$	5.	3.	1.4	2.	4.
$1 - 4$	3.8	2.1	1.1	1.7	3.1

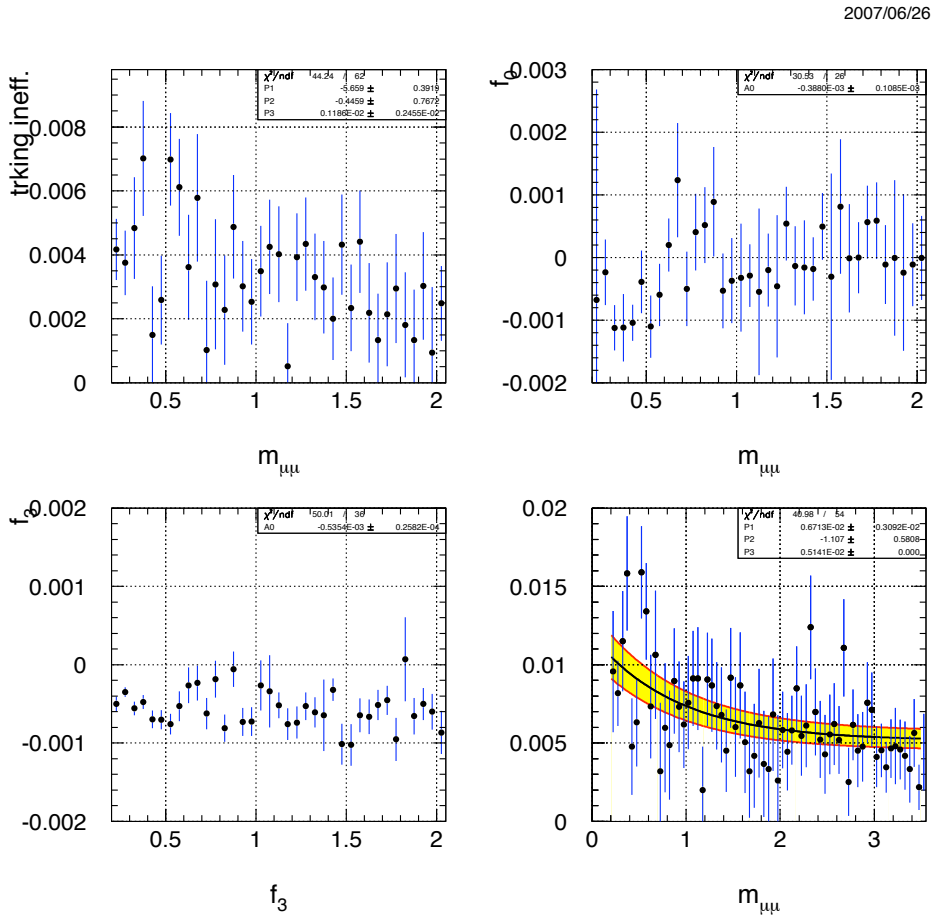

Figure 5.1: The data/MC corrections for tracking efficiency $(1-\epsilon^{data}_{track}/\epsilon^{MC}_{track}$, top-left), correlated 0-track fraction $(1-(1-f_0^{data})/(1-f_0^{MC})$, top-right), extra-track probability $(1-(1-f_3^{data})/(1-f_3^{MC})$, bottom left), and the overall correction $1-C^{\mu\mu}_{track}$ (see text) for the $\mu^+\mu^-\gamma$ cross section (bottom right). The band indicates the fit to the statistically uncorrelated data points. Runs 1-2.

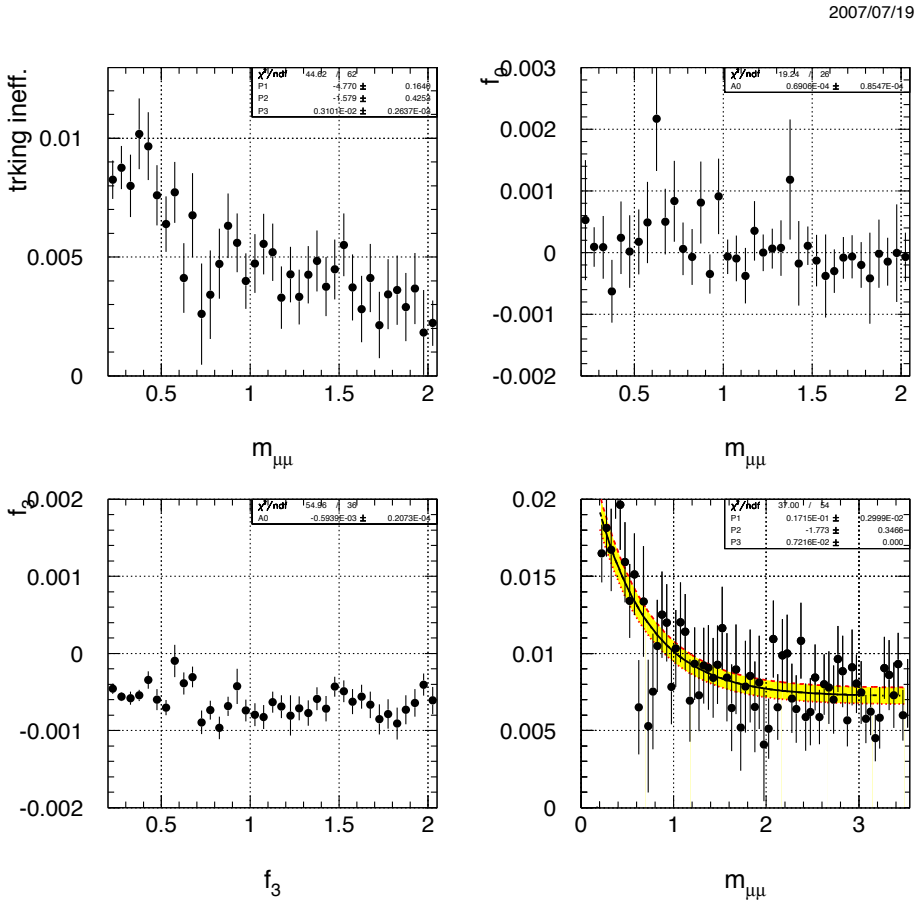

Figure 5.2: The data/MC corrections for tracking efficiency $(1 - \epsilon^{data}_{track}/\epsilon^{MC}_{track}$, top-left), correlated 0-track fraction $(1 - (1 - f_0^{data})/(1 - f_0^{MC})$, top-right), extra-track probability $(1 - (1 - f_3^{data})/(1 - f_3^{MC})$, bottom left), and the overall correction $1 - C^{\mu\mu}_{track}$ (see text) for the $\mu^+\mu^-\gamma$ cross section (bottom right). The band indicates the fit to the statistically uncorrelated data points. Runs 3-4.

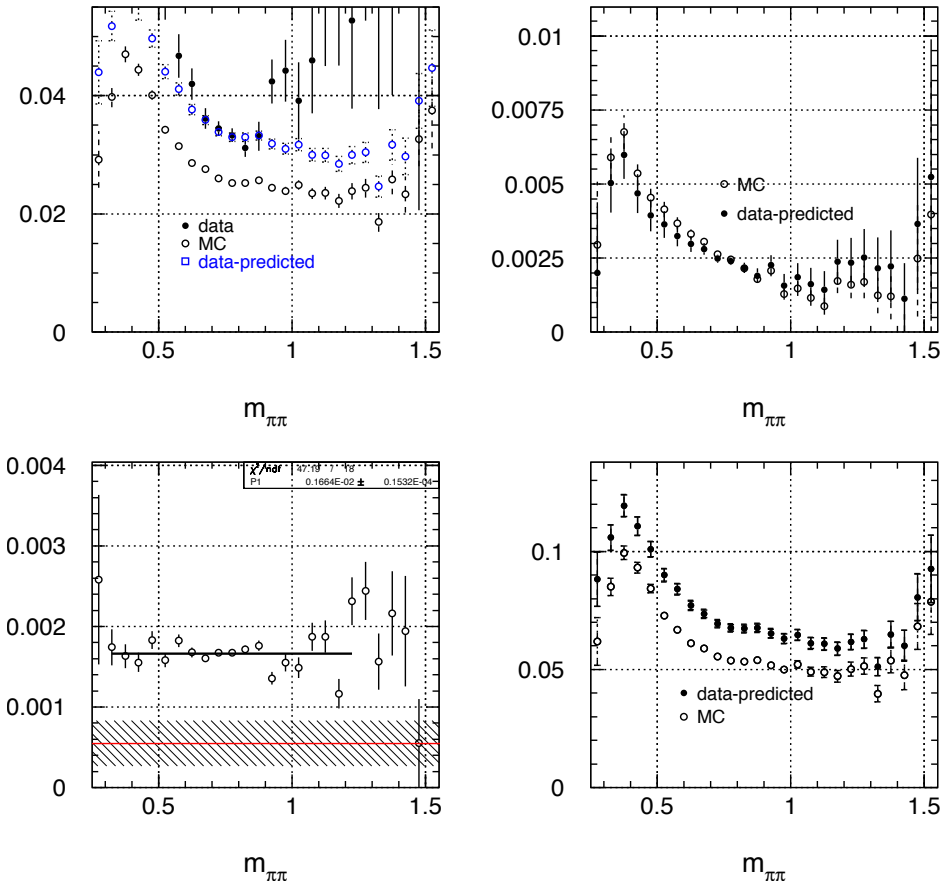

Figure 5.3: The tracking inefficiencies (top left), the 2-track correlated loss (f_0, top right), the probability of extra tracks (f_3, bottom left, the hatched band indicates the data determination), and one minus the total correction for tracking (bottom right) in $\pi\pi\gamma$ events ($1-\epsilon_{trk}^2(1-f_0-f_3)$): data (closed points), MC (open points), runs 1-2.

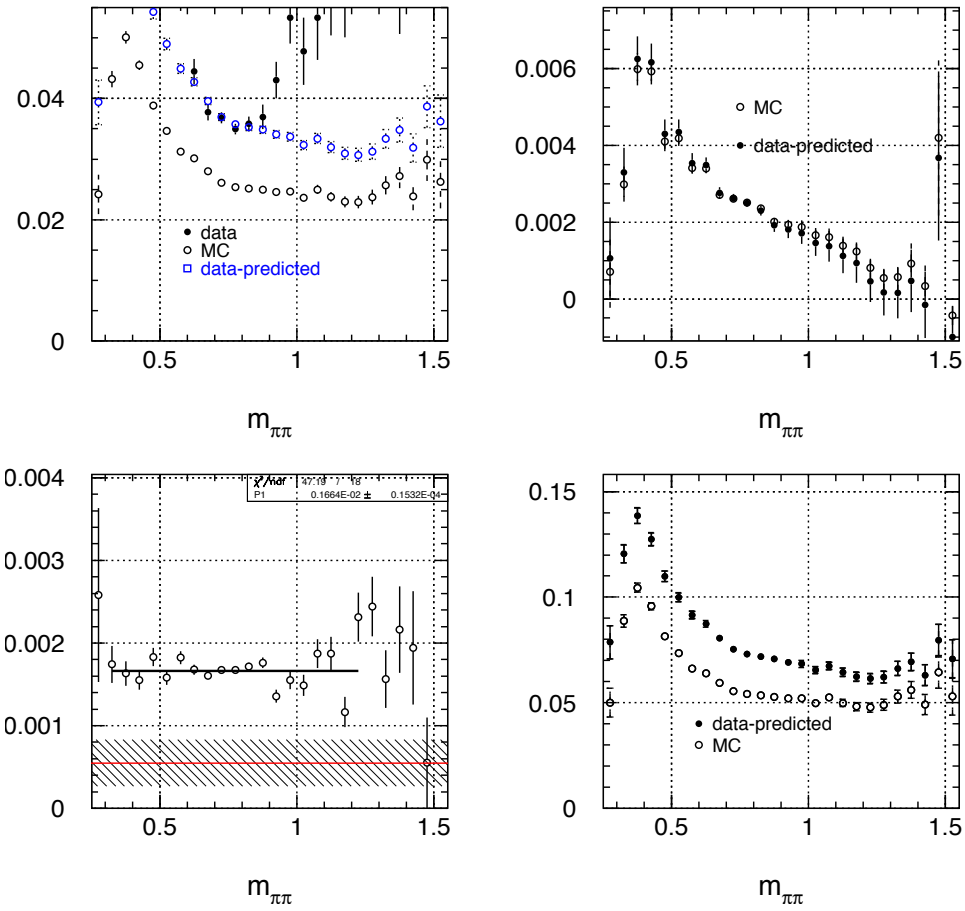

Figure 5.4: The tracking inefficiencies (top left), the 2-track correlated loss (f_0, top right), the probability of extra tracks (f_3, bottom left; the hatched band indicates the data determination), and one minus the total correction for tracking (bottom right) in $\pi\pi\gamma$ events ($1 - \epsilon_{trk}^2(1 - f_0 - f_3)$): data (closed points), MC (open points), runs 3-4.

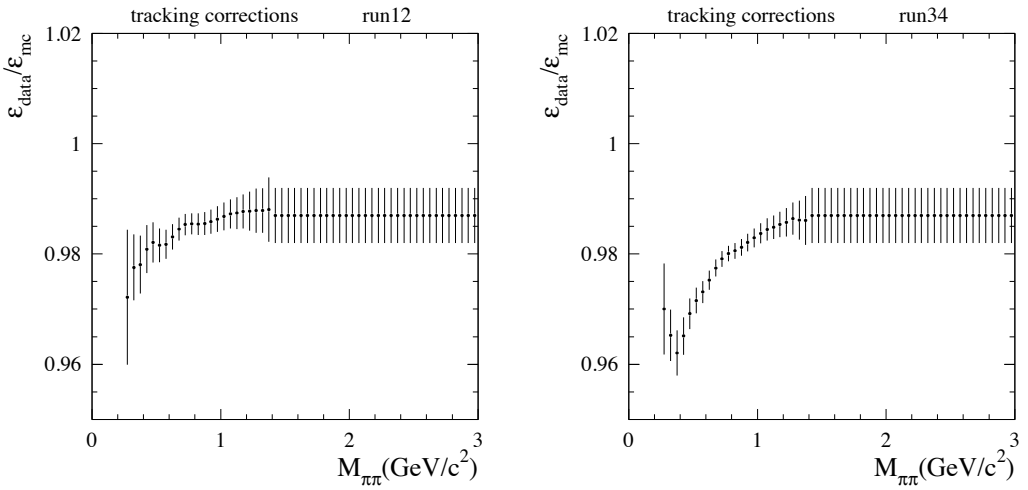

Figure 5.5: The overall tracking data/MC correction $C^{\pi\pi}_{track}$ for the $\pi\pi\gamma$ cross section (see text). Runs 1-2 (left) and 3-4 (right).

Chapter 6

Particle Identification

In fact, particle ID is the only tool to separate $\mu^+\mu^-\gamma$ and $\pi^+\pi^-\gamma$ events. The measurements of the particle ID efficiencies in this analysis aim at obtaining from data the values for all the elements $\epsilon_{i\ true \to j\ ID}$ of the efficiency matrix (Table 6.1), where i is one of e, μ, π, or K. Protons (antiprotons) are not included in the particle hypotheses since the $p\bar{p}\gamma$ final state occurs only at a very small rate, requiring a dedicated analysis already performed in *BABAR* (see Ref. [21]), and is subtracted statistically. Apart from the identification of physical particle types, the $'0'$ ID type is assigned when the number of photons in the DIRC is not sufficient to define a Cerenkov ring, thus preventing π-K separation. The ID classes defined in Table 6.1 constitute a complete and orthogonal set which is convenient for studying cross-feed between different final states.

6.1 Muon-ID Efficiency

6.1.1 Muon-ID and method

Particles are identified as muons if they fulfil the cut-based 'muMicroLoose' condition (see Table 6.2). The method to determine the muon ID efficiency makes use of the $\mu^+\mu^-\gamma$ sample itself, where one of the produced charged particles is tagged as muon. The sample is restricted to $m_{\mu\mu} > 2.5$ GeV to reduce the non-μ background at the $(1.1 \pm 0.1) \times 10^{-3}$ level, so that the ensemble of opposite particles constitutes a pure muon sample.

Since the performance of the IFR in runs 1-4 has been uneven and deteriorating with time, it has been necessary to map the behavior of the efficiency, both in space and in time. For this, the opposite muon track is extrapolated to the IFR where local coordinates (v_1, v_2) are defined depending on the IFR geometry. Efficiency maps are obtained for each running period (runs 1, 2a, 2b, 3, 4). Due

Table 6.1: Definition of particle ID types (first column) using combinations of experimental conditions (first row): "+" means "condition satisfied", "−" means "condition not satisfied", an empty box means "condition not applied". The conditions μ_{ID} and K_{ID} correspond to the cut-based 'muMicroLoose' and likelihood-based 'kLHTight' flags on the microDST, respectively. The variable E_{cal} corresponds to the energy deposit in the EMC associated to the track.

	μ_{ID}	$E_{cal}/p > 0.8$	$N_{DIRC} \leq 2$	K_{ID}
'μ'	+			
'e'	−	+		
'0'	−	−	+	
'K'	−	−	−	+
'π'	−	−	−	−

Table 6.2: Definition of μ ID classes according to Ref. [34]. Ecal: the energy deposited in the EMC; N_L: the number of IFR hit layers in a cluster; λ: the number of interaction length traversed by the track in the *BABAR* detector; $\Delta\lambda = \lambda_{\rm exp} - \lambda$, $\lambda_{\rm exp}$: the expected number of interaction length traversed by the track in the *BABAR* detector; $T_C = \frac{N_L}{L_h - F_h + 1}$ if the cluster has a inner RPC hit, otherwise $T_C = \frac{N_L}{L_h - F_h}$, F_h and L_h are the first and last IFR hit layer in the cluster respectively; m: the average multiplicity of hit strips per layer; σ_m: the standard deviation of m; χ^2_{trk}: the χ^2/DF of the IFR hit trips in the cluster with respect to the track extrapolation; χ^2_{fit}: the χ^2/DF of the IFR hit trips with respect to a 3-rd order polynomial fit of the cluster.

	VeryLoose	Loose	Tight	Very Tight
Ecal(GeV)	< 0.5	< 0.5	$(0.05, 0.4)$	$(0.05, 0.4)$
N_L	≥ 2	≥ 2	≥ 2	≥ 2
λ	> 2	> 2	> 2.2	> 2.2
$\Delta\lambda$	< 2.5	< 2.0	< 1	< 0.8
T_C	> 0.1	> 0.2	> 0.3	> 0.34
m	< 10	< 10	< 8	< 8
σ_m	< 6	< 6	< 4	< 4
χ^2_{trk}	−	< 7	< 5	< 5
χ^2_{fit}	−	< 4	< 3	< 3

to the mass cut, these maps provide the muon efficiency for isolated muon tracks. Special attention is given to optimize the granularity of the 3D maps (p, v_1, v_2).

The low-efficiency regions in the IFR are removed in order to keep as active areas only the regions where the μ-ID efficiency is reasonably homogeneous. This is the case for the crack areas between modules and some parts of the nominal active region where the IFR performance is strongly degraded. The definition of the latter removed regions are markedly run-dependent: in run 1 only cracks are removed, while in run 4 an additional $\sim 15\%$ of solid angle has to be cut out. As the $\mu^+\mu^-\gamma$ dynamics is known from QED, the corresponding loss of events is accurately evaluated and included in the overall acceptance.

The main problem affecting the determination of μ-ID efficiency is the correlation between close tracks in the IFR, occurring for $m_{\mu\mu} < 2.5$ GeV, *i.e.* the most interesting region for the R measurement.

For all details, see Ref. [33].

6.1.2 Muon ID efficiency for close tracks in the IFR

The efficiency maps for isolated tracks parameterize the local performances of the IFR at the track impact point. However, at $\mu\mu$ masses less than 2.5 GeV, tracks can get close in the IFR and their respective ID efficiencies are very significantly affected. First, one expects the efficiency to be reduced with respect to the 'isolated' track PID efficiency because the combination of the two sets of hits will cause some of the cuts to define a muon to fail. Also the recording of hits leads to losses due to the 1D-readout of each IFR module. Second, overlapping tracks will lead to a 'correlated' loss of both their ID, not accounted for by the product of their 'uncorrelated' single-track inefficiencies, as registered in the maps. These two effects have been carefully studied and evaluated.

The complete picture of the different 2-particle samples in terms of muon ID efficiencies is given by the following equations (neglecting here for simplicity the non-$\mu\mu$ background). We distinguish the true efficiencies for tracks 1 and 2 ($\epsilon_{true}^{(1,2)}$) defined by

$$\epsilon^{(1)} = \frac{N_{\mu X}}{N_{XX}}, \tag{6.1}$$

$$\epsilon^{(2)}_{true} = \frac{N_{X\mu}}{N_{XX}}, \tag{6.2}$$

where 'X' is for a muon with any identification from the measured efficiencies using muon tagging. The different topologies can be described in terms of true :

$$\begin{aligned} N_{\mu\mu} &= N^0_{\mu\mu} < \epsilon^{(1)}_{true}\epsilon^{(2)}_{true} > \\ N_{\mu\overline{\mu}} &= N^0_{\mu\mu} < \epsilon^{(1)}_{true}(1-\epsilon^{(2)}_{true}) > \\ N_{\overline{\mu}\mu} &= N^0_{\mu\mu} < \epsilon^{(2)}_{true}(1-\epsilon^{(1)}_{true}) > \\ N_{\overline{\mu\mu}} &= N^0_{\mu\mu} < (1-\epsilon^{(1)}_{true})(1-\epsilon^{(2)}_{true}) >, \end{aligned} \tag{6.3}$$

or measured efficiencies:

$$\begin{aligned} N_{\mu\mu} &= N^0_{\mu\mu}(1-f_2)\epsilon^{(1)}\epsilon^{(2)} \\ N_{\mu\overline{\mu}} &= N^0_{\mu\mu}(1-f_2)\epsilon^{(1)}(1-\epsilon^{(2)}) \\ N_{\overline{\mu}\mu} &= N^0_{\mu\mu}(1-f_2)\epsilon^{(2)}(1-\epsilon^{(1)}) \\ N_{\overline{\mu\mu}} &= N^0_{\mu\mu}[\,(1-f_2)(1-\epsilon^{(1)})(1-\epsilon^{(2)}) \;+\; f_2], \end{aligned} \tag{6.4}$$

where f_2 is the fraction of events where the 2 tracks have lost their ID in a correlated way. N_{ij} is the number of events in the different μ-ID configurations for the two tracks, and $N^0_{\mu\mu}$ the total number of $\mu\mu$ events regardless of their μ-ID. The standard efficiency determination relies only on the first 3 equations and is therefore independent of f_2.

The individual efficiencies $\epsilon^{(1,2)}$ have to be corrected from their values $\epsilon^{(1,2)}_0$, obtained for isolated tracks (efficiency maps) to account for the loss induced by the presence of the other close track. This is achieved by introducing correction factors f_{11} and f_{12} such that

$$\begin{aligned} \epsilon^{(1)} &= f_{11}\epsilon^{(1)}_0 \\ \epsilon^{(2)} &= f_{12}\epsilon^{(2)}_0 \\ f_1 &= f_{11}f_{12} \end{aligned} \tag{6.5}$$

While f_{11} and f_{12} can both be determined, only their product f_1 matters for the ID correction applied to the $\mu\mu$ mass spectrum for obtaining the cross section.

For any event sample in a given phase-space bin, the four unknowns, f_{11}, f_{12}, f_2, and $N^0_{\mu\mu}$, can be easily obtained. The first two involve only the first three equations in Eqs. 6.4 (at least one muon identified), while f_2 and $N^0_{\mu\mu}$ necessitate also the last equation:

$$f_{11} = \frac{N_{\mu\mu}}{(N_{\mu\mu} + N_{\overline{\mu}\mu}) < \epsilon^1_0 >} \tag{6.6}$$

$$f_{12} = \frac{N_{\mu\mu}}{(N_{\mu\mu} + N_{\mu\overline{\mu}}) < \epsilon^2_0 >} \tag{6.7}$$

$$N^0_{\mu\mu} = N_{\mu\mu} + N_{\overline{\mu}\mu} + N_{\mu\overline{\mu}} + N_{\overline{\mu\mu}} \tag{6.8}$$

$$f_2 = \frac{N_{\overline{\mu\mu}}}{N^0_{\mu\mu}} - \frac{N_{\mu\overline{\mu}} N_{\overline{\mu}\mu}}{N_{\mu\mu} N^0_{\mu\mu}} \tag{6.9}$$

In Eqs. 6.6 and 6.7, $< \epsilon_0^{(1,2)} >$ are the average values of the corresponding single-isolated-track efficiencies in the considered bin for the $(N_{\mu\mu} + N_{\overline{\mu}\mu})$ and $(N_{\mu\mu} + N_{\mu\overline{\mu}})$ samples, respectively. Two choices of phase-space bins are of interest: cells in (dv_1,dv_2) space to model the overlap loss (where $dv_{1,2}$ are the moduli of the difference between the $v_{1,2}$ local IFR coordinates of the 2 muon tracks) and $\mu\mu$ mass bins for the final physics results.

Non-$\mu\mu$ background from $\pi^+\pi^-\gamma$ (and to some extent $K^+K^-\gamma$) events is reduced with the help of some cuts, but remains important in the ρ region for the '$\mu - \bar{\mu}$' sample. The remaining background is statistically subtracted out using as input a pure $\pi\pi$ sample obtained with hard cuts (the so-called $\pi_h\pi$ sample, definition of π_h will be mentioned later in Section 6.2.2) and correcting it with the measured pion ID and mis-ID efficiencies. In the '$\bar{\mu} - \bar{\mu}$' sample the background is overwhelming and the small $\mu\mu$ component is extracted from a fit of the distribution about $P_{\pi/\mu}$ (see Section 6.1.4).

6.1.3 Loss of single-track ID efficiency (f_1)

The 1D readout of the IFR is expected to produce a hardware loss of efficiency for tracks at the same v_1 or v_2 value in a given module. Software can also be responsible for some loss for tracks overlapping in the same module or nearby modules. From the sample of events with at least one identified muon, the f_1 parameter can be determined as a function of $dv_1 = |v_1^{(1)} - v_1^{(2)}|$ and

$dv_2 = |v_2^{(1)} - v_2^{(2)}|$. The $\pi\pi$ background is subtracted out using data as outlined above. The f_1 maps are established for the relevant configurations of IFR parts hit by the 2 tracks: barrel-barrel (same module), barrel-barrel, barrel-overlap, overlap-overlap, endcap-endcap, endcap-endcap, and (barrel/overlap)-endcap.

It is observed that runs 1 and 2 on one hand, and runs 3 and 4 on another hand behave very closely as far as the f_1 maps are concerned, but the two groups of runs show a rather different behavior. In runs 1-2, ID losses are strongly peaked along the $dv_{(1,2)}$ axes, while it is much less so for runs 3-4 where the loss is concentrated for both small dv_1 and dv_2 values. This contrasting behavior is well reproduced by the simulation. To avoid low-efficiency areas for runs 1-2 we remove events in the two bands $dv_1 < 10$ cm or $dv_2 < 10$ cm, and the additional square $dv_1 < 20$ cm and $dv_2 < 20$ cm. These cuts are only applied if the two tracks hit the same IFR module. For runs 3-4 the observed loss is manageable ($f_1 > 0.54$) and no cut is applied.

As the high level of $\pi\pi$ background in the ρ region prevents a safe determination of an f_1 map to be made there, a procedure is set up using several maps determined in mass regions below and above the ρ peak. In this way parameters other than $dv_{1,2}$ are implicitly taken into account and we are less dependent on the granularity of the f_1 maps. Biases induced by this procedure are small and corrected for using a MC study. This is done by comparing two f_1 distributions as a function of mass: the first, determined through the map procedure, and the other (true value), obtained through Eq. (6.6). The residuals are consistent with zero with an rms of 3.3×10^{-3} and 2.2×10^{-3} for runs 1-2 and 3-4, respectively. The rms values are taken as local systematic uncertainty for the f_1 procedure. Since their determination in MC is statistics-limited, the two values are taken as uncorrelated. However, they are fully correlated over the overlap mass range, up to 2.5 GeV.

The same procedure is followed for data, taking account of the background. A direct and independent test of systematic effects can be done as in the simulation, by comparing the two determinations of f_1 in each mass bins. The distributions as a function of mass are shown in Fig. 6.1. The direct determination

is statistically limited, especially in the ρ region because of the large background subtraction in the $\mu\overline{\mu}$ sample, but it is found to agree with the map method. Here it is not possible to characterize the agreement locally, but an overall comparison in the mass range of interest from threshold to 1.5 GeV yields values for the ratio f_1^{map}/f_1^{direct} of 1.0010 ± 0.0025 and 0.9985 ± 0.0017 for runs 1-2 and 3-4, respectively. These values and their errors are well within the systematic uncertainties estimated from the simulation.

The f_1 distribution in MC is also shown in Fig. 6.1: although its shape is quite similar to data, there is a very significant difference in their magnitudes. At the ρ mass f_1, which represents directly the correction to the $\mu^+\mu^-\gamma$ cross section because of track IFR overlap, is about 2.5% (absolute) smaller in the simulation for runs 1-2 and 4% for runs 3-4.

6.1.4 Measurement of f_2

Access to the amount of correlated ID loss in $\mu\mu$ events requires the identification of the true $\mu\mu$ component in the $\overline{\mu\mu}$ ID sample. This is a real challenge as this sample is overwhelmingly dominated by $\pi\pi$ and KK events (the $p\overline{p}$ contribution is negligible). The overlap of tracks in the IFR not only causes a reduction of the efficiency (the $\sqrt{f_1}$ factor) as measured through μ-ID tagging, but is also at the origin of a correlated loss (the f_2 factor defined in Section 6.1.2).

The estimator $P_{\pi/\mu}$ has been constructed to further reject μ background from muons already mis-identified as $'\pi'$ (Section 6.2.2). Here we are just dealing with $'\pi\pi'$ events and two such estimators $P_{\pi/\mu}^{(1,2)}$ are available for the two tracks. A true $\mu\mu$ component in this sample will manifest itself with two large values of the estimators. Instead of fitting the 2D-distribution, a single estimator is built according to $E_{\pi/\mu} = \sqrt{\frac{1}{2}(P_{\pi/\mu}^{(1)\,2} + P_{\pi/\mu}^{(2)\,2})}$ and the corresponding 1D-distribution is adjusted to yield the true $\mu\mu$ and $\pi\pi$ components. A small correction is needed to extrapolate from the $'\pi\pi'$ (91.2%) to full $'\overline{\mu\mu}'$ samples. The distributions of the $\pi\pi$ and $\mu\mu$ estimators are taken from simulation, both adjusted to data in convenient places (the ρ peak for the former, the 4-7 GeV region for the latter).

The fits in wide mass bins (0.5 GeV) are shown in Figs. 6.2 and 6.3. The fits in 50-MeV bins in the 0.5-1.0 GeV range (Figs. 6.4, 6.5) yield consistent

results, although the accuracy is degraded near the ρ peak. Figure 6.6 shows the measured f_2 from the probability fits in wide mass bins (0.5 GeV).

Systematic uncertainties in the f_2 determination occur at two levels, in the probability fits and in the extrapolation from the $'\pi\pi'$ to the $'\overline{\mu\mu}'$ samples. They are discussed in Ref. [33] and included in Fig. 6.6.

6.1.5 Summary of systematic uncertainties from μ-ID

The systematic uncertainties from μ-ID are summarized in Table 6.3: they apply to the $\mu^+\mu^-\gamma$ cross section following Eq. (6.4), *i.e.* to the product $f_{11}\epsilon_0^{(1)} f_{12}\epsilon_0^{(2)}(1-f_2)$, where $\epsilon_0^{(1,2)}$ are the map efficiencies for the two tracks when isolated in the IFR, f_{11} and f_{12} the corresponding track-overlap reduction factors, and f_2 the correlated efficiency loss.

Table 6.3: Systematic uncertainties (in 10^{-3}) from muon-ID on the $\mu^+\mu^-\gamma$ cross section from the correction factor $f_{11}\epsilon_0^{(1)} f_{12}\epsilon_0^{(2)}(1-f_2)$, with $f_1 = f_{11}f_{12}$ (see text).

sources	runs 1-2	runs 3-4	runs 1-4
statistics efficiency sample	1.4	1.1	0.9
background efficiency sample	0.2	0.2	0.2
sample selection bias	0.3	0.3	0.3
time dependence within runs	0.2	0.2	0.2
granularity 3D efficiency maps	2.2	1.9	1.8
granularity 2D f_1 maps	3.3	2.2	2.2
f_2 determination	1.5	1.5	1.5
sum	4.5	3.5	3.3

The uncertainties are obtained and quoted separately for runs 1-2 and 3-4. Since they result from statistically-limited tests, they can be assumed to be uncorrelated, except for the background level and the selection bias in the efficiency sample for which the study was made for the combined sample of runs 1-4. For the uncertainties on the efficiency and f_1 maps, we assume a 50% correlation. Since f_2 has been determined for runs 1-4, its error is fully correlated

between runs 1-2 and 3-4. The overall systematic error from muon-ID on the $\mu\mu\gamma$ cross section for runs 1-4 amounts to 3.3×10^{-3}.

6.1.6 Overall μ-ID correction to the $\mu^+\mu^-\gamma$ cross section

According to Eqs. (6.4) and (6.5) the spectrum of $\mu\mu$-identified events must be divided by the factor

$$C_{ID} \;=\; \epsilon_0^{(1)}\epsilon_0^{(2)} f_1(1-f_2) \tag{6.10}$$

in order to obtain the true distribution of events before particle-ID. The distributions of C_{ID}^{MC} and C_{ID}^{data} as a function of $\mathrm{m}_{\mu\mu}$ are given in Figs. 6.7 for runs 1-2 and 6.8 for runs 3-4. The actual correction is done with the ratio $C_{ID}^{data}/C_{ID}^{MC}$, also shown: it is seen that, in the mass range below 1.7 GeV,the simulation underestimates the cross section correction by $\sim 3\%$ in runs 1-2 and $\sim 6\%$ in runs 3-4.

6.2 Pion-ID Efficiency

6.2.1 Pion-ID and Method

It should be noticed that π-ID is a set of negative conditions: a particle is identified as a pion if it does not satisfy the muon-ID (the standard μ-ID used in the analysis is based on the cut-based 'MuMicroLoose' selector), nor the electron-ID, nor the kaon-ID. In that sense the pion-ID is sensitive to the problems affecting the identification of all the other particle types.

The method to determine the pion ID efficiencies makes use of the $\pi\pi\gamma$ sample itself, where one of the produced charged particles is tagged as pion using a strict condition, called π_h, involving estimators to further separate true pions from 'π'-identified muons or electrons (see section 6.2.2). A cut $\chi^2_{1C} < 15$ is applied to strongly reduce multi-hadronic background. The sample is restricted to $0.6 < m_{\pi\pi} < 0.9$ GeV to reduce μ, K, and e backgrounds at the $(3.7 \pm 0.5) \times 10^{-3}$ level, so that the ensemble of opposite particles constitutes a pure pion sample. The small impurity is corrected in the efficiency determination.

Since the performance of the IFR in runs 1-4 is uneven and deteriorating with time, it has been necessary to map the behavior of the efficiency, both in space and in time. For this, the candidate pion track is extrapolated to the IFR where local coordinates (v_1, v_2) are defined depending on the IFR geometry. Low-efficiency regions in the IFR (defined using (v_1, v_2) are removed in order to keep as active areas only the regions where the μ-ID efficiency is reasonably homogeneous. Crack areas between modules and some parts of the nominal active region where the IFR performance is strongly degraded are removed. The definition of the bad areas is given in Ref. [33].

Unlike for muons where it is possible to measure the ID efficiencies for isolated tracks using events with a large $\mu\mu$ mass, the pion efficiency sample is from events in the ρ region where tracks often overlap in one detector or another: DCH, EMC, or IFR. Thus the pion track sample contains some average of overlap effects which are not possible to sort out in detail. Large-mass events are rare and polluted with background, so that it is not practical to consider a sample of isolated pion tracks.

In each mass bin the number of events $N_{\pi\pi}$ identified as '$\pi\pi$' is related to the detected number $N^0_{\pi\pi}$ before particle ID by

$$N_{\pi\pi} \quad = \quad N^0_{\pi\pi}\epsilon_1\epsilon_2(1 - f_2) \tag{6.11}$$

where $\epsilon_{1,2}$ are the measured ID efficiencies and f_2 is the probability of the correlated ID loss of the two tracks.

All mis-ID efficiencies are stored generally as 2D maps as a function of momentum and the z coordinate of the track impact in the most relevant detector (IFR or DIRC).

Biases from primary pion tagging and correlated 2-track π-ID loss are studied with the simulation and checked with data in some cases. Both effects are at the 10^{-3} level.

For all details, see Ref. [35].

6.2.2 The tighter π_h ID selection

The standard π-ID definition in Table 6.1 belongs to a complete and orthogonal set of PID conditions which is convenient for crosschecks involving all 2-body ISR processes. In some situations, however, it is necessary to tighten the π-ID definition in order to reduce the background from muons and electrons. This is the case for the determination of π-ID efficiencies which relies on a good purity of the pion sample, depending itself on the quality of the primary pion tagging. The tighter π_h-ID is used for the definition of the final physics sample in $m_{\pi\pi}$ regions outside the ρ resonance, where muon and electron backgrounds are more important.

So estimators $P_{\pi/\mu}$ and $P_{\pi/e}$ have been constructed to further reject μ and e background from muons and electrons already mis-identified as $'\pi'$. The $P_{\pi/\mu}$ is the relative ratio $(LH_\mu/(LH_\mu+LH_\pi))$ based on the likelihoods of the $'\pi'$-identified μ and π which are built using the product of several individual likelihood functions based on some reference distributions, where the EMC deposited energy E_{cal}, the track length in the IFR and total number of IFR hits are used. The $P_{\pi/e}$ is built in a similar approach, where E_{cal}, $(dE/dx)_{DCH}$ and $(dE/dx)_{SVT}$ are used. All the details can be found in Ref. [35].

The tighter pion selection, called 'pion hard' (π_h), is defined using two cuts on the two likelihood functions: $P_{\pi/\mu} < 0.15$ and $P_{\pi/e} < 0.5$

The measurement of the incremental π_h efficiency (*i.e.* the efficiency of 'π'-identified pions to be selected as 'π_h'), as well as the remaining mis-ID from other particles, are discussed later in this thesis.

6.2.3 Consistency test of the method with simulation

Since the pion ID efficiencies are determined on the ρ sample in the limited mass range 0.6-0.9 GeV, it is important to check that they are applicable for all masses. On one hand the ρ sample has large statistics and relatively background-free, so that efficiency maps can be measured for individual tracks taking into account the momentum and angular information. On the other hand, the correlation between the efficiencies of the two tracks can be different for different

mass regions and the ρ sample could contain biases in this respect. However we know that track overlap effects are less severe for pions than for muons, even if they involve more sub-detectors.

This bias can be studied at the simulation level for any $\pi\pi$ mass, following the same procedure as for data:

- All efficiencies are determined exactly as in data, with π_h-tagging and sample limited to 0.6-0.9 GeV mass range.
- The '$\pi\pi$'-identified mass spectrum with $\chi^2_{1C} < 15$ is used as the starting point. It is corrected by the π-ID efficiencies of the two tracks event-by-event in order to get a predicted spectrum of produced $\pi\pi$ events, $dN^0_{(\pi\pi)\ pred}/dm_{\pi\pi}$.
- All predicted 'ij' spectra $dN_{ij\ pred}/dm_{\pi\pi}$ are then obtained using $dN_{\pi\pi\ pred}/dm_{\pi\pi}$ and the relevant $\pi \to (i,j)$ mis-ID efficiencies obtained by sampling the corresponding maps.
- The predicted spectrum for each 'ij' identified final state is compared to the direct 'measured' one, and the relative difference is computed

$$\delta^{MC}_{ij} = \frac{dN_{ij\ pred}/dm_{\pi\pi} - dN_{ij}/dm_{\pi\pi}}{dN^0_{\pi\pi}/dm_{\pi\pi}} \tag{6.12}$$

- As a direct test, the predicted spectrum is compared to the generated $\pi\pi$ spectrum $dN_{\pi\pi\ true}/dm_{\pi\pi}$, and similarly the relative difference is extracted.

All the 'ij' topologies are tested, but the numerically relevant ones involve only one mis-ID, *i.e.* 'πi' configurations. As expected the relative differences in the ρ region are small, typically less than $2 \sim 3 \times 10^{-3}$, but some larger values are observed outside, especially for the mis-ID to K. Some cancellation occurs between the biases from different mis-ID's, as can be seen in the most important test concerning the ID correction for the '$\pi\pi$' spectrum in order to obtain the cross section. The test is shown in Fig. 6.9: it more or less follows the $\pi \to K$ bias, but somewhat attenuated. The agreement is excellent on the ρ peak with

some increase in the lower and higher mass regions. The somewhat high point at 0.55 GeV originates from $\pi \to e$ mis-ID and appears to be the result of a statistical fluctuation in the corresponding map or in the overlap bias correction.

Since this test cannot be fully performed with data because of non-$\pi\pi$ background, we assume the MC bias to occur there as well and assign a systematic uncertainty equal to 100% of the MC bias, namely 1% for $m_{\pi\pi} < 0.4$ GeV, 5 10^{-3} for $0.4 < m_{\pi\pi} < 0.6$ GeV,2 10^{-3} for $0.6 < m_{\pi\pi} < 0.9$ GeV, 4 10^{-3} for $0.9 < m_{\pi\pi} < 1.2$ GeV, and 1% for $m_{\pi\pi} > 1.2$ GeV.

6.2.4 Global PID test with data

A similar test is performed with the different mass spectra in data, but here one must take into account all contributing channels: $\pi\pi\gamma$, but also $\mu\mu\gamma$, $KK\gamma$, and ee background from $ee\gamma$ and $\gamma\gamma$ followed by a pair conversion (multi-hadronic background is reduced to a negligible level with the tight χ^2_{1C} cut ($\chi^2_{1C} < 15$).

Spectra with 'diagonal' ID, *i.e.* '$\pi\pi$', '$\mu\mu$', $KK\gamma$, are used as starting points, with subtraction of the backgrounds from the other channels. In principle an iterative procedure should be used, but in practice these contributions are small so that the backgrounds in the subtracted spectra are second-order effects which can be safely neglected. Therefore the diagonal spectra are only corrected once for background contributions.

The treatment of the background from electrons is different as it occurs mainly in the 'πe' and '$\pi\pi$' topologies, while being negligible in 'ee' due to the strong rejection of electrons at the ISR selector and the track definition levels. Thus the background in this case is taken from the 'πe' spectrum where it is clearly visible at small and large masses, which are used to normalize the ee spectrum obtained with the 'RadBhabha' flag, and transferred to the '$\pi\pi$' distribution using a factor $(\pi\pi)/(\pi e) \sim 2$ obtained from a study of large mass events.

The $(\mu\mu)_0$ ($\mu\mu$ spectrum before PID), $(\pi\pi)_0$, and $(KK)_0$ distributions are produced correcting the background-subtracted '$\mu\mu$', '$\pi\pi$', and 'KK' spectra with the measured ID efficiencies. Then any 'ij' spectrum is generated using

the measured efficiencies (predicted) and compared to the directly observed 'ij' distributions. As for the MC consistency check a relative difference is computed, this time normalized to the total number of predicted produced final states:

$$\delta_{ij}^{data} = \frac{dN_{ij\ pred}/dm_{\pi\pi} - dN_{ij}/dm_{\pi\pi}}{dN_{XX}/dm_{\pi\pi}} \tag{6.13}$$

where XX refers to the full sample without PID. By choice, the comparison is made as a function of the $\pi\pi$ mass.

The comparison plots for the most important cases, '$\pi 0$', 'πe', '$\pi\mu$', 'πK', can be found in Ref. [35]. All differences δ_{ij}^{data} are within a few per mil. Some excess in the predicted rate is observed in the $\pi\mu$ spectrum in the 0.4-0.6 GeV range in both runs 1-2 and 3-4.

It is possible to perform a global comparison of the full XX spectrum and the predicted one, obtained by summing the $(\pi\pi)_0$,$(\mu\mu)_0$, and $(KK)_0$ contributions. Fig. 6.10 shows the relative difference $(N_{predicted} - N_{XX})/N_{XX}$ for the full data of runs 1-4. This plot contains all the information available in data on the validity of the ID corrections applied to the different '$i-i$' spectra. The purpose of this global ID test with data is to verify if observed differences are within the quoted systematic uncertainties on the different ID efficiencies. In fact, we see no places where this test would fail:

- at masses less than 0.5 GeV the spectrum is dominated by muons. Fitting the deviations with a constant value yields $(0.5 \pm 1.4) \times 10^{-3}$ which is well within the quoted error on μ-ID of 3.3×10^{-3}.

- above 0.9 GeV muons again are dominant and the fitted value is $(1.4 \pm 1.2) \times 10^{-3}$, also consistent with the quoted systematic error.

- between 0.6 and 0.9 GeV pions dominate and the fit of the observed deviations yields $(0.7 \pm 0.8) \times 10^{-3}$, smaller than the estimated systematics of 2.4×10^{-3}. The latter value is obtained by combining the errors 2.0×10^{-3} from the correction method (Section 6.2.3), 1.0×10^{-3} from the purity of the pion efficiency sample, and 1.0×10^{-3} from the correlated ID-loss.

- the region between 0.4 and 0.6 GeV shows a deviation $(3.7 \pm 2.1) \times 10^{-3}$, which is harder to attribute to muons or pions, which have similar rates, but is consistent with the uncertainties of 3.2×10^{-3} for muons and 5.2×10^{-3} for pions.

- since the kaons are never dominant in any mass range, even on the ϕ resonance, we are not sensitive to their systematic effects on the global plot. However the observed 'πK' distributions [35] show that deviations at this level are within 3×10^{-3}, in agreement with estimated uncertainties.

The blue band in Fig. 6.10 represents the limits given by the quadratic sum of the estimated systematic uncertainties on the $\mu\mu$, $\pi\pi$, and KK components. Within the statistical uncertainties of the data sample, all deviations are consistent with the band, thus validating the estimates of the systematic errors.

6.2.5 Systematic uncertainties on π-ID measurement

The various systematic uncertainties are summarized in Table 6.4: they apply to the $\pi^+\pi^-\gamma$ cross section following Eq. (6.11), *i.e.* to the product $\epsilon^{(1)}\epsilon^{(2)}(1 - f_2)$, where $\epsilon^{(1,2)}$ are the ID efficiencies for the two tracks measured in the ρ sample and f_2 the correlated efficiency loss.

The systematic errors on the efficiencies come from the limited granularity of the mis-ID maps, the biases caused by π_h tagging, and the application of maps determined in the ρ region (0.6-0.9 GeV) to other mass ranges. Two global ways of estimating these uncertainties have been studied.

- The consistency check with the simulated $\pi\pi$ sample (Section 6.2.3). Here deviations between the derived $(\pi\pi)_0$ using efficiency corrections as in data and the true spectrum allow one to evaluate the biases of the full method at the simulation level. The systematic effect in the data is taken as 100% of the full bias in simulation.

- The global PID test in data (Section 6.2.4) is more direct, but involves all 3 ISR processes. Although some conclusions can be drawn in mass

regions where one channel dominates, the assignment of deviations to a particular channel is sometimes ambiguous. Nevertheless, a good agreement is obtained with the previous method.

The 2-ID correlated loss factor f_2 is taken from the simulation and is assigned a 100% uncertainty.

The time dependence within runs which could lead to a bias because of the non-linear character of Eq. (6.11) has been studied and found to yield a negligible effect.

All uncertainties are given for the full sample of runs 1-4. The overall systematic error from pion-ID on the $\pi^+\pi^-\gamma$ cross section is 2.4×10^{-3} in the main ρ region, and increases up to 1% below 0.4 GeV and above 1.2 GeV.

Table 6.4: Systematic uncertainties (in 10^{-3}) from pion-ID on the $\pi\pi\gamma$ cross section from the correction factor $\epsilon^{(1)}\epsilon^{(2)}(1-f_2)$ (see text) to go from the '$\pi\pi$'-identified sample to the full produced $\pi\pi$ yield. Different $m_{\pi\pi}$ ranges in GeV are indicated. Runs 1-4.

sources \ mass ranges (GeV)	<0.4	0.4-0.6	0.6-0.9	0.9-1.2	>1.2
background efficiency sample	1.0	1.0	1.0	1.0	1.0
granularity/biases efficiency maps	10.	5.0	2.0	4.0	10.
correlated loss (f_2)	1.0	1.0	1.0	1.0	1.0
sum	10.1	5.2	2.4	4.2	10.1

6.2.6 Final π-ID correction to the $\pi^+\pi^-\gamma$ cross section

As a summary the complete π-ID correction '$\pi\pi$'$\to (\pi\pi)_0$ is given in Fig. 6.11 for runs 1-2 and 3-4. They are more consistent than the corresponding plots for muons, which reflects a lesser sensitivity of the π-ID efficiency to the IFR conditions. Although they have been obtained using maps determined in the ρ region only, they show only a few % variations with mass, consistent with the fact that correlated ID losses are small.

These corrections are compared to those found in simulation using the same method. They generally follow a similar shape. Since we use the full simulation

including PID, these ratios are the relevant quantities to correct the overall MC event acceptance.

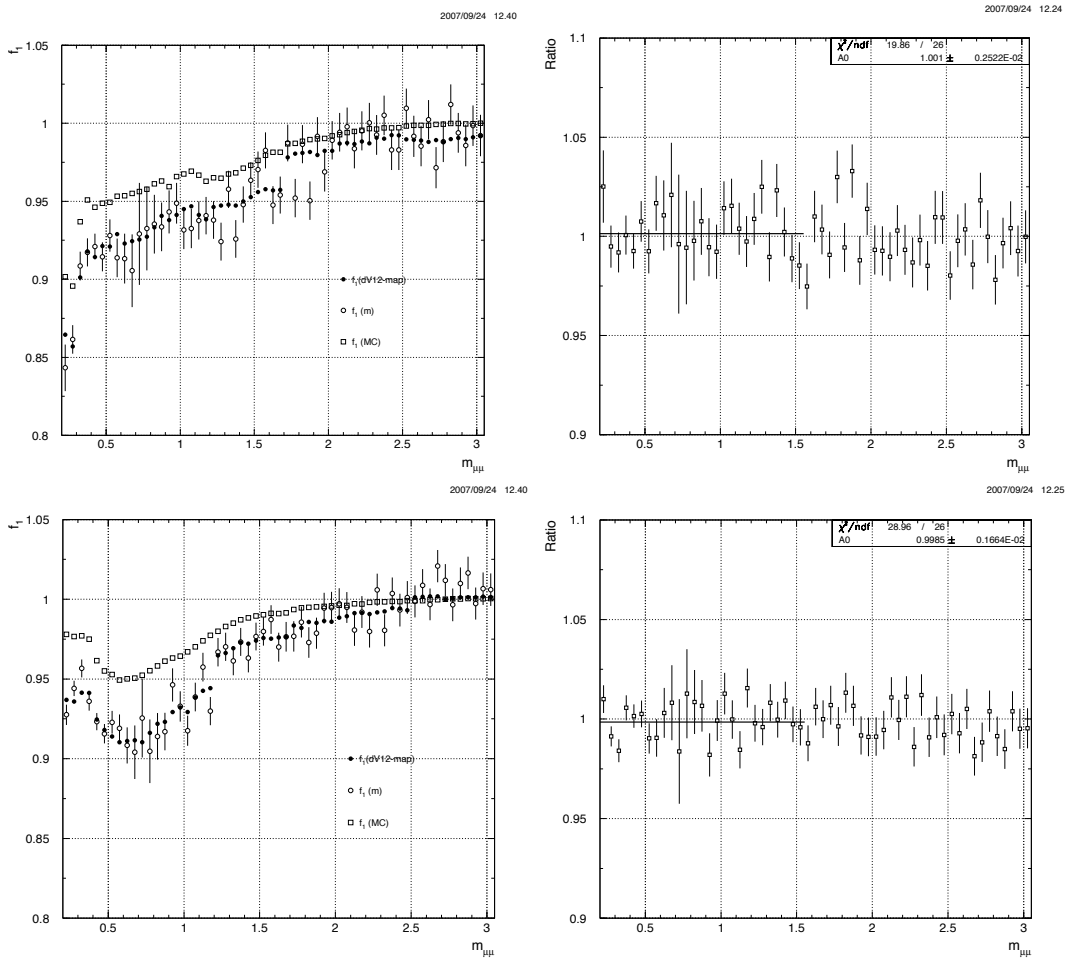

Figure 6.1: The f_1 distributions for runs 1-2 (top) and runs 3-4 (bottom) for muons. The open circles stand for the direct determination in data after background subtraction, the closed circles also for data, but using (dv_1, dv_2) maps, and the open squares for MC. The plots at right show the ratio of f_1^{map}/f_1^{direct}.

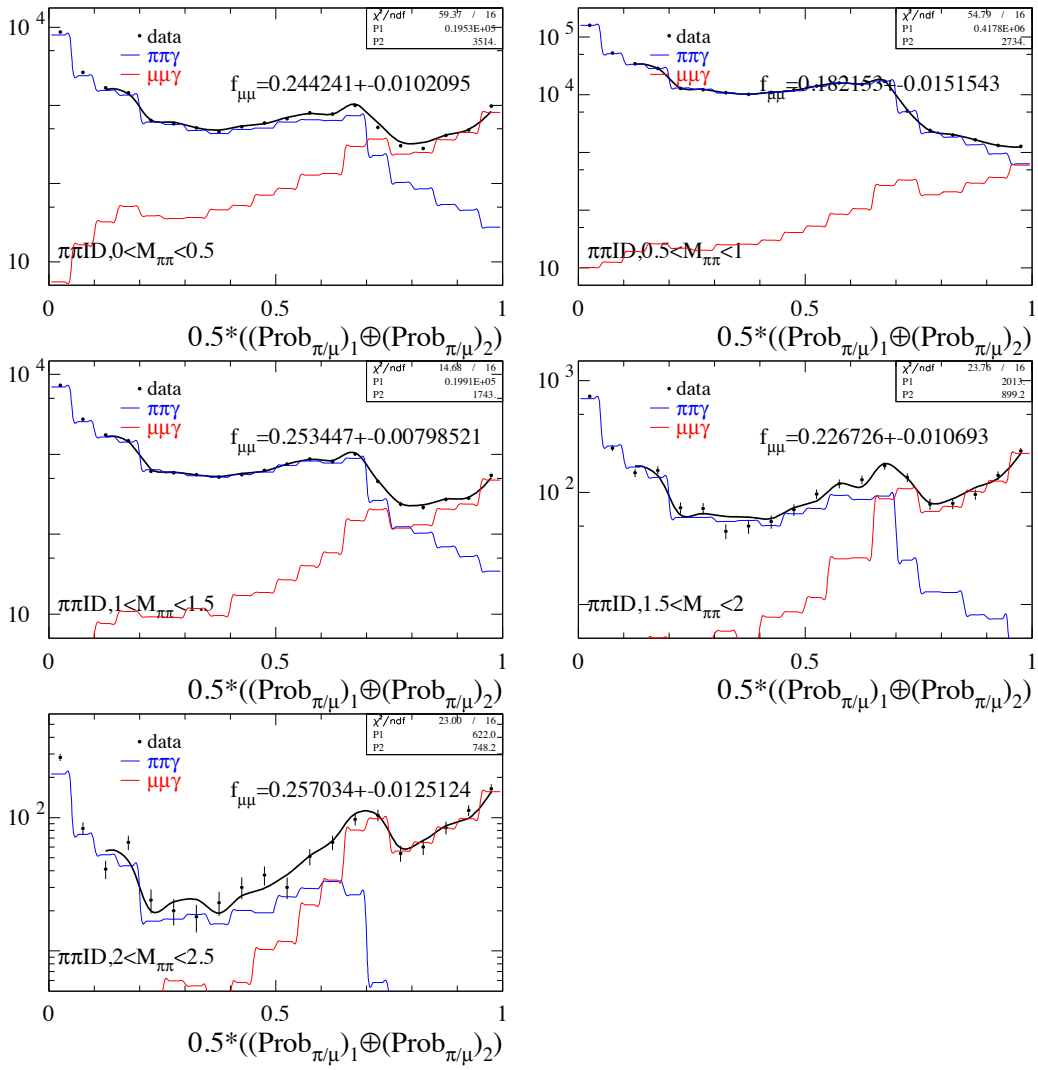

Figure 6.2: The distributions of the $\pi\pi/\mu\mu$ estimator $E_{\pi/\mu}$ for events with $'\pi\pi'$ ID in 0.5 GeV- mass bins are fitted to $\mu\mu$ (peaking at 1) and $\pi\pi$ (peaking at 0) components, obtained as described in the text. The black curve is the best fit with the two adjusted contributions. The insert gives the fitted number of events for $\pi\pi$ (P1) and $\mu\mu$ (P2), and the value given for $f_{\mu\mu}$ represents the normalization of the found $\mu\mu$ component in data with respect to the corresponding absolute number in the $\mu\mu$ MC. The relative error on $f_{\mu\mu}$ has been enlarged by $\sqrt{\chi^2/DF}$. All plots for runs 1-4.

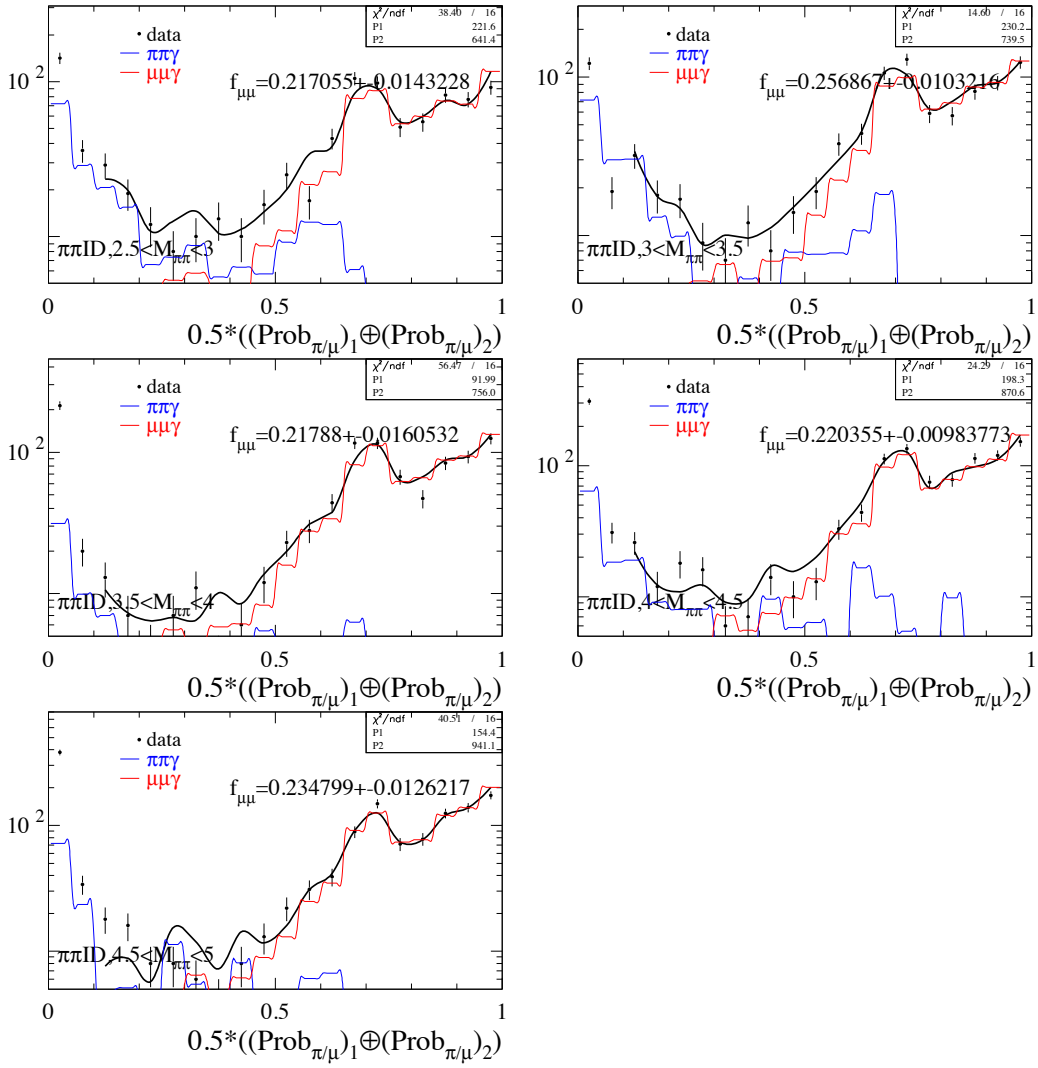

Figure 6.3: The distributions of the $\pi\pi/\mu\mu$ estimator $E_{\pi/\mu}$ for events with $'\pi\pi'$ ID in 0.5 GeV- mass bins are fitted to $\mu\mu$ (peaking at 1) and $\pi\pi$ (peaking at 0) components, obtained as described in the text. The black curve is the best fit with the two adjusted contributions. The insert gives the fitted number of events for $\pi\pi$ (P1) and $\mu\mu$ (P2), and the value given for $f_{\mu\mu}$ represents the normalization of the found $\mu\mu$ component in data with respect to the corresponding absolute number in the $\mu\mu$ MC. The relative error on $f_{\mu\mu}$ has been enlarged by $\sqrt{\chi^2/DF}$. All plots for runs 1-4.

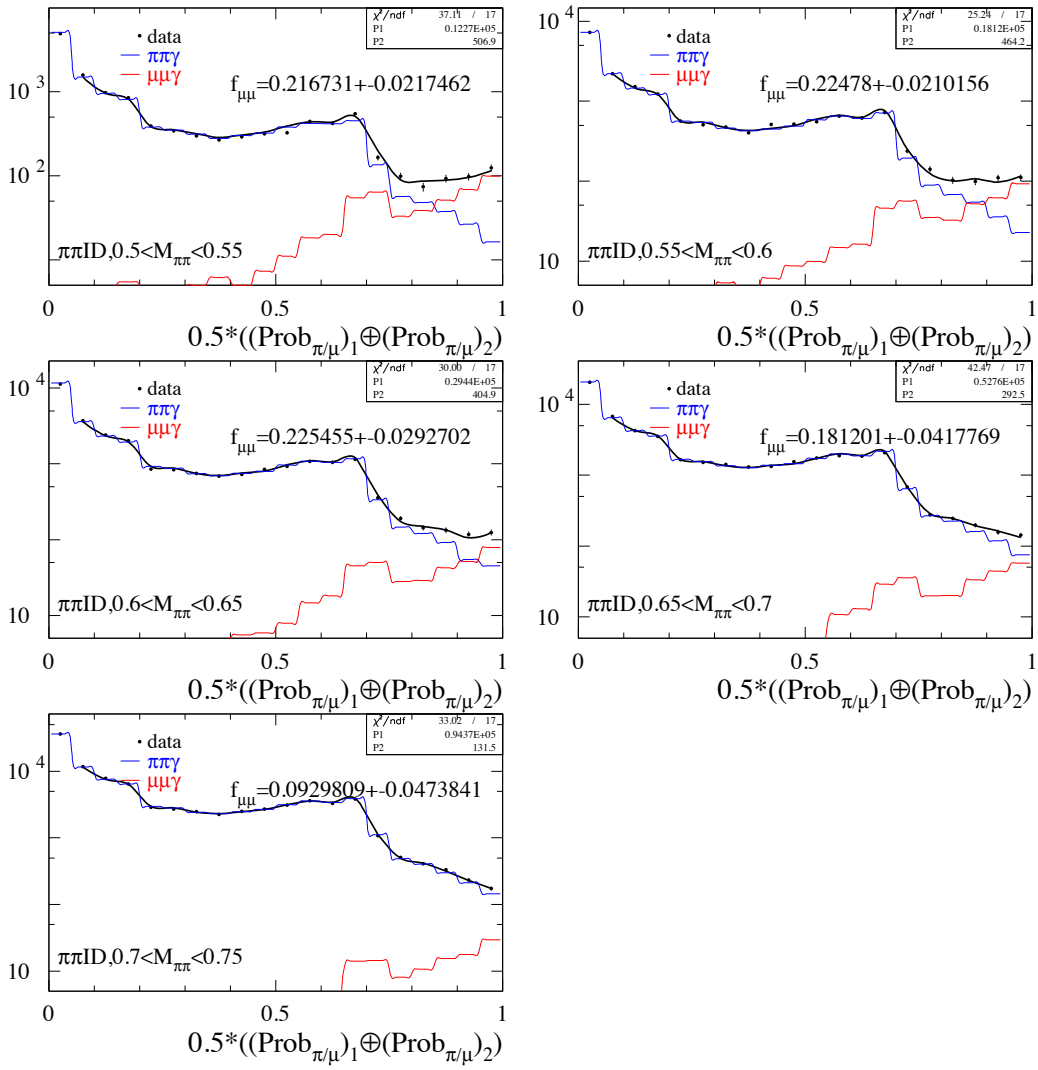

Figure 6.4: The distributions of the $\pi\pi/\mu\mu$ estimator $E_{\pi/\mu}$ for events with $'\pi\pi'$ ID in 50-MeV mass bins (ρ region) are fitted to $\mu\mu$ (peaking at 1) and $\pi\pi$ (peaking at 0) components, obtained as described in the text. The black curve is the best fit with the two components. The insert gives the fitted number of events for $\pi\pi$ (P1) and $\mu\mu$ (P2), and the value given for $f_{\mu\mu}$ represents the normalization of the found $\mu\mu$ component in data with respect to the corresponding absolute number in the $\mu\mu$ MC. The relative error on $f_{\mu\mu}$ has been enlarged by $\sqrt{\chi^2/DF}$. All plots for runs 1-4.

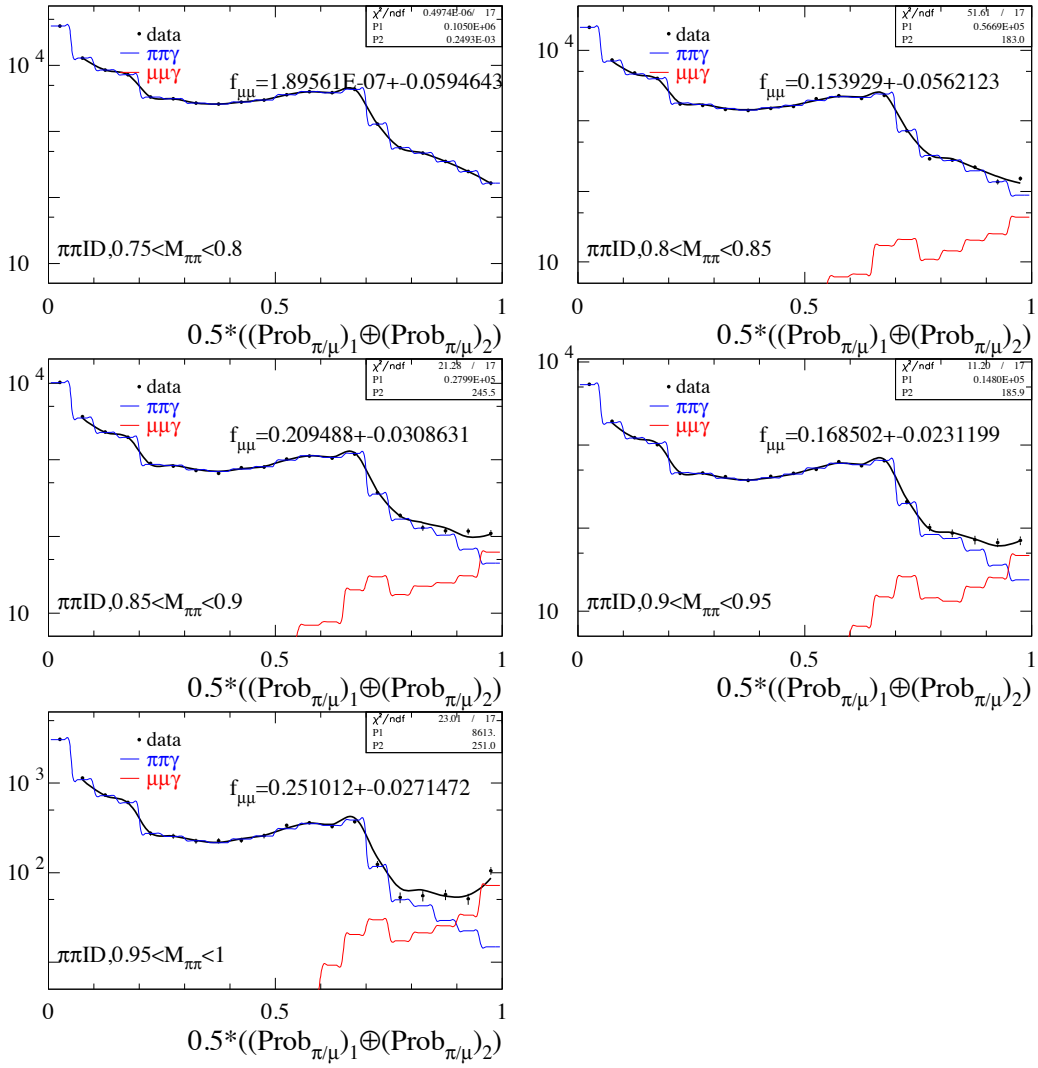

Figure 6.5: The distributions of the $\pi\pi/\mu\mu$ estimator $E_{\pi/\mu}$ for events with $'\pi\pi'$ ID in 50-MeV mass bins (ρ region continued) are fitted to $\mu\mu$ (peaking at 1) and $\pi\pi$ (peaking at 0) components, obtained as described in the text. The black curve is the best fit with the two components. The insert gives the fitted number of events for $\pi\pi$ (P1) and $\mu\mu$ (P2), and the value given for $f_{\mu\mu}$ represents the normalization of the found $\mu\mu$ component in data with respect to the corresponding absolute number in the $\mu\mu$ MC. The relative error on $f_{\mu\mu}$ has been enlarged by $\sqrt{\chi^2/DF}$. All plots for runs 1-4.

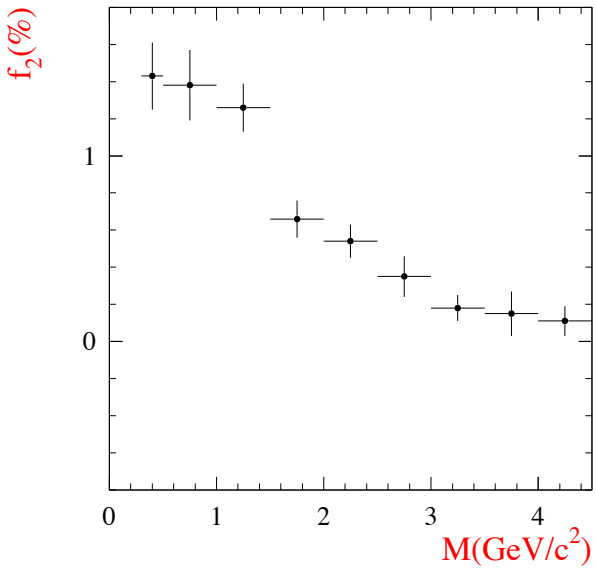

Figure 6.6: The values of the correlated ID loss f_2 for 2-muon ID obtained directly from data.

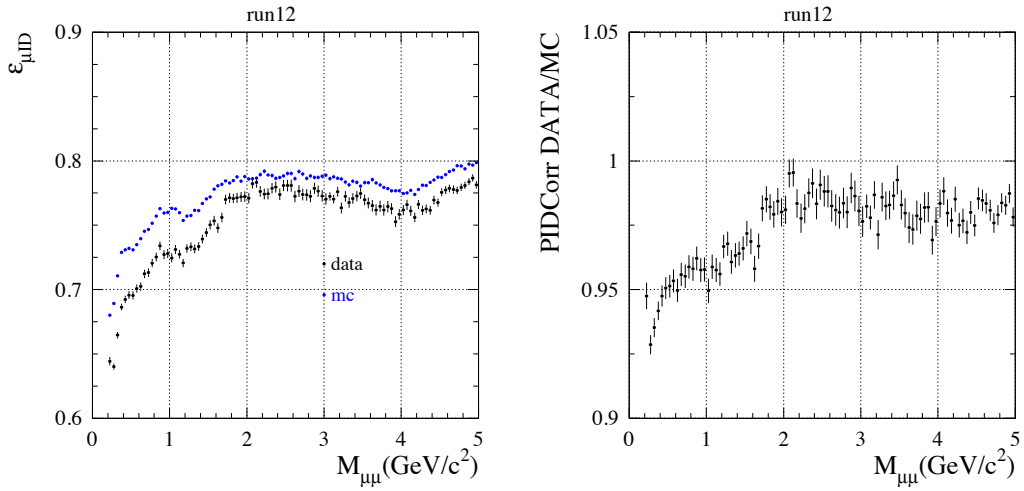

Figure 6.7: The full μ-ID correction to $\mu^+\mu^-\gamma$ cross section for runs 1-2: data and MC (left) and the ratio data/MC (right).

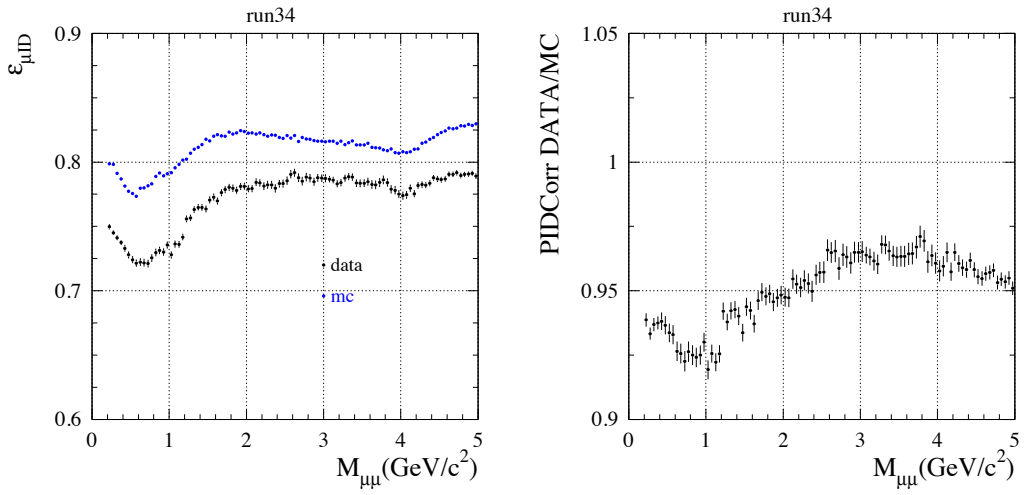

Figure 6.8: The full μ-ID correction to $\mu^+\mu^-\gamma$ cross section for runs 3-4: data and MC (left) and the ratio data/MC (right).

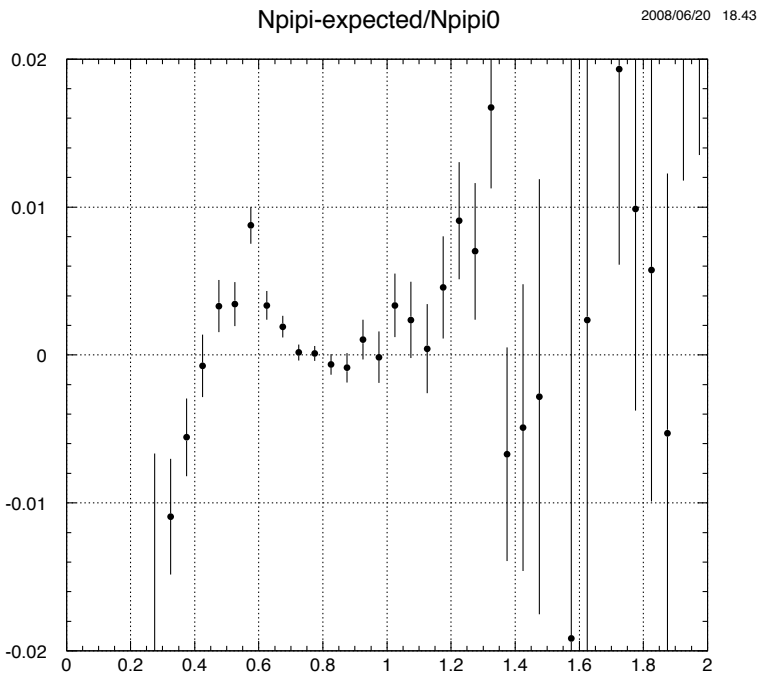

Figure 6.9: The overall consistency test on the simulation (runs 1-4): the difference between the $m_{\pi\pi}$ spectra predicted from the identified '$\pi\pi$' distribution corrected by the ID-efficiencies following the procedure on data (see text) and the true generated sample, normalized to the true spectrum.

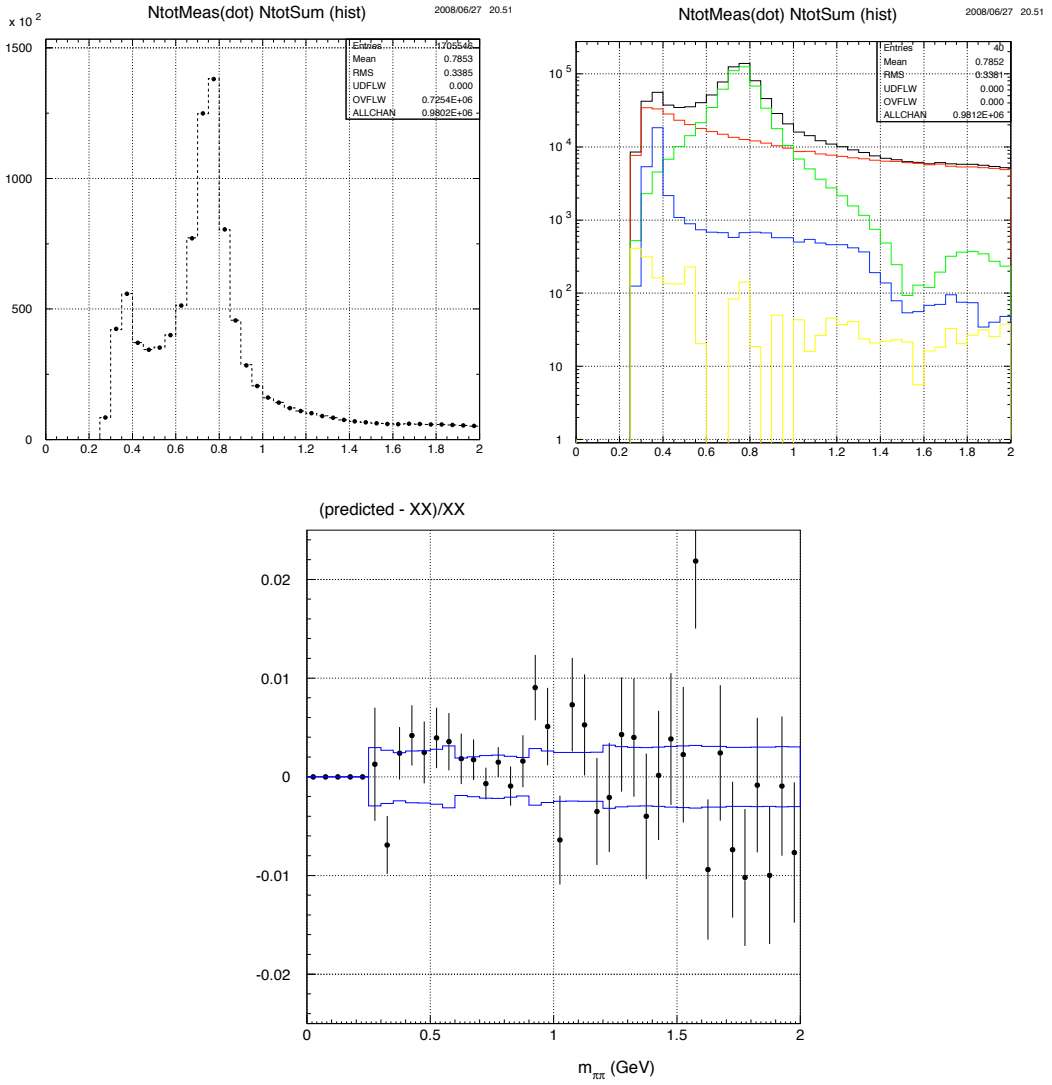

Figure 6.10: The global PID test on data (runs 1-4). Top left: the $m_{\pi\pi}$ spectrum of all $XX\gamma$ events (no PID applied, data points) compared of the sum of identified 'ii' distributions corrected by the measured ID-efficiencies ($(\mu\mu)_0 + (\pi\pi)_0 + (KK)_0 + ee$ background, histogram). Top right: the different components of the histogram in the top left plot, $(\mu\mu)_0$ (red), $(\pi\pi)_0$ (green), $(KK)_0$ (blue), ee background (yellow), and their sum (black). Bottom: the relative difference of the two spectra in the top left plot (ID-predicted - no PID)/no PID. The deviations are statistically compatible with the estimated systematic uncertainties shown by the blue band.

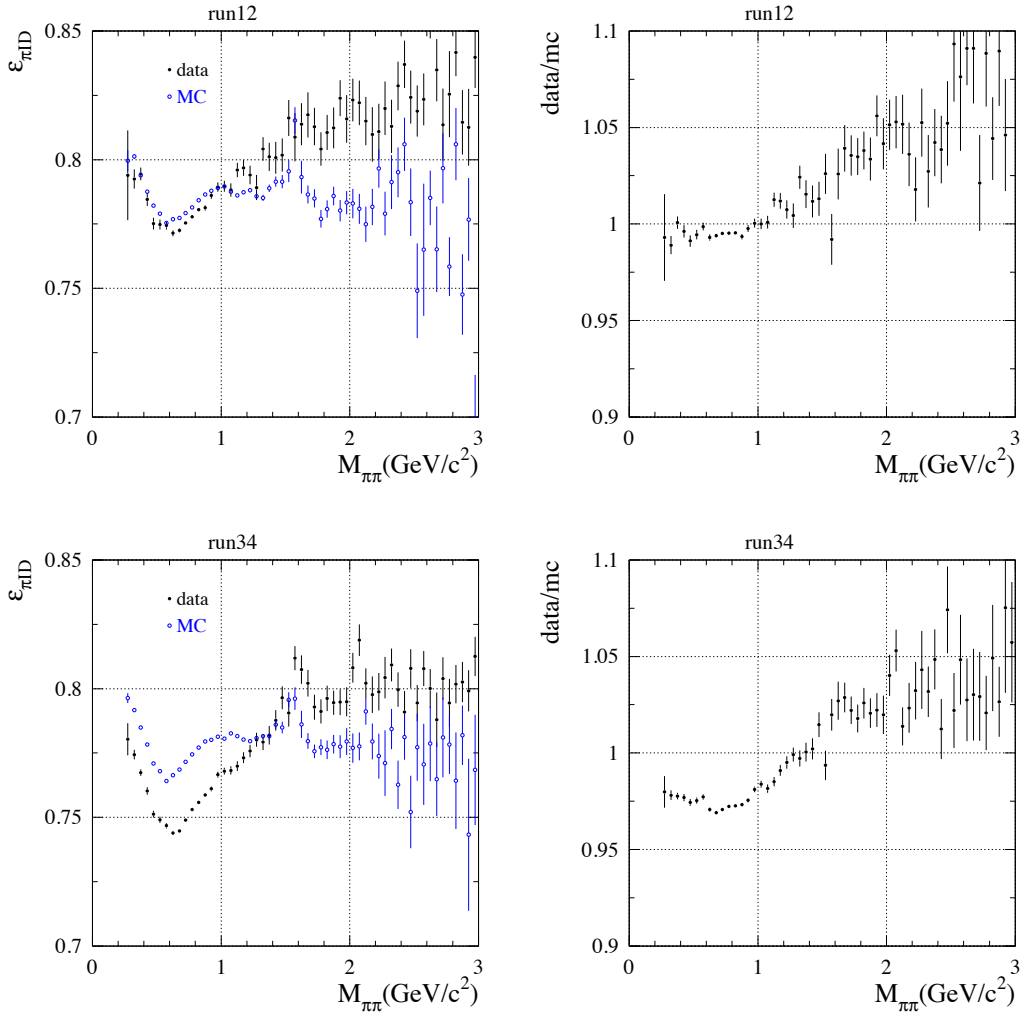

Figure 6.11: The total PID efficiency for the '$\pi\pi$' mass spectrum as a function of $m_{\pi\pi}$ (GeV) for data (black points) and simulation (open blue points) in order to obtain the produced $\pi\pi$ spectrum (left), and the correction data/MC (right), both for runs 1-2. The plots on the second row are the corresponding ones for runs 3-4.

Chapter 7

Kinematic Fitting and Backgrounds

7.1 ISR kinematic fit with possibly one additional photon

So far BaBar ISR analyses have used χ^2 cuts after kinematically fitting the events to the relevant $X\gamma$ hypothesis. Because of resolution effects, but mostly because of additional radiation, the χ^2 distributions have long tails and the efficiency after the χ^2 cut is usually around 70-80%. As the understanding of this efficiency at the per mil level would be a real challenge, we proceed here differently in order to reach a large efficiency which can be controlled to this precision.

Therefore the event definition is enlarged to include the radiation of one photon in addition to the already required ISR photon. Two types of fits are considered, according to the following situations:

- The additional photon is detected in the EMC, in which case its energy and angles can be readily used in the fit: we call this a 3C FSR fit, although the extra photon can be either from FSR or from ISR at large angle. The energy of the primary ISR photon is not used in the fit, as it brings little information (at least for relatively low masses). The threshold for the additional photon is kept low (20 MeV in lab frame). This can introduce some background, but with little effect as the fit in that case would not be different in practice to a standard fit to the $\mu^+\mu^-\gamma$ or $\pi^+\pi^-\gamma$ hypothesis.

- The additional photon is assumed to be from ISR at small angle to the beams. Since no more information [1] is available it is postulated that the

[1] This is not strictly true as the missing photon could be completely reconstructed if the ISR photon energy is used in the kinematic fit. However the relative quality of this supplementary information does not permit a significant improvement for the fitted direction of the additional ISR photon over the collinear assumption.

extra photon is perfectly aligned with either the e^+ or the e^- beams. The corresponding so-called 2C ISR fit ignores additional photons measured in the EMC and returns the energy of the fitted collinear ISR photon.

Each event is characterized by the χ^2 values, $\chi^2_{add.FSR}$ and $\chi^2_{add.ISR}$ from the two fits which can be reported on a 2D plot. In practice the quantities $\ln(\chi^2+1)$ are used so that the long tails can be properly visualized. Events without any extra measured photons have only the $\chi^2_{add.ISR}$ value and they are plotted separately on a line above the $\chi^2_{add.FSR}$ overflow. It is easy to visualize the different interesting regions in the 2D χ^2 plane, as outlined in Fig. 7.1 for the $\pi^+\pi^-\gamma(\gamma)$ channel, chosen for illustration because of its larger background. Most of the events peak at small values of both χ^2, but the tails along both axes clearly indicate events with additional radiation: small-angle ISR along the $\chi^2_{add.FSR}$ axis (with large ISR energies at large values of $\chi^2_{add.FSR}$), FSR or large-angle ISR along the $\chi^2_{add.ISR}$ axis (with large FSR energies at large values of $\chi^2_{add.ISR}$). Events along the diagonal do not satisfy either hypotheses and result from resolution effects for the tracks or the primary ISR, or possibly additional radiation of more than one photon. Non-2-body background is expected to populate the region where both χ^2 are large and consequently a *background region* is defined in the 2D χ^2 plane. This region has to be optimized as a compromise between efficiency and background contamination in the signal region. More practically, the optimization is rather on the control of the corresponding systematic uncertainties.

The definition of the physical (accepted) region uses the .OR. of the following χ^2 conditions (corresponding to the contour of the 'background'-labeled region shown in Fig. 7.1) :

- $\ln(\chi^2_{add.FSR}+1) < 2.5$
- $\ln(\chi^2_{add.ISR}+1) < 4.615$ and $\ln(\chi^2_{add.FSR}+1) < 4.115$
- $\ln(\chi^2_{add.ISR}+1) - \ln(\chi^2_{add.FSR}+1) < 0.5$ and $0.4115 < \ln(\chi^2_{add.FSR}+1) < 7.5$
- $\ln(\chi^2_{add.ISR}+1) < 7.5$ and $\ln(\chi^2_{add.FSR}+1) > 7.$
- $\ln(\chi^2_{add.FSR}+1) > 11.$

This 2D-χ^2 cut (loose χ^2-cut) is used in the $\mu^+\mu^-\gamma(\gamma)$ analysis as well as in the central ρ region ($0.5 < m_{\pi\pi} < 1$ GeV) for $\pi^+\pi^-\gamma(\gamma)$. And a tighter cut $\ln(\chi^2_{add.ISR}+1) < 3$ is applied in the outside region ($m_{\pi\pi} < 0.5$ GeV or > 1 GeV) because of less signal and relative more backgrounds there (see Chapter 13).

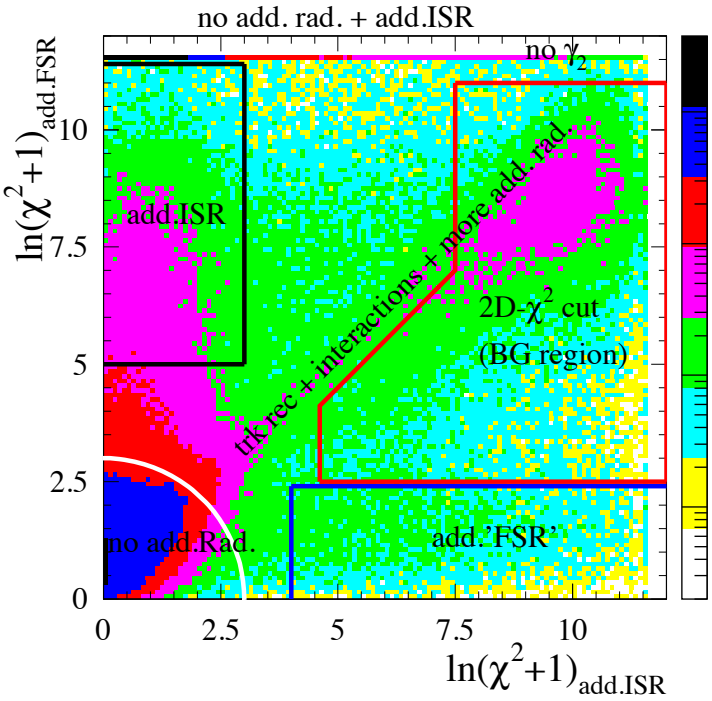

Figure 7.1: The 2D-χ^2 distribution for $\pi^+\pi^-\gamma(\gamma)$ (data) for $0.5 < m_{\pi\pi} < 1.0$ GeV, where different interesting regions are defined.

7.2 Backgrounds in '$\mu^+\mu^-\gamma(\gamma)$'

7.2.1 Separation of muon channel using particle identification

The measurement of PID efficiencies using pure data samples of muons [33], pions [35] and kaons [36] allows one to separate the different 2-body ISR channels in a reliable way. In each mass bin (computed with the $\mu\mu$ mass hypothesis here, $\pi\pi$ mass hypothesis will be computed when we study pion channel) of the spectra

for identified pairs of type 'i', $N_{\prime ii\prime}$, the following equations

$$\begin{aligned} N_{\prime\mu\mu\prime} &= N^{(0)}_{\mu\mu}\varepsilon_{\mu\mu\to\prime\mu\mu\prime} + N^{(0)}_{\pi\pi}\varepsilon_{\pi\pi\to\prime\mu\mu\prime} + N^{(0)}_{KK}\varepsilon_{KK\to\prime\mu\mu\prime} \\ N_{\prime\pi\pi\prime} &= N^{(0)}_{\mu\mu}\varepsilon_{\mu\mu\to\prime\pi\pi\prime} + N^{(0)}_{\pi\pi}\varepsilon_{\pi\pi\to\prime\pi\pi\prime} + N^{(0)}_{KK}\varepsilon_{KK\to\prime\pi\pi\prime} + N_{ee\to\prime\pi\pi\prime} \\ N_{\prime KK\prime} &= N^{(0)}_{\mu\mu}\varepsilon_{\mu\mu\to\prime KK\prime} + N^{(0)}_{\pi\pi}\varepsilon_{\pi\pi\to\prime KK\prime} + N^{(0)}_{KK}\varepsilon_{KK\to\prime KK\prime} \end{aligned} \quad (7.1)$$

are solved for the produced (before identification) numbers of particle pairs of each type, $N^{(0)}_{\mu\mu}$, $N^{(0)}_{\pi\pi}$, and $N^{(0)}_{KK}$. In Eqs. (7.1), the quantities $\varepsilon_{jj\to\prime ii\prime}$ represent the product of the ID-efficiencies $j \to\prime\ i\prime$ and correlation factors which have been established in each PID study. The term $N_{ee\to\prime\pi\pi\prime}$ takes into account the small ee background in the '$\pi\pi$' channel, obtained through studies of the 'πe' and 'RadBhabha' mass spectra.

It is to be noted that the measured '$\pi\pi$' and 'KK' spectra also contain contributions of multi-hadronic background, from higher-multiplicity ISR and $q\overline{q}$ processes. They are not from two body ISR channels, but the final particles are real pions or kaons, so here they are treated like pions or kaons so that the pion and kaon channels subtraction in '$\mu\mu$' sample will automatically takes into account the multi-hadronic background. There is also a contribution from the ISR $p\overline{p}\gamma$ process which appears dominantly in the '$\pi\pi$' spectrum. In this procedure it is treated like pion pairs, but it has been found that the induced bias in the '$\mu\mu$' topology is negligible. The effect of the mistreatment of multi-hadron events where the final state involves a $K\pi$ pair has also been considered and it was likewise found to produce a bias at the 10^{-4} level.

At this point the $N^{(0)}_{\mu\mu}$ mass spectrum is obtained. However it is still useful to consider the μ-identified sample $N_{\prime\mu\mu\prime}$ for checks. In particular it is interesting to visualize the result of the implicit background subtraction involved in Eqs. (7.1) for the original '$\mu\mu$' sample. These contributions are shown in Fig. 7.2 for $\pi\pi$ and KK sources, dominated by 2-body ISR processes, but also containing multi-hadron events. They are small, except on the ρ peak where they reach 5%.

Because of the non-negligible $\pi^+\pi^-\gamma$ background at the ρ peak and since the presence of this background was a major complication in the determination of the μ-ID efficiency in data, it is important to perform an independent check of this

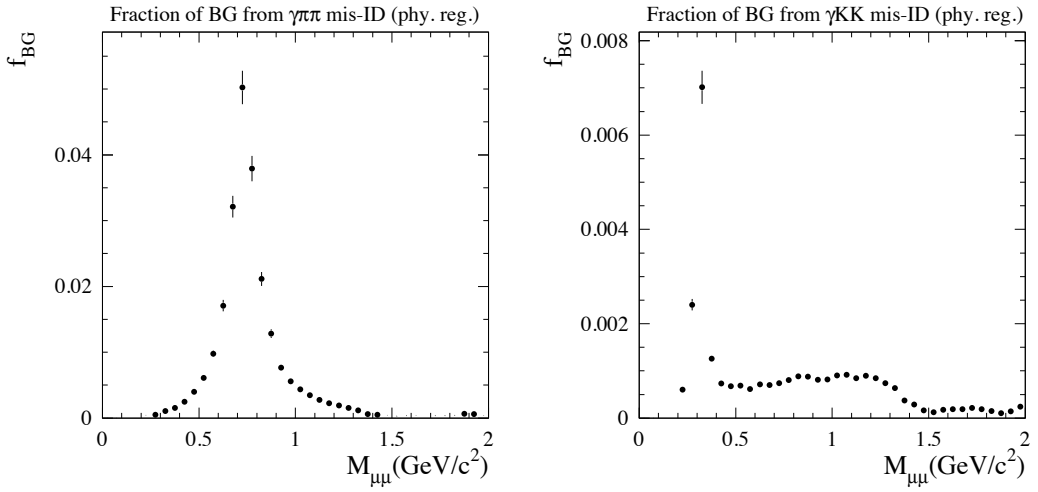

Figure 7.2: The fractional contributions from $\pi\pi$ (left) and KK (right) events to the $m_{\mu\mu}$ spectrum through double mis-ID. The dominant part is from the 2-body ISR processes.

contribution. For this we have fitted the data '$\mu\mu$' mass spectrum between 0.3 and 1.5 GeV, using the $\mu\mu$ and $\pi\pi$ mass shapes given by the simulation. The total number of $\pi\pi$ events found is 2930 ± 362 to be compared with the PID prediction of 2596 ± 104 used in Eqs. 7.1. The fit is repeated with stronger μ-ID, with both muons required to be 'Tight', then 'VeryTight' (using the cut-based MuonMicro selector). The resulting $\pi\pi$ values are found to be 1720 ± 341 for 'Tight-Tight' and 479 ± 265 for 'VeryTight-VeryTight', in agreement with the expected $\pi\pi$ reduction in the simulation, giving 1643 ± 18 and 371 ± 9, respectively. This is evidence that the excess near 0.75 GeV does come, as expected, from the $\pi\pi$ background as opposed to an unaccounted systematic effect in the μ-ID efficiency.

7.2.2 Background from J/ψ and ψ' decays

One must still consider background to the '$\mu\mu$' sample from processes producing real muons.

ISR-produced J/ψ decay to $\mu\mu$ is not a background to the complete $\mu^+\mu^-\gamma$ process, but to the purely QED reaction to be used for the determination of the ISR luminosity. The ψ' case is different as it contributes to the studied reaction as a background through its decays to J/ψ, either following the $\pi^0\pi^0 J/\psi$ transition

or radiative decays through charmonium states. Both contributions are removed excluding events where the measured $\mu\mu$ mass is in the 3.0-3.2 GeV/c^2 window. Since the finally used $\mu\mu$ mass is the fitted one from the kinematic fit, the cut will not produce a sharp hole in the final mass spectrum. Evidence for direct and indirect J/ψ production is given in Fig. 7.3.

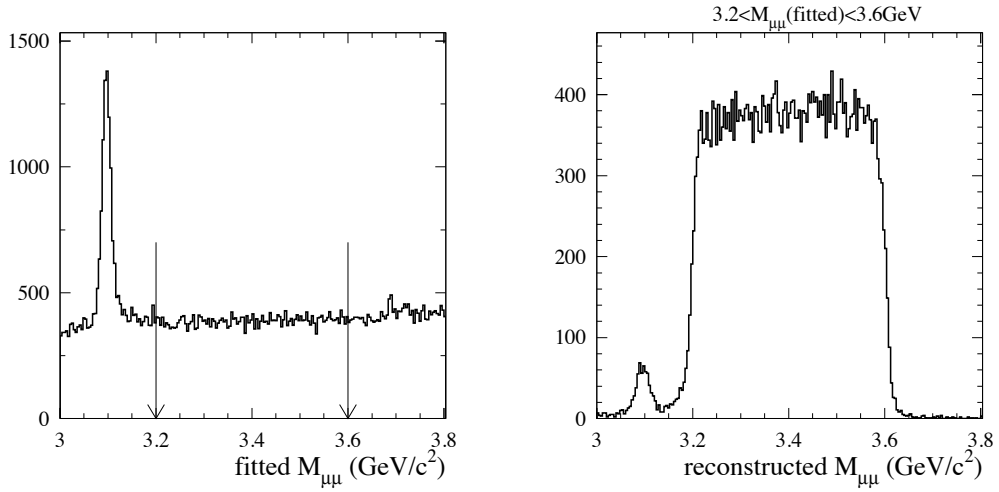

Figure 7.3: The $\mu\mu$ mass obtained from the results of kinematic fits (left) and directly calculated from reconstructed tracks for the events with fitted $\mu\mu$ mass between 3.2 and 3.6 GeV/c^2 (right).

Another hidden background from J/ψ comes from the radiative decay $J/\psi \to \mu^+\mu^-\gamma$. This contribution is seen on the $\mu^+\mu^-\gamma$ mass spectrum: using an event sample with an additional FSR photon with $E_\gamma > 100$ MeV, a 3-parameter gaussian fit yields 136 ± 58 events, with a mass (3098 ± 4) MeV and a standard deviation (16.3 ± 3.4) MeV. The contribution to the $\mu\mu$ mass spectrum between 2 and 3 GeV is of order 1×10^{-3} and neglected.

7.2.3 Background from $\tau\tau$ events

The process $e^+e^- \to \tau^+\tau^-$ can contribute to the '$\mu\mu$' sample through $\mu\mu$ and $\mu\pi$ decay final states. Fully hadronic final states are already taken into account when solving Eqs. (7.1). The contribution from muons is estimated by MC and

found to be small, except at masses above 2 GeV where it reaches a fraction of $\sim 1 \times 10^{-3}$ (Fig. 7.4).

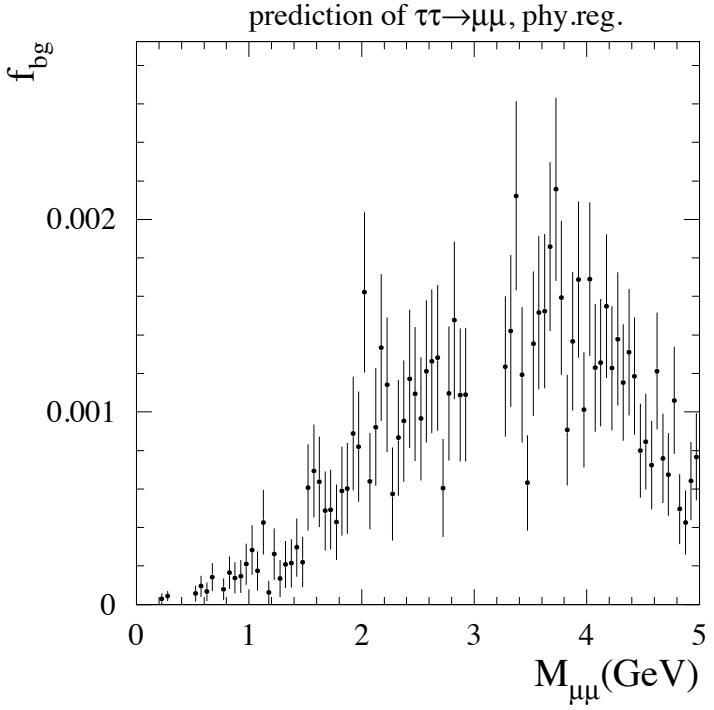

Figure 7.4: The fractional contribution from $ee \to \tau\tau$ with one or two muons in the final state as a function of $m_{\mu\mu}$ (MC).

7.3 Generalities on the backgrounds in '$\pi^+\pi^-\gamma(\gamma)$'

7.3.1 Backgrounds from $\mu^+\mu^-\gamma$ and $K^+K^-\gamma$

As already discussed in section 7.2.1, the backgrounds from $\mu^+\mu^-\gamma$ and $K^+K^-\gamma$ can be obtained from solving Eqs. (7.1). Of course, $\pi\pi$ mass hypothesis should be used here.

7.3.2 Background from $e^+e^-\gamma$ events

Radiative Bhabha events are very strongly suppressed in the event selection because of the track definition which contains a veto on electrons (see Section

3.2) using E_{cal}/p and dE/dx. Remaining events of this type are from distribution tails and various pathologies. Because of this large selection bias there are very few events actually identified as $'ee'\gamma$ in our identification process. They appear in the $'e\pi'$ and $'\pi\pi'$ ID topologies, in about 1/3 and 2/3 of the cases, respectively. This background is identifiable near threshold and at large masses, where it is large. It cannot be detected in the rho region and its magnitude is estimated by interpolation using the mass shape provided by the down-scaled 'RadBhabha' sample obtained at the selector stage. The normalization of the shape will be discussed in the following section.

7.3.3 Photon Conversions and cut on displaced vertices

There is also a background from electromagnetic processes where one of the final state particles interacts with the detector material, allowing the selection criteria to be satisfied. This is the case at threshold from the $e^+e^- \to \gamma\gamma$ process followed by a photon conversion, and at large masses from Bhabha scattering where one of final electrons (positrons) undergoes bremsstrahlung in the beam pipe. In both cases one or both of the detected tracks does not originate from the interaction point. In order to reduced this contamination (when both electrons are identified as pions) the vertex of the 2 tracks is reconstructed in the transverse plane and its distance V_{xy} from the average interaction point is computed.

The electron background from conversions is expected to yield a rather wide V_{xy} distribution, while prompt particles ($e^+e^-\gamma$ and $\pi^+\pi^-\gamma$) give a peak at zero. Fig. 7.5 shows the V_{xy} distribution as a function of $m_{\pi\pi}$ for the '$\pi^+\pi^-\gamma$' sample. Contributions from events with displaced vertices are seen near threshold (conversions) and at masses larger than 3.7 GeV (bremsstrahlung). The latter sharp cut-off is a consequence of the 1-GeV track momentum cut.

The $\pi^+\pi^-\gamma$ signal is peaked at low V_{xy}, typically less than 1-2 mm. A long tail is visible in the high-statistics ρ region, partly from secondary pion interactions. A cut $V_{xy} < 0.5$ cm is applied for the mass region outside of ρ ($m_{\pi\pi} < 0.5$ GeV or > 1 GeV).

The efficiency of the V_{xy} cut for $\pi^+\pi^-\gamma$ events is controlled by a geometric effect and pion secondary interactions. Events at low mass have a small $\Delta\phi$

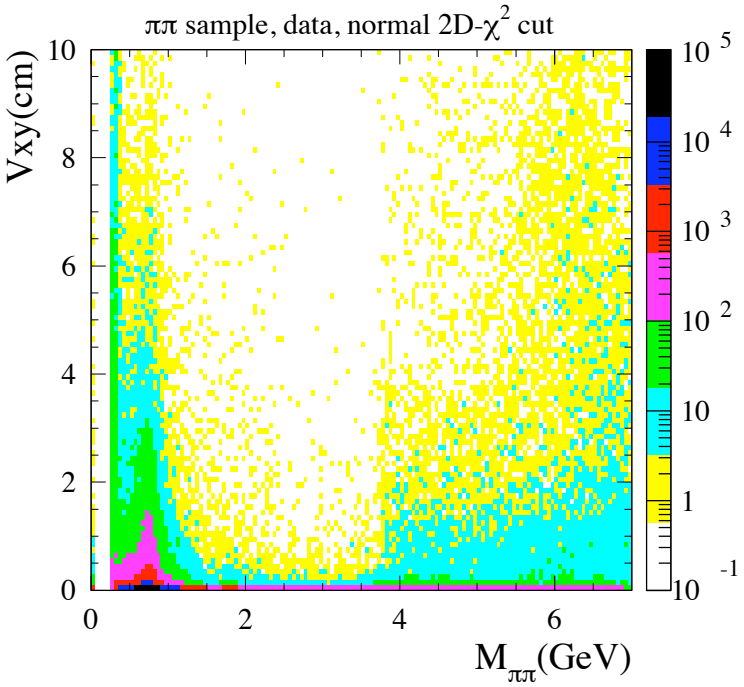

Figure 7.5: The distribution of V_{xy} (distance in cm in the transverse plane between the 2-track vertex and the beam spot) vs. $m_{\pi\pi}$ in GeV for '$\pi^+\pi^-\gamma$' events (runs 1-4) showing background with displaced vertices from $e^+e^- \to \gamma\gamma$ followed by a photon conversion near threshold and $e^+e^- \to e^+e^-$ with bremsstrahlung at large masses. The prominent ρ signal is peaked at small V_{xy}. The cut $V_{xy} < 0.5$ cm is used to select $\pi^+\pi^-\gamma$ events.

opening angle between the 2 tracks in the transverse plane and the uncertainty on V_{xy} is degraded. This effect is common to pion and muon events and therefore can be conveniently studied with the background-free $\mu^+\mu^-\gamma$ in data. The effect of secondary interactions cannot be studied in data at very low mass, because of background, but in the ρ region.

The dependence on $\Delta\phi$ and mass is studied in MC and data for the $\mu^+\mu^-\gamma$ sample. The corresponding plots are given in Fig. 7.6. The $\Delta\phi$ dependence is similar in data and simulation, with a large loss below 0.2 radian. The data efficiency is lower than for simulation by 3-4% in this range. The mass dependence of the data/MC correction can be obtained by sampling the $\Delta\phi$ variation of the efficiency ratio. The comparison with the data/MC efficiency ratio, directly

determined as a function of $m_{\mu\mu}$, is satisfactory as seen in Fig. 7.7. Therefore it is justified to use the same data/MC $\Delta\phi$ input sampled with $\pi^+\pi^-\gamma$ MC events to obtain the geometric correction to apply to pions as a function of $m_{\pi\pi}$, which is also given in Fig. 7.7.

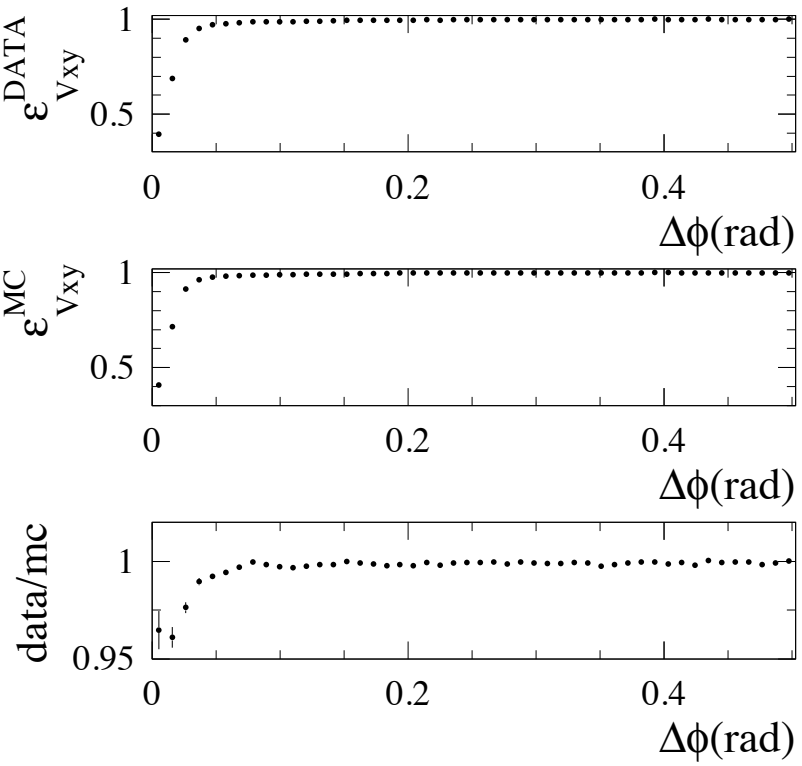

Figure 7.6: The $\Delta\phi$ dependence of the $V_{xy} < 0.5$ cm cut efficiency for $\mu^+\mu^-\gamma$ events in data (top) and in simulation (middle), and their ratio (bottom).

The effect of the pion secondary interactions on the V_{xy}-cut efficiency is studied in the ρ region, both in data and MC. The correction found there for the ratio of efficiencies data/MC is $(4.1 \pm 0.5) \times 10^{-3}$, higher than the value obtained with muons by 1.3×10^{-3}. An additional systematic uncertainty of 1.3×10^{-3} is added to the correction shown in the right plot in Fig. 7.7.

Thus the loss correction is 2% below 0.3 GeV, decreasing to 1% in 0.3-0.35 GeV, 3×10^{-3} at the ρ peak, and less than 10^{-3} above 1.7 GeV. In practice

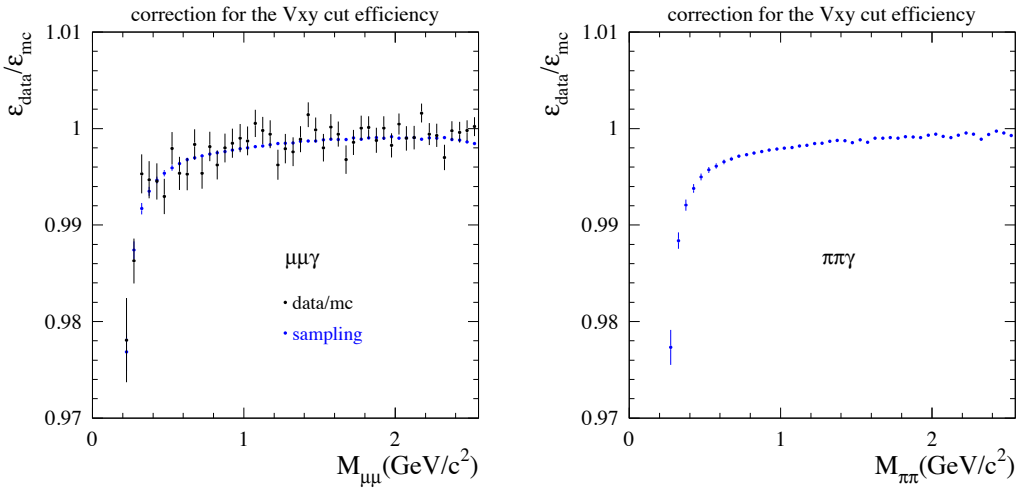

Figure 7.7: Left: the $m_{\mu\mu}$ dependence of the $V_{xy} < 0.5$ cm cut efficiency data/MC ratio for $\mu^+\mu^-\gamma$ events obtained by sampling the $\Delta\phi$ dependence (small blue points) and the directly measured ratio (black points with larger errors). Right: the same ratio for $\pi^+\pi^-\gamma$ using sampling of the muon $\Delta\phi$ dependence.

the V_{xy} cut is not needed from 0.5 to 3 GeV (no significant contribution from conversion or bremmsstrahlung). For reasons of simplicity, the V_{xy} cut is applied uniformly in the ρ tails region ($m_{\pi\pi} < 0.5$ and > 1 GeV), but not in the central region.

The $V_{xy} < 0.5$ cm cut strongly reduces the background from conversions and bremsstrahlung, but still leaves some remaining ee contribution from these sources and $ee\gamma$. As said before the mass shape of these contributions is obtained from 'RadBhabha'-flagged events. However it needs to be properly normalized to the actual background in data. A convenient normalization point is obtained near threshold where the pion contribution is small and ee background the largest. The two contributions can be cleanly separated by looking at the angular distribution in the $\pi\pi$ center-of-mass system, assuming the pion mass for the particles.

The distribution of $|\cos\theta^*|$ of events for $m_{\pi\pi} < 0.32$ GeV after subtraction of $\mu^+\mu^-\gamma$ background (obtained from data and measured ID efficiencies) is given in Fig. 7.8. It is fitted with 3 components: $\pi^+\pi^-\gamma$ and $K^+K^-\gamma$, both with shapes taken from the simulation, and ee background with a shape obtained from the

'RadBhabha' sample. The latter contribution has a characteristic sharp peak near one with a long tail. The fit is reasonable, with some small deviations observed around $|\cos\theta^*| \sim 0.8$. This is adequate to obtain the ee normalization with the required precision in the ρ region (see later).

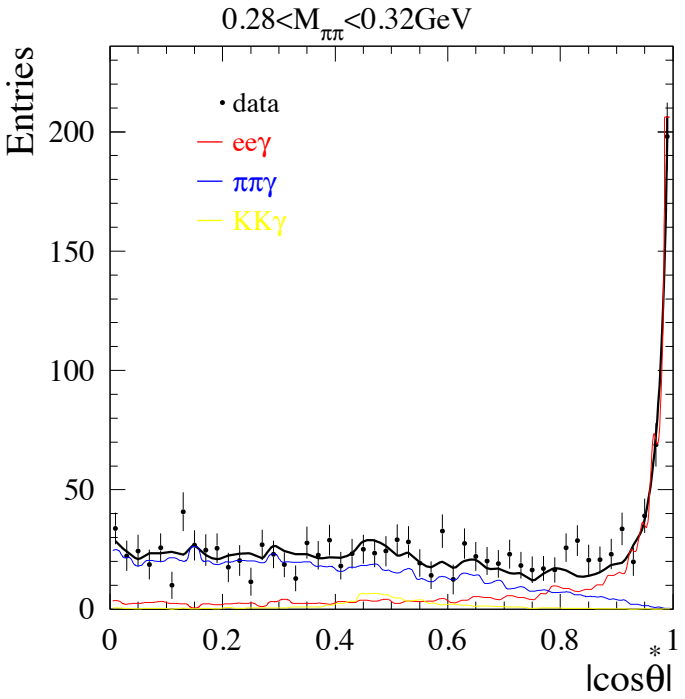

Figure 7.8: The distribution of $|\cos\theta^*|$ of $\pi^+\pi^-\gamma$ events for $m_{\pi\pi} < 0.32$ GeV after subtraction of $\mu^+\mu^-\gamma$ background and $V_{xy} < 0.5$ cm (with standard π-ID and 2D-χ^2 cut, runs 1-4). Fit is adjusted with 3 free components: ee from 'RadBhabha' sample (red), $\pi\pi\gamma$ (blue) and $KK\gamma$ (yellow), both from simulation.

7.3.4 $p\bar{p}\gamma$ process

Proton ID has not been considered in the particle identification process, since the process $p\bar{p}\gamma$ contributes at a very small level in ρ mass region. With the chosen ID classes protons are classified as pions, and antiprotons sometimes as electrons. The cross section for this process has been measured by *BABAR* [21] and the results can be used to reweight the MC prediction. Also the MC

does not include the contribution from $J/\psi \to p\bar{p}$. This was also included in the reweighting, using the branching ratio from PDG [47]. As seen in Fig. 7.9 this contribution appears near 2.5 GeV in the $\pi\pi$ mass spectrum, with some indication for it in data. The overall contamination is taken from the reweighted simulation and subtracted statistically.

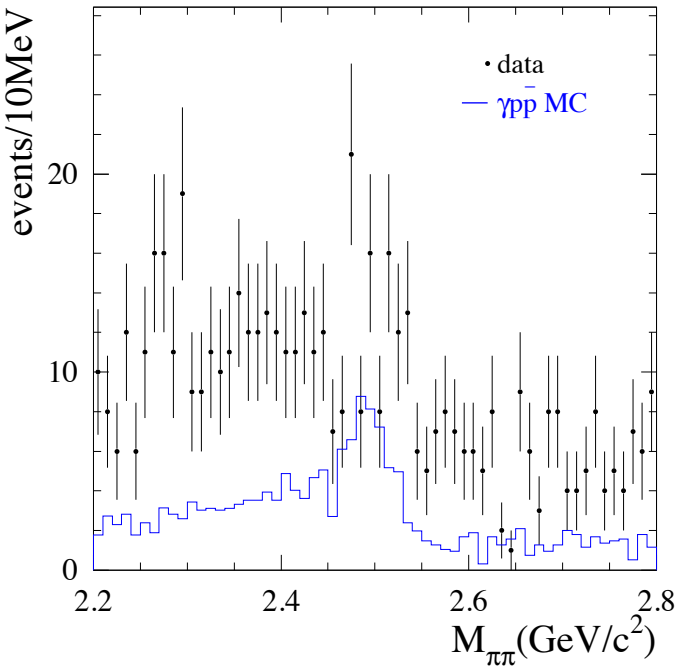

Figure 7.9: The $m_{\pi\pi}$ distribution of data (points) and the $p\bar{p}\gamma$ MC (histogram) reweighted to include the $J/\psi \to p\bar{p}$ contribution.

7.3.5 Multi-hadrons from the $q\bar{q}$ process

Hadronic processes, either directly or ISR-produced, introduce a pollution in the pion sample which is considerably reduced by the requirement of only two good tracks and the χ^2 cut of the kinematic fit.

The background is estimated using simulated samples of the $e^+e^- \to q\bar{q}$ process (see the corresponding entry in Table 7.1). For these events the ISR photon candidate originates from an energetic π^0.

Table 7.1: The simulated processes used to estimate the backgrounds.

Final States	σ(pb)	N_{expect}	$N_{available}$	$f = \frac{N_{expect}}{N_{available}}$
$K_S K_L \gamma$	1.53	354k	608k	0.58
$p\bar{p}\gamma$		20k	190k	0.105
$\pi^+\pi^-\pi^0\gamma$	2.6	603k	372k	1.6
$\pi^+\pi^-2\pi^0\gamma$	3.9	905k	744k	1.2
$2(\pi^+\pi^-)2\pi^0\gamma$	0.1	23k	378k	0.06
$2(\pi^+\pi^-)\gamma$	3.0	696k	564k	1.2
$\eta 2\pi\gamma$	0.25	58k	286k	0.20
uds(non-ISR)	2090	485M	734M	0.66
$\tau\tau$	890	206M	470M	0.44

The JETSET prediction for $q\bar{q}$ fragmentation into low-multiplicity final states being questionable, the MC rate is renormalized using data. Since in this case the ISR photon candidate originates from π^0 decay, it is possible to search for such a signal both in data and in MC by pairing the ISR photon candidate with all detected additional photons. The retained pair is chosen on the basis of the best kinematic fit for 2 charged tracks + 2 detected photons. Fits to $\gamma\gamma$ mass distributions are performed in data and MC taking into account 'background' from $\pi\pi\gamma$ events taken from the simulation, possible other contributions and a gaussian shape for the π^0 signal. Background from $\tau\tau$ events are previously subtracted using MC.

Looking at the 2D-χ^2 distribution from $q\bar{q}$ events in the 0.5-1 GeV mass range (Fig. 7.10) we see that the contamination predicted by JETSET lies very close to the χ^2 cut boundary, as expected. The contribution from the $\pi^+\pi^-\pi^0$ final state, which should appear at small χ^2 values, is tiny, less than 3% of the total $q\bar{q}$ contamination, thus less than a few 10^{-4} of the $\pi\pi\gamma$ signal. Contributions at larger χ^2 involve higher multiplicities. In order to see the π^0 signal the fit is performed in a χ^2 region close to the boundary, but inside the signal region: this 'sleeve' is indicated in Fig. 7.10.

The π^0 fits are done in wide $\pi\pi$ mass bins (0.5 GeV) between threshold and 3 GeV, covering the practical range for the analysis. Examples of fits are shown in Fig. 7.10. Fits are also performed in the background region to check the sensitivity to the final state multiplicity. The corresponding ratios between the π^0 yields in data and $q\overline{q}$ MC are given in Fig. 7.10. JETSET is found to overestimate the background contributions by a factor of 1.3 (~ 0.5 compared to 0.66 from the luminosities as given in Table 7.1), almost independently of the $\pi\pi$ mass and whether it is situated in the signal or background region in the 2D-χ^2 plane.

Two questions remain in this determination. First, the validity of the π^0 method could be questioned since the fragmentation in JETSET will produce different final states which could have different efficiencies for finding the π^0 signal. This effect is likely to be small since we see little variation either with mass or χ^2. We checked this possibility by selecting true final states in MC and measuring the probability to find a π^0 in each case. The results are 0.274 ± 0.021 for $\pi^+\pi^-\pi^0$, 0.285 ± 0.016 for $\pi^+\pi^-\pi^0\pi^0$, to be compared with 0.260 ± 0.007 for the full $q\overline{q}$ contribution in the signal region and 0.259 ± 0.003 in the background region, indicating variations less than $\pm 5\%$. Second, the state with lowest multiplicity, $\pi^+\pi^-\pi^0$, is in fact identical to the signal $\pi\pi\gamma(\gamma)$ events and is expected to populate the good χ^2 region where the signal is huge. JETSET predicts this contribution to be only 3% of the total contamination, but how can we be sure in data? Since the $\pi\pi$ mass distribution in JETSET peaks between 1 and 2 GeV, one can exploit the fact that the $\pi\pi$ signal is much smaller there and try to find a π^0 signal in data. This attempt, shown in Fig. 7.11 for $ln(\chi^2_{add.ISR} + 1) < 2.5$ and $ln(\chi^2_{add.FSR} + 1) < 2.5$, and $1.2 < m_{\pi\pi} < 2.0$ GeV, gives a weak signal, consistent with JETSET expectation with 50% uncertainty.

7.3.6 Multihadronic ISR processes

The background is estimated using simulated processes which are listed in Table 7.1. The dominant contributions are from $e^+e^- \to \pi^+\pi^-\pi^0\gamma$ and $e^+e^- \to \pi^+\pi^-2\pi^0\gamma$.

An approach similar to $q\overline{q}$ comparing data and MC is followed for the 3π

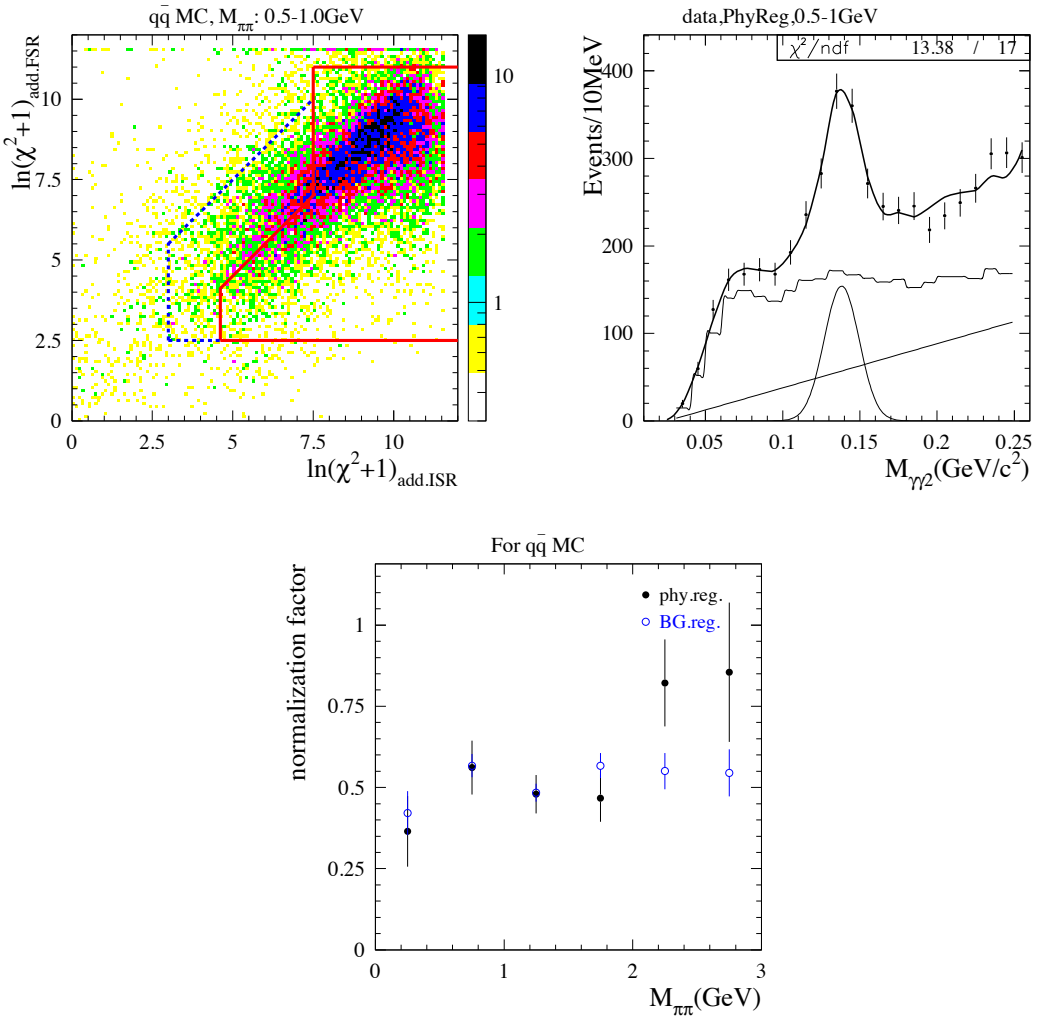

Figure 7.10: Adjustment of the level of $q\bar{q}$ background predicted by JETSET, using the π^0 signal in the $\gamma_{ISR}\gamma$ mass distribution. Top left: 2D-χ^2 distribution of $q\bar{q}$ MC events normalized to the data luminosity for $0.5 < m_{\pi\pi} < 1$ GeV. The solid broken line indicates the χ^2 cut used in this region, while the dashed defines a 'sleeve' in the signal region where most of the background is concentrated. Top right: the corresponding gaussian π^0 fit for data events in the sleeve. The wiggly histogram is the $\pi\pi\gamma$ MC distribution. Additional contributions are represented by the linear term. Bottom: the ratio between the number of π^0's found in data and in the $q\bar{q}$ MC in 0.5-GeV bins for the sleeve (black points) and the full rejected background region (blue points). The ratios below 2 GeV are consistent for different masses and in the two regions.

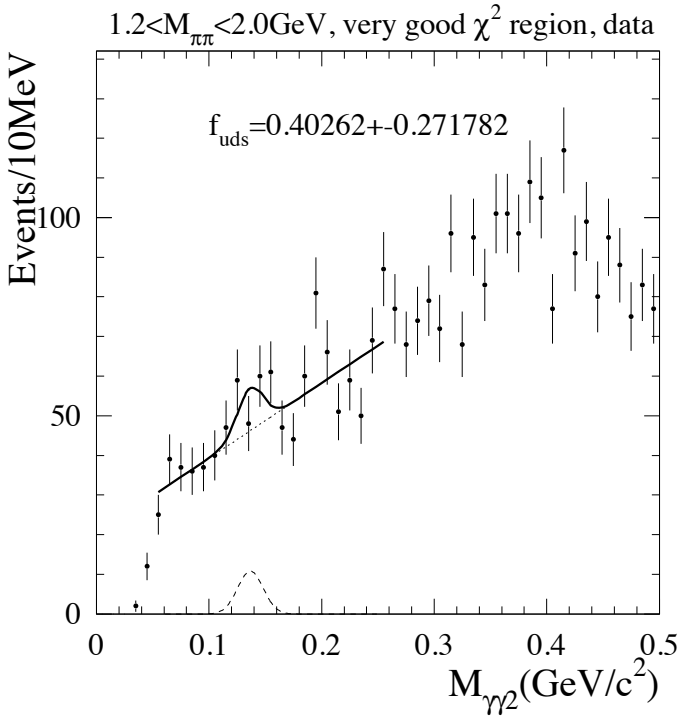

Figure 7.11: Search for a π^0 signal in data from $ee \to \pi^+\pi^-\pi^0$ in good χ^2 region, $ln(\chi^2_{add.ISR}+1) < 2.5$ and $ln(\chi^2_{add.FSR}+1) < 2.5$, and in the intermediate mass range $1.2 < m_{\pi\pi} < 2.0$ GeV.

ISR process, although here we expect the simulation to work reasonably well. The higher part (1.05 to 3 GeV) of the 3π mass distribution is reweighted using the measured *BABAR* cross section [19] since it is not well described in the simulated data. This process is dominated by the production of the ω and ϕ narrow resonances which can be used as calibration signals. In practice a kinematic fit to the $\pi^+\pi^-3\gamma$ final state is performed using a π^0 constraint, and the 3π mass distribution is fitted to two components: signal ($\pi\pi$) and background (3π), both obtained from the corresponding MC simulation, as shown in Fig. 7.12. The ratio of 3π contributions in data and MC is found to be 1.60 ± 0.06 (the error has been increased by the factor $\sqrt{(\chi^2_{3\pi\gamma}/DF)}$) in the wide signal region used for the ρ region, in agreement with the luminosity ratio between data and MC (1.62). As only 6% (from MC) of the $\omega\gamma$ and $\phi\gamma$ events have lost the second photon from

the π^0 decay, the result is representative of the full contribution of this process in the signal region.

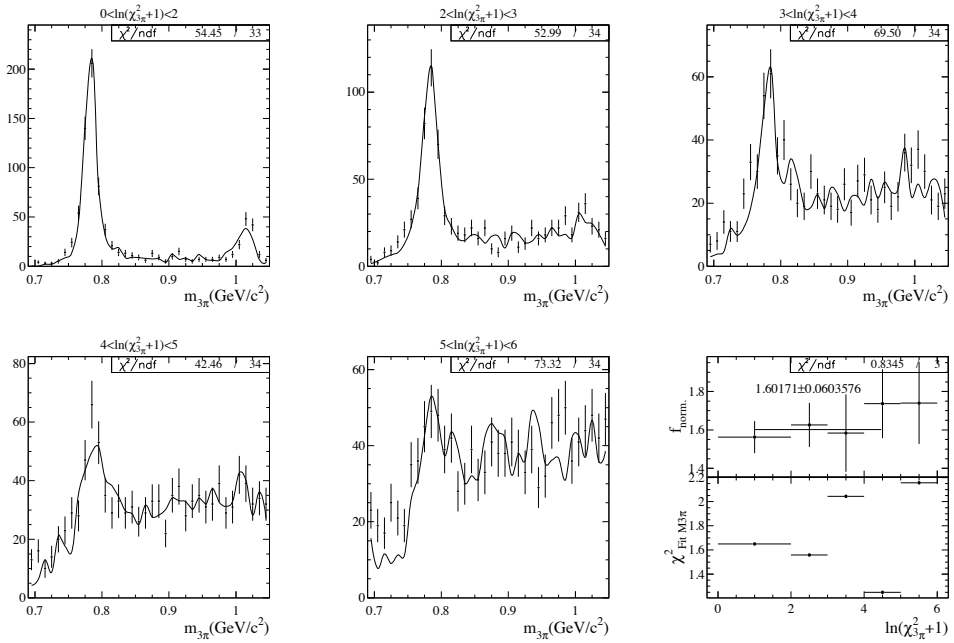

Figure 7.12: Left from right: the 3π mass distribution in the loose-χ^2 region for different ranges of the χ^2 of the kinematic fit to the $\pi^+\pi^-3\gamma$ final state, with data points and curves from the MC shapes fitted to the data in magnitude. Bottom right: ratio of the fitted $\gamma 3\pi$ in data over the MC prediction (top) and χ^2 of 3π mass fit (bottom) both as function of the χ^2 of the $\gamma 3\pi$ kinematic fit.

The contribution from the remaining most important processes $2\pi 2\pi^0$ and $e^+e^- \to \tau^+\tau^-(\gamma)$ are at a smaller level and they are estimated from MC alone, assuming a normalization uncertainty of 10%.

Fig. 7.13 shows the 2D-χ^2 distributions in the 0.5-1 GeV $m_{\pi\pi}$ range for $\pi\pi\gamma$ data and simulation, as well as all the dominant contributions considered. Different processes populate different χ^2 regions with their tails contributing in the selected region.

The background fractions in the '$\pi\pi\gamma$' sample are given later in the different mass regions considered which are analyzed with different χ^2 cuts.

7.4 Additional Radiation

Fig. 7.14 shows the 2D χ^2 distributions for $\mu^+\mu^-\gamma$ data and MC, in the 0.5-1 GeV mass interval. Distributions in other mass regions behave similarly.

A cut is defined in the 2D χ^2 plane to separate a 'background' region and a 'signal' region (or physical region). As mentioned above this is really necessary only for the $\pi\pi\gamma(\gamma)$ process, but the same cut is applied to both pion and muon channels. The cut has been optimized for pions as a compromise between large efficiency and small remaining background.

The raw $m_{\mu\mu}$ spectra of the selected $\mu^+\mu^-\gamma(\gamma)$ events are shown for data and MC in Fig. 7.15.

7.4.1 Additional small-angle ISR

To study additional ISR at small angles to the beams the cuts $\ln(\chi^2_{add.FSR}+1) > \ln(\chi^2_{add.ISR}+1)$ and $E^*_{\gamma_{add\ ISR}} > 200$ MeV are used in addition to the global 2D condition, where $E^*_{\gamma_{add\ ISR}}$ is the energy of the additional ISR photon in the e^+e^- CM which is derived from the additional ISR fit. This cut selects a large enough additional ISR photon energy, resulting into a bad $\chi^2_{add.FSR}$ value. Events without extra detected photons are also considered.

The $\chi^2_{add.ISR}$ distributions of these events are shown in Fig. 7.16 for data and AfkQed MC in $m_{\mu\mu} < 1$ GeV for $\mu^+\mu^-\gamma(\gamma)$ and $0.5 < m_{\pi\pi} < 1.0$ GeV for $\pi^+\pi^-\gamma(\gamma)$. The agreement between data and MC is poor as the data shows a much longer tail than simulation. This is expected as the fit is performed assuming the additional photon to be collinear to the beams. Since additional radiation in AfkQed is generated through the structure-function method and exclusively along the beams, the corresponding χ^2 distribution is well behaved. So the longer tail in data is evidence that additional ISR photons do have some angular distribution, as expected in real life.

The additional ISR photon energy distributions are given in Fig. 7.17. The distribution in simulation drops around 2.3GeV as a result of the $m_{x^+x^-\gamma_{ISR}(\gamma_{FSR})} > 8$ GeV ($x = \mu$ or π) cut used at generation level. Below this value the rate in

data is lower by about 7%, because events with a detected large-angle additional ISR photon have a good $\chi^2_{add.FSR}$ and are not included in this sample.

So the results found for additional ISR in $\pi\pi\gamma(\gamma)$ and $\mu\mu\gamma(\gamma)$ channels are in agreement. The lack of angular distribution and events with $m_{x^+x^-\gamma(\gamma_{FSR})} < 8$ GeV ($x = \mu$ or π) in AfkQed is corrected at the 4-vector level using Phokhara (will be described in Chapter 8), but its effect cancels in the $\pi\pi/\mu\mu$ ratio.

7.4.2 Additional FSR and large-angle ISR

Similarly one can select a sample of events with an extra measured photon (thus in the detector acceptance). An energy cut $E > 200$MeV in lab frame is applied for the fitted additional large-angle photon. The corresponding $\ln(\chi^2_{add.FSR}+1)$ distribution of $\mu^+\mu^-\gamma(\gamma)$ is given in Fig. 7.18 for data and simulation. They are in fair agreement. The $\chi^2_{add.FSR}$ distribution of $\pi^+\pi^-\gamma(\gamma)$ in data is strongly affected by multi-hadronic background in the tails. The part up to the cut $\ln(\chi^2_{add.FSR}+1) < 2.5$ agrees well with the MC shape, as the case for the $\mu\mu\gamma(\gamma)$ process. This is expected as the respective kinematic fits are almost identical.

The contributions of large-angle ISR and FSR can be identified looking at the photon angular distribution with respect to the outgoing muons or pions. In Fig. 7.19 the distribution of the smaller of the two angles with either muons is given for $m_{\mu\mu} < 1$ GeV: it shows a clear correlation, thus indicating a true FSR signal in data in agreement with the simulation. Evidence for large-angle ISR is also seen in data, at variance with AfkQed. This major discrepancy was expected, as additional ISR in AfkQed is constrained to be collinear with the beams.

For $\pi^+\pi^-\gamma(\gamma)$, an additional cut $\ln(\chi^2_{add.FSR}+1) < 2.5$ is used to reduce the backgrounds, and the distributions of the smaller of the two angles with either pion are given in Fig. 7.20, where the remained backgrounds dominated by $\pi^+\pi^-\pi^0\gamma$ events. The similar behaviors to $\mu^+\mu^-\gamma(\gamma)$ are also observed in $\pi^+\pi^-\gamma(\gamma)$.

The photon energy distributions for $\mu^+\mu^-\gamma(\gamma)$ are given in Fig. 7.21 for the total rate (FSR + large-angle-ISR) and the FSR component separated using a

cut $\theta_{\mu\gamma_2} < 20°$. Since no large-angle ISR is available in AfkQed the comparison is only done for the shape. However for the FSR component the absolute rates are compared, showing a good agreement up to $E_\gamma \sim 2$ GeV, and a small excess in data in the tail above. But after correcting for the remaining ISR contribution below 20° (taken with a 25% systematic uncertainty) the ratio data/MC for the additional FSR contribution amounts to 0.96 ± 0.06. So the use of PHOTOS to generate FSR photons is in good agreement with data and adequate for our precision goal, since the uncertainty represents about 8×10^{-4} of the total $\mu^+\mu^-\gamma(\gamma)$ sample.

The photon energy distributions for $\pi\pi\gamma(\gamma)$ are given in Fig. 7.22, before and after background subtraction, for $\theta_{\pi\gamma_2} < 20°$ and 10°. The tighter cut keeps less ISR events in data and the agreement between data and simulation is good, except at larger photon energies where an excess in data is observed. The ratio data/MC of FSR events for $\theta_{\pi\gamma_2} < 20°$ is equal to 1.21 ± 0.05. Background subtraction is substantial at large energies, but it should be well estimated, as it comes solely from the $\pi^+\pi^-\pi^0\gamma$ process. Thus the excess is real and indicates that the description of FSR using PHOTOS is less successful for pions than for muons, but only for large energies.

The physics of the final-state radiative event sample will be discussed later. For the moment we concentrate on the deviation between data and simulation which leads to a systematic shift in the AfkQed-computed acceptance (Section 7.5.3).

7.5 Determination of the χ^2 cut efficiency

7.5.1 The χ^2 cut efficiency for $\mu\mu\gamma(\gamma)$

The efficiency of the 2D χ^2 cut for $\mu\mu\gamma(\gamma)$ is obtained in data by solving again Eqs. (7.1) in each mass bin, but this time in the rejected background region. The procedure yields directly the produced spectrum of muon events there which, combined with the spectrum in the signal region yields the efficiency. A small contribution from $\tau\tau$ must be explicitly subtracted: relative to the total number of muons, it has approximately the same shape and magnitude as in the signal

region shown in Fig. 7.4.

Fig. 7.23 gives the measured χ^2 efficiency, as a function of $m_{\mu\mu}$. It is lower than the prediction from AfkQed and the simulation by 1.2%. Most of the discrepancy arises from the absence of large-angle ISR in AfkQed, which is present in data and generates some loss when the large χ^2 tails are cut out. Otherwise the efficiency decreases with $m_{\mu\mu}$ because of the loss of large-χ^2 FSR events. The same behavior is observed in data and simulation, consistent with the fact that additional FSR for $\mu\mu\gamma(\gamma)$ is well described in AfkQed.

The systematic uncertainty on the determination of the χ^2 efficiency for $\mu\mu\gamma(\gamma)$ comes exclusively from the estimate of the background, dominated by the evaluation of the normalization factors data/MC. These uncertainties are incorporated in the point-to-point errors.

7.5.2 Comparison between $\pi\pi\gamma$ and $\mu\mu\gamma$

Unlike for muons it is not possible to directly measure in data the efficiency of the 2D-χ^2 cut for $\pi\pi\gamma(\gamma)$ because of overwhelming background in the cut-out region. The rejected signal events with large χ^2 are of several types:

- bad input to the kinematic fits, mostly from the direction of the ISR photon,
- tails of the χ^2 distributions of events with additional ISR or FSR,
- more than one additional photon (mostly ISR),
- secondary interactions.

Except for the last type which is specific to pions, the other sources are common to pions and muons. A small difference is also expected for the tail of the FSR-fit χ^2, as the FSR level is slightly different for pions and muons.

So the strategy here is to rely on the data/MC corrections from the muon study to take into account the common losses and to further investigate the points specific to pions. Therefore the χ^2-cut efficiency in data for $\pi\pi\gamma(\gamma)$ will be derived from the following expressions:

$$\varepsilon_{\chi^2}^{\pi\pi\gamma(\gamma)\ data} = \varepsilon_{\chi^2}^{\mu\mu\gamma(\gamma)\ data} - \delta\varepsilon_{\chi^2}^{\pi/\mu} - \delta\varepsilon_{\chi^2}^{data/MC\ \pi\pi} \quad (7.2)$$

$$\delta\varepsilon_{\chi^2}^{\pi/\mu} = \varepsilon_{\chi^2}^{\mu\mu\gamma(\gamma)\ MC} - \varepsilon_{\chi^2}^{\pi\pi\gamma(\gamma)\ MC} \quad (7.3)$$

7.5.3 Effect of additional FSR

In Eq. (7.2) the μ/π correction term $\delta\varepsilon_{\chi^2}^{\pi/\mu}$ takes into account the difference in additional FSR between pions and muons, at least according to the PHOTOS procedure in AfkQed. It should be noted that the proper variable to study these effects is $\sqrt{s'}$ rather than $m_{\pi\pi}$: indeed the FSR probability in the $\pi\pi\gamma\gamma$ channel is strongly influenced by the ρ lineshape, as seen in Fig. 7.24. The expected difference in FSR rate due to the $\pi - \mu$ mass difference is clearly visible, as the decrease with $\sqrt{s'}$ of ϵ_{χ^2}, which results from FSR, shows a relative 30% drop with pions compared to muons. This difference arises both from FSR and secondary interactions for pions. The dependence with $m_{\pi\pi}$ of the χ^2-cut efficiency has a pronounced pattern in the ρ region, as expected for FSR.

The relation of this effect with FSR can be demonstrated by looking at the fraction of events in the FSR region with a fitted photon energy $E_{\gamma\ FSR} > 0.2$ GeV. The ρ pattern with $m_{\pi\pi}$ is clearly seen in Fig. 7.25, while the $\sqrt{s'}$ dependence is uniform, similar to the featureless variation for muons.

We now consider the comparison of data and simulation for additional-FSR in quantitative terms. From the comparison of data and MC events in the FSR region defined by $\ln(\chi^2_{add.FSR} + 1) < 2.5$, $E_{\gamma\ FSR} > 0.2$ GeV, and $\theta_{\pi\gamma_2} < 20°$, some excess is observed in data. In the 0.5-1.0 GeV mass range the excess is $(21 \pm 5)\%$, taking into account subtraction of background and the large-angle ISR contribution. The corresponding value determined with muons is $(-4 \pm 6)\%$. Using the fraction of excess additional FSR in data and the fraction of events lost by the $\ln(\chi^2_{add.FSR} + 1.)$ cut (about 30%), the data/MC correction to the 2D-χ^2 cut is estimated to be $(0.6 \pm 0.3) \times 10^{-3}$.

It is interesting to notice that most of the discrepancy with the PHOTOS prediction in AfkQed comes from large photon energies, as seen in Fig. 7.22.

7.5.4 Pion interactions

• Effect of interactions on the χ^2-cut efficiency

As already mentioned , the effects of secondary interactions are mostly seen in the tracking efficiency because of the tight cuts imposed on the track pointing to the interaction region. The residual effect in the kinematic fit χ^2-cut efficiency is smaller. It is possible to estimate it using the simulation, essentially by comparing the behavior of muon and pion events.

From Fig. 7.24 the difference of χ^2-cut efficiencies between $\pi\pi\gamma$ and $\mu\mu\gamma$ is about 1.2×10^{-3} at 0.75 GeV. But we know that the loss of additional-FSR events is smaller for pions, as indicated by the respective FSR fractions in Fig. 7.25. It can be derived as a function of $\sqrt{s'}$ since almost the full dependence results from the FSR loss. Indeed in AfkQed additional ISR is collinear to the beam and the loss of ISR events through the 2D-χ^2 cut is very small. In fact, the efficiency in the muon channel $\varepsilon_{\mu\mu}$ almost extrapolates to one (different by only 5×10^{-4}) at threshold where FSR vanishes. Under the assumption that this minuscule ISR loss is flat in the 0-1 GeV mass range, one can derive the contribution of secondary interactions to the χ^2-cut efficiency for pions:

$$\begin{aligned} \bar{\varepsilon}^{inter}_{\pi\pi}(\sqrt{s'}) &= \varepsilon_{\mu\mu} - \varepsilon_{\pi\pi} + \bar{\varepsilon}^{FSR}_{\mu\mu}\left(\frac{f^{FSR}_{\pi\pi}}{f^{FSR}_{\mu\mu}} - 1\right) \\ &\simeq \varepsilon_{\mu\mu}(2m_\mu) + (\varepsilon_{\mu\mu}(\sqrt{s'}) - \varepsilon_{\mu\mu}(2m_\mu))\frac{f^{FSR}_{\pi\pi}}{f^{FSR}_{\mu\mu}} - \varepsilon_{\pi\pi}(\sqrt{s'}) \quad (7.4) \end{aligned}$$

using $\bar{\varepsilon}$ as a notation for inefficiency. The result, given in Fig. 7.26, gives an inefficiency from interactions, at a level of 2.8×10^{-3}.

• check of interactions in the simulation:

(1) secondary vertices

Even if the effect of interactions, as predicted by the simulation, is quite small, it is important to check the size of the effect in data. To do so a method has been developed to isolate interacting events in both data and MC, allowing one to compare their respective rates. Interactions are tagged by the presence of 'bad' tracks (i.e. standard BaBar tracks, but not satisfying the track requirements of the ISR 2-body analysis) in addition to the 2 good tracks of the selected events,

provided a secondary vertex can be found between a bad track and one of the 2 good tracks. This is achieved by searching the best intersection in space among all possible associations.

Because of the strict requirements on good tracks, such a secondary vertex cannot be very far from the interaction point and extends at most over 8 cm in radius. The dominant source is the beam pipe, with further contributions from the SVT. Indeed simulated events in the range $2.4 < R_{xy} < 3.0$ cm show a characteristic distribution in the 2D-χ^2 plane (Fig. 7.27): they populate the diagonal region, extending through the χ^2-cut boundary. Thus events in this region will affect the χ^2-cut efficiency.

It is possible to increase the interaction signal ratio over the background of accidental vertices, by requiring the $doca_{xy}$ of the interacting good track to be larger than 0.05 cm (see Fig. 7.28 left). In this way one can determine the expected shape in R_{xy} of the interaction events, free of background. The corresponding distribution is shown in Fig. 7.28 (right) for the simulation. Reference distributions are obtained separately for data and MC, using the same method.

Finally, Fig. 7.29 presents the fits in data and MC of the R_{xy} distributions without any $doca_{xy}$ restriction, in order to keep the full interaction signal. The background from non-interacting events is fitted on the distribution using exponentials and is mainly determined for $R_{xy} < 2$ cm where no interactions occur.

The data/MC ratio of interacting events is found to be 1.44 ± 0.10 in the 2D-χ^2 region, and 1.43 ± 0.13 in the background region. The procedure keeps about 10% of the events with secondary interactions in the physical region and 25% in the background region.

(2) $doca_{xy}^{max}$ distribution

A larger fraction of interacting events can be tested with another method. The quantity $doca_{xy}^{max}$ is defined to be the largest of the $doca_{xy}$ for the two tracks in the event, each limited by the cut at 0.5 cm used in the good track definition. The sensitivity of this variable to secondary interactions can be appreciated in Fig. 7.30. There is a striking difference in the tail of the distributions for pions

and muons, and also for pions in events with tight or loose χ^2, as expected from secondary interactions. Keeping events with $doca_{xy}^{max} > 0.1$ cm retains about 50% of interactions with a background of non-interacting events which can be estimated from the muon distribution. To properly normalize the muon distribution attention is paid to the difference of FSR events for pions and muons in the intermediate χ^2 region.

Again it is found that the level of secondary interactions is underestimated in the simulation, with a ratio data/MC of 1.52 ± 0.03 in the intermediate χ^2 region (no reliable determination could be done in the background region with this method, because of the multi-hadronic background). Some correlation exists between the two samples used to determine the ratio (the secondary vertices and the $doca_{xy}^{max}$ tail), but not very large, as the first method keeps event at small $doca_{xy}$ and the second does not require a reconstructed secondary vertex. In any case the second determination is more accurate and dominates the average (1.51 ± 0.03).

Thus, the data/MC correction to the loose χ^2-cut amounts to $(1.3 \pm 0.4) \times 10^{-3}$ for secondary interactions and $(0.6 \pm 0.3) \times 10^{-3}$ for FSR. The total correction is $(1.9 \pm 0.5) \times 10^{-3}$.

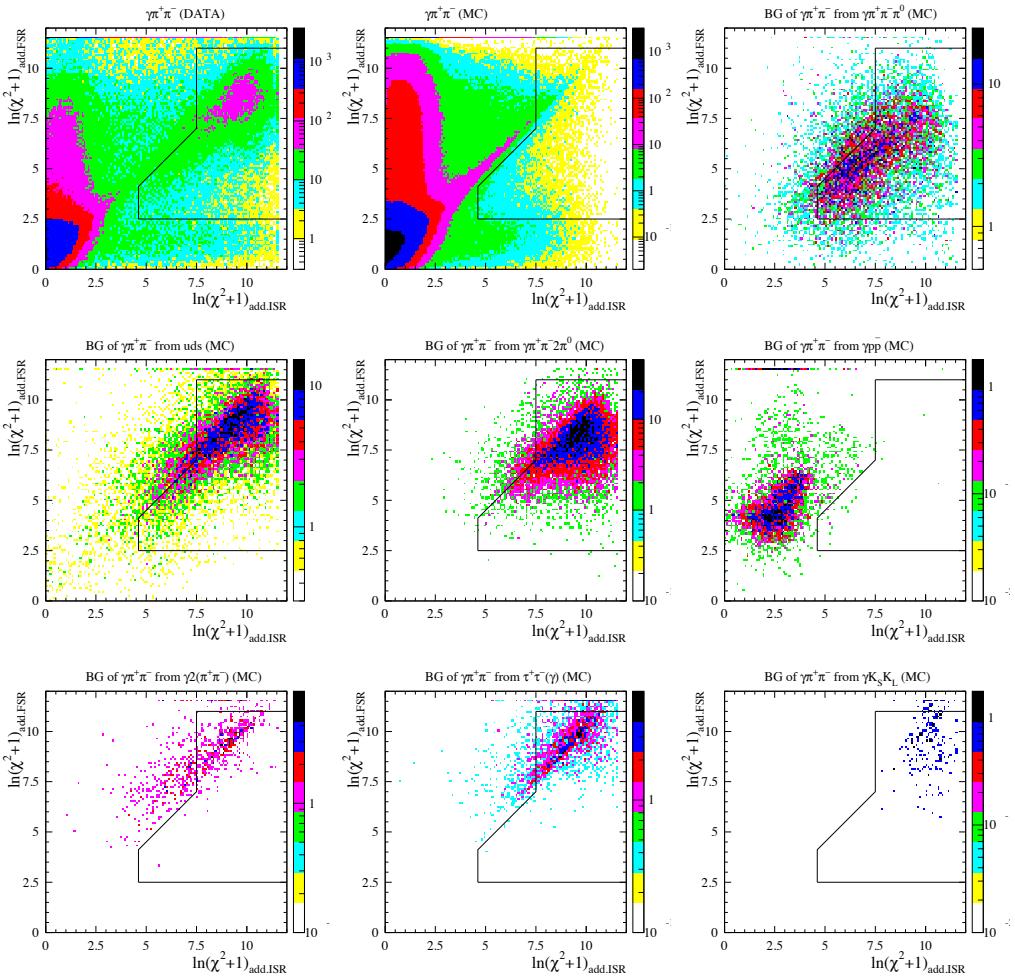

Figure 7.13: The 2D-χ^2 distributions for $0.5 < m_{\pi\pi} < 1$ GeV of '$\pi\pi\gamma(\gamma)$' events from (starting from top left) data, $\pi\pi\gamma$ MC, and leading backgrounds (in order of decreasing importance) which are subtracted out using MC samples normalized to the data luminosity, with data/MC corrections applied for the dominant ones: $2\pi\pi^0\gamma$, $q\overline{q}$, $2\pi2\pi^0\gamma$, $p\overline{p}\gamma$, $4\pi\gamma$, $\tau\tau$, and $K_SK_L\gamma$.

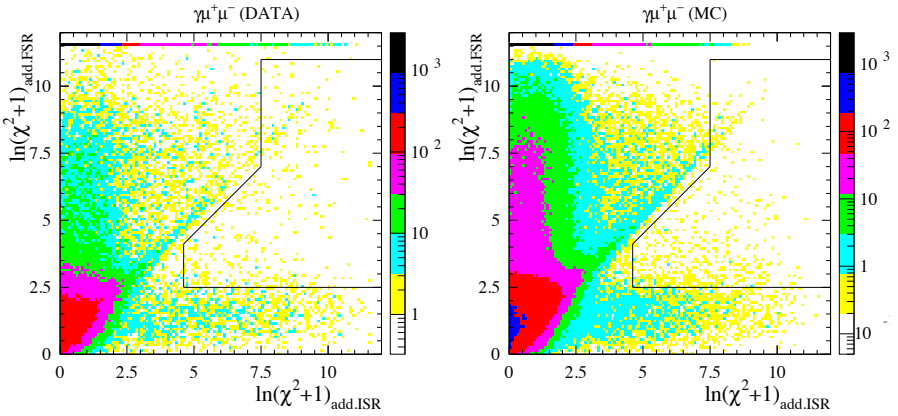

Figure 7.14: The 2D-χ^2 plots of $\mu^+\mu^-\gamma(\gamma)$ events with $0.5 < M_{\mu\mu} < 1.0$GeV for data and $\mu^+\mu^-\gamma(\gamma)$ MC, with the 2D-χ^2 cut indicated.

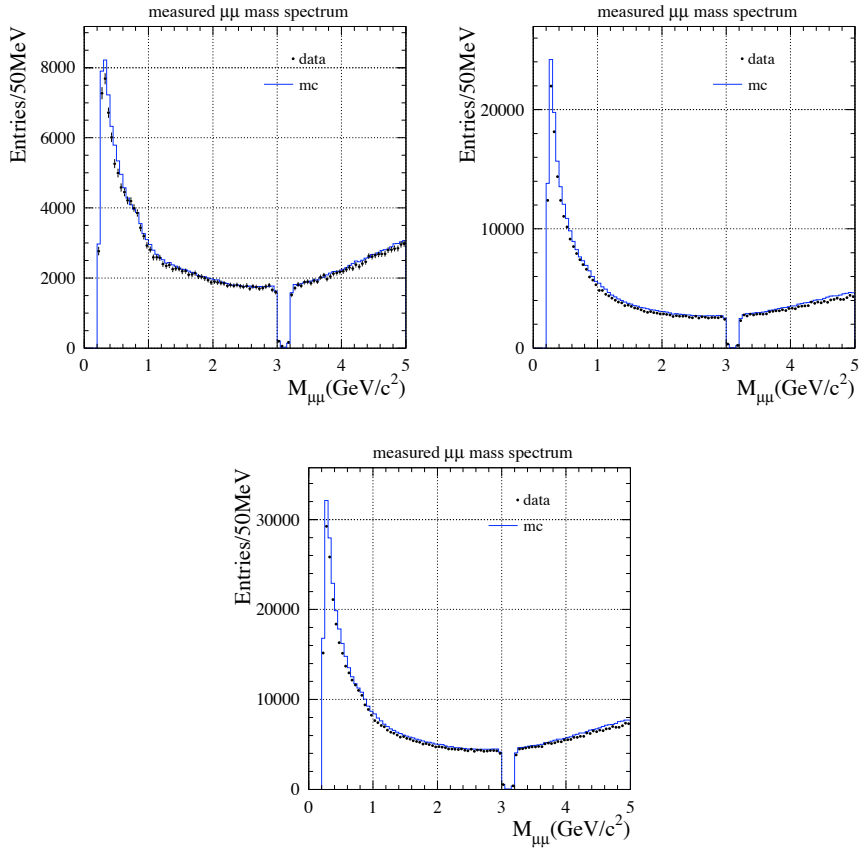

Figure 7.15: The raw $m_{\mu\mu}$ mass distributions of '$\mu\mu$'-identified events for runs 1-2 (top-left), runs 3-4 (top-right), and runs 1-4 (bottom): data (points), MC (blue histogram).

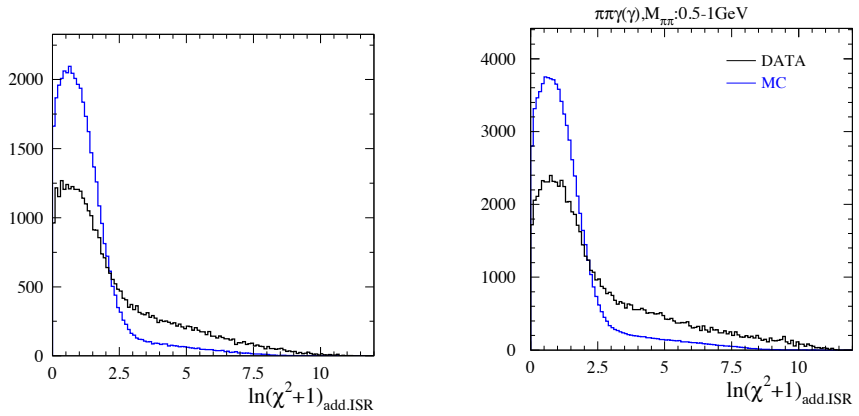

Figure 7.16: The $\chi^2_{add.ISR}$ distributions of the events with $\ln(\chi^2_{add.FSR}+1) > \ln(\chi^2_{add.ISR}+1)$, $E^*_{\gamma_{add\ ISR}} > 200$ MeV, $m_{\mu\mu} < 1$ GeV for $\mu^+\mu^-\gamma(\gamma)$ (left) and $0.5 < m_{\pi\pi} < 1.0$ GeV for $\pi^+\pi^-\gamma(\gamma)$ (right), where MC is normalized to data according to the luminosity. (data: black, MC: blue)

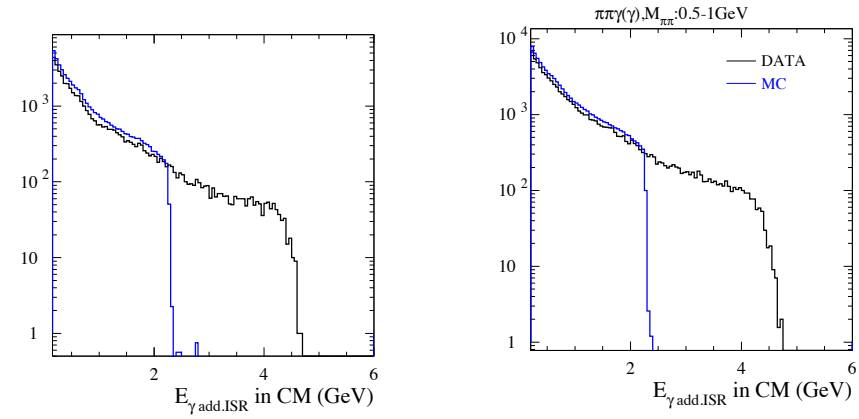

Figure 7.17: The additional ISR photon energy distributions in e^+e^- CM of the events with $\ln(\chi^2_{add.FSR}+1) > \ln(\chi^2_{add.ISR}+1)$, $E^*_{\gamma_{add\ ISR}} > 200$ MeV, in $m_{\mu\mu} < 1$ GeV for $\mu^+\mu^-\gamma(\gamma)$ (left) and $0.5 < m_{\pi\pi} < 1.0$ GeV for $\pi^+\pi^-\gamma(\gamma)$ (right), where MC is normalized to data according to the luminosity. (data: black, MC: blue)

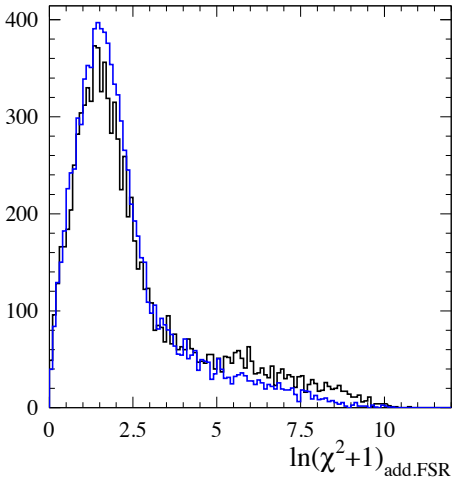

Figure 7.18: The $\chi^2_{add.FSR}$ distributions of $\mu^+\mu^-\gamma(\gamma)$ events with $\ln(\chi^2_{add.FSR}+1) < \ln(\chi^2_{add.ISR}+1)$, $E_{\gamma_{add\ FSR}} > 200$ MeV and $m_{\mu\mu} < 1$ GeV (data: black, MC: blue), where MC is normalized to data according to the number of events.

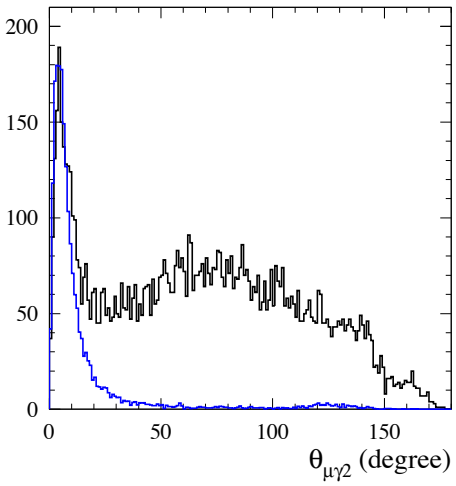

Figure 7.19: The additional 'FSR' photon angular distribution with respect to the closer outgoing muon for the $\mu^+\mu^-\gamma(\gamma)$ events with $\ln(\chi^2_{add.FSR}+1) < \ln(\chi^2_{add.ISR}+1)$, $E_{\gamma_{add\ FSR}} > 200$ MeV and $m_{\mu\mu} < 1$ GeV (data: black, MC: blue), where MC is normalized to data according to the luminosity.

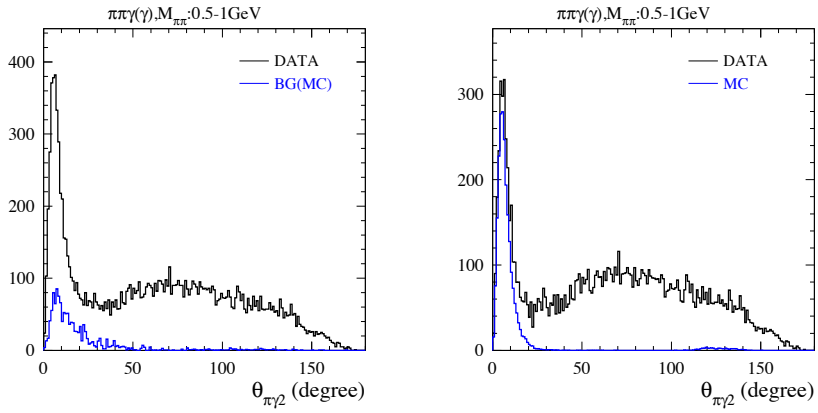

Figure 7.20: The additional 'FSR' photon angular distribution with respect to the closer outgoing pion for the $\pi\pi\gamma(\gamma)$ events with $\ln(\chi^2_{add.FSR}+1) < \ln(\chi^2_{add.ISR}+1)$, $\ln(\chi^2_{add.FSR}+1) < 2.5$, $E_{\gamma_{add\ FSR}} > 200MeV$ and $0.5 < m_{\pi\pi} < 1$ GeV. Left: data (black), background (blue). Right: background-subtracted data (black), $\pi\pi\gamma(\gamma)$ MC (blue), where MC is normalized to data according to the luminosity (there is no large-angle ISR in AfkQed). The FSR signal is clearly seen in data and MC at small angle.

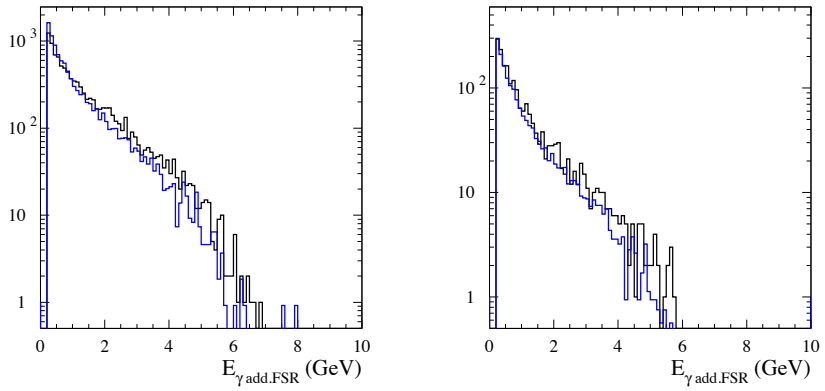

Figure 7.21: Left: The additional 'FSR' photon energy distributions for the $\mu^+\mu^-\gamma(\gamma)$ events with $\ln(\chi^2_{add.FSR}+1) < \ln(\chi^2_{add.ISR}+1)$, $E_{\gamma_{add\ FSR}} > 200$ MeV and $m_{\mu\mu} < 1$ GeV (data: black, MC: blue), where MC is normalized to data according to the number of events (no large-angle ISR in AfkQed). Right: The additional FSR photon energy distributions for the $\mu^+\mu^-\gamma(\gamma)$ events with additional cuts, which are $\ln(\chi^2_{addFSR}+1) < 2.5$ and $\theta_{\mu\gamma_2} < 20^\circ$ (data: black, MC: blue), here MC is normalized to the *BABAR* luminosity (runs 1-4).

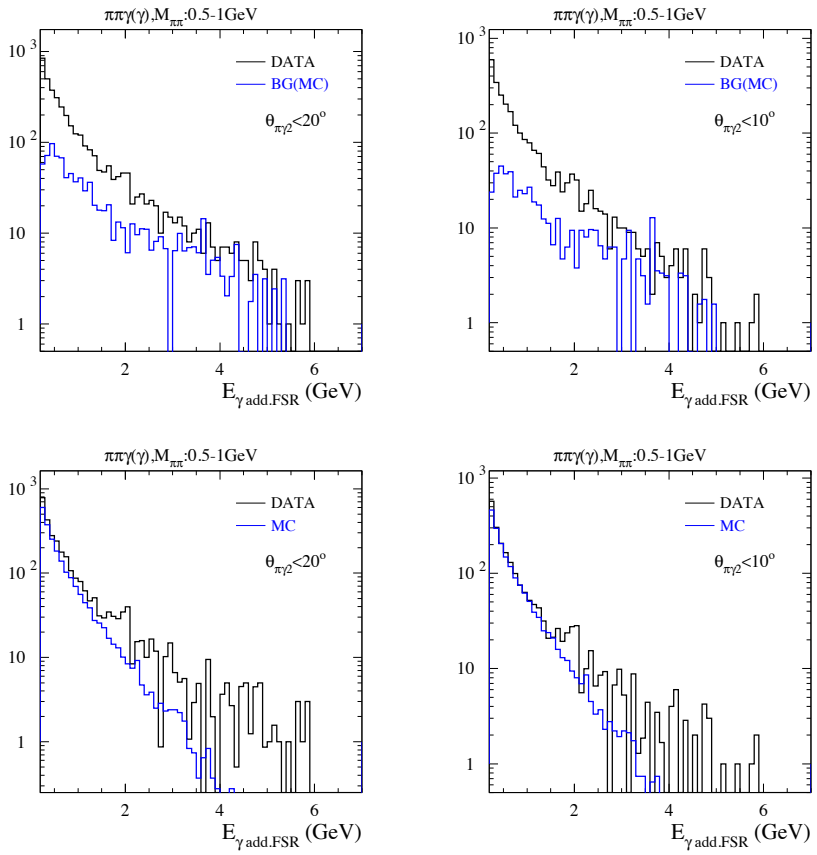

Figure 7.22: The additional FSR photon energy distributions for the $\pi\pi\gamma(\gamma)$ events with $\ln(\chi^2_{add.FSR}+1) < \ln(\chi^2_{add.ISR}+1)$, $E_{\gamma_{add\ FSR}} > 200$ MeV, $0.5 < m_{\pi\pi} < 1$ GeV, and $\theta_{\pi\gamma_2} < 20°$ (left), $\theta_{\pi\gamma_2} < 10°$ (right). Top row: data (black), background (blue). Bottom row: background-subtracted data (black), $\pi\pi\gamma(\gamma)$ MC (blue), where MC is normalized to luminosity (there is no large-angle ISR in AfkQed).

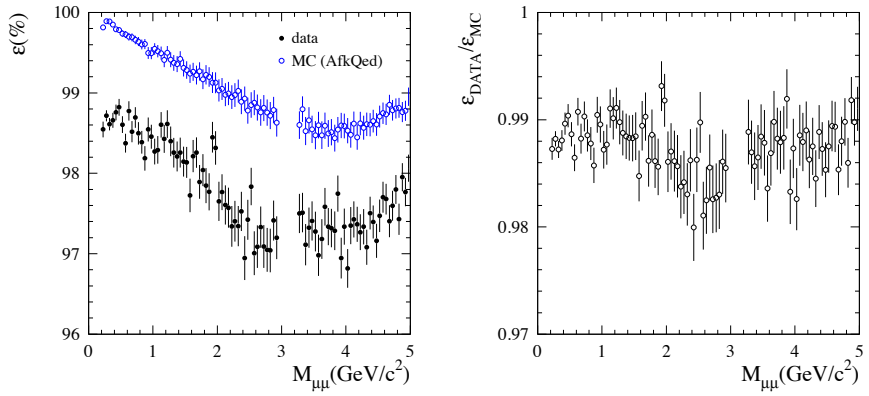

Figure 7.23: The χ^2 efficiency (left) for data (after background subtraction), MC (AfkQed), and the ratio of data to MC (right), as a function of $m_{\mu\mu}$.

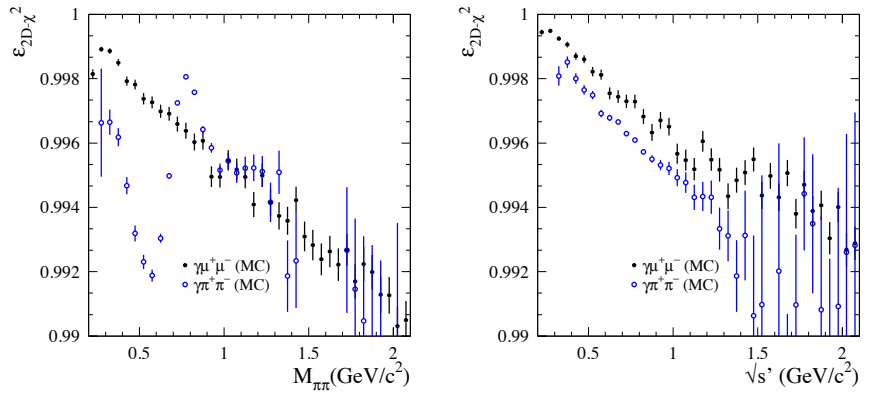

Figure 7.24: Left: the χ^2-cut efficiency in simulation for $\mu\mu\gamma(\gamma)$ (black) and $\pi\pi\gamma(\gamma)$ (blue) events plotted as a function of $m_{\pi\pi}$ (or $m_{\mu\mu}$ for muons). Right: the same as a function of $\sqrt{s'} = m_{\pi\pi(\gamma_{FSR})}$.

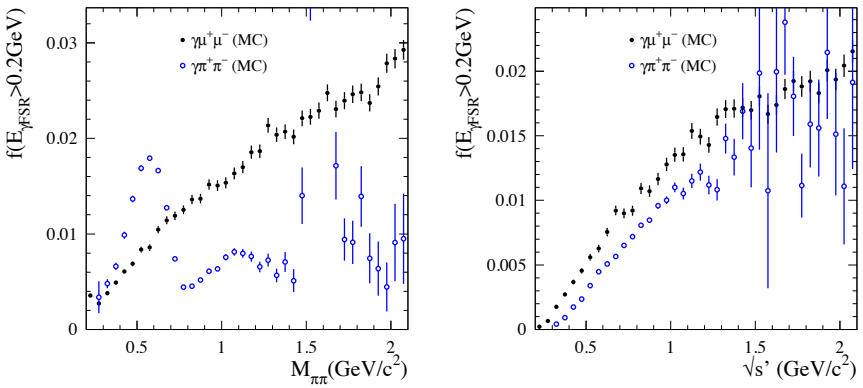

Figure 7.25: Left: the fraction of additional-FSR events with $E_{\gamma\ FSR} > 0.2$ GeV in simulation for $\mu\mu\gamma(\gamma)$ (black) and $\pi\pi\gamma(\gamma)$ (blue) events plotted as a function of $m_{\pi\pi}$ (or $m_{\mu\mu}$ for muons). Right: the same as a function of $\sqrt{s'} = m_{\pi\pi(\gamma_{FSR})}$.

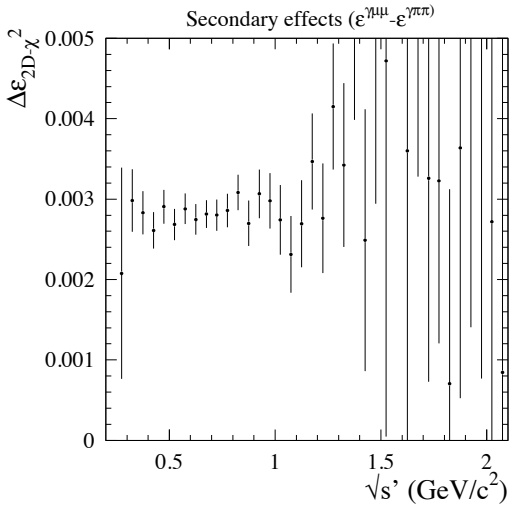

Figure 7.26: The effect of secondary interactions on the χ^2-cut efficiency, estimated from $\mu\mu\gamma(\gamma)$ and $\pi\pi\gamma(\gamma)$ simulation using Eq. (7.4), as function of $\sqrt{s'} = m_{\pi\pi(\gamma_{FSR})}$.

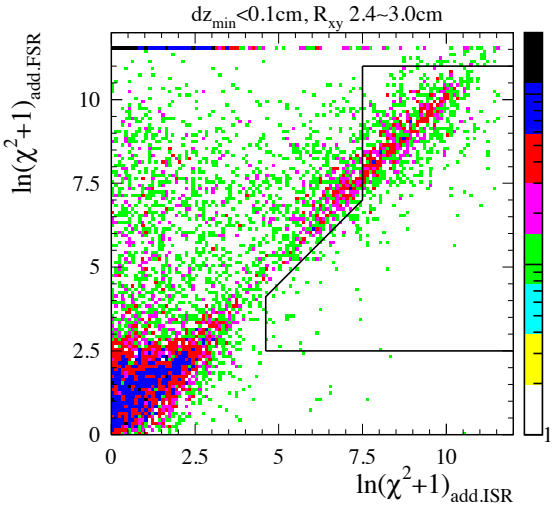

Figure 7.27: 2D-χ^2 distribution of events with a secondary vertex at a radius near the beam pipe, $2.4 < R_{xy} < 3.0$ cm, in simulation.

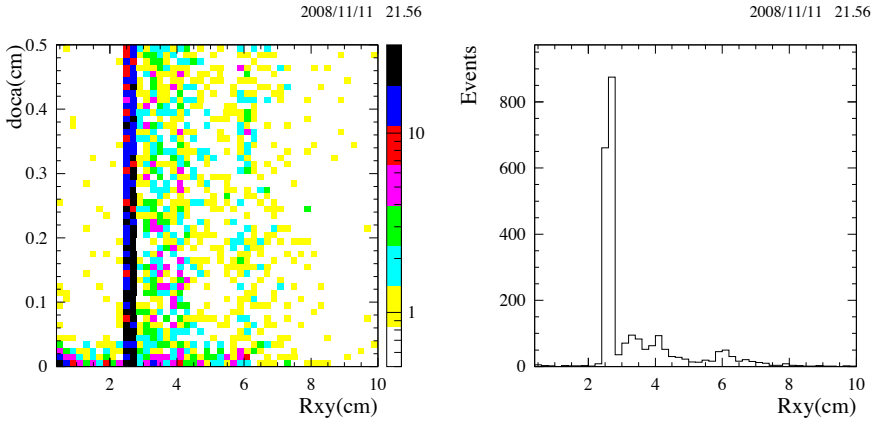

Figure 7.28: Left: the transverse distance of closest approach to the interaction point $doca_{xy}$ vs. the transverse radius R_{xy} of the secondary vertex. There is a clear interaction signal at the beam pipe and in the first part of the SVT. Right: the R_{xy} distribution for $doca_{xy} > 0.05$ cm provides the shape for the interaction events. Both from simulation.

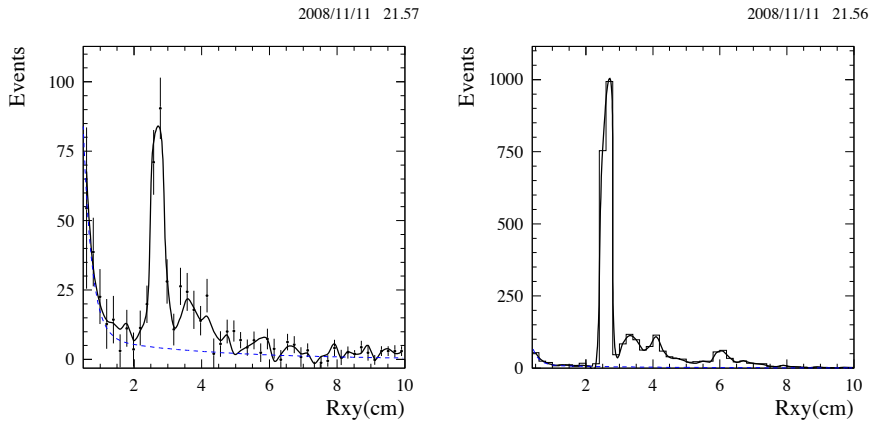

Figure 7.29: The fits of the R_{xy} distributions of the secondary vertex for data (left) and simulation (right). The dashed curve is the contribution from accidental vertices, fitted to the distributions.

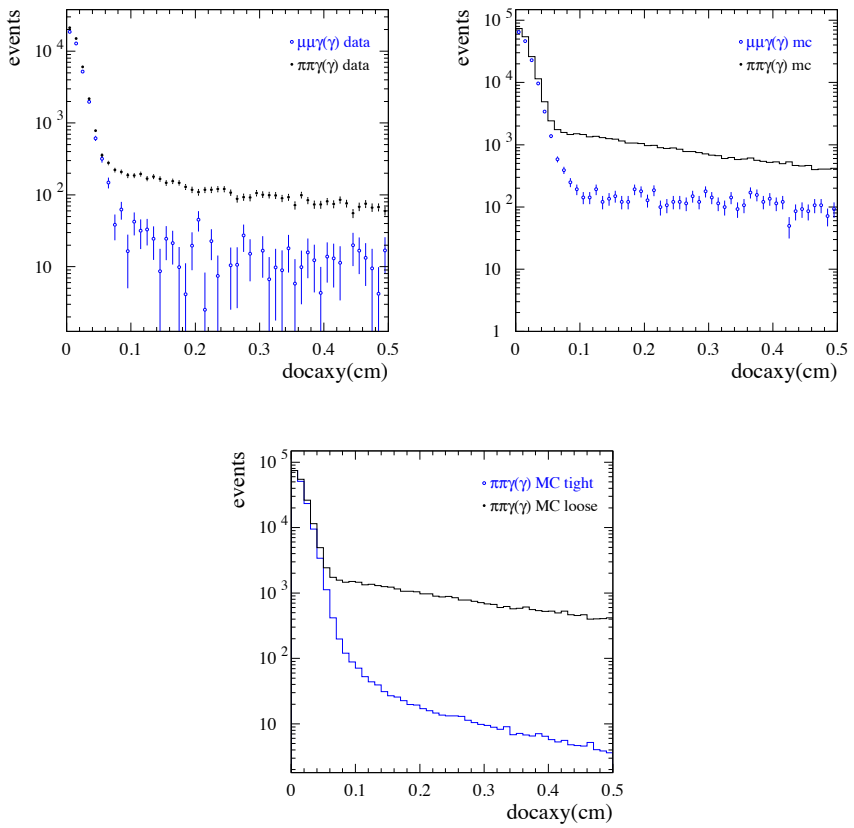

Figure 7.30: Top left: the distribution of the largest of the two transverse distances of closest approach to the interaction point $doca_{xy}^{max}$ for pions and muons in data, for the intermediate χ^2 region. Top right: the distribution of the largest of the two transverse distances of closest approach to the interaction point $doca_{xy}^{max}$ for pions and muons in simulation, for the intermediate χ^2 region. Bottom: the distribution of the largest of the two transverse distances of closest approach to the interaction point $doca_{xy}^{max}$ for pions in simulation, for the loose and tight χ^2 cuts.

Chapter 8

Event acceptance

8.1 Extra radiation in the MC generators

Acceptance is calculated using the AfkQed generator and the full simulation. The LO $\mu^+\mu^-\gamma$ or $\pi^+\pi^-\gamma$ process follows QED (if one forgets the pion form factor) and therefore we do not expect any problem there. The situation is different at the NLO level where approximations are made in AfkQed: additional ISR photons are generated with the structure function method in the collinear approximation and additional FSR photons by PHOTOS. And as already mentioned, $m_{x^+x^-\gamma_{ISR}(\gamma_{FSR})} > 8$ GeV ($x = \mu$ or π) is used at generation level which means that very hard additional ISR is suppressed in AfkQED but in practice it can happen in real data. The QED angular distribution for additional ISR, is sharply peaked along the beams, but with long tails. The angular distribution of hard additional ISR photons cannot be neglected as it produces a significant transverse momentum which affects the event acceptance. This can be studied with the Phokhara 4.0 (last version available for the muon channel) generator. The advantage of Phokhara is that it uses the almost-exact QED NLO calculation (without ISR-FSR interferences, which anyway vanishes for a charge-symmetric acceptance).

Phokhara can provide a MC sample with additional ISR following the QED angular distribution, which allows us to investigate the acceptance for collinear and non-collinear additional ISR events. The study [37] shows a significant decrease of the acceptance as a function of the polar angle of the additional hard (> 0.2 GeV) ISR photon. Therefore a correction must be applied to the acceptance computed with AfkQed.

Good evidence for a photon angular distribution is obtained from the discrepancy between the $\chi^2_{add.ISR}$ distributions in data and MC (Fig. 7.16), whereas

the corresponding distributions for $\chi^2_{add.FSR}$ are in good agreement (Fig. 7.18). A direct test of the adequacy of the angular distribution in Phokhara is made for additional photon angles in the EMC range using the 'FSR' fit, separating the true FSR contribution by a cut on $\theta_{\mu\gamma_2}$. The shapes of the distributions of the polar angle and the energy of the large-angle ISR photon in data and for Phokhara (generator level) are in good agreement.

However, contrary to AfkQed, Phokhara does not include the contribution from two FSR photons and NNLO ISR. The first case of two FSR photons for muons is suppressed by the smallness of both LO FSR, about 1% at 1GeV and 15% at 3 GeV, and NLO FSR, $<$ 1% at 1GeV and 2.7% at 3 GeV for photon energies above 200 MeV in the $\mu\mu\gamma_{NLO}$ CM. Even at 3 GeV the expected contribution of 4×10^{-3} will have a negligible effect on the acceptance for muons. The first effect for pions is even smaller, because there is almost no LO FSR for pion channel. In the second case of three ISR photons, the acceptance can be modified only if the third photon has a significant energy. From the acceptance change between Phokhara and AfkQed (we will see later), and the fraction of NLO ISR above photon energies of 1 GeV in the ee CM one can estimate a maximum acceptance bias of 2×10^{-3} at threshold and 10^{-3} at 1 GeV. Therefore, the first effect is negligible for both muons and pions, while the second is expected to be at a very small level, and contributing equally to pions and muons.

After all the studies, one can conclude that for the additional ISR events, Phokhara provides a much better description, on account of the photon angular distribution which is checked in data.

Because the approximations made in AfkQed are about additional ISR which should be common for $\mu\mu\gamma\gamma$ and $\pi\pi\gamma\gamma$ channels. As a consequence, when one takes the ratio of $\pi\pi$ and $\mu\mu$, the effects from the approximations in AfkQed are expected to be canceled.

8.2 Geometrical acceptance calculation using fast simulation

The main criteria affecting the geometrical acceptance are: both tracks (muon or pion) in the polar angle range $0.4 < \theta < 2.45$ (rad), with momenta larger than 1 GeV, the most energetic photon in the CM (ISR candidate) with $E^*_\gamma > 3$ GeV in the polar angle range $0.35 < \theta_\gamma < 2.4$ (rad).

Since we can compare Phokhara and AfkQed only at 4-vector level, we have tried to take into account the detector effects by performing a fast simulation of its performance. First, track and photon parameters are smeared using resolution functions obtained from data. Then models of the various efficiencies are constructed following our measurements: a function of $\Delta\phi$ (difference of ϕ angles of the 2 tracks) for the trigger and BGFilter efficiency [31], a 2-component model for the tracking using the overlap parametrization with $\Delta\phi$ and the isolated track efficiency, and simple parametrizations for μ-ID.

The geometric acceptance computed with the smeared 4-vectors in Phokhara on one hand and AfkQed with the $m_{\mu\mu\gamma} > 8$ GeV cut on the other hand is given in Fig. 8.1 as a function of $m_{\mu\mu}$. The fast drop from threshold to 0.5 GeV comes from the $p > 1$ GeV requirement on both muons. The ratio of the two acceptances (Phokhara/AfkQed) is also shown. The correction is $\sim 3.5\%$ at the $\mu\mu$ mass threshold, decreasing to $\sim 2.8\%$ at 1 GeV and consistent with zero above 3 GeV. The main effects are the $m_{\mu\mu\gamma} > 8$ GeV cut used at generation level in AfkQed, and the lack of an angular distribution for the additional ISR photon in AfkQed.

It is interesting to see how sensitive these results are to the quality of the fast simulation used. The effect of smearing generates a shift of 1.0×10^{-3} for the correction. We have left separate the corrections resulting from the modeled efficiencies to check the sensitivity of the result to their contribution. Changes up to a few 10^{-3}, essentially in the lower mass region are observed in Fig. 8.2. This indicates that the approximate nature of the fast simulation should not introduce a significant bias in the acceptance correction.

The ratio of the acceptances for $\pi\pi\gamma(\gamma)$ calculated with full Phokhara and AfkQed with the $m_{\pi\pi\gamma} > 8$ GeV cut, is shown in Fig 8.3. The correction is

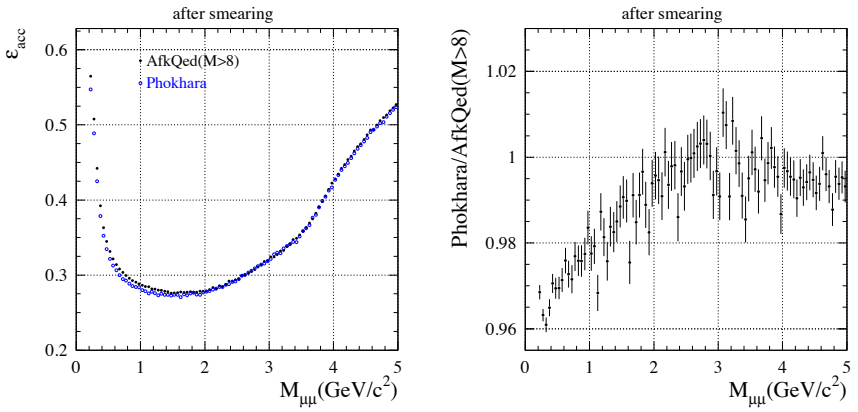

Figure 8.1: The geometric acceptance (angles and momenta cuts) computed with Phokhara and AfkQed at 4-vector level with smearing of tracks and photon (left) and the ratio Phokhara/AfkQed (right).

$\sim 4\%$ at the $\pi\pi$ mass threshold, decreasing to $\sim 2.5\%$ at 0.75 GeV. As in the muon case, the effects of resolutions and efficiencies are at the 10^{-3} level and fast simulation should capture most of the detector effects.

It should noted that the acceptance corrections between AfkQed and Phokhara for the muon and the pion are almost identical. A fit of the ratio of the two corrections yields a value consistent with one within one per mil. This is understandable because the effects which are corrected are the same in both cases, since they involve additional ISR which factorizes. This is also the case for the effects of the pre-selection cut on the angle between the ISR photon and the missing momenta (see the next Section). One could expect very small differences coming from different trigger, tracking and PID efficiencies. But since we have seen that these effects only contribute at the per mil level, it is clear that no significant difference is expected. A systematic error of 1.0×10^{-3} is assigned.

8.3 Efficiency of the ISR pre-selection cut

All the selected data in this analysis have passed the pre-selection conditions discussed in Section 3.2. The only practically relevant one here is the requirement that the missing momentum vector (including in the final state the charged

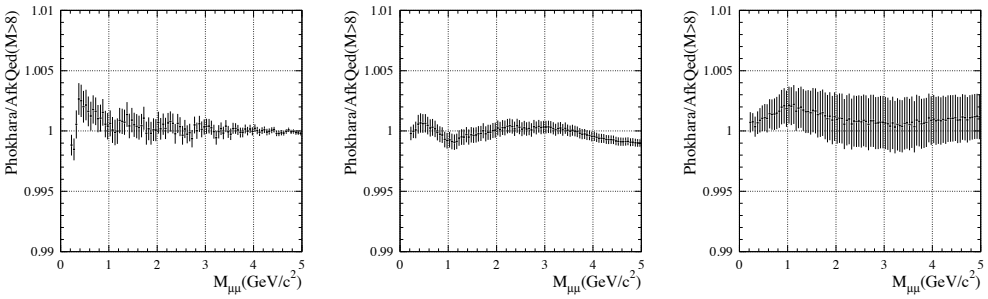

Figure 8.2: The effect of the efficiencies for trigger (left), tracking (middle), and μ-ID (right) on the acceptance ratio for Phokhara and AfkQed, the latter with $m_{\mu\mu\gamma} > 8$ GeV cut, using a fast simulation.

tracks and all photons excluding the ISR candidate) points within 0.3 rad of the ISR photon. Since this cut is of a kinematic nature, the events with hard additional initial-state radiation at small polar angle are expected to have lower efficiency than non-radiating events. The simulated sample using AfkQed with the $m_{\mu\mu\gamma(\gamma_{FSR})} > 8$ GeV cut is not adequate to estimate this efficiency, which has to be studied again with Phokhara using fast simulation. It is to be noted that the rejected events would have been found in the good $\chi^2_{add.ISR}$ region (tight χ^2 condition). Some loss could also be expected at large 2D-χ^2 because of multiple radiation, but this contribution turned out to be really negligible in AfkQed.

The photon/missing-momentum cut efficiencies in AfkQed and Phokhara are given in Fig. 8.4, together with their ratio. The Phokhara efficiency is 2% lower up to 3 GeV, due to the harder additional ISR energy spectrum and the extended angular distribution. Above 3 GeV the difference goes rapidly to zero because of reduced phase-space for extra radiation. The correction is needed for the determination of the absolute $\mu\mu$ cross section.

Since the correction for the Phokhara/AkfQed originates from additional ISR, in principle it cancels in the $\pi\pi/\mu\mu$ ratio. The pre-selection cut on the angle between the ISR photon and the missing momenta could produce very small differences coming from different trigger, tracking and PID efficiencies for pions and muons. But from the overall agreement of the Phokhara/AfkQed MC corrections for $\mu\mu$ and $\pi\pi$ at the per mil level, it is clear that no significant

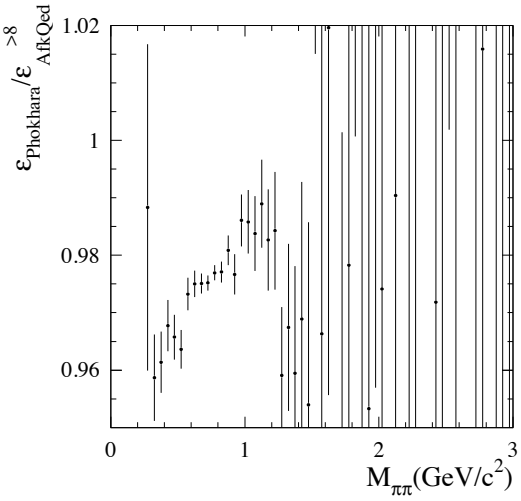

Figure 8.3: The ratio of the acceptances at 4-vector level for Phokhara and AfkQed, the latter with $m_{\pi\pi\gamma} > 8$ GeV cut.

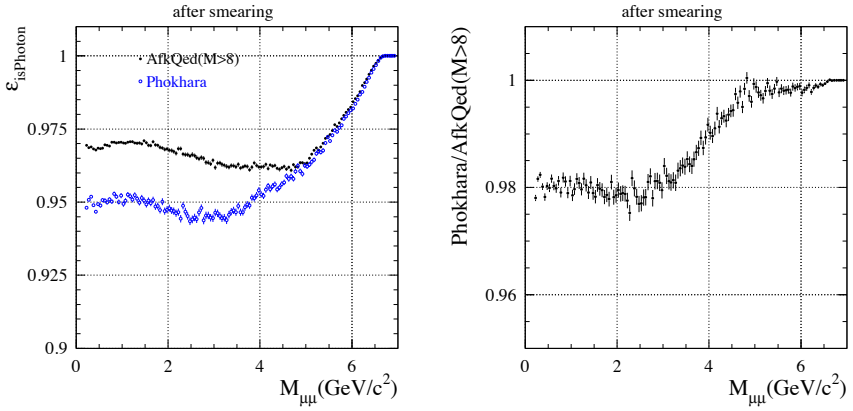

Figure 8.4: Pre-selection photon/missing-momentum cut efficiencies using AfkQed (with $m_{\mu\mu\gamma(\gamma_{FSR})} > 8$ GeV) and Phokhara at 4-vector level within acceptance with a fast simulation, as a function of $m_{\mu\mu}$ (left). Ratio Phokhara/AfkQed (right).

difference is expected.

However, two effects could occur that would break the cancellation for the $\pi\pi/\mu\mu$ ratio. The first one arises from the fact that at lowest-order both QED FSR and ISR amplitudes contribute to $\mu\mu\gamma$ whereas only ISR matters in practice for the $\pi\pi\gamma$ cross section. This effect should be small in the ρ region because the $|FSR|^2$ contribution is less than 1% for muons. It could not be the case at larger masses, but, as Fig. 8.5 (left) demonstrates, no significant deviation within 1-2 10^{-3} occurs up to 1.5 GeV, above which the MC $\pi\pi$ statistics does not permit a test at better than 1-2% level, well sufficient compared to the data statistical error in this region.

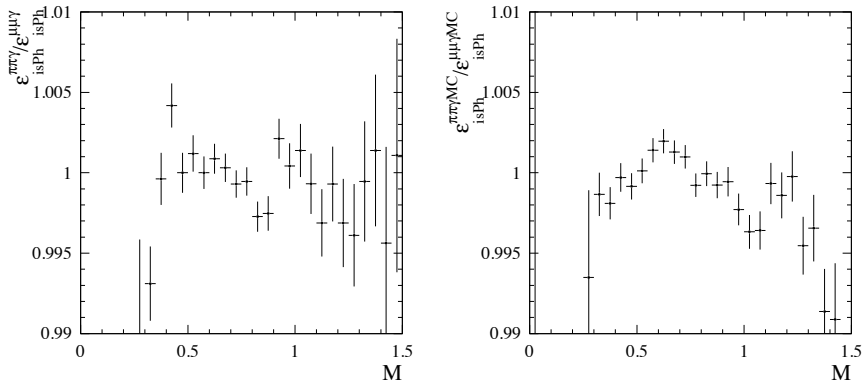

Figure 8.5: The ratio of the preselection cut efficiencies for pions and muons at generator level with fast simulation (Phokhara, left) and with full simulation (AfkQed, right).

A second effect of the pre-selection cut could arise from pion secondary interactions because of their different rate in data and simulation. This can only be studied with MC, not imposing the pre-selection cut. The overall effect of the full simulation is shown in Fig. 8.5 (right). Some pattern of deviation is observed at masses above 0.9 GeV, but the ratio is consistent with 1 within 1.5×10^{-3} below.

The effect of pion interactions can be studied more specifically. A pure sample of interacting events is obtained in the 0.5-1.0 GeV mass range requiring (*c.f.* Section 7.5.4) $doca_{xy}^{max} > 0.1$ cm and $\ln(\chi^2_{add.ISR} + 1) > 3$.. The distribution of

the γ_{ISR}, p_{miss} angle of this sample is given in Fig. 8.6: 12.5% of the events are beyond the pre-selection cut of 0.3 rad. Considering that 1.1% of the events in the intermediate χ^2 region (between 'loose' and 'tight' regions) originate from secondary interactions in the simulation and that the measured ratio of interactions between data and MC is 1.52 ± 0.03, one can estimate the excess loss from the pre-selection in data compared to MC to be $0.52 \times 0.125 \times 0.011 \ = \ 7 \times 10^{-4}$.

Taking as systematic uncertainty 100% of the effect observed in the simulation an error of $1.5\ 10^{-3}$ is assigned to the $\pi\pi\gamma$ cross section below 0.9 GeV in order to account for these non-cancelling effects. The error is increased to $3\ 10^{-3}$ between 0.9 and 1.4 GeV, and 1% above.

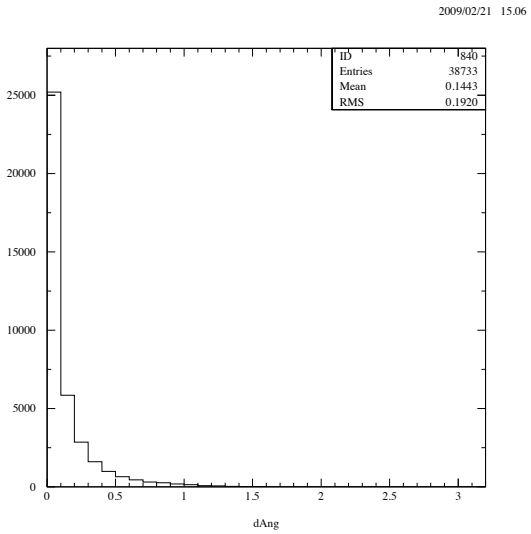

Figure 8.6: The angle between the ISR photon and the missing momentum from the $\pi^+\pi^-(\gamma_{FSR})$ system for a sample of interacting events in the simulation satisfying the acceptance criteria, but not imposing the ISR preselection cuts.

Chapter 9

Checking kinematic distributions

9.1 Comparison of data and MC distributions for $\mu\mu\gamma(\gamma)$

The comparison of distributions of relevant kinematic variables (polar angles of the ISR photon and of the muons, momentum of the muons) for data and simulation is an important cross check of the analysis of $\mu\mu\gamma(\gamma)$. However, all the detailed corrections which have been applied to the simulation as a function of the $\mu\mu$ mass are not available for these variables. We expect that the trigger and tracking corrections do not introduce large effects, as they are mostly controlled by the $\Delta\phi$ angle between the two muons. It is different for μ-ID corrections which certainly depend on the track parameters of the muons. So we have only considered corrections from PID for this test. Thus other effects remain uncorrected, such as for instance data/MC differences in photon efficiency. Since full simulation is needed and knowing some deficiencies of AfkQed for additional radiation, the comparison is made for events without excessive extra radiation, requiring the 1C-fit χ^2 to be less than 15.

The angular distribution (θ^*) of the muons in the $\mu\mu$ center-of-mass with respect to the ISR photon direction in this frame is of particular interest since it is predicted by QED (up to very small deviations due to the high virtuality of the incoming electron/positron which radiated the ISR photon) to behave as

$$\frac{dN}{d\cos\theta^*} \sim 1 + \cos^2\theta^* + (1-\beta^2)\sin^2\theta^* \tag{9.1}$$

for pure ISR production, with $\beta = \sqrt{1 - 4m_\mu^2/s'}$. So we expect the distribution to be flat at threshold and $1 + \cos^2\theta^*$ at intermediate mass. At large masses a larger fraction of the 'ISR'-selected photon comes in fact from FSR, increasingly modifying the $\cos\theta^*$ distribution.

Figs. 9.1-9.6, show the distributions in different mass intervals. In each case the data and MC have been normalized to each other as we are interested in testing the shapes. The agreement with the simulation is good, except for the ISR photon distribution at small angles where the data lies below the simulation. We return on this point below.

The distributions of $|\cos\theta^*|$ for different mass intervals agree well with expectation as seen in Fig. 9.7. Although they are strongly biased by the $p < 1$ GeV requirement which cuts out the region near one, distributions in the threshold region indeed show the expected behaviour from Eq. (9.1).

9.2 Angular distribution in the $\pi\pi$ center-of-mass

The distributions of kinematic variables such as the ISR photon polar angle, the pion momenta and angles, depend on the hadronic structure we seek to measure. So comparisons between data and MC distributions are not meaningful. However, one distribution, namely the pion angular distribution in the $\pi\pi$ center-of-mass with respect to the ISR photon direction in that frame, is model-independent. The $\cos\theta^*_\pi$ distribution behaves as $\sin^2\theta^*_\pi$ as a consequence of the P-wave between the 2 pions, but it is strongly distorted at $|\cos\theta^*_\pi|$ values near one by the $p > 1$ GeV cut on the tracks.

The $|\cos\theta^*_\pi|$ distributions for background-subtracted data and MC are compared in Fig. 9.8 for the 0.5-1 GeV mass range: they agree with each other within the statistical errors, as expected for a pure pion sample.

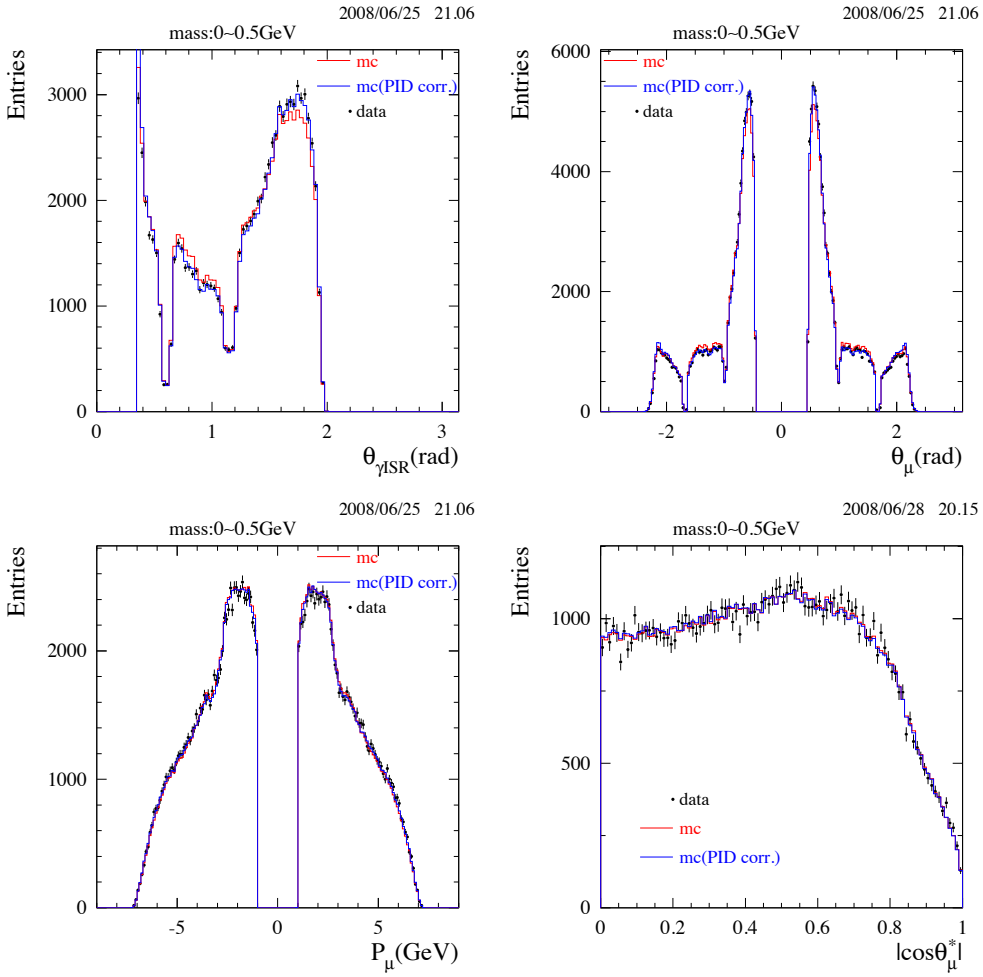

Figure 9.1: The comparison between the distributions of data (points with errors) and simulation uncorrected for data/MC differences (black histogram), corrected for PID (blue histogram), for θ_γ in radians (top left), $\theta_{\mu^\pm}$ in radians (top right), $p_{\mu^\pm}$ in GeV (bottom left), and $|\cos\theta^*|$ (bottom right): $m_{\mu\mu} < 0.5$ GeV, runs 1-4.

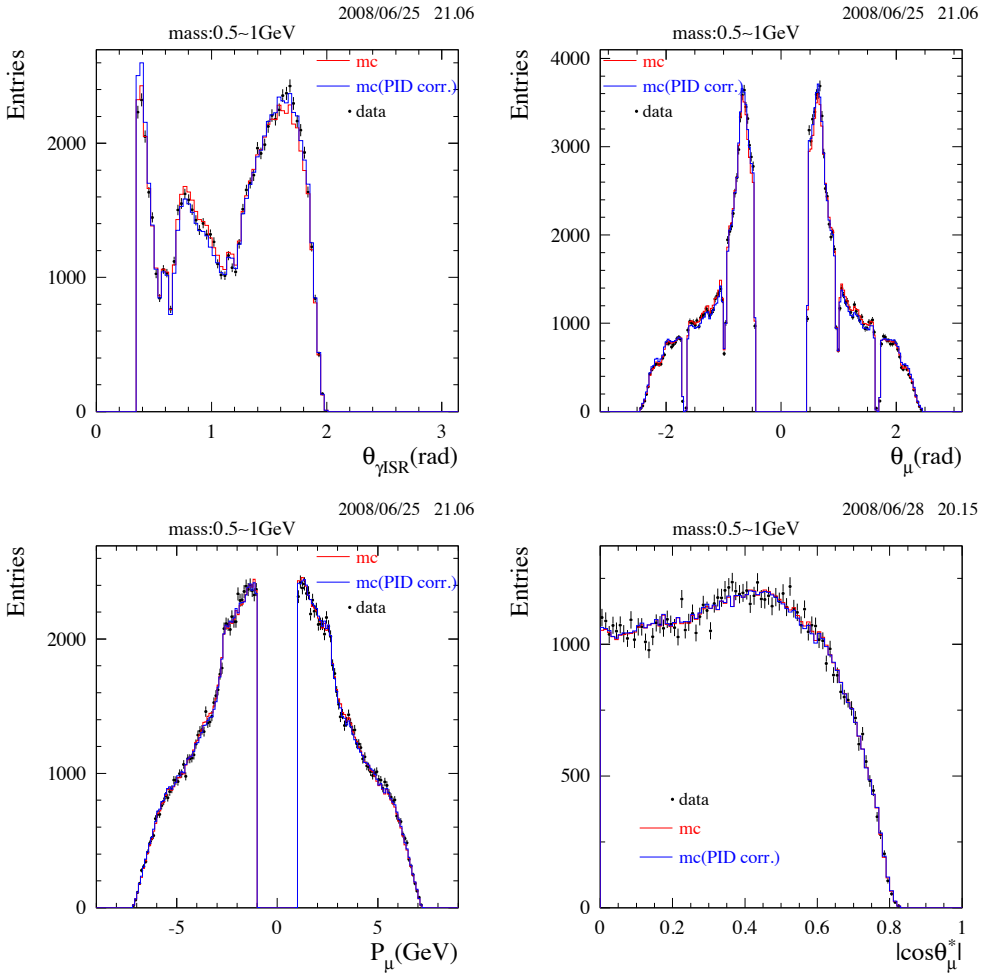

Figure 9.2: The comparison between the distributions of data (points with errors) and simulation uncorrected for data/MC differences (black histogram), corrected for PID (blue histogram), for θ_γ in radians (top left), $\theta_{\mu^\pm}$ in radians (top right), $p_{\mu^\pm}$ in GeV (bottom left), and $|\cos\theta^*|$ (bottom right): $0.5 < m_{\mu\mu} < 1$ GeV, runs 1-4.

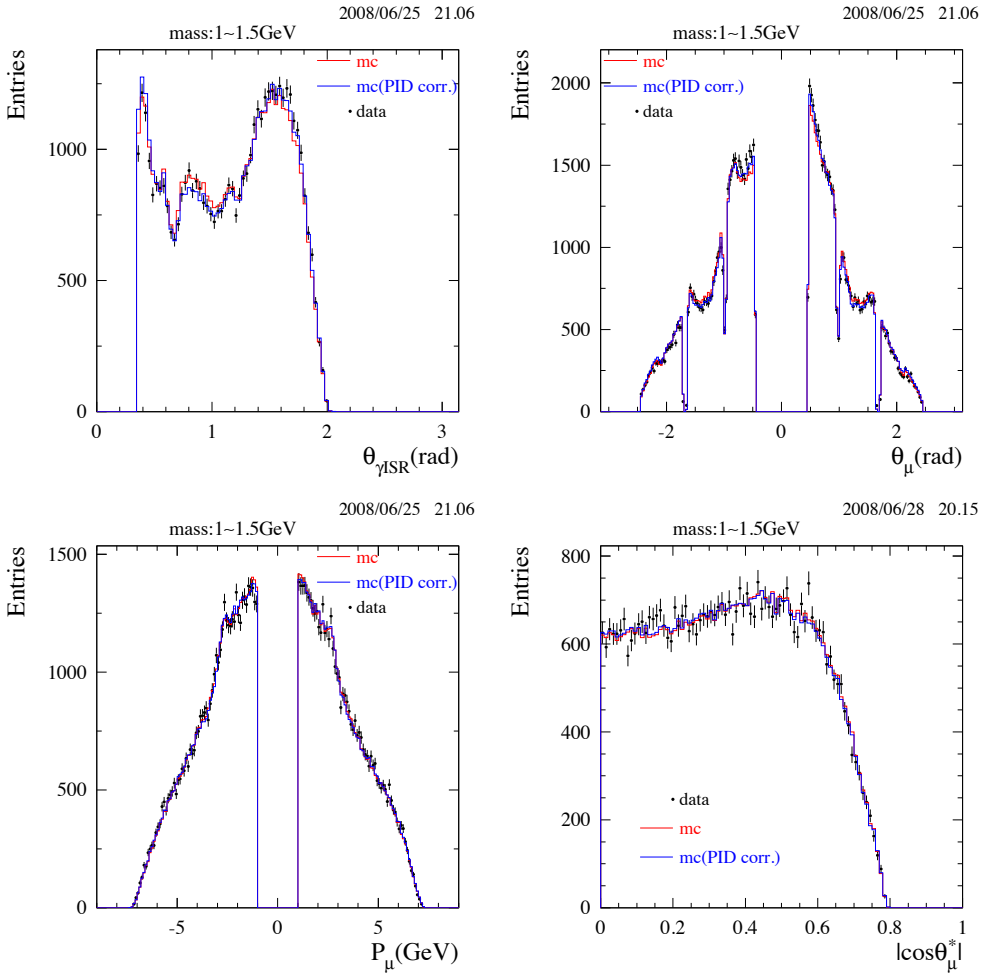

Figure 9.3: The comparison between the distributions of data (points with errors) and simulation uncorrected for data/MC differences (black histogram), corrected for PID (blue histogram), for θ_γ in radians (top left), $\theta_{\mu^\pm}$ in radians (top right), $p_{\mu^\pm}$ in GeV (bottom left), and $|\cos\theta^*|$ (bottom right): $1 < m_{\mu\mu} < 1.5$ GeV, runs 1-4.

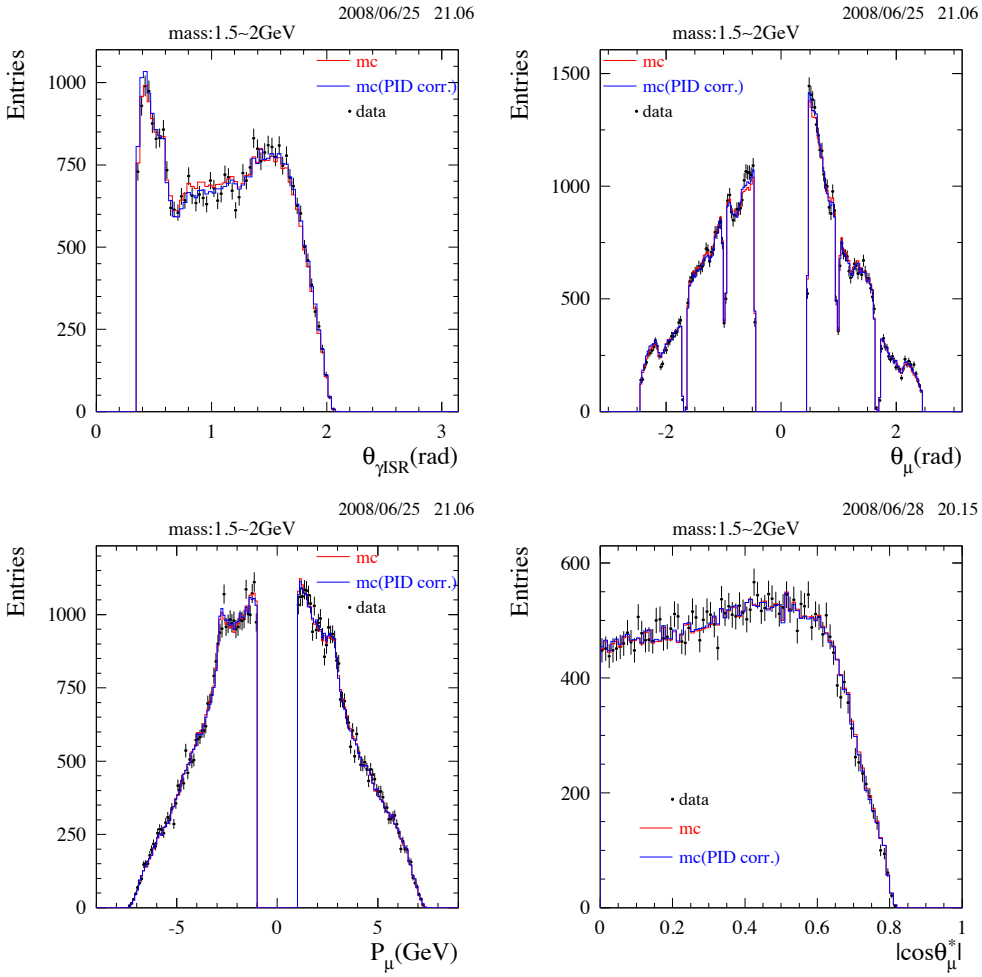

Figure 9.4: The comparison between the distributions of data (points with errors) and simulation uncorrected for data/MC differences (black histogram), corrected for PID (blue histogram), for θ_γ in radians (top left), $\theta_{\mu^\pm}$ in radians (top right), $p_{\mu^\pm}$ in GeV (bottom left), and $|\cos\theta^*|$ (bottom right): $1.5 < m_{\mu\mu} < 2$ GeV, runs 1-4.

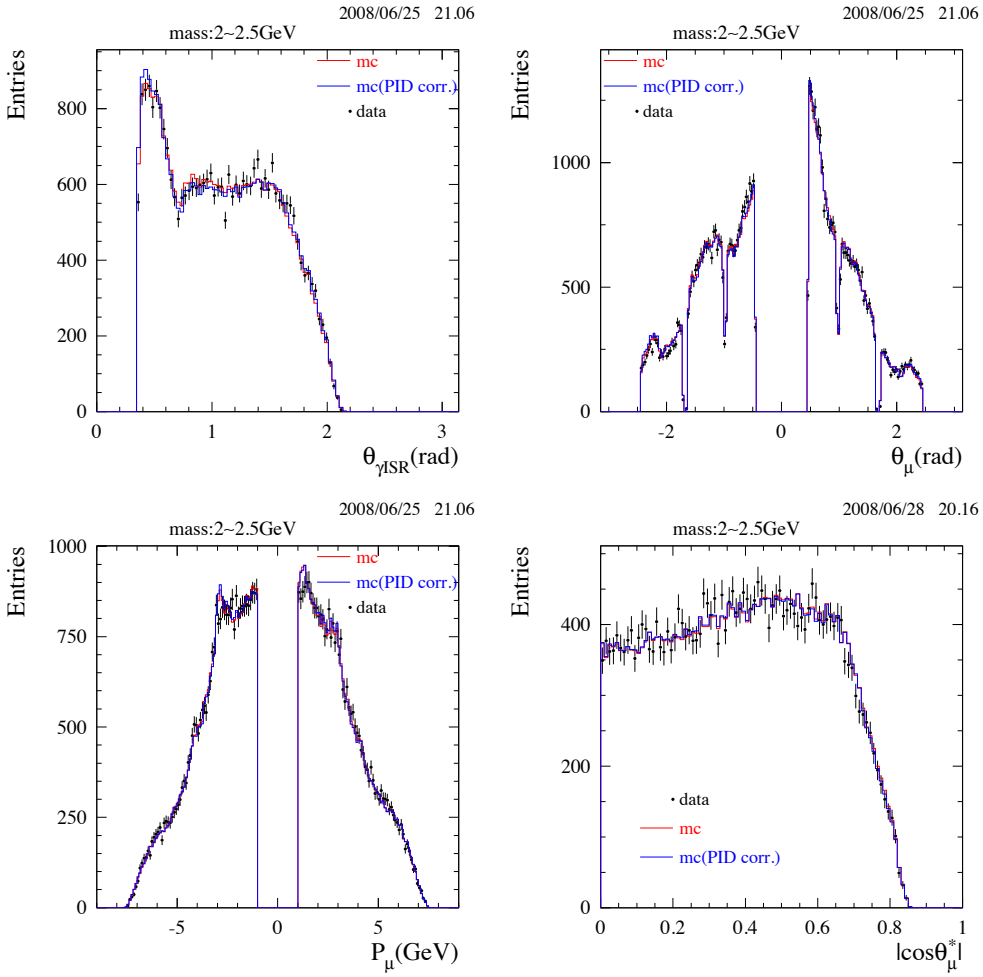

Figure 9.5: The comparison between the distributions of data (points with errors) and simulation uncorrected for data/MC differences (black histogram), corrected for PID (blue histogram), for θ_γ in radians (top left), $\theta_{\mu^\pm}$ in radians (top right), $p_{\mu^\pm}$ in GeV (bottom left), and $|\cos\theta^*|$ (bottom right): $2 < m_{\mu\mu} < 2.5$ GeV, runs 1-4.

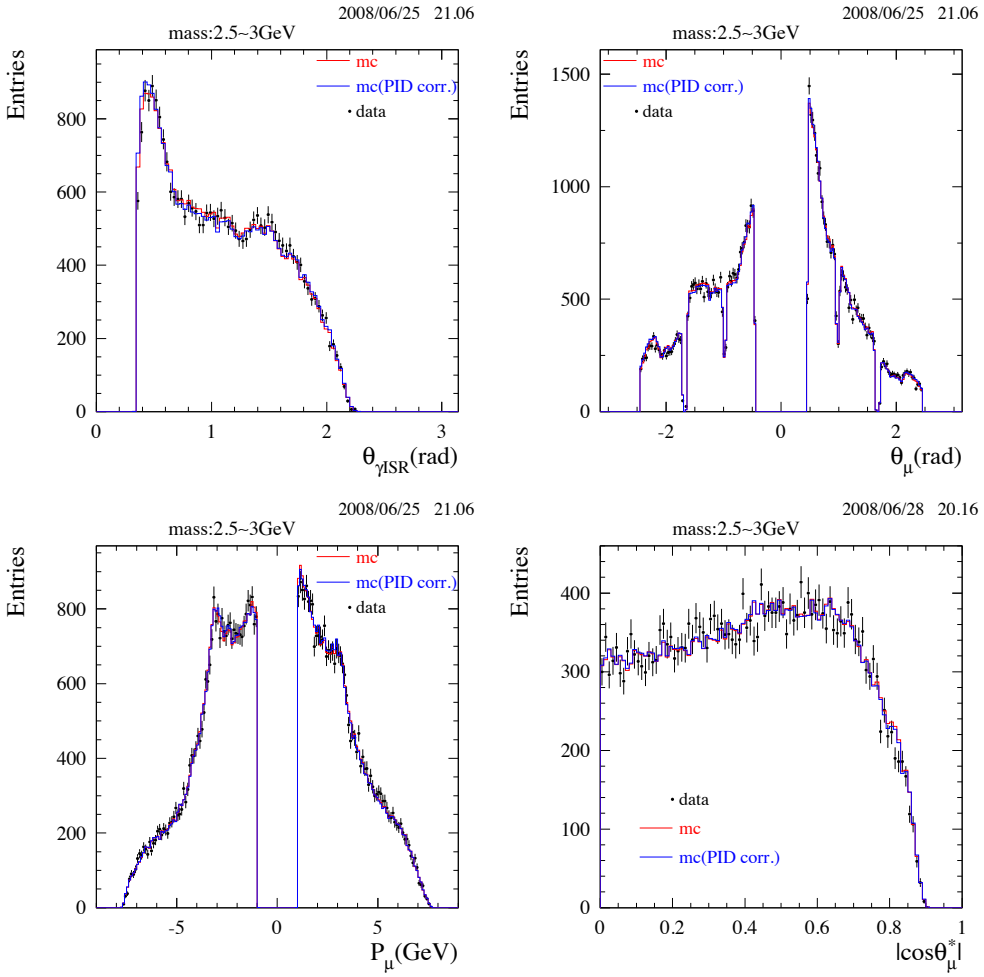

Figure 9.6: The comparison between the distributions of data (points with errors) and simulation uncorrected for data/MC differences (black histogram), corrected for PID (blue histogram), for θ_γ in radians (top left), $\theta_{\mu^\pm}$ in radians (top right), $p_{\mu^\pm}$ in GeV (bottom left), and $|\cos\theta^*|$ (bottom right): $2.5 < m_{\mu\mu} < 3$ GeV, runs 1-4.

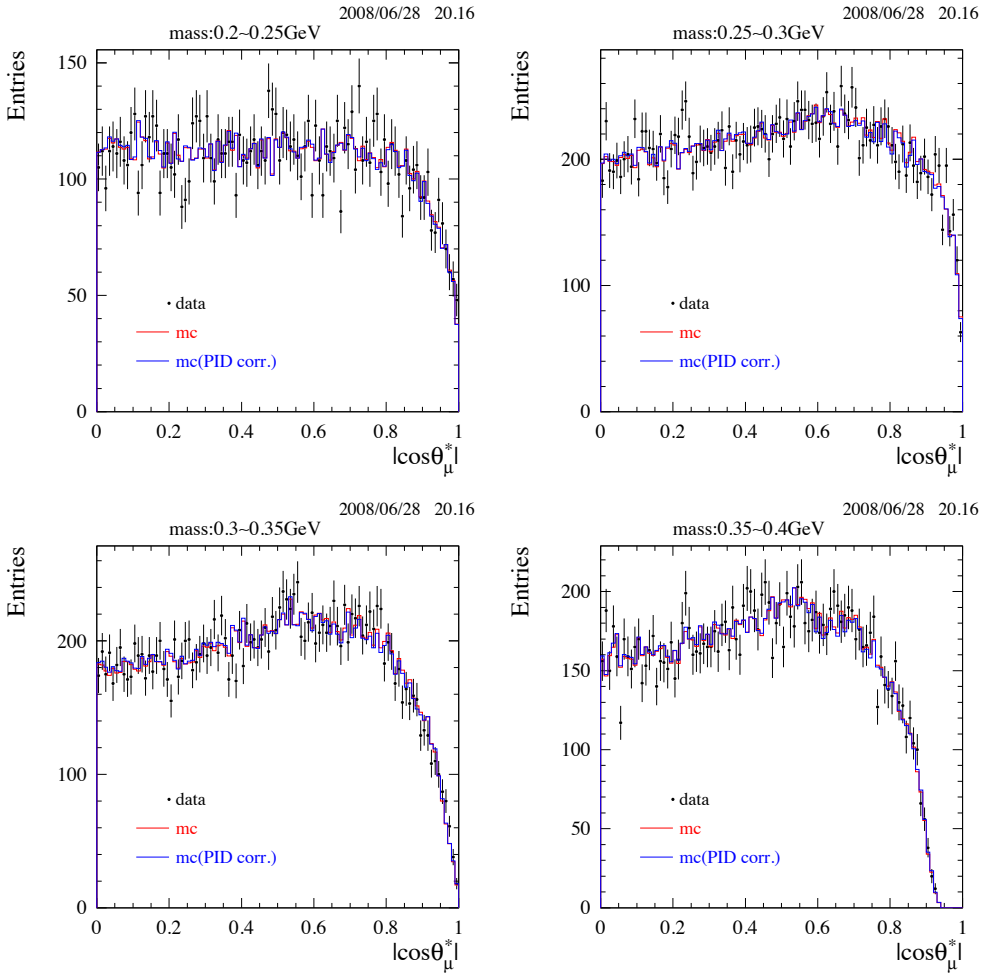

Figure 9.7: The comparison between the distributions of data (points with errors) and simulation uncorrected for data/MC differences (black histogram), corrected for PID (blue histogram) for $|\cos\theta^*|$: $0.20 < m_{\mu\mu} < 0.25$ GeV (top left), $0.25 < m_{\mu\mu} < 0.30$ GeV (top right), $0.30 < m_{\mu\mu} < 0.35$ GeV (bottom left), $0.35 < m_{\mu\mu} < 0.40$ GeV (bottom right), runs 1-4.

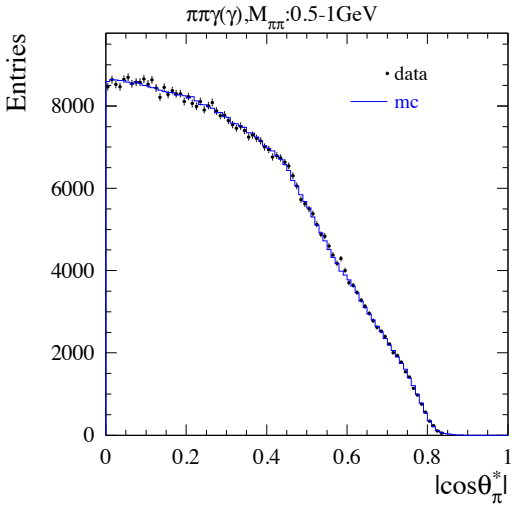

Figure 9.8: The angular pion distribution in the $\pi\pi$ system with respect to the ISR photon direction as function of $|\cos\theta^*_\pi|$ for background-subtracted $\pi\pi\gamma(\gamma)$ data (points) in the ρ central region ($0.5 < m_{\pi\pi} < 1$ GeV) for runs 1-4. The blue histogram is the shape obtained in the simulation, normalized to data.

Chapter 10

Measurement of $\sigma(e^+e^- \to \mu^+\mu^-(\gamma))$ and comparison with QED

10.1 Principle

An important crosscheck of our $\mu\mu\gamma(\gamma)$ analysis is the *absolute* comparison of the observed mass spectrum, corrected for efficiencies and acceptance, with the expectation of NLO QED. We emphasize that this procedure is to be understood as a consistency check, as our physics goal is a measurement of R, which is based on a relative measurement of hadrons vs. muons.

Let us summarize all the needed ingredients and corrections for this test, the details of which were discussed in the previous section:

- the $\mu\mu$ mass spectrum of data is corrected for remaining background from the 2-body ISR $\pi\pi$, KK, and $p\bar{p}$ processes, and multi-hadronic processes of both ISR and annihilation origin.
- AfkQed is used for produce large samples of simulated data. The simulation is corrected by relative measurements performed on data and MC of the efficiencies: trigger, background filter, tracking, PID, kinematic fitting.
- the event geometric acceptance obtained from the simulation is corrected using Phokhara to take into account some deficiencies of AfkQed at NLO.

10.2 ISR photon efficiency

We emphasize that this correction is not needed for the measurement of the ratio of ISR hadronic to ISR $\mu\mu$ production, as photon efficiency cancels in the ratio. However it is required for the absolute measurement of the $\mu\mu\gamma$ process as presented in this chapter.

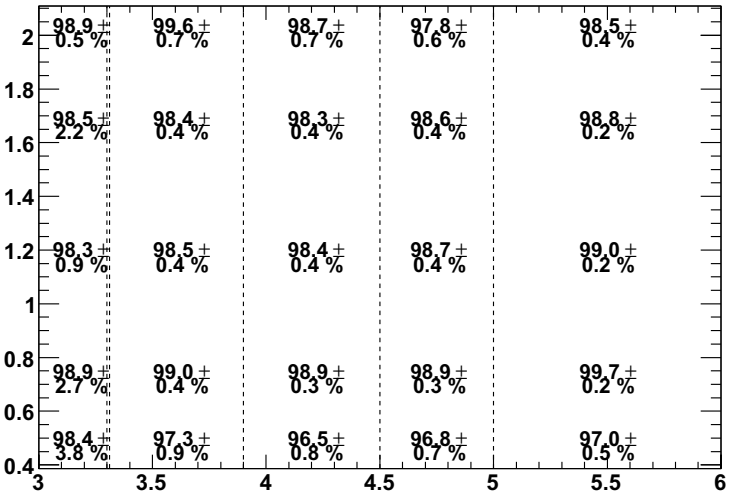

Figure 10.1: The correction as a function of $(E^*_\gamma, \theta_\gamma)$ for the photon efficiency of MC, x-axis stands for E^*_γ the photon center-of-mass energy in GeV and y-axis stands for θ_γ polar angle in lab frame in rad [38].

The photon efficiency has been measured independently in an analysis of R using an inclusive method in Ref. [38]. The procedure is based on $\mu\mu\gamma$ events triggered and selected only from the muon tracks. The efficiency is obtained in $(E^*_\gamma, \theta_\gamma)$ cells where E^*_γ and θ_γ are the photon center-of-mass energy and lab angle, respectively. Both data and MC are treated in the same way. The measurements include the photon loss from both reconstruction efficiency in the EMC and conversions in the detector material before the DCH. The correction as a function of $(E^*_\gamma, \theta_\gamma)$ for the photon efficiency of MC is shown in Fig 10.1. Unfortunately the bins in θ_γ are rather wide.

Since the data/MC discrepancy in the θ_γ distribution in the forward region (essentially in the endcap EMC) is seen in all mass intervals at the same level we can average all masses up to 7 GeV and compare it to the efficiency measurement, also averaging all E^*_γ above the cut value of 3.3 GeV in Ref. [38]. The comparison is shown in Fig. 10.2: indeed the trend exhibited by the data/MC comparison is in fair agreement with the efficiency determination, although the wide bins used prevent a detailed test to be performed.

To avoid most of this problem the angular range for the ISR photon for the determination of the absolute $\mu\mu$ cross section is restricted to the region effectively covered in the efficiency measurement, *i.e.* $\theta_\gamma > 0.386$ rad.

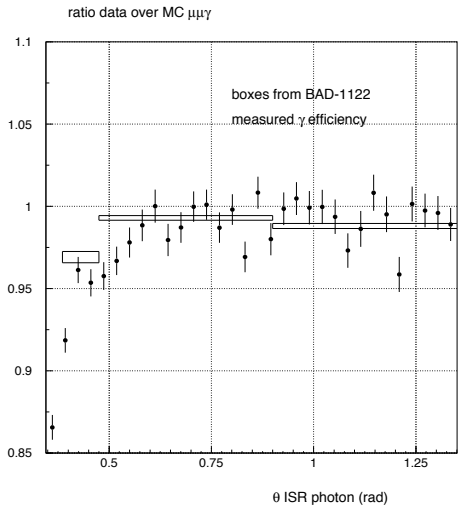

Figure 10.2: The ratio data over MC corrected for μ-ID data/MC differences only as a function of the ISR photon angle θ_γ in radians for 1C-fit $\chi^2 < 15$ and $m_{\mu\mu} < 7$ GeV (data points, runs 1-4), compared to the independent determination of the data/MC correction for ISR photon efficiency (boxes, taken from Ref. [38]).

The correction data/MC for the ISR photon efficiency is obtained as a function of $m_{\mu\mu}$ by sampling the efficiency maps using the simulated sample. The result for the ratio is shown in Fig. 10.3: the efficiency is smaller in data by $(1.5 \pm 0.1)\%$ below 2 GeV, slightly decreasing above. In fact the analysis in Ref. [38] was performed only on runs 2-4. We apply their results to run 1 as well adding a systematic uncertainty of 1% for the ratio in this part, thus introducing a 2.5×10^{-3} systematic error for runs 1-2 and 1×10^{-3} for runs1-4.

An additional systematic uncertainty of 3×10^{-3} is assigned to cover the poorer knowledge of the correction at small angles. This value is obtained by taking the discrepancy between the data/MC comparison and the applied correction from Ref. [38] as systematic uncertainty.

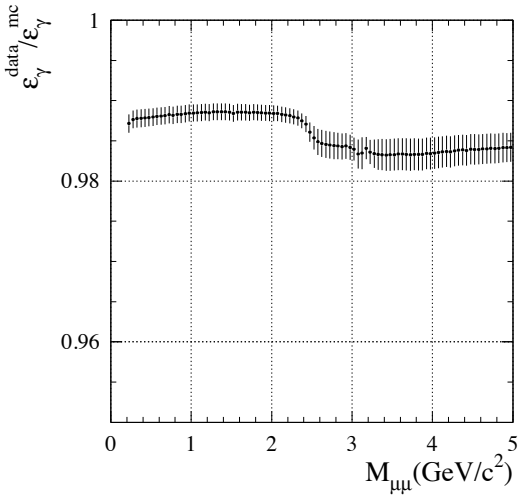

Figure 10.3: The ratio of the ISR photon efficiencies in data over MC vs. $m_{\mu\mu}$, obtained from the dedicated analysis in Ref. [38].

10.3 Effect of muon-photon overlap

For large $\mu\mu$ masses the angle between one of the muons and the ISR photon can be small and the possibility of an overlap in the EMC occurs. This problem was studied for μ-ID [33] and these overlap events were removed in the efficiency determination, since efficiencies are mostly needed at lower masses where this effect does not occur. It was found that simulation badly underestimates the corresponding loss of muon identification. However the μ-ID loss is not the only consequence of the overlap, as the measured photon energy may also fail the $E^*_\gamma > 3$ GeV cut applied in the event selection. The overlapping event can even be rejected at the trigger/BGFilter level or in the ISR selector. In the latter case a looser cut ($E^*_\gamma > 0.5$ GeV) is used if one muon is identified (in that case the isolated muon, opposite to the ISR photon). A final effect is the loss of the track as standard ISR tracks are defined with an electron veto (see Section 3.2), which can be satisfied if the track is linked to enough energy deposit from the ISR photon.

So the loss of overlapping events is not included in the μ-ID efficiency. It is not taken into account either in the measurement of the ISR photon efficiency,

since 2 identified muons were used in this study. An additional data/MC correction would be needed to account for deviations between data and simulation. Such a deviation was observed for the μ-ID part, probably because the transverse shower size and its fluctuations are not well simulated. Finally the track loss is not included either in the measured tracking efficiency, since for this study a kinematic fit with a tight χ^2 cut is needed and uses the measured ISR photon energy, much reduced for overlapping events.

Unfortunately it is not possible to determine the efficiency in data of the complete loss from the pre-selection as no selected sample allows one to reconstruct the different components: $E^*_\gamma < 0.5$ GeV (including the complete photon loss), track loss from electron veto, μ-ID. The full effect can only be determined in simulation, with the above-mentioned caveat. Figure 10.4 shows the efficiency of the $E^*_\gamma > 0.5$ GeV cut on the simulated events satisfying the angular acceptance cuts. One clearly see the onset of the overlap loss above 3.5 GeV. Below this value the inefficiency comes mainly from EMC cracks and conversions, both effects included in the measurement of the ISR photon efficiency. At 5 GeV the overlap efficiency loss is about 3%. With the large discrepancy with data observed for μ-ID it is clear that the simulation cannot be relied upon for this effect at the level of precision of 0.5% achieved in the $\mu\mu\gamma$ cross section. Since the main purpose of the analysis is the R measurement below 3 GeV, it is reasonable to perform the QED test in the region unaffected by the muon-photon overlap, conservatively set below 3.5 GeV.

10.4 Systematic errors

The statistical errors of the measured efficiencies are included with the main statistical uncertainty on the $\mu\mu$ mass spectrum. However, in some cases, remaining systematic uncertainties are attached to the efficiency measurement process. These estimated systematic uncertainties on the measured cross section are summarized in Table 10.1 for the mass range from threshold to 2 GeV. Above 2 GeV the uncertainties are smaller, essentially because of the more straightforward determination of the muon-ID efficiencies. In some cases no systematic error is

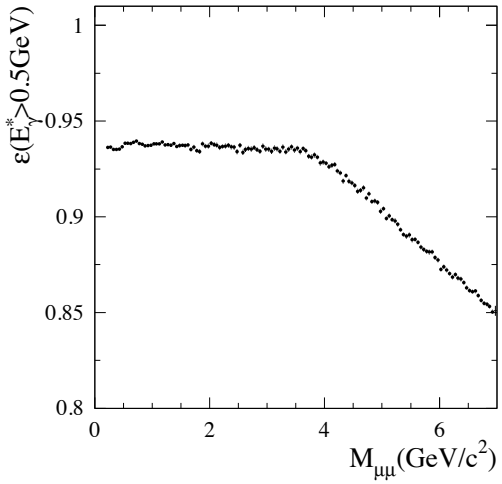

Figure 10.4: The efficiency of the preselection cut $E^*_\gamma > 0.5$ GeV as a function of the $\mu\mu$ mass, obtained for simulated events satisfying the angular acceptance cuts. The loss of muon-photon overlapping events is rapidly increasing above 3.5 GeV.

quoted when all uncertainties proceed from measurements and are already included in the point-to-point statistical errors.

The overall systematic uncertainty on the absolute $\mu\mu(\gamma_{FSR})$ cross section is 1.1%, dominated by the *BABAR* luminosity error.

10.5 Comparison of the measured cross section for $e^+e^- \to \mu^+\mu^-(\gamma_{FSR})$ to QED

The comparison is made through the ratio as a function of $m_{\mu\mu}$ of the distributions of data, subtracted from background, and of the simulation based on AfkQed, corrected from all data/MC detector and reconstruction effects and from the NLO generator problems using the Phokhara/AfkQed comparison with fast simulation, and normalized to the data luminosity. Because of the latter adjustments, discussed in detail in Chapter 8, this ratio is equivalent to a direct comparison of data to QED.

The QED prediction for the $m = m_{\mu\mu}$ distribution is obtained in the follow-

Table 10.1: Systematic uncertainties (in 10^{-3}) on the absolute $\mu\mu(\gamma_{FSR})$ cross section from the determination of the various efficiencies in the $\mu\mu$ mass range up to 2 GeV. The statistical part of the efficiency measurements is included in the total statistical error in each mass bin. For those contributions marked '-' all the relevant uncertainties come from measurements and are already counted in the statistical errors.

sources	runs 1-2	runs 3-4	runs 1-4
triggers and background filter	-	-	-
tracking	1.3	1.3	1.3
muon ID	4.5	3.6	3.3
$\pi\pi$ and KK backgrounds	-	-	-
multihadronic background	-	-	-
χ^2 cut efficiency	-	-	-
angle and momentum acceptance	2.0	2.0	2.0
ISR photon efficiency	3.9	3.0	3.4
e^+e^- luminosity	9.4	9.4	9.4
NNLO corrections to σ_{QED}	2.0	2.0	2.0
sum	11.5	10.9	11.0

ing way:

$$\frac{dN_{QED}}{dm} = L_{ee}\,\sigma^{NLO}_{Phokhara}\,\left(\frac{1}{N_0}\frac{dN}{dm}\right)^{AfkQed,M>8}_{fullsim}\,\frac{\left(\frac{1}{N_0}\frac{dN}{dm}\right)^{Phokhara}_{fastsim}}{\left(\frac{1}{N_0}\frac{dN}{dm}\right)^{AfkQed,M>8}_{fastsim}}\,C_{data/MC}\ , \tag{10.1}$$

where for each case N_0 is the generated number of events, dN/dm the mass spectrum of events satisfying all criteria. The ratio of spectra at generator level with fast simulation are labeled '$fastsim$', while '$fullsim$' denotes the spectrum of events with full detector simulation. AfkQed was run with a cut limiting hard additional ISR, noted '$M > 8$', namely $m_{\mu\mu\gamma_{ISR}(\gamma_{addFSR})} > 8$ GeV. Finally the $C_{data/MC}$ factor incorporates all corrections from data to the simulation for detector efficiencies, such as trigger, tracking, muon ID, χ^2 cut.

The ratio of spectra Phokhara/AfkQed at fast-simulation level is given in

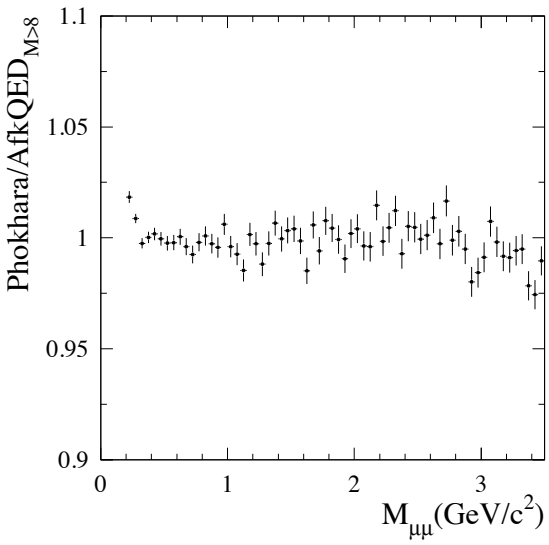

Figure 10.5: The ratio of the $\mu\mu$ mass spectra within acceptance cuts in Phokhara and AfkQed at generator level with fast simulation.

Fig. 10.5 for events satisfying the geometrical acceptance and the muon momentum cut. It is rather flat with a sharp increase at threshold, caused by the expected change of cross section in Phokhara for NLO FSR, which is not present in AfkQed. This contribution is small everywhere in the spectrum (see Section 11.3). The $C_{data/MC}$ correction is shown in Fig. 10.6, the largest effect being from muon ID.

The ratio data/QED is shown in Fig. 10.7 separately for runs 1-2 and runs 3-4. Both distributions are flat from threshold to 3.5 GeV and consistent with unity within errors with satisfactory χ^2 values. Fits with a constant value give

$$\frac{\sigma^{data}_{\mu\mu\gamma(\gamma)}}{\sigma^{NLO\ QED}_{\mu\mu\gamma(\gamma)}} = 1 + (7.8 \pm 3.1 \pm 6.7 \pm 9.4)\ 10^{-3} \quad \text{runs } 1-2 \qquad (10.2)$$

$$= 1 + (1.8 \pm 2.4 \pm 5.6 \pm 9.4)\ 10^{-3} \quad \text{runs } 3-4 \qquad (10.3)$$

where the errors are statistical (data, MC, efficiencies), systematic from our measurements, and systematic from the *BABAR* luminosity, respectively.

Both groups of runs are consistent within errors: the difference of the ratios for runs 1-2 and runs 3-4 in the 0.2-3 GeV range is $(6.0 \pm 3.3 \pm 3.9 \pm 4.4) \times 10^{-3}$,

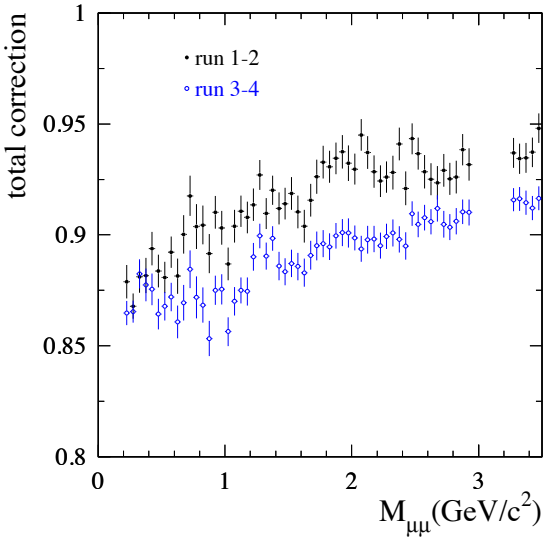

Figure 10.6: The total correction data/MC for the detector simulation as a function of $m_{\mu\mu}$ for runs 1-2 and 3-4.

where the first error is statistical, the second from uncommon systematics (photon efficiency ratio for run 1, uncorrelated parts of the μ-ID systematic uncertainties), and the third from the *BABAR* luminosity. The two results can thus be combined (Fig. 10.8), yielding

$$\frac{\sigma^{data}_{\mu\mu\gamma(\gamma)}}{\sigma^{NLO\ QED}_{\mu\mu\gamma(\gamma)}} = 1 + (4.0 \pm 1.8 \pm 5.7 \pm 9.4) \times 10^{-3} \quad \text{runs } 1-4 \qquad (10.4)$$

The values found for the ratio are consistent with 1 over the full mass range explored in this analysis. We conclude that our measurement of the $ee \to \mu\mu\gamma(\gamma)$ cross section using the *BABAR* luminosity agrees with NLO QED in the $\mu\mu$ mass range from threshold to 3.5 GeV within the overall accuracy of 1.1%.

10.6 Independent determination of the *BABAR* luminosity for runs 1-4

Since the largest uncertainty in the measurement comes from the luminosity, the result can be inverted to yield an independent determination of the *BABAR*

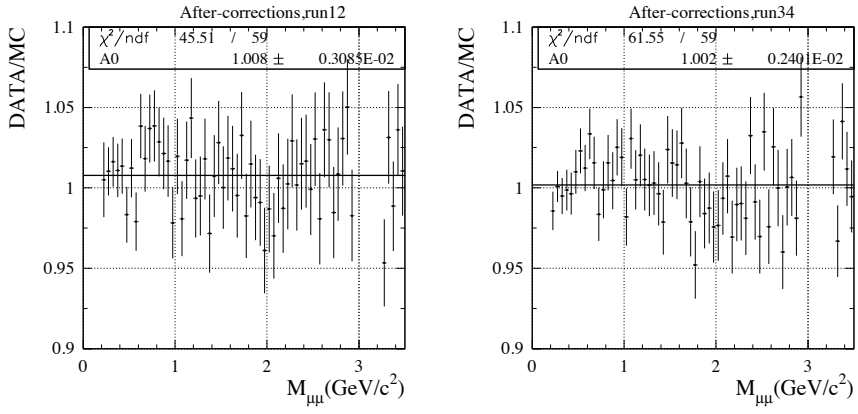

Figure 10.7: The ratio of the $\mu\mu$ mass spectrum in data over the absolute prediction from QED using the BaBar luminosity: runs 1-2 (left), runs 3-4 (right). The NLO QED prediction is obtained from the data-corrected (for detector simulation) and Phokhara-corrected (for NLO effects) AfkQed mass spectrum. The solid line is a fit of the 0.2-5 GeV with a free constant.

luminosity assuming the process cross section is predicted by QED. The runs in the 1-4 periods used in this analysis yield the luminosity result

$$L_{ee}^{\mu\mu\gamma\ measurement} = (231.7 \pm 1.4)\ \text{fb}^{-1} \tag{10.5}$$

to be compared to the best standard *BABAR* value [39, 40]

$$L_{ee}^{standard\ BaBar} = (230.8 \pm 2.2)\ \text{fb}^{-1} \tag{10.6}$$

It is seen that the luminosity determination based on our $\mu\mu\gamma$ measurement is consistent with the standard *BABAR* result, while being more precise (5.9×10^{-3} relative error).

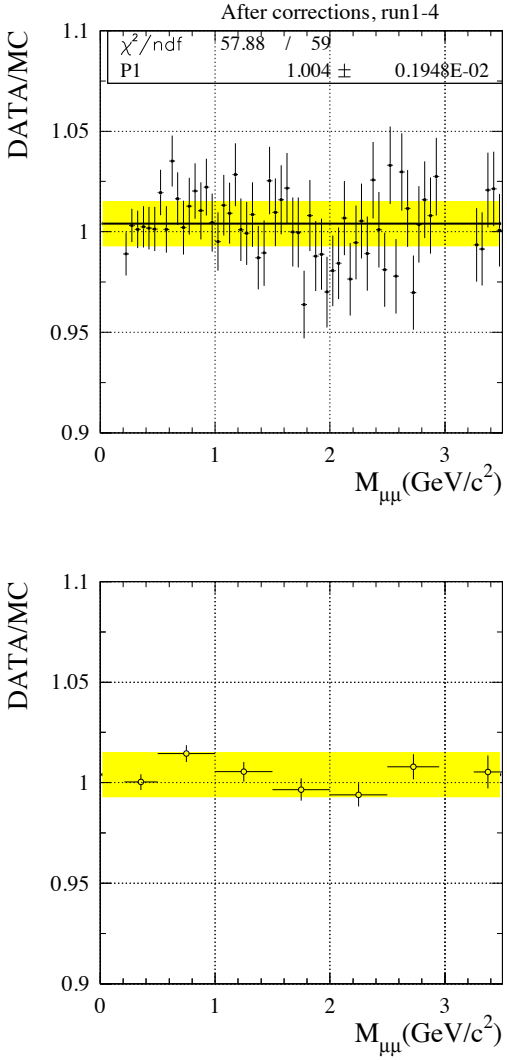

Figure 10.8: The ratio of the $\mu\mu$ mass spectrum in data over the absolute prediction from QED using the BaBar luminosity: runs 1-4. The NLO QED prediction is obtained from the data-corrected (for detector simulation) and Phokhara-corrected (for NLO effects) AfkQed mass spectrum. The band is drawn around the fit of the 0.2-3.5 GeV to a free constant, with a half-width given by the total expected systematic uncertainty (from this analysis and from the BaBar ee luminosity). Top: 50-MeV bins. Bottom: 500-MeV bins.

Chapter 11

Determination of the effective ISR Luminosity

In this chapter we express the obtained results on the $\mu\mu\gamma(\gamma)$ sample in terms of the effective ISR luminosity, following Eqs. (1.20) and (1.21). This quantity can be used together with any measurement of a hadronic process with the ISR method, such as $\pi^+\pi^-(\gamma_{FSR})$, $K^+K^-(\gamma_{FSR})$, or $X(\gamma_{FSR})$ where X is a multi-hadronic final state. In order to facilitate its use we will give results as a function of $\sqrt{s'}$ with $\sqrt{s'} = m_{X(\gamma_{FSR})}$, rather than s', since ISR results on cross sections have been given so far in this way.

As discussed in chapter 8 the $\mu\mu\gamma(\gamma)$ event acceptance appearing in Eq. (1.20) is obtained from a large simulated sample generated with AfkQed. Corrections have been applied at the simulation level for detector and reconstruction effects.

Several effects need to be considered in addition: (1) the unfolding of the data from $m_{\mu\mu}$ to $\sqrt{s'}$, thus including the possible emission of an additional FSR photon, (2) the LO FSR correction from Eq. (1.19), and (3) the QED cross section $\sigma_0^{ee\to\mu\mu(\gamma_{FSR})}(s')$ at the Born level concerning ISR, but including FSR. We take these points in turn before giving the final results.

11.1 Unfolding the $\sqrt{s'}$ distribution

As the ISR luminosity should be expressed as a function of $\sqrt{s'}$ which is the relevant variable for the process $ee \to \mu\mu(\gamma_{FSR})$, the $\sqrt{s'}$ distribution must be unfolded from the background-subtracted and data/MC-corrected $m_{\mu\mu}$ spectrum. This procedure should take into account mass resolution effects and additional FSR which shifts from $\sqrt{s'}$ to $m_{\mu\mu}$. Both sources produce small distortions of the spectrum.

We have used an unfolding technique [43], which will be described in some

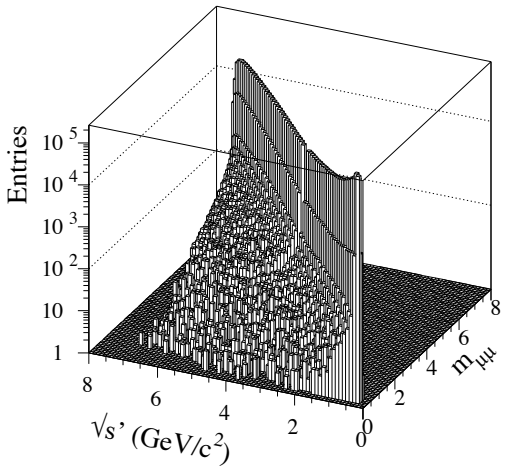

Figure 11.1: The mass transfer matrix from $\sqrt{s'}$ to $m_{\mu\mu}$ from the AfkQed simulation.

detail in Chapter 15 for $\pi\pi$ mass unfolding. So it will not be repeated here. The method is based on a MC-generated mass-transfer matrix to perform the deconvolution of the spectrum. The $(\sqrt{s'_{true}}\,, m_{\mu\mu\ reconstructed})$ mass matrix, where the reconstructed mass is obtained from the kinematic fit, has the structure of a sharp ridge along the diagonal with a width resulting from resolution effects and a low-level tail from FSR, as seen in Fig. 11.1. Compared to the $\pi\pi$ analysis with the prominent ρ resonance, the $\mu\mu$ unfolding is uncritical. The mass spectrum is uniformly decreasing and resolution effects play a very small role. In fact the larger effect to correct is the FSR event shift.

The following procedure is used:

- the data spectrum of the fitted mass $m_{\mu\mu}$ is subtracted for backgrounds and the data/MC corrections for efficiencies are applied;
- the mass-transfer matrix records the probability that an event generated in a $\sqrt{s'}$ bin i is reconstructed in a $m_{\mu\mu}$ bin j. It is obtained from the simulation and corrected for differences with data;
- the unfolding procedure is applied to the $m_{\mu\mu}$ spectrum, yielding the $\sqrt{s'}$ spectrum;

- the overall acceptance correction from the simulation is applied.
- systematic tests of the unfolding procedure are performed.

The method delivers the unfolded distribution in the same 50-MeV mass bins as for the input spectrum. A large mass range 0-6 GeV is considered, although we need only the first part of the spectrum for luminosity purposes. A covariance matrix containing the statistical correlations between the bin contents is obtained with toy simulations, where both the data and the transfer matrix are statistically fluctuated.

Inadequacies in the detector simulation, essentially μ-ID, are corrected by comparing the distributions for data and reconstructed MC, thus modifying the transfer matrix. Only one step is necessary, but one can use a second step to check the stability of the unfolded spectrum. Figure 11.2 shows the data - reconstructed MC difference before and after one iteration, with a clear improvement, while Fig. 11.3 demonstrates that the second iteration does not bring further improvement to the unfolded spectrum.

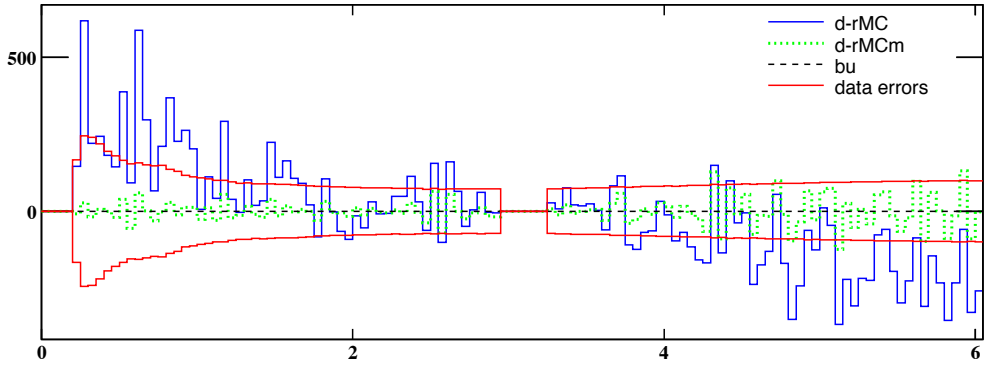

Figure 11.2: Data - reconstructed MC difference for the $\mu\mu$ spectrum, before($d-rMC$) and after ($d-rMCm$) one iteration. These values are compared to the statistical data errors.

As for the $\pi\pi$ unfolding, extensive toy studies with MC samples have been used to study the robustness and the accuracy of the unfolding method. These

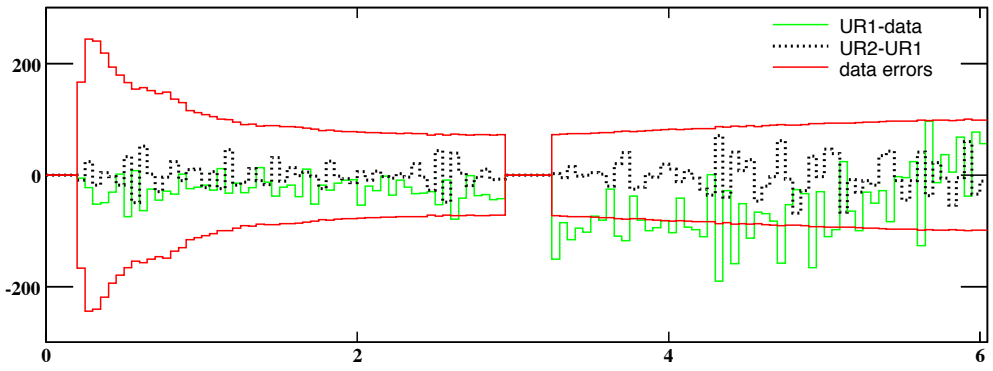

Figure 11.3: Correction of the $\mu\mu$ spectrum by the first unfolding(UR1-data) and by one iteration(UR2-UR1). These values are compared to the statistical data errors.

tests show that the systematic uncertainty from the unfolding method is within 10^{-3}.

11.2 Lowest-order FSR correction

The most energetic detected photon is assumed to be emitted by the initial state. This is largely true at low mass, but there is an increasing probability at larger s' values that this photon originates from muon radiation. Thus the observed $\mu\mu$ mass spectrum has to be corrected in order to keep only ISR production, since for all practical purposes at *BABAR* , where $\sqrt{s} \sim 10.58$ GeV and $\sqrt{s'} < 5$ GeV, main FSR production ('main' as opposed to 'additional' FSR) is completely negligible for hadronic processes.

Fig. 11.4 shows the quantity δ_{FSR} obtained with AfkQed at the generator level, since the final mass spectrum is already corrected for acceptance and efficiencies. The correction is defined as

$$\delta_{FSR} = \frac{|FSR + (FSR + addISR, FSR)|^2}{|ISR + (ISR + addISR, FSR)|^2} \tag{11.1}$$

as a function of $\sqrt{s'}$, where $FSR(ISR)$ means events with LO FSR only, $(FSR(ISR)+ addISR, FSR)$ means events with two photons the more energetic one is from

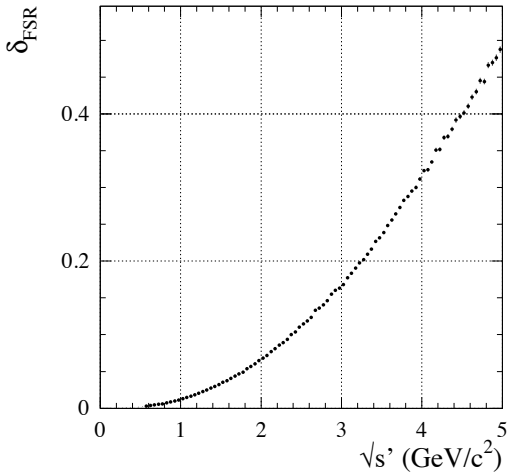

Figure 11.4: The FSR correction $\delta^{\mu\mu}_{FSR} = \frac{|FSR|^2}{|ISR|^2}$ obtained with AfkQed.

FSR (ISR). It would have been preferable to use Phokhara instead, as we know addISR is approximate in AfkQed, but by construction the labels FSR or ISR for photons are not available in Phokhara, hence s' is not accessible on an event-by-event basis. However the difference is expected to be at a negligible level, about 10^{-4} and $2\,10^{-3}$ at 1 and 3 GeV, respectively.

In fact the importance of main FSR production can be experimentally determined in the case of 2-body processes $x^+x^-\gamma$ using the measurement of a charge asymmetry which projects the interference between ISR and FSR amplitudes. The charge asymmetry, being dependent on the relative FSR and ISR amplitudes, is a sensitive test of an FSR contribution. Such a measurement has been already carried out for the $\mu^+\mu^-\gamma$ and $\pi^+\pi^-\gamma$ processes. The preliminary results show a good agreement within a few % for muons with the large asymmetry predicted by AfkQed (QED) at large mass with its characteristic shape. We can thus rely on the AfkQed prediction for the FSR fraction as a function of mass.

11.3 Born QED cross section with additional FSR

The cross section for $e^+e^- \to \mu^+\mu^-(\gamma_{FSR})$, at Born level for the initial state and without vacuum polarization, can be calculated exactly in QED at NLO. It

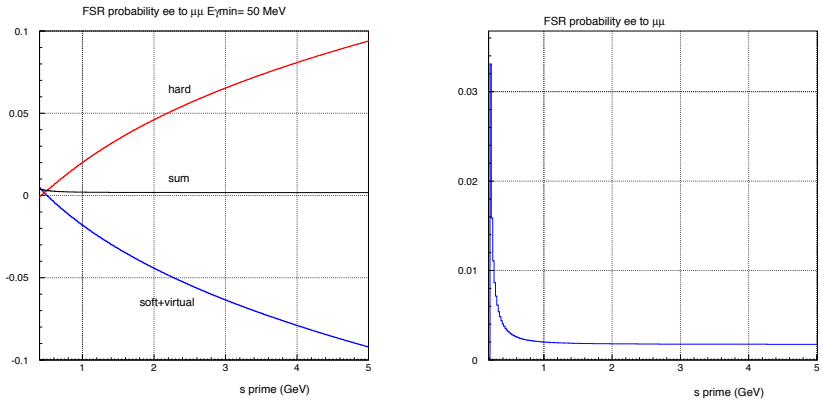

Figure 11.5: The relative FSR contributions as a function of s' in the process $e^+e^- \to \mu^+\mu^-(\gamma_{FSR})$, $\frac{\alpha}{\pi}\eta_{h,v+s}$ at NLO (left), and their sum (right). The separation between hard and soft radiation has been chosen at 50 MeV in the $\mu\mu\gamma$ center-of-mass.

has the form:

$$\sigma_0^{\mu\mu(\gamma)}(s') = \sigma_{pt}(s') \left[1 + \frac{\alpha}{\pi}\eta(s')\right] \tag{11.2}$$

with

$$\sigma_{pt}(s') = \frac{4\pi\alpha^2}{3s'} \frac{\beta(3-\beta^2)}{2} \tag{11.3}$$

$$\beta = \sqrt{1 - \frac{4m_\mu^2}{s'}} \tag{11.4}$$

$$\eta(s') = \eta_h(s') + \eta_s(s') + \eta_v(s') \tag{11.5}$$

where $\eta_{h,s,v}$ are the $O(\alpha)$ contributions (in the final state) from hard and soft bremsstrahlung, and the one-loop/Born interference. The sum of η_v and η_s is IR-finite, while the total sum is independent of the choice of the energy used to separate soft and hard photons (within reasonable limits). Expressions for all 3 components can be found in many papers, for ex. in Refs. [41, 42]. By virtue of the KLN theorem, the dominant logarithmic terms cancel between the (soft+virtual) and hard contributions. As seen in Fig. 11.5, although each term reaches a level of a few % with opposite signs, the sum stays in the few 10^{-3} range. This explains why we see a sizeable additional-FSR signal in data, despite the fact that the total additional-FSR contribution ($\eta(s')$) is very small.

11.4 Effective ISR luminosity for the $\pi\pi$ (KK) analysis

We distinguish two cases for evaluating the ISR luminosity:

- for our $\pi\pi$ and KK analysis, the luminosity L_{eff}^{full} integrate all configurations of 2 ISR photons with at least one with $E_\gamma^* > 3$ GeV and $20^\circ < \theta_\gamma^* < 160^\circ$,
- for the standard ISR analyses already performed, the luminosity $L_{eff}^{M>8\ GeV}$ satisfies the same conditions for the 'main' ISR photon, but with the restriction on the energy of the second ISR photon such that $m_{\mu\mu(\gamma_{FSR})} > 8$ GeV.

The first determination is given now, while the second is considered in the following section.

To obtain the measured full effective ISR luminosity $dL_{eff}^{full}/d\sqrt{s'}$ according to (Eq.1.20) the event acceptance is taken from AfkQed, as the generator-level corrections using Phokhara cancel in the ratios $\pi^+\pi^-/\mu\mu$ and $KK/\mu\mu$.

The measured full effective ISR luminosity $dL_{eff}^{full}/d\sqrt{s'}$ for runs 1-4 is given in Fig. 11.6 in 50 MeV bins.

The obtained luminosity can be compared to the standard estimate using LO QED, given by

$$\frac{dL_{LO}}{d\sqrt{s'}} = \frac{\alpha}{\pi x}\left[(2-2x+x^2)\ln\frac{1+c}{1-c} - x^2 c\right]\frac{2\sqrt{s'}}{s}\left(\frac{\alpha(s')}{\alpha(0)}\right)^2 L_{ee} \qquad (11.6)$$

where $x = 1 - s'/s$ and $c = \cos\theta^*_{\gamma\ min}$ with $\theta^*_{\gamma\ min} = 180^\circ - \theta^*_{\gamma\ max} = 20^\circ$. We have left the vacuum polarization factor in Eq. (11.6) for a convenient comparison. The LO prediction is superimposed to the measured luminosity in Fig. 11.6. The agreement is fair, with some deterioration at large mass. The vacuum polarization (VP) factor includes both leptonic and hadronic contributions. The hadronic contribution is taken from the parametrization used in AfkQed and it has been checked that it agrees well with independent determinations [44].

11.5 Effective ISR luminosity for standard ISR analyses

All ISR measurements of hadronic cross sections have used AfkQed-generated samples with a cut at the generator level $m_{\mu\mu(\gamma_{FSR})} > 8$ GeV designed to suppress

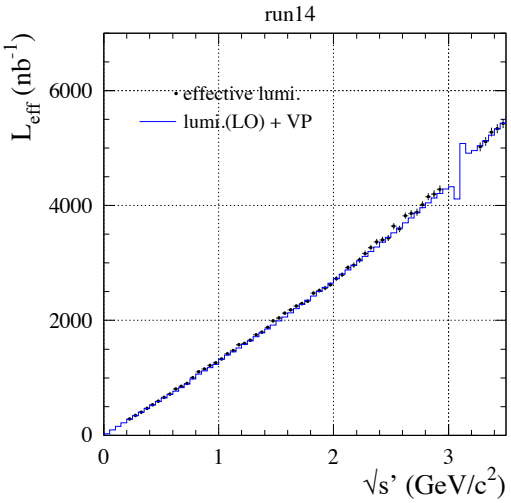

Figure 11.6: The effective ISR luminosity in runs 1-4 for the $\pi\pi$ and KK analyses: the data points give ΔL_{eff}^{full} in $\Delta\sqrt{s'} = 50\,\text{MeV}$ bins. Conditions for the detected/identified ISR photon are $E_\gamma^* > 3\,\text{GeV}$ and $20^\circ < \theta_\gamma^* < 160^\circ$ in the ee CM frame, while one additional ISR photon is allowed without any restriction. The superimposed histogram is the lowest-order ISR prediction following Eq. (11.6). The J/ψ mass region is cut out for the data.

hard additional ISR photons. This cut is generally not applied on data, but in those measurements this is irrelevant as tight χ^2 cuts are applied on kinematic fits, not allowing for hard extra radiation. Event acceptances are computed with respect to this restricted generated sample.

In these analyses a correction for radiative corrections is applied to the measured ISR $X\gamma$ process. This correction C_{rad} is computed with the AfkQed generator as

$$C_{rad} = \frac{\sigma[ee \to X\gamma(\gamma_{ISR})(\gamma_{FSR})]}{\sigma[ee \to X\gamma]} \tag{11.7}$$

and turns out to be very close to one, within a few 10^{-3}. The fact that such a correction is small is rather accidental, as it would rapidly increase (decrease) if the generation cut is chosen below (above) 8 GeV. Figure 11.7 shows the correction C_{rad} in AfkQed and Phokhara with and without the 8-GeV cut. We find again here the deficiency of hard extra ISR photons in AfkQed (structure functions) compared to Phokhara (exact NLO). So clearly this cut is beneficial in

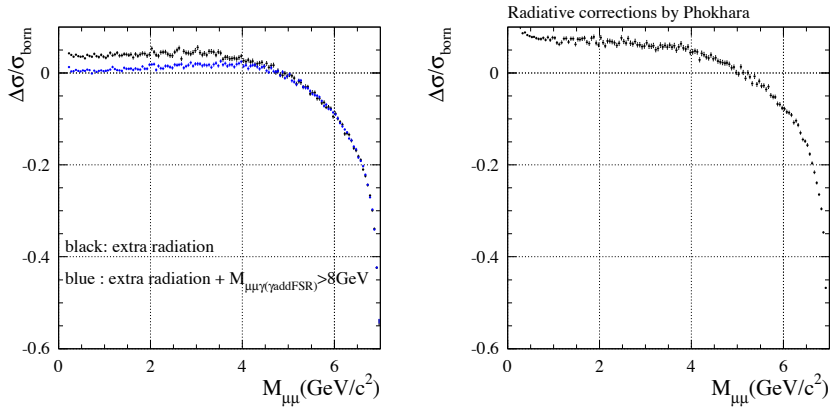

Figure 11.7: The radiative correction C_{rad} defined in Eq. (11.7) for AfkQed (left) and Phokhara (right).

restricting AfkQed to a region of better-controlled radiation; however the small value of the correction is fortuitous.

The ratio $dL_{eff}^{M>8}/dL_{LO}$ is given in Fig. 11.8 (left), after correcting for the difference in efficiencies for ISR photon detection in data compared to simulation. This is the relevant comparison for the intrinsic ISR luminosity function in those analyses where a correction is applied explicitly for the ISR photon efficiency (such as 3π, $p\overline{p}$, $\Lambda\overline{\Lambda}$). The ratio is slightly above one and shows some negative slope. Nevertheless there is a fair agreement with the $\pm 1.7\%$ systematic uncertainty quoted in these analyses (1.2% for BaBar lumi $\oplus$ 1% for radiative effects $\oplus$ for photon efficiency).

For the other analyses (such as 4π, 5π, 6π, $K\overline{K}\pi$, and $K\overline{K}2\pi$) the situation is less clear concerning the ISR photon efficiency correction. But here one can directly compare to the parameterizations of the ISR luminosity which were used [45]. Also as the VP factor is not included in these functions, it is corrected for in our luminosity determination before computing the ratio.

The comparison is presented in Fig. 11.9 separately for runs 1-2 and 3-4, and their sum. In all cases, one sees large deviations below 0.5 GeV which are of no consequence for the published results, as the typical energy range for multi-hadronic cross sections lies inside these limits, the lower one from kinematics

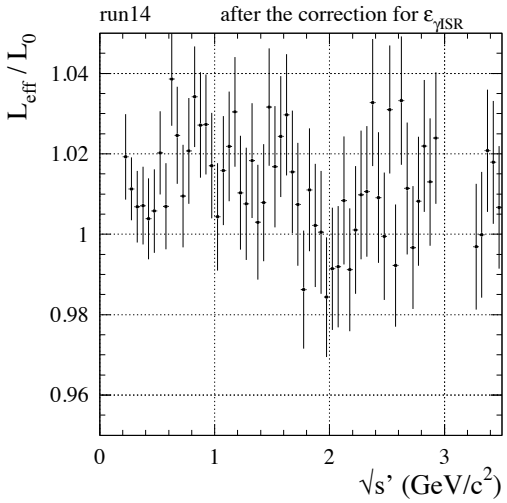

Figure 11.8: The ratio $dL_{eff}^{M>8}/dL_{LO}$ as a function of $\sqrt{s'}$ after correction for the ISR photon efficiency ratio data/MC, *i.e.* $dL_{eff}^{M>8}/dL_{LO} \times \epsilon_{ISR\gamma}^{MC}/\epsilon_{ISR\gamma}$.

and the higher one from limitations from statistics and background. While some wavy behavior is observed in between, fits to a constant between 1 and 3 GeV give values for the deviation from one of $(0.4 \pm 0.4)\%$ for runs 1-2, $(-0.4 \pm 0.3)\%$ for runs 3-4, and $(-0.1 \pm 0.2)\%$ for the whole set. These values are well within the systematic uncertainty of $\pm 3\%$ quoted in these analyses, but larger deviations are seen near threshold and above 2.5 GeV.

It is interesting to note that the wavy pattern at $\pm 2\%$ level and the larger deviations at lower and higher masses are also seen when $L_{'standard'}$ is directly compared to the LO luminosity function $L_{0\ no\ VP}$, as demonstrated in the bottom-right plot of Fig. 11.9. Thus they are features of the parametrization used [45].

Our more precise ISR luminosity determination can be used to improve the corresponding systematic uncertainty which is common to all published results of multi-hadronic cross sections by *BABAR* [46].

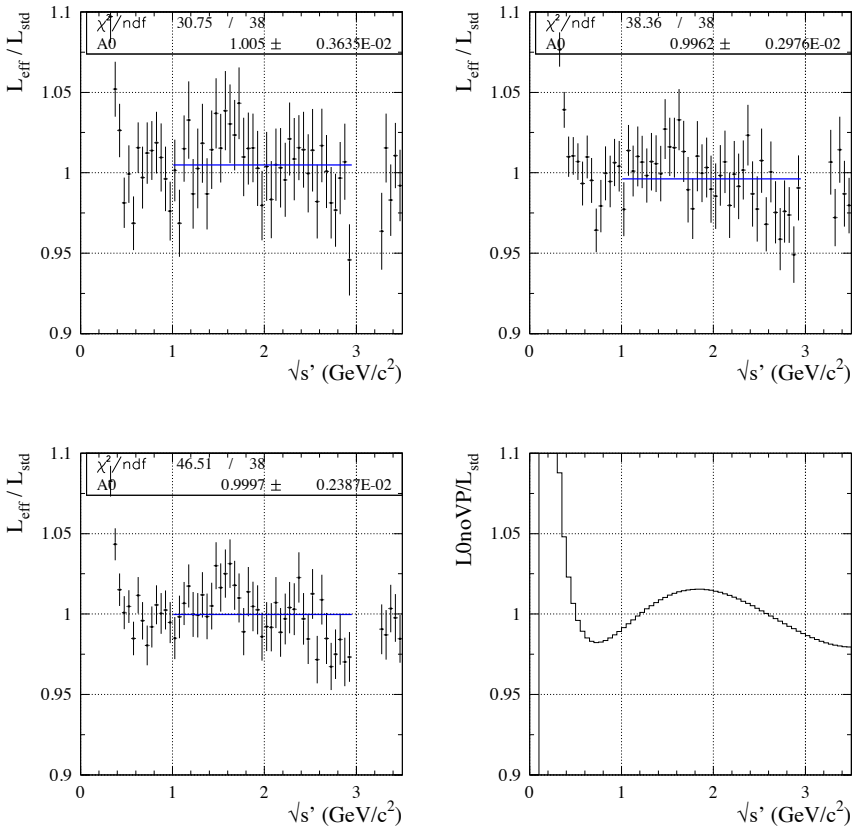

Figure 11.9: The ratio $dL^{M>8}_{eff\ no\ VP}/dL_{'standard'}$ as a function of $\sqrt{s'}$ where 'standard' refers to luminosity used so far in most multihadron ISR analyses [45]: runs 1-2 (top left), 3-4 (top right), 1-4 (bottom left). The ratio $dL_{LO\ no\ VP}/dL_{'standard'}$ as a function of $\sqrt{s'}$ (bottom right).

Chapter 12

The Central ρ Region ($0.5 < m_{\pi\pi} < 1$ GeV)

12.1 Strategy

The mass region between 0.5 and 1 GeV is dominated by the ρ resonance. The corresponding large cross section provides a dominant contribution to vacuum-polarization dispersion integrals, so it has to be known with small systematic uncertainties. It also means that the background will be at a small level. These two considerations militate for large efficiencies, in order to keep systematics sufficiently low. Therefore a loose χ^2 cut (see Section 3.2), the same as for the $\mu\mu\gamma$ analysis, and normal π-ID for both tracks are used.

The $m_{\pi\pi}$ spectrum obtained in these conditions is shown in Fig. 12.1. Only the statistical errors in the 2-MeV mass bins are given, amounting to 1.4% on peak and 4.4% near the boundaries. Apart from the ρ resonance shape, a clear $\rho - \omega$ interference pattern is observed.

12.2 Backgrounds

12.2.1 Summary of backgrounds

Following Section 7.3 the backgrounds are obtained and displayed in Fig. 12.2. The dominant contribution is from multi-hadronic processes, mostly ISR ($\pi^+\pi^-\pi^0\gamma$, $\pi^+\pi^-2\pi^0\gamma$) and $q\bar{q}$, with a fraction amounting to 8.0 10^{-3} at the ρ peak. The $p\bar{p}\gamma$ contribution is much smaller ($< 10^{-3}$). For illustration we also show the $\mu\mu$ and KK background contributions in the '$\pi\pi$'-identified sample, although they are implicitly subtracted when solving Eqs. (7.1) for $N^{(0)}_{\pi\pi}$.

The total background fraction as a function of $m_{\pi\pi}$ is also shown in Fig. 12.2. It is 1.3% at the ρ peak, but reaches ~16% at 0.5 GeV and ~7% at 1 GeV. These sharp increases justify the limits chosen to define the 'central region'. At

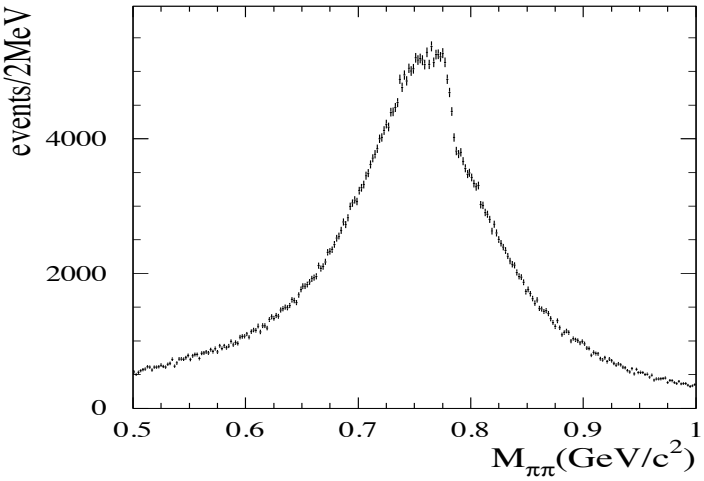

Figure 12.1: The raw $m_{\pi\pi}$ spectrum of $\pi\pi\gamma(\gamma)$ events in the ρ region, in 2-MeV bins.

the worst place (near 0.5 GeV) the absolute uncertainty on the estimated non-$\mu\mu/KK$ background fraction is $5.4\,10^{-3}$, which is still tolerable. At the peak the error is only $0.6\,10^{-3}$. The fractions for all the considered backgrounds is given in Table 12.1 at three mass values.

12.2.2 Overall test of the multi-hadronic background

Since the multi-hadron background fraction is reaching sizeable values near the boundaries of the central ρ region, but with a small enough uncertainty, it is important to make sure that no other process contributes at a level larger than the quoted uncertainty and that the mass distribution estimated from the simulation is appropriate. The uncertainty on the multi-hadron background fraction is 5.4×10^{-3} at 0.5 GeV and 2.7×10^{-3} at 1 GeV, the value at the ρ peak being irrelevant.

Possible ISR processes not considered in Table 12.1 are higher-multiplicity π^0 hadronic states such as $2\pi 3\pi^0\gamma$. This cross section has not yet measured by *BABAR*, but should be close to that of $4\pi\pi^0\gamma$ dominated by $\eta 2\pi\gamma$ (considered above) and $\omega 2\pi\gamma$ (which should be twice $\omega 2\pi^0\gamma$). Since the $2\pi 3\pi^0\gamma$ process has 5 missing photons in the kinematic fit, one expects large χ^2 values which, together with the expected rate, makes its contribution smaller than 10^{-3}. Possibly the

Table 12.1: Estimated background fractions (in %) in the '$\pi\pi$' sample for $m_{\pi\pi}$=0.525, 0.775, 0.975 GeV.

process	0.525 GeV	0.775 GeV	0.975 GeV
$\mu\mu$	3.87 ± 0.15	0.33 ± 0.01	2.54 ± 0.11
KK	0.08 ± 0.01	0.01 ± 0.01	0.08 ± 0.01
$\gamma 2\pi\pi^0$	8.04 ± 0.41	0.39 ± 0.05	0.88 ± 0.19
$q\bar{q}$	1.11 ± 0.17	0.26 ± 0.03	1.81 ± 0.19
$\gamma 2\pi 2\pi^0$	1.29 ± 0.16	0.06 ± 0.01	0.46 ± 0.09
$\gamma 4\pi$	0.20 ± 0.04	0.09 ± 0.01	0.24 ± 0.06
$\gamma p\bar{p}$	0.22 ± 0.02	0.04 ± 0.01	0.52 ± 0.06
$\gamma\eta 2\pi$	0.02 ± 0.01	0.03 ± 0.01	0.09 ± 0.01
$\gamma K_S K_L$	0.18 ± 0.03	0.01 ± 0.01	0.10 ± 0.02
$\gamma 4\pi 2\pi^0$	< 0.01	< 0.01	< 0.01
$\tau\tau$	0.17 ± 0.03	0.04 ± 0.01	0.31 ± 0.05
γee	0.63 ± 0.63	0.03 ± 0.03	0.27 ± 0.27
total	15.77 ± 0.81	1.27 ± 0.07	7.20 ± 0.42

largest unaccounted contribution could come from $\omega 2\pi\gamma$ with $\omega \to \pi^0\gamma$, but again one can estimate that it will not reach the 10^{-3} level.

A test can be performed with data to assess both the rate and the mass distribution of the multi-hadron background in the 2D-χ^2 region where it is the largest, *i.e.* in the 'sleeve' outlined in Fig. 7.10. The $\pi\pi$ mass distribution in this region is presented in Fig. 12.3: a very significant background is seen under the ρ line shape and it is found to qualitatively agree with the MC expectation. To be more quantitative, a fit is performed with the MC background and signal components and the ratio of the fitted background to the estimated one in Sections 7.3.5 and 7.3.6 is found to be 0.968 ± 0.037, showing no excess and compatible with unity, which can be translated to an uncertainty of 4.5×10^{-3} at 0.5 GeV and 1.5×10^{-3} at 1 GeV on the background fraction in the full $\pi\pi$ sample. These values are below the quoted uncertainties and they provide a good check of the

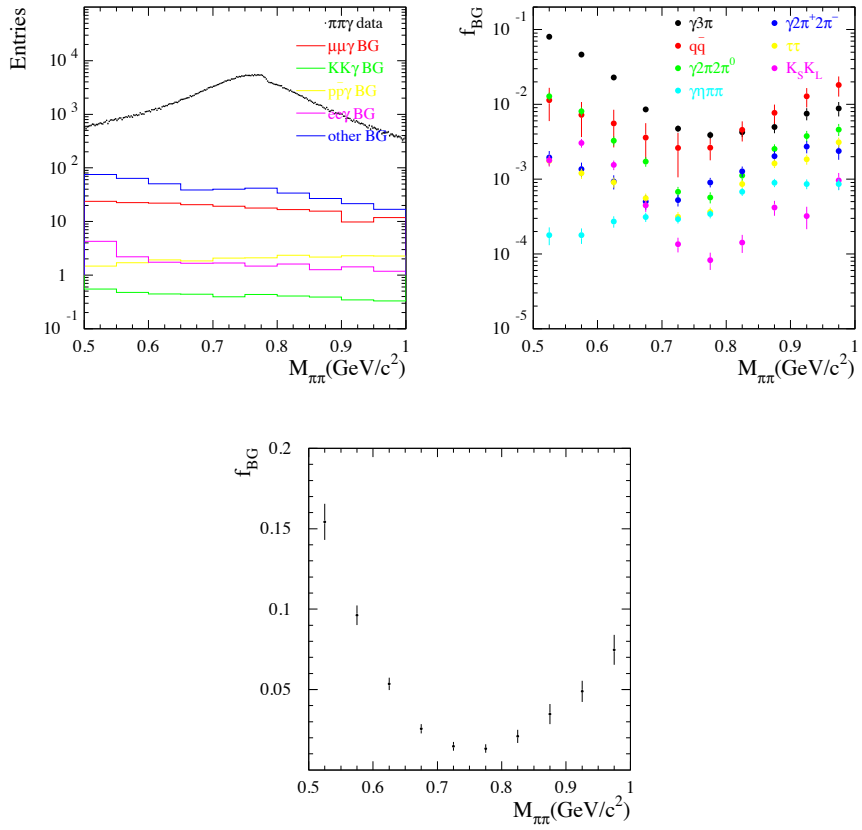

Figure 12.2: Top left: the $m_{\pi\pi}$ distribution with the estimated background contributions from $\mu\mu\gamma$, $K^+K^-\gamma$, $p\bar{p}\gamma$, $ee\gamma$, and multihadronic processes. Top right: the background fractions for the dominant multihadronic processes and $\tau\tau$. Bottom: the total background fraction.

multi-hadron background estimate.

12.3 Two-pion mass resolution and calibration

The absolute $\pi\pi$ mass scale depends on the momenta and angles measurement and the kinematic fit. Systematic effects can be studied using ISR-produced $J/\psi \to \mu\mu$ events, which are treated in the same way as the di-pion sample.

Muon pairs ('$\mu\mu$' identified) are selected with otherwise the same criteria as $\pi\pi$ events. The $\mu\mu$ mass distribution is fitted in the 3.0-3.2 GeV range to a linear term for the QED background and a signal shape obtained by convoluting

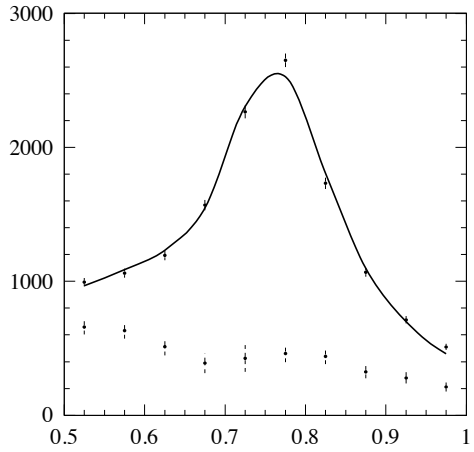

Figure 12.3: The $m_{\pi\pi}$ (in GeV) distribution in the 'sleeve' (background-rich region in the selected 2D-χ^2 region, see text) is fitted with $\pi\pi$ signal and multi-hadron background components, with their shapes taken both from simulation. The fitted background is consistent with the estimated level.

the sum of the natural J/ψ Breit-Wigner and the QED-J/ψ interference with a gaussian resolution shape. The free parameters are the amplitude of the signal, the J/ψ mass $m_{J/\psi}$, the resolution σ_m and the two coefficients for the background. Fits are made in 5 boxes in the folded momentum space of the two tracks with successive boundaries 1-3-5-8 GeV.

Whereas σ_m increases for larger momenta as expected, the fitted values for $m_{J/\psi}$ are consistent for all boxes, showing no evidence for a momentum-dependent calibration change. Therefore the whole sample can be considered and the corresponding fit is shown in Fig. 12.4. The χ^2/DF is only 1.7 and there is evidence for an small symmetric excess in the tails (a double gaussian resolution function would improve the fit), but this does not affect significantly the central value. The result yields

$$m_{J/\psi} = (3096.30 \pm 0.13) \text{ MeV} \quad (12.1)$$

$$\sigma_m = (9.38 \pm 0.04) \text{ MeV} \quad (12.2)$$

to be compared with the world-average value [47], (3096.92 ± 0.01) MeV. The

difference, (-0.62 ± 0.10) MeV, is interpreted as a momentum scale shift of $(-2.00 \pm 0.04)\ 10^{-4}$.

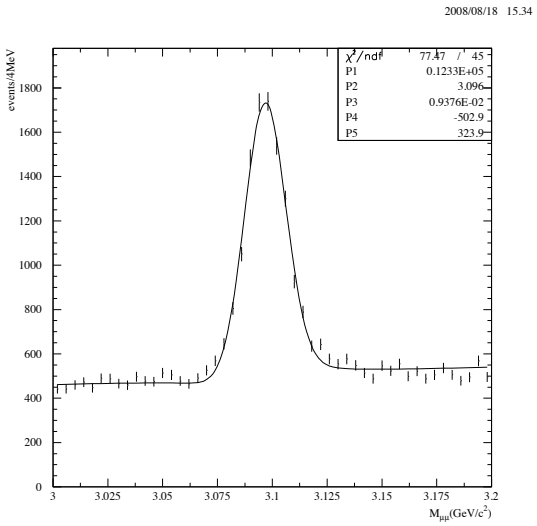

Figure 12.4: Fit of the '$\mu\mu$' mass distribution in the J/ψ region including the QED-J/ψ interference as a momentum calibration test.

This momentum-calibration scale factor translates into a shift for the ρ mass of (-0.16 ± 0.16) MeV where the full correction has been taken as systematic uncertainty.

The mass resolution obtained with the J/ψ data sample, (9.4 ± 0.1) MeV, is a bit better than the result from the simulation of continuum $\mu\mu\gamma$ events in the 3.0-3.2 GeV range (no J/ψ generated) which is found out to be (10.0 ± 0.1) MeV.

12.4 Systematic uncertainties

The systematic uncertainties are summarized in Table 16.1 in Section 16.2, together with those from outside the ρ mass region.

Chapter 13

The ρ Tails Region ($m_{\pi\pi} < 0.5$, > 1 GeV)

13.1 Need for a different treatment

The pion form factor drops very fast off the ρ peak, while the backgrounds are slowly vary with $\pi\pi$ mass. The fractions of $\mu\mu\gamma$, KKγ, $p\bar{p}\gamma$ and multi-hadronic backgrounds in the physical sample (with the loose 2D-χ^2 cut used in ρ region) are shown in Fig. 13.1. So outside the ρ region, the background level is too large and it is necessary to tighten the selection of $\pi\pi\gamma$ events.

13.2 Strategy

For multi-hadronic backgrounds, the kinematic fitting with assumption of $\pi\pi\gamma(\gamma)$ final states yields in general much worse χ^2 values than signal. So a tighter χ^2 cut $\ln(\chi^2_{add.ISR}+1) < 3$ is chosen to reduce multi-hadronic background, while still keeping a good efficiency for signal. Fig. 13.2 shows the tighter χ^2 cut and the 2D-χ^2 distributions below and above the central ρ region. This cut retains events with additional ISR since this region in the χ^2 plane is free of multi-hadronic background. The reduced χ^2 efficiency on signal from the tighter cut will result into a larger relative uncertainty, but it will be shown to be still reasonable, considering the much smaller $\pi\pi$ contribution in the ρ tails.

For $\mu\mu\gamma$ and ee backgrounds (the latter including $ee\gamma$, $\gamma\gamma$ with photon conversion, Bhabha events with bremsstrahlung), the tighter χ^2 cut is helpless, because they have a kinematics similar to signal. So a harder π identification, 'π_h' (see Section 6.2.2) is required for at least one of the two 'π' identified tracks, giving a further rejection of μ and e. The reduction factor of $\mu\mu$ background using such a 'π_h' identification is shown in Fig. 13.3 to be ~ 7 compared to the $\mu\mu\gamma(\gamma)$ MC sample already mis-identified as '$\pi\pi\gamma$'. The effect on ee background is discussed later.

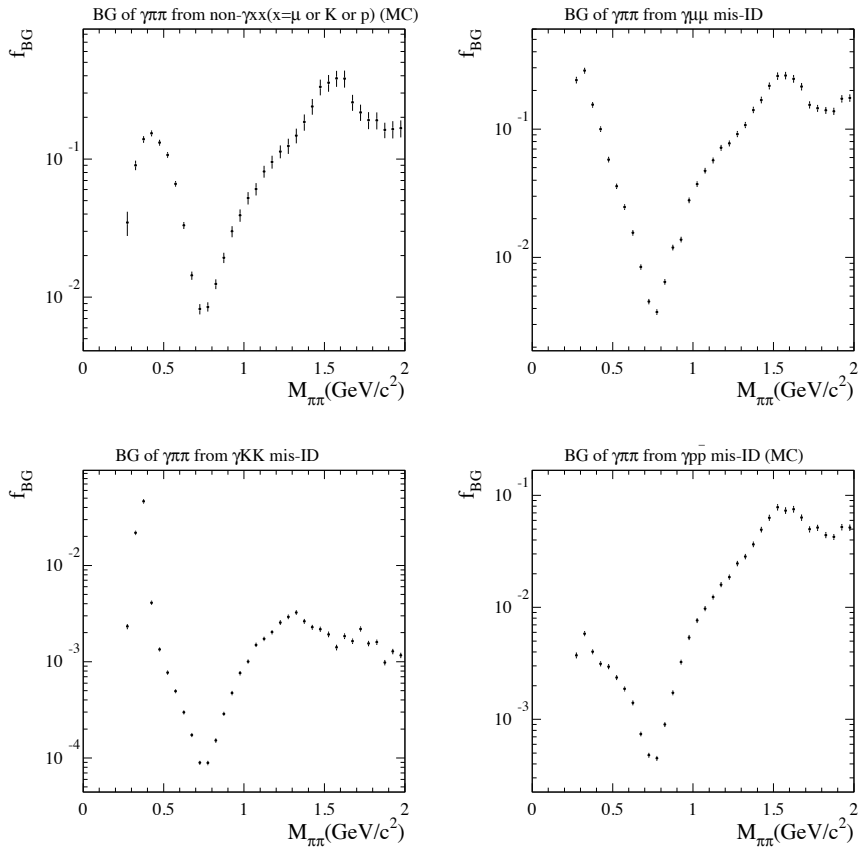

Figure 13.1: The fractions of different backgrounds in the physical sample with the loose 2D-χ^2 cut and nominal '$\pi\pi$'-ID (as used in the ρ region) as a function of the $\pi\pi$ mass. Top left: multi-hadrons, including $\tau\tau$. Top right: $\mu\mu\gamma$ (data + measured mis-ID). Bottom left: $KK\gamma$ (data + measured mis-ID). Bottom right: $p\bar{p}\gamma$ (MC).

The $KK\gamma$ and $p\bar{p}\gamma$ fractions in the '$\pi\pi\gamma$' sample are not large, so no additional requirement is needed and they are subtracted directly.

Just like in the central ρ region, the correction data/MC for the $\ln(\chi^2_{add.ISR}+1) < 3$ cut efficiency is studied, starting from the similar $\mu\mu\gamma$ study.

Considering that the data/MC corrections for $\pi\pi \to' \pi\pi'$ are already studied, only '$\pi\pi$' to '$\pi_h\pi$' efficiencies need to be investigated here.

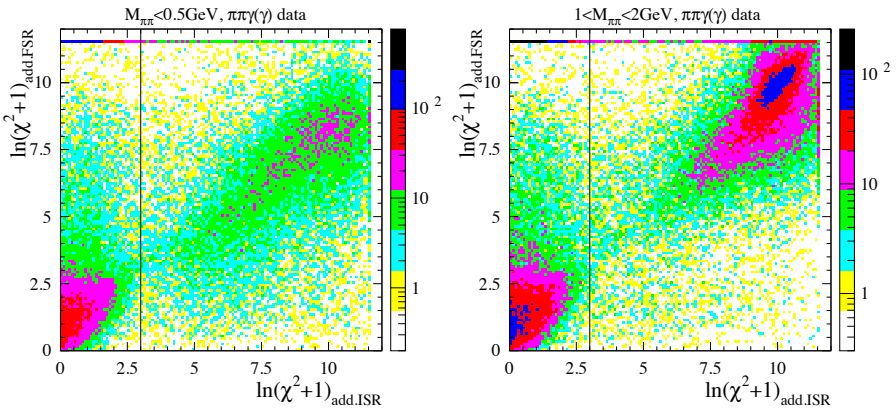

Figure 13.2: The 2D-χ^2 distributions below (left) and above (right) the central ρ region (data). The line indicates the tighter value for the χ^2 cut.

13.3 Backgrounds

13.3.1 $'\pi_h\pi'$ misidentified $\mu\mu$ events

The muon fraction in fact could be directly determined because one can use the non-π_h track to try to separate π-identified muons from true pions. This can be done using a π/μ estimator $P_{\pi/\mu}$ built as a likelihood with proper reference distributions [35]: tracks with $P_{\pi/\mu} \sim 1$ are muon-like, while values near 0 correspond to pions. Fitting the $P_{\pi/\mu}$ distributions yields the respective true muon and pion components. The distributions for pure pions and muons used in the fit are obtained from simulation with corrections applied by comparing to data distributions obtained at the ρ peak (pions) and large masses (muons). Fits are made in 0.5-GeV-wide mass bins and are shown in Figs. 13.4 and 13.5 for the mass range 0-2.5 GeV and 2.5-5 GeV, respectively.

Except for the 0.5-1 GeV interval the small $\mu\mu$ component can be well determined. Above 3 GeV the muon contribution becomes dominant, despite the $'\pi_h\pi'$ ID. The pion signal is lost above 4 GeV. The results of the fits are summarized in Fig. 13.6: for each mass interval the $\mu\mu$ fraction in data is expressed as the ratio to the prediction from the generated $\mu\mu$ MC sample. A second-order polynomial fit to all points allows one to smoothly interpolate between the low and high mass regions. The band indicates the error envelope of the fit.

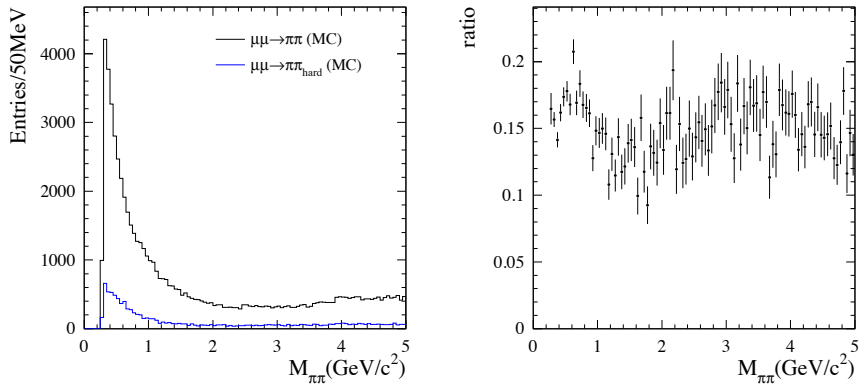

Figure 13.3: Left: the mass spectrum of '$\pi\pi$' and '$\pi_h\pi$' mis-identified $\mu\mu\gamma(\gamma)$ MC events. Right: the rejection, given by the ratio '$\pi_h\pi$'/'$\pi\pi$'.

13.3.2 $'\pi_h\pi'$ misidentified KK events

The $'\pi_h\pi'$ ID brings no significant reduction of the $KK\gamma(\gamma)$ background compared to $'\pi\pi'$, but its efficiency needs to be evaluated. Since the KK sample is dominated by the narrow ϕ resonance, one can use this feature to determine the KK component directly in data. The procedure is illustrated in Fig. 13.7. The left plot gives the expected KK mass distribution in simulation for events identified as $'\pi_h\pi'$. The shape of this distribution is taken to fit a KK signal in the corresponding data distribution (right plot), using a linear term to describe the predominant $\pi\pi$ component. In the $\pi\pi$ mass spectrum the ϕ peak is wider and distorted, and the fit-renormalized MC contribution is subtracted from the data.

13.3.3 $'\pi\pi' \to' \pi_h\pi'$ efficiency for ee events

For all ee backgrounds, no simulated MC sample is available. In any case, because of the cuts against electrons applied already at track definition level, the remaining contribution is small, but rather pathological, and must be studied in data.

From the events tagged as 'RadBhabha', 1/40 of which are kept in the selected ISR sample, one can get the mass distribution and $\cos\theta^*$ distribution for

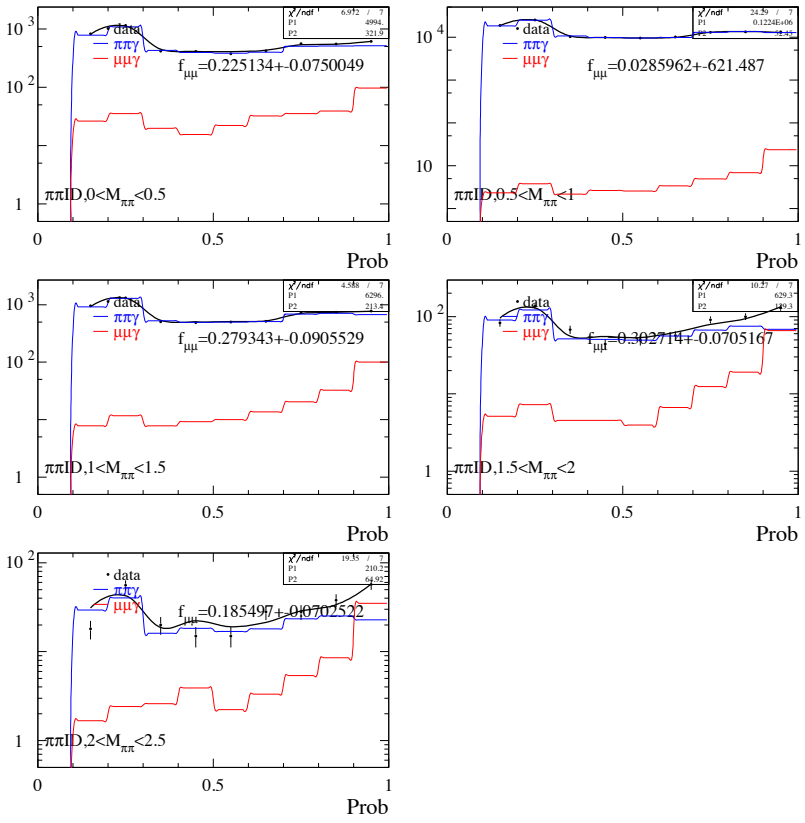

Figure 13.4: The two-component fits of the $\pi-\mu$ probability distributions for '$\pi\pi$'$\rightarrow$'$\pi_h\pi$' events from $\mu\mu\gamma$ and $\pi\pi\gamma$ sources. The $\mu\mu$ fraction in data is expressed in terms of the ratio to the $\mu\mu$ MC sample. Each plot corresponds to a 0.5-GeV mass bin in the range 0-2.5 GeV.

$ee\gamma$ events. In the mass range $0.28 < m_{\pi\pi} < 0.32$ GeV just above threshold, there is still a remaining $ee\gamma$ contribution even with the $\pi_h\pi$ identification, which can be obtained by fitting the $|\cos\theta^*_\pi|$ distribution. This separation from $\pi\pi\gamma$ events is possible because the $|\cos\theta^*_\pi|$ dependence of ee events has a sharp peak at one, while the $\pi\pi\gamma$ signal behaves as $\sin^2\theta^*_\pi$. In practice, the shape of the $\pi\pi\gamma$ signal is taken from the simulation and the shape for ee is obtained from the 'RadBhabha' sample. The contribution of $\mu\mu\gamma$ events is subtracted out before fitting. The fit is shown in Fig. 13.8. It provides the normalization factor (0.03) to be applied to 'RadBhabha' to describe the $ee\gamma$ background in the '$\pi_h\pi$' sample.

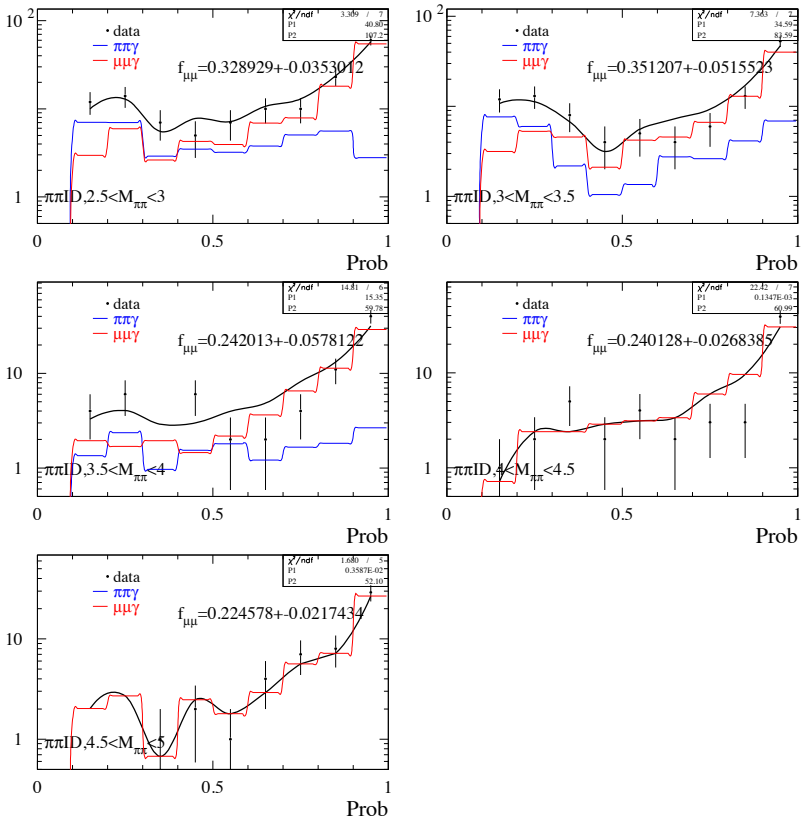

Figure 13.5: The two-component fits of the $\pi-\mu$ probability distributions for '$\pi\pi$'→'$\pi_h\pi$' events from $\mu\mu\gamma$ and $\pi\pi\gamma$ sources. The $\mu\mu$ fraction in data is expressed in terms of the ratio to the $\mu\mu$ MC sample. Each plot corresponds to a 0.5-GeV mass bin in the range 2.5-5 GeV.

The events identified as '$e\pi$' are rather pure $ee\gamma$ events outside the ρ region, but they have smaller statistics. However these events should be more similar to the '$\pi_h\pi$' identified $ee\gamma$ events. The ratio of the mass spectra of '$e\pi$' events to 'RadBhabha' sample is shown in Fig. 13.9. One finds that the ratio takes consistent values away from the ρ, *i.e.* just above threshold and in the 1.5-3.5 GeV range, with some variation above. To be conservative, 100% uncertainty is assigned to the normalization factor determined at threshold, which will be applied from threshold to ~ 4 GeV.

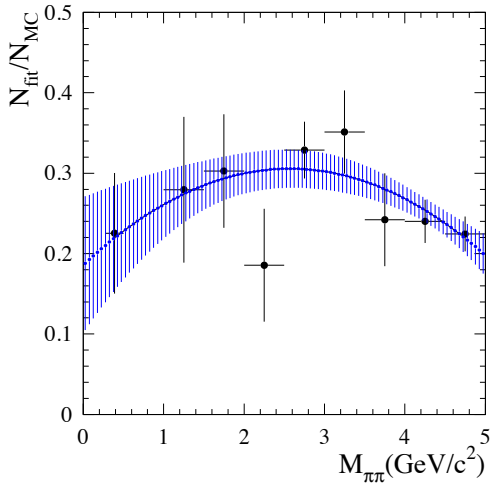

Figure 13.6: The correction factor data/MC for $'\pi\pi' \rightarrow' \pi_h\pi'$ identification for $\mu\mu\gamma$, including the luminosity factor ($\sim$0.20). The curve with the error band is a second-order polynomial fit to the data points, needed to interpolate in the ρ mass region.

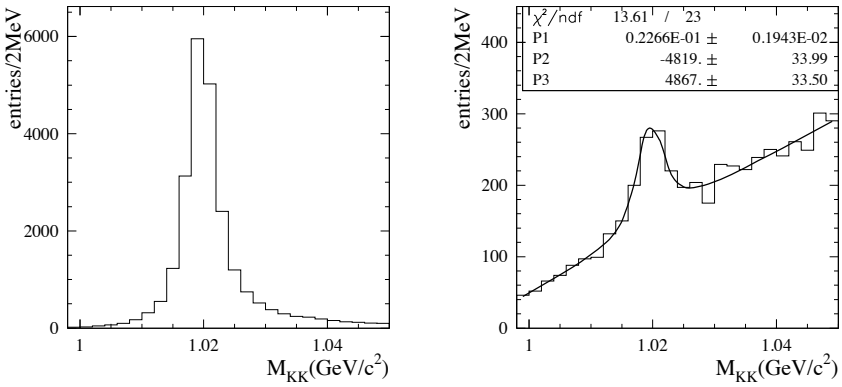

Figure 13.7: Left: the KK mass distribution for $KK\gamma$ MC in the $'\pi_h\pi'$ ID sample. Right: the KK mass distribution in the $\pi_h\pi$ ID data sample, fitted with the MC shape (left plot) and a linear component from $\pi\pi\gamma$ (including very small background contributions). The adjustment provides a direct measurement of the KK component in the data sample.

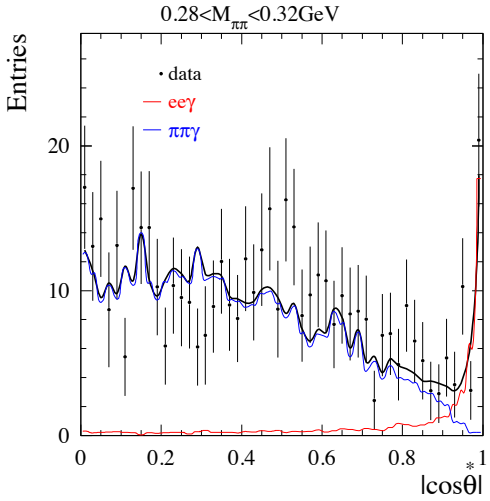

Figure 13.8: The $|\cos\theta^*|$ distribution of '$\pi_h\pi$' data in the 0.28-0.32 GeV $m_{\pi\pi}$ range, fitted (black curve) to two free components: $\pi\pi\gamma$ from MC (blue) and ee background from 'RadBhbha'-flagged events (red). The small $\mu\mu\gamma$ contribution is subtracted out.

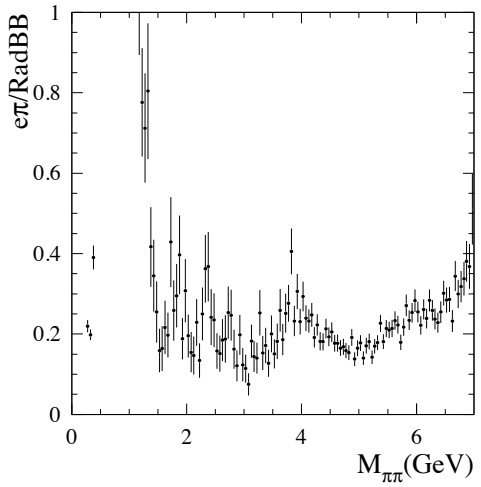

Figure 13.9: The ratio of the mass spectra of '$e\pi$' events and 'RadBhabha' sample. There is a strong contribution from mis-identified $\pi\pi$ events in the ρ region.

Table 13.1: Estimated background fractions (in %) in the '$\pi_h\pi$' sample for $m_{\pi\pi}$=0.325, 0.475, 0.975, 1.375, 1.975, and 2.975 GeV. The entries marked as '–' correspond to a negligible fraction. Processes with fractions less than 0.05% in all intervals are not listed.

process	0.325 GeV	0.475 GeV	0.975 GeV	1.375	1.975	2.975
$\mu\mu$	3.9 ± 0.5	0.8 ± 0.1	0.2 ± 0.1	1.9 ± 0.3	5.6 ± 1.0	32.5 ± 9.2
KK	4.6 ± 0.3	0.2 ± 0.1	0.1 ± 0.1	0.4 ± 0.1	0.3 ± 0.1	1.7 ± 1.3
$\gamma 2\pi\pi^0$	0.4 ± 0.2	0.3 ± 0.1	0.1 ± 0.1	–	–	–
$q\bar{q}$	0.1 ± 0.1	0.1 ± 0.1	0.3 ± 0.1	5.0 ± 2.0	0.8 ± 0.7	3.4 ± 3.9
$\gamma p\bar{p}$	0.7 ± 0.1	0.3 ± 0.1	0.4 ± 0.1	4.3 ± 0.5	8.8 ± 1.4	24.5 ± 6.8
total	9.7 ± 0.6	1.7 ± 0.2	1.1 ± 0.2	11.6 ± 2.1	15.5 ± 1.9	62.1 ± 12.2

13.3.4 Total background contribution

The different fractions of background in the $\pi\pi\gamma$ sample in the ρ tails region with '$\pi_h\pi$' ID and $\ln(\chi^2_{add.ISR} + 1) < 3$ are given in Fig. 13.10. The improvement compared to Fig. 13.1 is clear. Fractions at specified masses are listed in Table 13.1. The total background contribution is obtained by summing all the individual contributions obtained above.

13.4 Background-subtracted mass distribution

The background-subtracted $m_{\pi\pi}$ distribution of $\pi\pi\gamma$ events using '$\pi_h\pi$' identification and $\ln(\chi^2_{add.ISR} + 1) < 3$ plotted from threshold to 3 GeV in 10-MeV and 50-MeV mass bins in Fig. 13.11. A dynamic range of 10^3-10^4 is observed between the ρ peak and either the first bin above threshold or at 3 GeV. The dip structure at 1.6 GeV is confirmed with high statistics and a new structure shows up near 2.2 GeV.

13.5 $'\pi\pi' \rightarrow' \pi_h\pi'$ efficiency for $\pi\pi$ events

The efficiency of the '$\pi\pi' \rightarrow' \pi_h\pi$' identification as a function of $\pi\pi$ mass for $\pi\pi\gamma$ events can be obtained from simulation, but the correction of data over MC can only be determined in the central ρ mass region where backgrounds are small

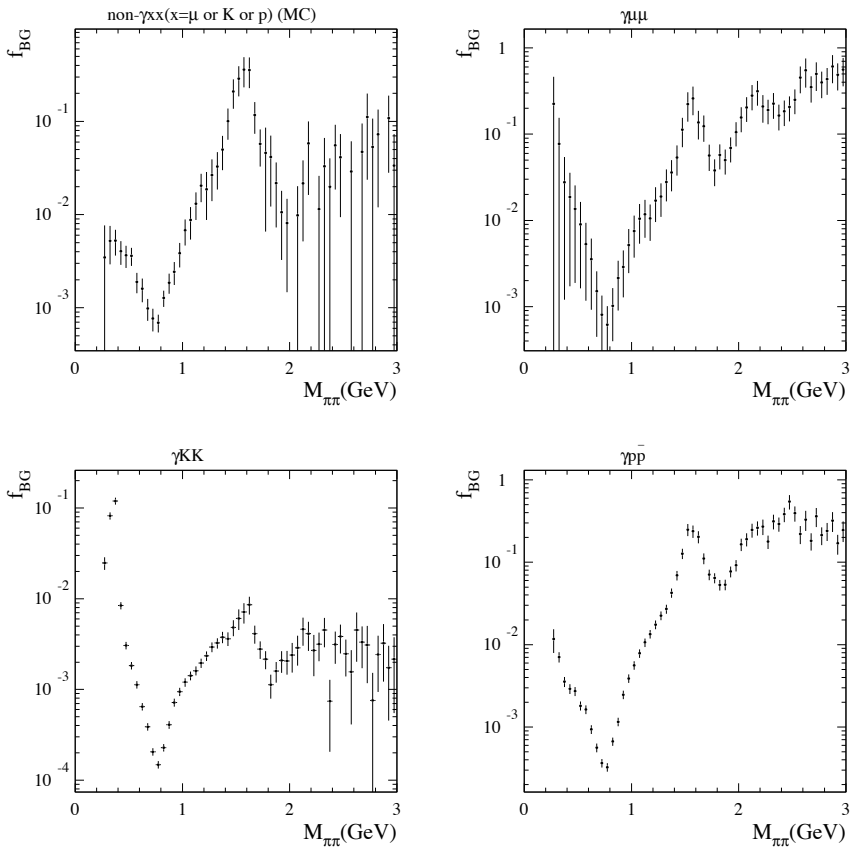

Figure 13.10: The fractions of different backgrounds in the physical sample with the tight 2D-χ^2 cut and strengthened '$\pi_h\pi$'-ID (as used in the ρ tails region) as a function of the $\pi\pi$ mass. Top left: multihadrons, including $\tau\tau$. Top right: $\mu\mu\gamma$ (data + measured mis-ID). Bottom left: $KK\gamma$ (data + measured mis-ID). Bottom right: $p\bar{p}\gamma$ (MC).

in the '$\pi\pi$' sample. Backgrounds are subtracted in the '$\pi\pi$' and '$\pi_h\pi$' samples using the measured '$\pi\pi' \to' \pi_h\pi$' identification for $\mu\mu$ events. The efficiencies for $\pi\pi\gamma$ in data and simulation are given in Fig. 13.12: it is smaller in data by about 4%. Their ratio is shown in Fig. 13.13, exhibiting no significant mass dependence between 0.4 and 1 GeV. Some drop occurs beyond 1 GeV which could be due to an imperfect representation of the large background in this region for the '$\pi\pi$' sample. A linear fit is performed for $0.6 < m_{\pi\pi} < 0.9$ GeV and extrapolated outside with error propagation.

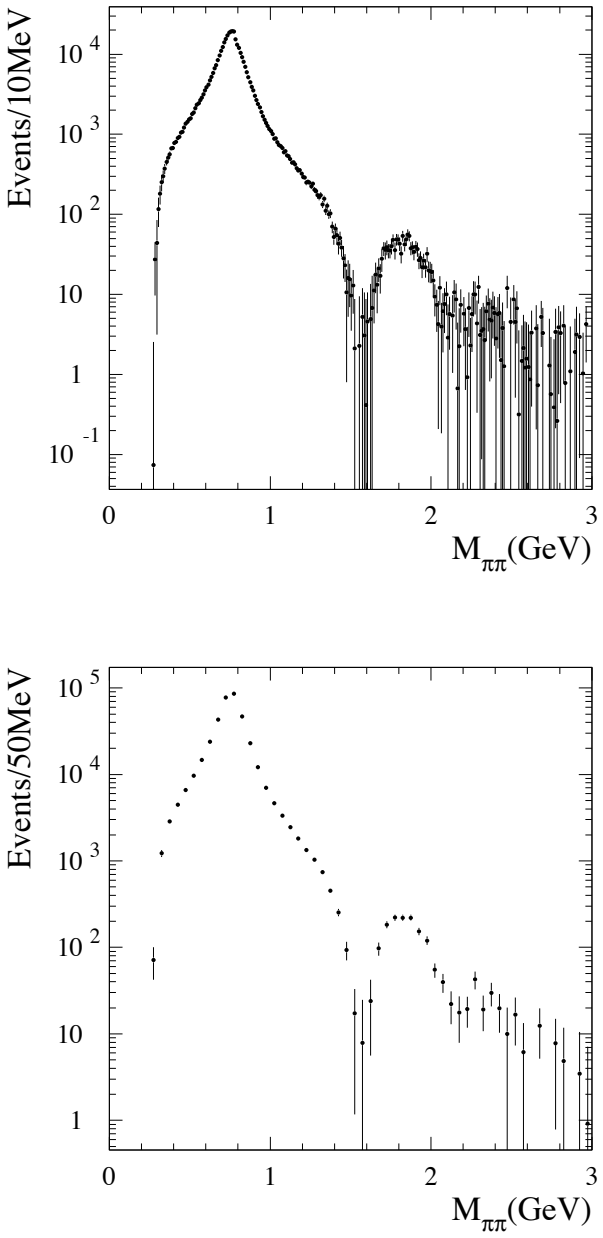

Figure 13.11: The $m_{\pi\pi}$ distribution of $\pi\pi\gamma$ events selected with '$\pi_h\pi$' identification and the tight $\ln(\chi^2_{add.ISR}+1) < 3$ cut, from threshold to 3 GeV, in 10-MeV bins (top) and 50-MeV bins (bottom).

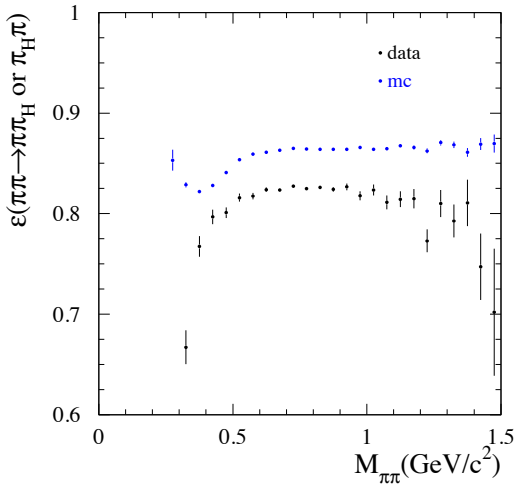

Figure 13.12: The efficiency of '$\pi_h\pi$' identification for '$\pi\pi$' identified $\pi\pi\gamma(\gamma)$events.

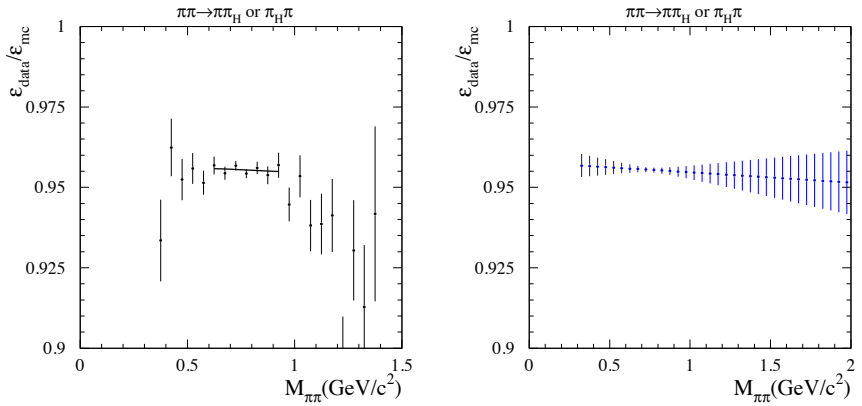

Figure 13.13: Left: The ratio of the efficiency of '$\pi_h\pi$' identification for '$\pi\pi$' identified $\pi\pi\gamma(\gamma)$events for data and MC, the line is the fitting result (p1) in ρ region. Right: The extrapolation of the ratio fitted in ρ region.

13.6 χ^2 cut efficiency

The determination of the tighter χ^2-cut efficiency follows the same procedure as described in Section 7.5 for the loose χ^2 cut used in the central region.

The starting point is a re-evaluation of the efficiency for $\mu\mu\gamma$ events under the new χ^2-cut. The result is shown in Fig. 13.14.

As for the central region a correction for FSR is applied, but it is now larger, $(1.9 \pm 0.8) \times 10^{-3}$, since all the FSR events are lost with the tight χ^2 cut.

Using the same approach as for the loose χ^2 conditions, the effect of secondary interactions is estimated by taking the difference in simulation between the $\pi\pi\gamma$ and $\mu\mu\gamma$ χ^2-cut efficiencies. The result is shown in Fig. 13.15. The data/MC correction on the level of secondary interactions follows the results already presented in Section 7.5.4, giving a bias of $(7.1 \pm 0.4) \times 10^{-3}$.

Adding the contributions from FSR and secondary interactions, the total correction on the tight χ^2-cut efficiency amounts to $(9.0 \pm 0.9) \times 10^{-3}$.

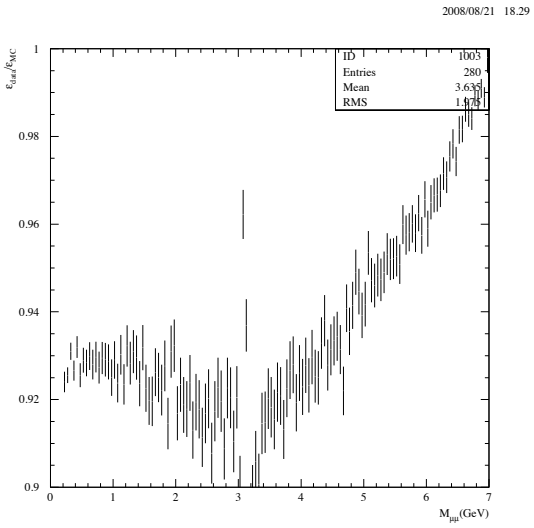

Figure 13.14: The correction for the difference between data and MC on the efficiency of $\ln(\chi^2_{add.ISR} + 1) < 3$ cut, which is determined in $\mu\mu\gamma(\gamma)$ data.

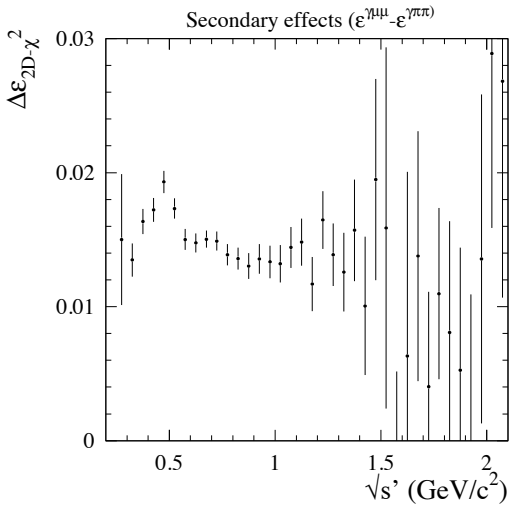

Figure 13.15: The effect of secondary interactions on the χ^2-cut efficiency (tight cut) estimated from $\mu\mu\gamma(\gamma)$ and $\pi\pi\gamma(\gamma)$ simulation using Eq. (7.4), as function of $\sqrt{s'} = m_{\pi\pi(\gamma_{FSR})}$.

Chapter 14

Summary of Checks Performed before Unblinding and of Corrections

This section summarizes all the important tests we have required to be passed before unblinding the absolute $e^+e^- \to \pi^+\pi^+(\gamma_{FSR})$ cross section. They involve checks performed separately on the measured $\pi\pi\gamma$ and $\mu\mu\gamma$ samples, using their respective efficiencies and background subtractions.

14.1 Global PID test

In Section 6.2.4 a global consistency check of the PID procedure was performed: all the different ID topologies for the 2-track events have been checked to be consistent with the determined $\pi\pi$, KK, $\mu\mu$ mass spectra, the ee background determination and the measured ID efficiencies. Agreement was found within the estimated systematic uncertainties.

This is a very important test as the 2-body ISR processes we measure are identified exclusively by PID. The test is possible because all selected 2-track (and one photon) events are classified using a complete and orthogonal set of ID conditions.

14.2 Test of PID correction using the $\pi\pi$ mass distribution

All the determination of PID efficiencies come from tagged particle samples. A global test of the correction applied to the '$\pi\pi$' mass spectrum to obtain the produced spectrum can be done by fitting the $\pi\pi$ line shape in the mass spectrum before particle identification. In practice '$\mu\mu$'- identified events are removed in order to bring the background to a tolerable level. The corresponding loss of $\pi\pi$ events is small, 2×10^{-3} from our PID studies in the 0.6-0.9 mass range used for the fit, and corrected. The background (dominated by $\mu\mu$ events) is fitted

with a second-order polynomial, while the signal is taken from the '$\pi\pi$' spectrum. The PID efficiency for the cross section is then obtained, as the ratio between the numbers of '$\pi\pi$' and fitted signal events in the full spectrum. Fits are made separately for runs 1-2 and 3-4 since the correction factors are markedly different. The results,

$$\begin{aligned} \varepsilon_{\pi\pi}^{fit\ 1-2} &= 0.7782 \pm 0.0039, \\ \varepsilon_{\pi\pi}^{fit\ 3-4} &= 0.7491 \pm 0.0029, \end{aligned} \tag{14.1}$$

can be compared to the factors actually used and obtained in the track PID studies, with quoted systematic uncertainties,

$$\begin{aligned} \varepsilon_{\pi\pi}^{PID\ 1-2} &= 0.7782 \pm 0.0023, \\ \varepsilon_{\pi\pi}^{PID\ 1-2} &= 0.7530 \pm 0.0022. \end{aligned} \tag{14.2}$$

The results are in good agreement.

14.3 $\mu\mu(\gamma)$ absolute cross section compared to QED

As described in Section 10.5, the absolute cross section for $e^+e^- \to \mu^+\mu^+(\gamma_{FSR})$ has been obtained for runs 1-2 and 3-4 independently and compared to NLO QED. This comparison involves quantities which are not required in the pion analysis, as they cancel in the $\pi\pi$ to $\mu\mu$ ratio, or in the absolute pion cross section obtained with the effective ISR luminosity measured with the muons. This is the case for the *BABAR* ee luminosity and the efficiency of the ISR photon, which contribute in fact the major part of the uncertainty in the comparison: 1.0% compared to 0.44% for the muon errors contributing to the R ratio.

The results are in agreement with QED within 1.1% and consistent between runs 1-2 and 3-4. This latter conclusion shows that the different detector conditions, particularly regarding the IFR performance, have been properly treated.

14.4 Check of known distributions

Distributions in the $\mu\mu\gamma$ channel have been successfully compared to the corresponding AfkQED distributions (QED) (see Section 9.1).

In the pion channel only the angular distribution in the $\pi\pi$ center-of-mass is model-independent. Data are in very good agreement with the simulation, and therefore with the $\sin^2\theta^*_\pi$ dependence expected for a pair of spin-0 particles (Section 9.2).

14.5 Understanding of additional radiation

At the level of a few per mil accuracy, the NLO effects should be carefully taken into account. The event selection method relies on kinematic fits including the emission of one extra photon, either along the beams (additional ISR) or in the detector range (additional FSR or large-angle ISR). Both extra ISR and FSR have been directly compared in data and simulation, and understood (Sections 7.4.1 and 7.4.2). The shortcomings of AfkQed regarding additional ISR and the consequences on the event acceptance have been studied using the NLO QED Phokhara generator both for muons and pions. However these effects cancel in the ratio.

In past experiments with pions additional FSR was usually dealt with at simulation level only. Here we have provided a measurement of extra FSR which has been found to agree with enough accuracy with the bremsstrahlung model of point-like charged pions (PHOTOS) used in AfkQed.

14.6 Consistency between different runs

An additional consistency check of the analysis is the comparison of the mass spectra for the two data-taking periods of runs 1-2 and 3-4. They correspond to different detector conditions, mostly because of the IFR performance, which plays the major role in the π/μ separation. Major efficiencies have been measured separately for these two periods.

Fig. 14.1 shows the ratio of the efficiency-corrected $\pi\pi$ mass spectra for runs 1-2 and 3-4. The spectra are compatible within statistical and uncommon systematic uncertainties and their ratio is consistent with a flat distribution. This comparison is made both in 2- and 50-MeV bins.

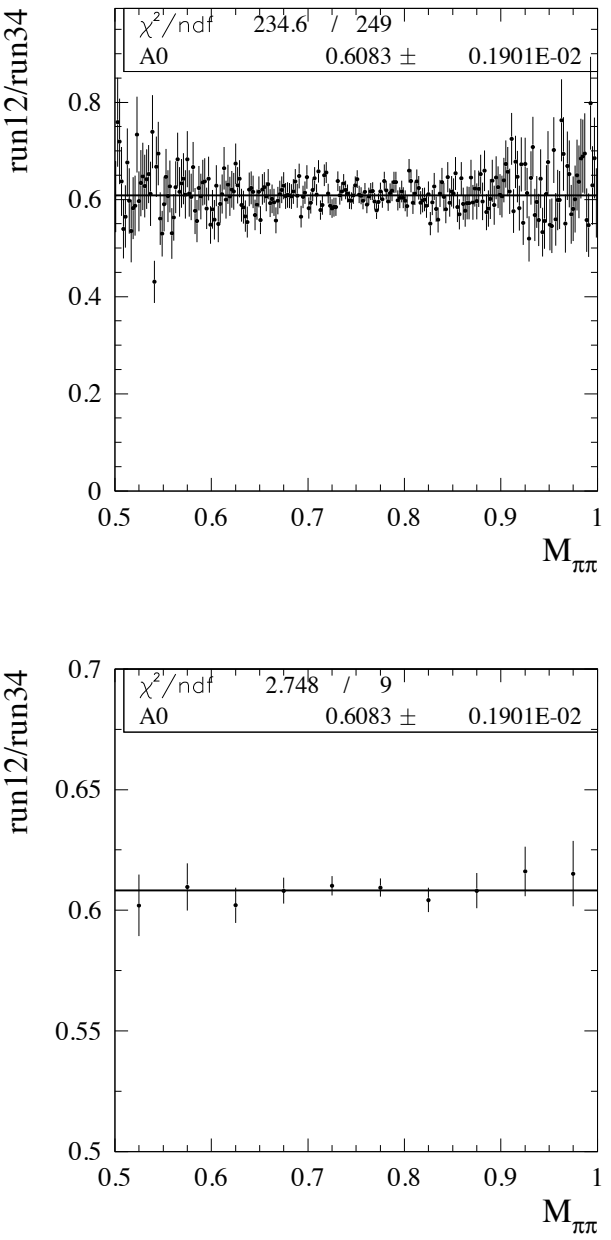

Figure 14.1: The ratio of the $m_{\pi\pi}$ spectra in the central ρ region for runs 1-2 over runs 3-4, both corrected for efficiencies and acceptance, and background-subtracted. Top: 2-MeV mass bins. Bottom: 50-MeV mass bins. The ratio is flat over the full mass range within the statistical errors.

The ratio of the corrected $\pi\pi$ spectra provides another measurement of the ratio for runs 1-2 and 3-4 of the product of the luminosity and the ISR photon efficiency:

$$\left(\frac{L_{ee}^{1-2}\varepsilon_\gamma^{1-2}}{L_{ee}^{3-4}\varepsilon_\gamma^{3-4}}\right)_{\pi\pi} = 0.6083 \pm 0.0019 \pm 0.0014 \tag{14.3}$$

where the first error is statistical and the second from uncorrelated systematics. This ratio is consistent with the similar result found in the $\mu\mu\gamma$ analysis, for masses between 0.5 and 3 GeV:

$$\left(\frac{L_{ee}^{1-2}\varepsilon_\gamma^{1-2}}{L_{ee}^{3-4}\varepsilon_\gamma^{3-4}}\right)_{\mu\mu} = 0.6088 \pm 0.0039 \pm 0.0028\,. \tag{14.4}$$

The ratio of ratios is

$$\frac{\left(\frac{L_{ee}^{1-2}}{L_{ee}^{3-4}}\right)_{\pi\pi}}{\left(\frac{L_{ee}^{1-2}}{L_{ee}^{3-4}}\right)_{\mu\mu}} = 0.9992 \pm 0.0071 \pm 0.0051 \tag{14.5}$$

is consistent with one within 0.87%. This number can be compared with the differences of data/MC corrections between runs 1-2 and 3-4 of 2.5% for pions and 3.4% for muons.

Since the two values are consistent, they can be averaged to provide the best luminosity×ISR photon efficiency 1-2/3-4 ratio (dominated by the pion result)

$$\left(\frac{L_{ee}^{1-2}\varepsilon_\gamma^{1-2}}{L_{ee}^{3-4}\varepsilon_\gamma^{3-4}}\right)_{\pi\pi+\mu\mu} = 0.6084 \pm 0.0021 \tag{14.6}$$

This value can be compared to the similar ratio using the standard BaBar luminosity determination. From the lumi script, one gets $(L_{ee}^{1-2}/L_{ee}^{3-4}) = 0.6040$, with an uncertainty which is not readily available. From the information given in Refs. [39] and [40], one can obtain the statistical part of the uncertainty for each run giving 0.0013, but for systematics it is less clear. One can assume that the experimental uncertainty is mostly correlated, as well as the theoretical uncertainties on the QED cross sections, of course. An overall uncertainty of 0.5% on the block 1-3 and 0.2% on 4-5 is given to cover time dependence of the cuts used. Therefore one can expect (and they see) more variation between each runs and

we (tentatively) take a value of 0.7% for the ratio 1-2/3-4, giving an uncertainty of 0.0042 on the ratio.

The ratio of ISR photon efficiencies in runs 1-2 and 3-4 has a dominant statistical part from the measurement [38] and an additional systematic error since run 1 was not included in their analysis. An estimate of the uncertainty from these sources on the luminosity ratio is $(2.2 \oplus 2.5)\ 10^{-3}$.

Thus the relative difference between the result given in Eq. (14.6) and the ratio of the standard BaBar luminosity values is $(7.3 \pm 6.4_{ISR} \pm 7.0_{BaBar\ lumi}\ [9.5_{tot}]) \times 10^{-3}$ and is consistent with 0 within the estimated uncertainty.

14.7 Summary of corrections to the $\pi\pi$ mass spectrum

Fig. 14.2 gives the total efficiency of the $\pi\pi\gamma$ event selection as computed with the simulation based on AfkQed. The reference sample is generated for ISR photon polar angle between 20° and 160° in the e^+e^- CM frame. There is a marked difference between runs 1-2 and 3-4 because of the specifically defined active areas of the IFR and mostly because of the track overlap cut in the IFR applied in runs 1-2 only, which affects the lower part of the mass spectrum. The total efficiency is shown separately for the 'in ρ' (central mass region)and 'out ρ' (tails) conditions (i.e. 'in ρ' condition: loose χ^2-cut, normal $\pi\pi$-ID; 'out ρ' condition: tight χ^2-cut, $\pi_h\pi$-ID, V_{xy}-cut).

A summary of the full data/MC corrections to runs 1-2 and 3-4 is shown in Fig. 14.3. Again significant differences are seen between the two data periods which again reflect the behaviour of the IFR, as measured in the analysis. The corrections are larger for the 'out ρ', with its much tighter χ^2 cut, because of the lack of angular distribution for additional ISR in AfkQed. This effect cancels in the $\pi\pi$ to $\mu\mu$ ratio, *i.e.* in the measured $\pi\pi$ cross section. The total data/MC correction on the $\pi\pi$ cross section is given in Fig. 14.4.

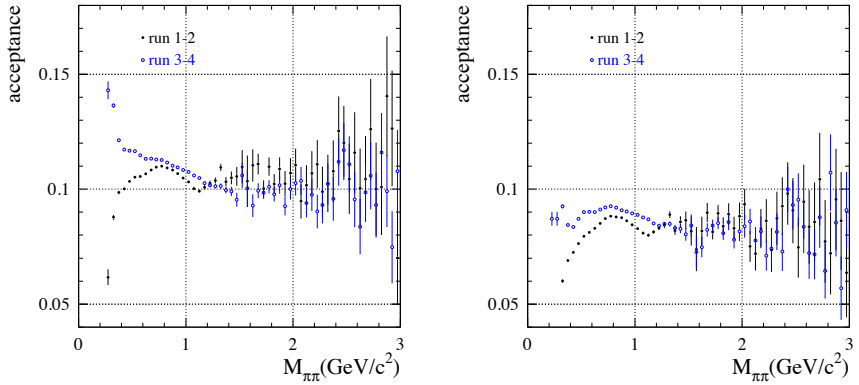

Figure 14.2: The full MC efficiency for pions as a function of $m_{\pi\pi}$ for runs 1-2 and 3-4. Left: central-region conditions. Right: tails-region conditions.

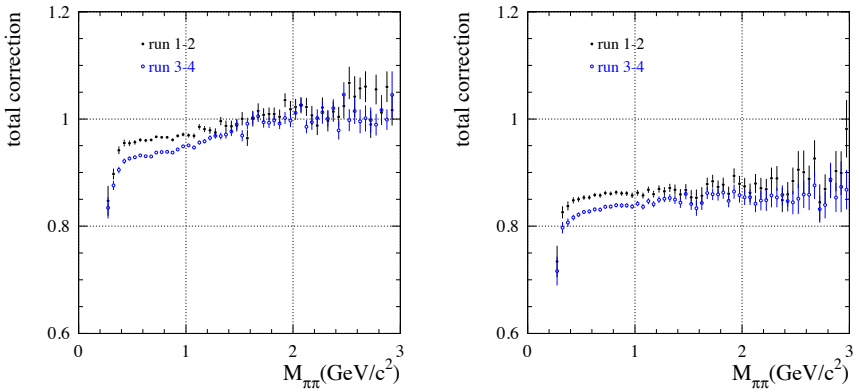

Figure 14.3: The total data/MC efficiency correction for pions as a function of $m_{\pi\pi}$ for runs 1-2 and 3-4. Left: central-region conditions. Right: tails-region conditions.

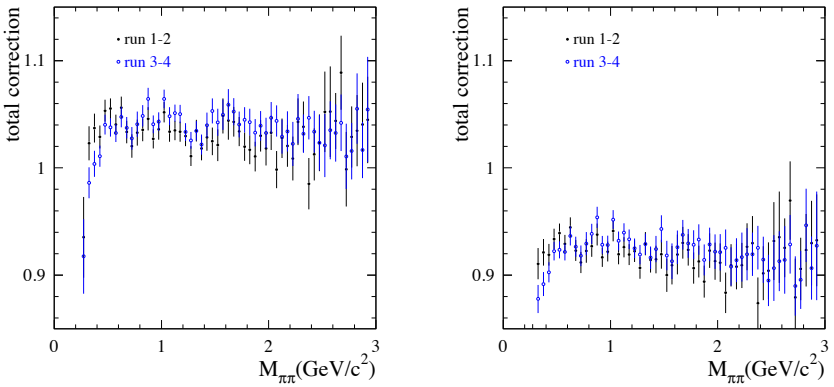

Figure 14.4: The total data/MC efficiency correction for the $\pi\pi$ cross section as a function of $m_{\pi\pi}$ for runs 1-2 and 3-4. Left: central-region conditions. Right: tails-region conditions.

Chapter 15

Unfolding the mass spectrum

15.1 Procedure

The distribution of the fitted $\pi\pi$ mass is altered by several effects: reconstruction, resolution, kinematic fit, FSR, all resulting in transfer of events between different mass regions. All these effects are included in the MC simulation of the detector response, but it needs to be corrected to take into account differences between data and MC.

The following procedure is used:

- the data spectrum of the fitted mass $m_{\pi\pi}$ is subtracted for backgrounds and the data/MC corrections for efficiencies are applied;
- the mass-transfer matrix records the probability that an event generated in a $\sqrt{s'}$ bin i is reconstructed in a $m_{\pi\pi}$ bin j. It is obtained from the simulation and corrected for differences with data;
- the unfolding procedure is applied to the $m_{\pi\pi}$ spectrum, yielding the $\sqrt{s'}$ spectrum;
- the overall acceptance correction from the simulation is applied;
- systematic tests of the unfolding procedure are performed.

15.2 The unfolding method

The unfolding technique used is a simplified version of a method developed for more complex unfolding problems [43]. It is based on the idea that if the MC describes relatively well the data and the folding probabilities [1] are well simulated,

[1] The folding probability is the probability of an event generated in a true bin j to be reconstructed in a bin i. It can be computed directly from the transfer matrix: $P_{ij} = A_{ij} / \sum_{k=1}^{N} A_{kj}$.

one can use the transfer matrix to compute a matrix of unfolding probabilities [2]. In this unfolding method, the data-reconstructed MC difference is corrected for the previously mentioned transfers of events. The corrected difference is added to the true MC yielding the unfolded spectrum. By doing this we benefit from the fact that passing from the reconstructed to the true MC, automatically provides the main correction of the spectrum. A regularization function is used to discriminate between real significant deviations and statistical fluctuations. The significant deviations are more likely to be unfolded, whereas the ones which seem to be due to statistical fluctuations are kept with a larger probability in their original respective bins.

If the first condition is not fulfilled, several steps are considered where the transfer matrix is improved by re-weighting the true MC, keeping the folding probabilities (related to the detector response) unchanged. Usually such iterative methods could be sensitive to statistical fluctuations which can be interpreted as true differences between data and MC distributions. In this case, the stability of the method is provided in part by the use of the regularization function, to avoid unfolding large fluctuations in the data (which could be due for example to a large background subtraction), which could significantly bias the final result. Details on the method are given in Ref. [43].

15.3 Implementation

The same energy range 0-3 GeV is chosen for data and the MC transfer matrix. The $'\pi\pi'$ (central ρ region) and $'\pi_h\pi'$ (ρ tails) spectra are unfolded separately over the full mass range, and the unfolded spectra are combined afterwards, each being used in its respective mass region. Different bin sizes are used: 10 MeV for the 'tails' condition (300×300 matrix) and 2 MeV for the 'central' condition (1500×1500 matrix). The method delivers the unfolded distribution in the same mass bins as for the input spectrum, and a covariance matrix containing the statistical correlations between the bin contents. The covariance matrix is

[2] The matrix of unfolding probabilities indicates which is the probability for an event reconstructed in a bin i to originate from the 'true' bin j. It can is computed from the (improved) transfer matrix: $P'_{ij} = A_{ij} / \sum_{k=1}^{N} A_{ik}$

obtained with toy simulations, where both the data and the transfer matrix are statistically fluctuated. The significant covariance matrix elements lie near the diagonal over a width of typically 6-8 MeV for 2 MeV bins, corresponding to the mass resolution of 6 MeV. Thus the diagonal element alone yields a statistical uncertainty in a given bin which is roughly a factor of two smaller than the original error. As a result of the unfolding, and by the transfer of events mainly from neighbouring bins, the mass spectrum becomes smoother.

Fig. 15.1 shows the initial mass-transfer matrix from the simulation using in the AfkQed generator a model of the pion form factor. It is seen that the matrix is reasonably diagonal, with small tails from resolution effects and FSR.

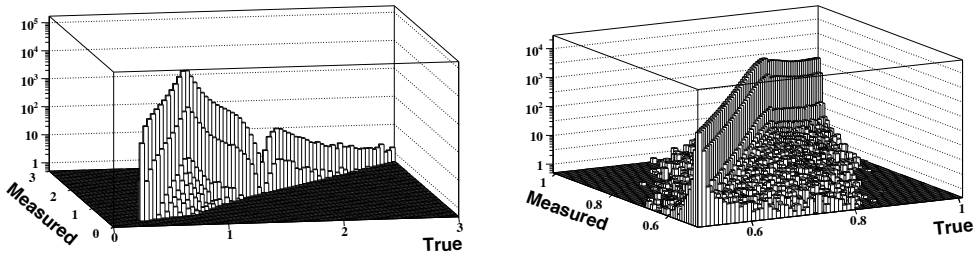

Figure 15.1: The initial mass-transfer matrix from the simulation giving the number of events generated with a (true) mass $\sqrt{s'}$ in a bin i and reconstructed with a (measured) mass $m_{\mu\mu}$ in a bin j, both masses in GeV. The $\sqrt{s'}$ dependence comes from a model of the pion form factor used in the generator. Left: outside ρ conditions. Right: central ρ conditions (the full mass matrix is used in the unfolding, but only the range 0.5-1.0 GeV is shown).

As seen in Fig. 15.2 (top plot) the most significant data − reconstructed MC difference in relative terms corresponds to the region 1.7-2 GeV, where the pion form factor is not well simulated. This difference is much larger than the data statistical errors in this region. Some other smaller differences are observed in the ρ lineshape, but not exceeding the statistical errors. This is also true in the $\rho - \omega$ interference region where a bipolar glitch is observed. These differences can be corrected in an iterative way, but it is observed that already at the first step the difference is reduced to a negligible level.

In fact these systematic differences have no effect on the result of the unfolding, as proven in Fig. 15.2 (bottom plot). The first unfolding result is very close to the initial data (well within the statistical error), except in the $\rho - \omega$ interference region, as expected since the interference pattern which is controlled by the ω width (8.4 MeV) is comparable to the mass resolution. Adding one iteration in the unfolding does not show any further improvement.

15.4 Systematic uncertainty from the mass-matrix

The resolutions effects are relatively small, except in the $\rho - \omega$ interference region. However, events in the intermediate χ^2 region have longer resolution tails which need systematic corrections. These tails are mostly due to bad additional-ISR fits and to a lesser extent to secondary interactions. We know from the χ^2 efficiency studies that additional ISR in AfkQed is only generated along the beams, unlike in data. Thus there are much more data events in the $\chi^2_{add.ISR}$ tail than MC. This effect has been studied in detail with muon pairs.Therefore MC events in the intermediate χ^2 region with $\chi^2_{add.ISR} < \chi^2_{add.FSR}$ are re-weighted in constructing the mass-transfer matrix.

Fig. 15.3 shows the correction factor applied for these events, as a function of mass, and the relative effect on the unfolding result (result after correction/result before correction - 1). Taking into account the precision of the correction, we get a systematic uncertainty from the mass-matrix smaller than 0.1%. The uncertainty on the a_μ integral coming from this effect is even smaller due to anti-correlations in the unfolded spectrum.

The effect due to secondary interactions is estimated to be one order of magnitude smaller and consequently ignored.

15.5 Tests of the unfolding technique

A direct test of the unfolding procedure has been performed, investigating potential systematic biases introduced by the method. The test uses toy distributions of true and reconstructed data, the latter produced with a transfer matrix A identical to the real one. The toy reconstructed data are then unfolded with

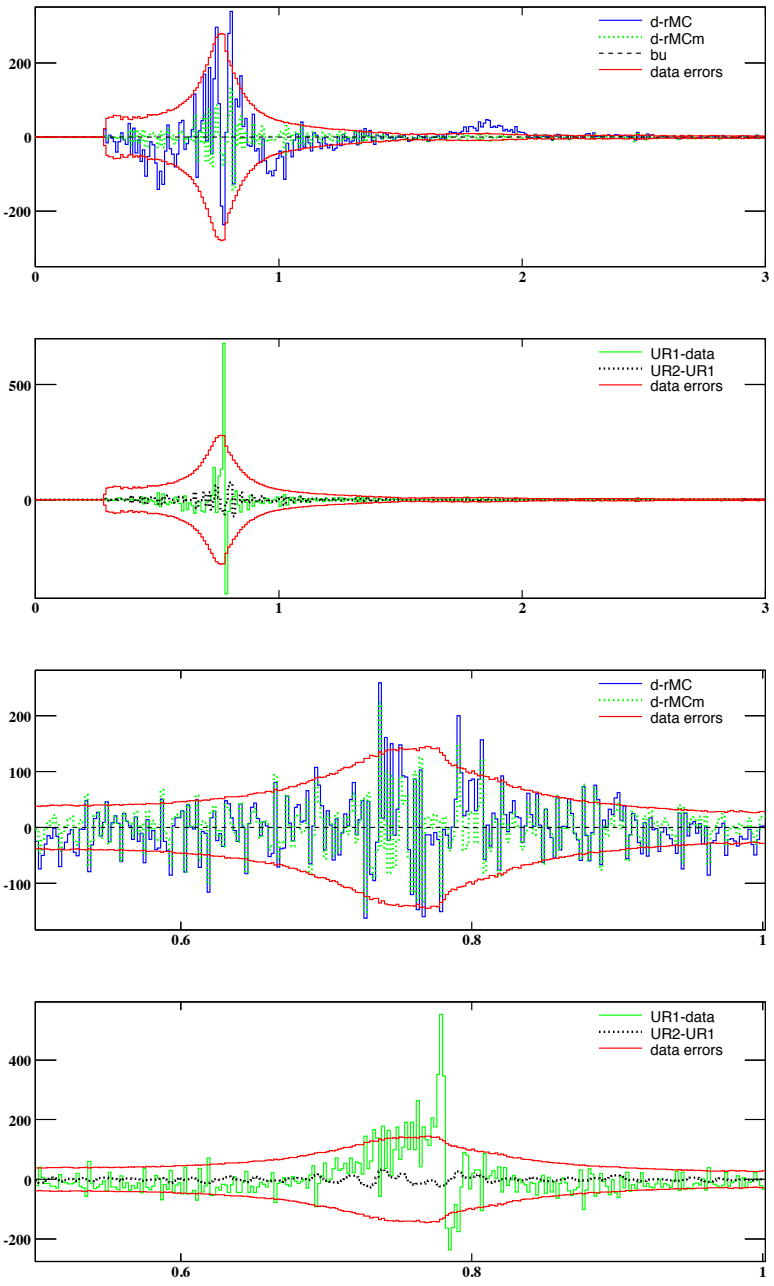

Figure 15.2: From top to bottom: (1) The difference between the mass distributions (outside ρ conditions) of data and reconstructed MC at the first step (d-rMC) and after one iteration (d-rMCm). The data statistical errors ($\pm$ data errors) are shown for comparison. (2) The difference between the result of the first unfolding (UR1) and the initial data exceeds the data statistical error only in the $\rho - \omega$ interference region. No significant improvement is observed between the first (UR1) and second (UR2) unfolding results. (3) and (4) Same plots for the central ρ conditions with longer resolution tails. (x-axis: mass in GeV, y-axis: number of events)

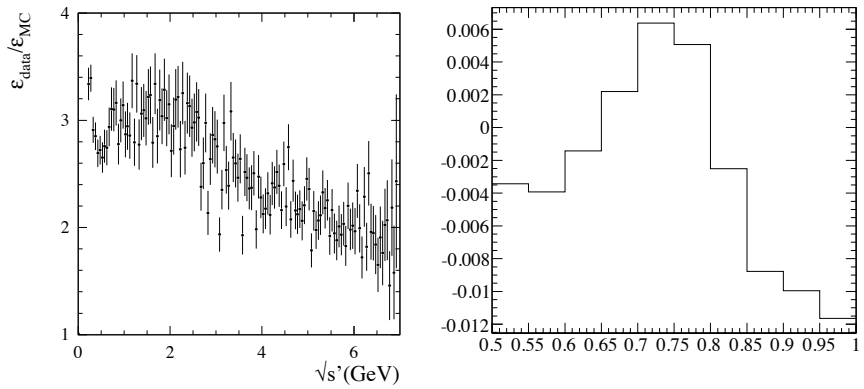

Figure 15.3: Re-weighting factor of the MC events in the intermediate χ^2 region due to bad simulation of additional ISR (left). Total relative effect of the mass-transfer matrix correction on the unfolded spectrum (right).

a transfer matrix (A') obtained after statistically fluctuating A. The unfolding result is then compared to the true toy data.

The true data distribution is constructed from the true MC with a bias added. In order to build a test as close as possible to the real situation, the bias is taken as the difference between data and the normalized initial reconstructed MC. Two variations of the test have been considered, where the reconstructed data are additionally fluctuated statistically or not. The first situation is closer to the real unfolding operation and could reveal spurious effects due to the limited statistics in the data (and MC). The second test allows one to more easily search for potential systematic effects of the method.

The results of the tests are given in Fig. 15.4. No systematic bias is observed already in the first step, and also after one iteration. This result still stands after additional fluctuation of the input data. By averaging over wider bins to reduce statistical fluctuations we find that the systematic bias from the unfolding technique is below the 10^{-3} level.

Combining the effects from the knowledge of the transfer matrix and the robustness of the unfolding technique, the total systematic uncertainty of the unfolding procedure is estimated to be 1.0×10^{-3}.

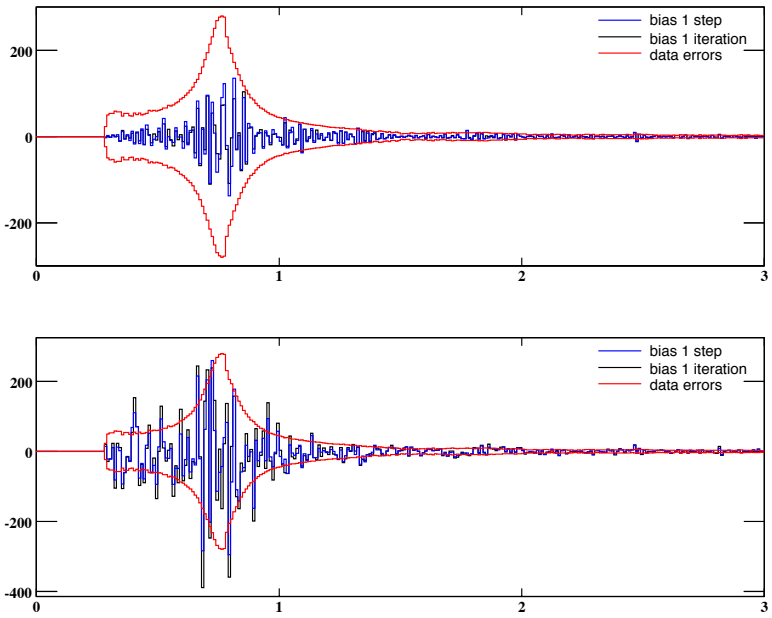

Figure 15.4: Systematic test of the unfolding technique using toy data obtained from the MC distribution distorted by a known bias (outside ρ conditions). The plots show the difference with the true data of the first unfolding result and the result after one iteration step. These values are compared to the statistical data errors. For the top plot there were no data fluctuations, whereas statistical fluctuations were introduced for the bottom plot.

The spectra of corrected $\pi\pi\gamma$ events are compared in Fig. 15.5 before and after unfolding. The main change is in the $\rho-\omega$ interference region, but a closer observation, the relative differences in Fig. 15.6 reveals also the correcting effect of resolution tails. It amounts to about 3% at 0.5 GeV and 2% at 1.0 GeV for the loose χ^2 cut. If the tighter χ^2 cut is used instead ($\ln(\chi^2_{add.ISR}+1) < 3.$), the unfolding correction is significantly reduced ($\sim$1%) in the tails, corresponding to a better mass resolution due to the removal of most secondary interactions and effects from a bad reconstruction.

15.6 Consistency check with tight and loose χ^2 selection

The loose χ^2-cut (defined in Section 3.2) is used in the ρ central region, while the tight one is used in the tails where backgrounds are larger. However

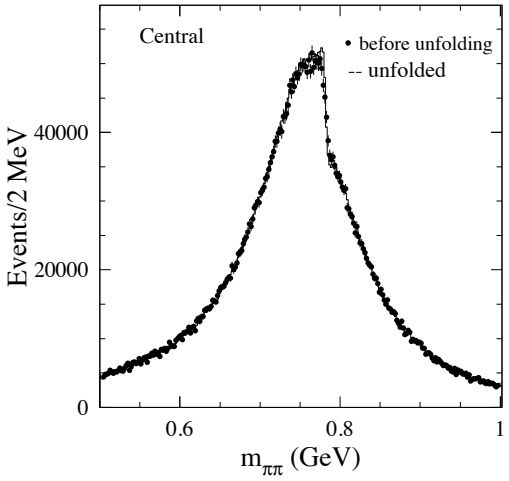

Figure 15.5: The comparison of the mass distributions before ($m_{\pi\pi}$ in GeV) and after ($\sqrt{s'}$ in GeV) unfolding for the 'ρ central' conditions (loose χ^2).

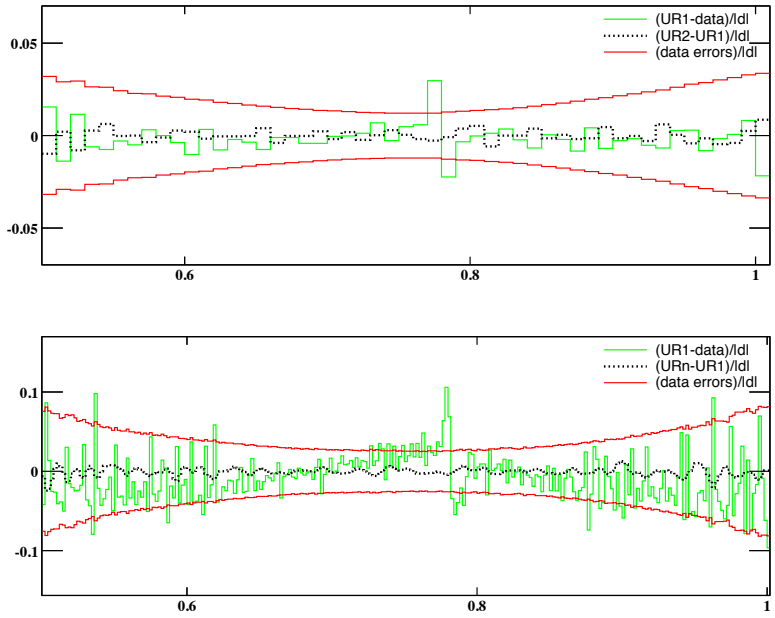

Figure 15.6: The relative difference of the mass distributions before ($m_{\pi\pi}$ in GeV) and after ($\sqrt{s'}$ in GeV) unfolding for the 'ρ central' conditions, but imposing either the tight (top), or the loose (bottom) χ^2 cut. The unfolding of the increased resolution tails is verified in the latter case.

it is possible to compare the results obtained with both methods in the central region. This provides a test of the χ^2-cut efficiency and of the multi-hadronic background. It is also sensitive to the unfolding, as the mass resolutions are different in the different 2D-χ^2 regions. In order to keep the test at these levels only, the same $'\pi\pi'$-ID is used for both, namely the $'\pi_h\pi'$-ID and the V_{xy}-cut are removed for the tight χ^2 condition.

The result of the test, expressed as the ratio of the corrected and unfolded spectra for loose/tight, is shown in Fig. 15.7. The ratio is consistent with 1 for the full central mass range, 0.5-1.0 GeV within errors, being equal to 0.9982 ± 0.0049 with a χ^2/DF of 50.49/49, and within the estimated systematic uncertainties for the χ^2-cut efficiencies.

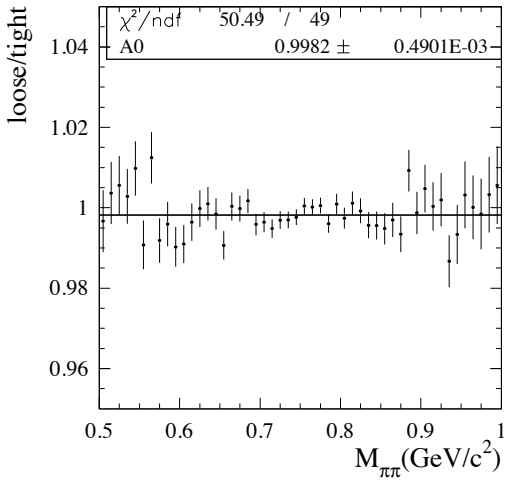

Figure 15.7: The ratio of the corrected and unfolded mass spectra for loose over tight 2D-χ^2 cuts in the central ρ region.

Chapter 16

Results on the $e^+e^- \to \pi^+\pi^-(\gamma)$ Cross Section

16.1 Effective ISR luminosity and uncertainty

The effective ISR luminosity as a function of $\sqrt{s'}$ is taken from the $\mu\mu\gamma$ analysis (Section 11.4). For convenience we consider in 50-MeV bins the ratio between the measured luminosity and the product of the lowest-order QED luminosity function $\times$ the vacuum polarization correction (see Eq. 11.6).

In this way the detailed local features of the vacuum polarization (fast variations around the ω and ϕ resonances) are incorporated, while preserving the measured effective luminosity as a function of mass. The chosen bin size is small enough that we do not expect any unaccounted-for systematic trend on that scale. The 50-MeV bin procedure leads to a full correlation of the luminosity errors in the 25 2-MeV bins used for the $\pi\pi$ cross section. This effect is included in the full covariance matrix used for the computation of the dispersion integral. We have explicitly checked that the statistical error on the integral does not depend on the chosen bin size, from 50 down to 2 MeV.

Fig. 16.1 shows the effective luminosity ratio in 50-MeV bins.

The statistical errors on the ISR effective luminosity from the measurement of efficiencies are included in the statistical point-to-point uncertainties, while the systematic errors from the different procedures are accounted for separately as systematic uncertainties. These errors are 1.3×10^{-3} for tracking, 2.9×10^{-3} for μ-ID, and 2.0×10^{-3} for acceptance, for a total systematic uncertainty of 3.8×10^{-3}. The f_2 uncertainty (correlated loss of μ-ID for both tracks) is not included here, since it is anticorrelated with the pion rate. It is counted in the $\pi\pi$ systematic errors.

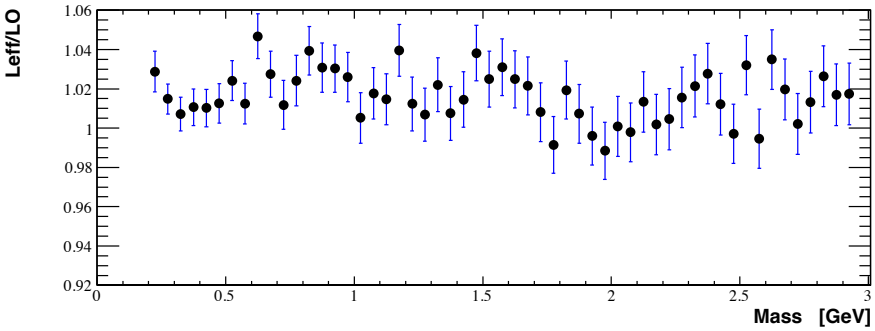

Figure 16.1: The ratio between the effective ISR luminosity measured with the $\mu\mu\gamma$ sample and the lowest-order QED prediction including vacuum polarization, as a function of $\sqrt{s'}$ for runs 1-4.

16.2 Summary of systematic uncertainties for the $\pi\pi$ sample

Here we summarize all systematic uncertainties affecting the $\pi\pi$ sample in different mass regions. The statistical errors of the measured efficiencies are included with the main statistical uncertainty on the $\pi\pi$ mass spectrum. However, in some cases, remaining systematic uncertainties are attached to the efficiency measurement process. The results on all systematic uncertainties are listed in Table 16.1. For those cases where no systematic error is quoted, all uncertainties proceed from measurements and are included in the point-to-point statistical errors.

The overall relative systematic uncertainty on the $\pi\pi(\gamma_{FSR})$ cross section is 5.4×10^{-3} in the 0.6-0.9 GeV mass range, but significantly larger below and above the central region.

16.3 The Born cross section with additional FSR

The results for the $e^+e^- \to \pi^+\pi^-(\gamma)$ bare cross section including FSR, $\sigma^0_{\pi\pi(\gamma)}$, are given after unfolding in Figs. 16.2, 16.3, 16.4.

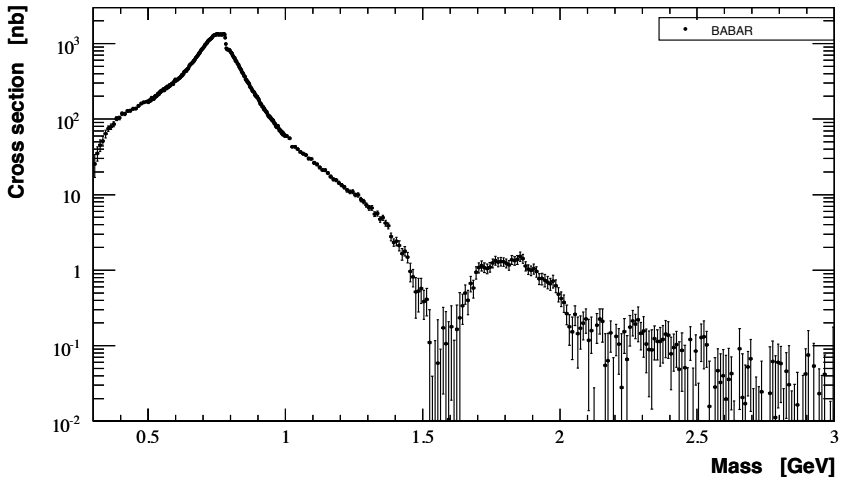

Figure 16.2: The measured cross section for $e^+e^- \to \pi^+\pi^-(\gamma)$ over the full mass range. Systematic and statistical uncertainties are shown, but only the diagonal elements of the covariance matrix.

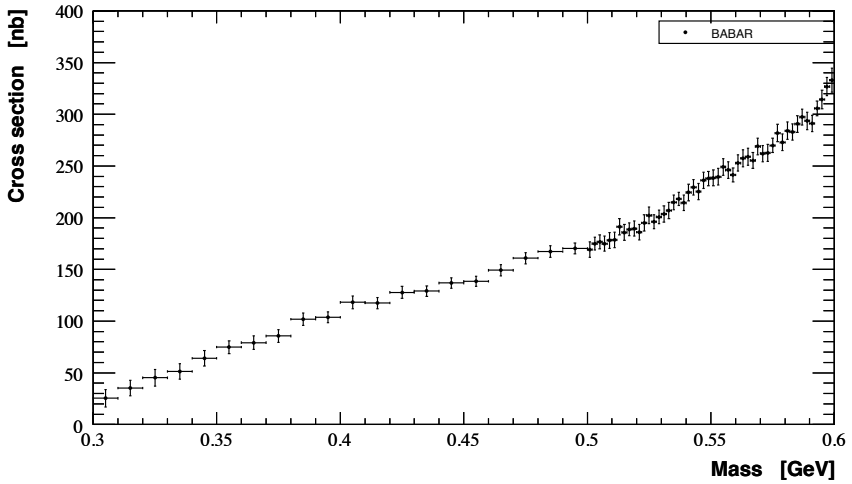

Figure 16.3: The measured cross section for $e^+e^- \to \pi^+\pi^-(\gamma)$ in the lower mass range. Systematic and statistical uncertainties are shown, but only the diagonal elements of the covariance matrix.

Table 16.1: Systematic uncertainties (in 10^{-3}) on the cross section for $e^+e^- \to \pi\pi(\gamma_{FSR})$ from the determination of the various efficiencies in different $\pi\pi$ mass ranges (in GeV) for runs 1-4. The statistical part of the efficiency measurements is included in the total statistical error in each mass bin. The last line gives the total systematic uncertainty on the $\pi\pi$ cross section, including the systematic error on the ISR luminosity from muons.

sources	< 0.4	0.4–0.6	0.6–0.9	0.9–1.2	1.2–1.4	1.4–3.0
trigger/ filter	1.5	1.5	0.8	0.5	0.5	0.5
tracking	3.8	2.1	1.1	1.7	3.1	3.1
π-ID	10.1	5.2	2.4	4.2	10.1	10.1
background	3.5	5.2	0.4	1.0	7.0	12.0
acceptance	1.0	1.0	1.0	1.0	1.0	1.0
kinematic fit (χ^2)	2.8	1.8	0.7	1.8	2.8	2.8
correlated $\mu\mu$ ID loss	3.0	3.0	1.3	2.0	3.0	10.0
$\pi\pi/\mu\mu$ ISR lumi	1.5	1.5	1.5	3.0	3.0	10.0
unfolding	1.0	1.0	1.0	1.0	1.0	1.0
ISR luminosity ($\mu\mu$)	3.8	3.8	3.8	3.8	3.8	3.8
sum	12.9	9.6	5.4	7.4	13.9	21.9

16.4 The pion form factor

The square of the pion form factor is defined as usual by the ratio of the dressed cross section without FSR, divided by the lowest-order cross section for point-like spin 0 charged particles. Thus,

$$|F_\pi|^2(s') = \frac{3s'}{\pi\alpha^2(0)\beta_\pi^3}\,\sigma_{\pi\pi}(s') \tag{16.1}$$

with

$$\sigma_{\pi\pi}(s') = \frac{\sigma^0_{\pi\pi(\gamma)}(s')}{1+\frac{\alpha}{\pi}\eta(s')}\left(\frac{\alpha(s')}{\alpha(0)}\right)^2 \tag{16.2}$$

The FSR correction [41, 42] $\alpha/\pi\ \eta(s')$ is slowly varying with s' and amounts to 8.0×10^{-3} at the ρ mass.

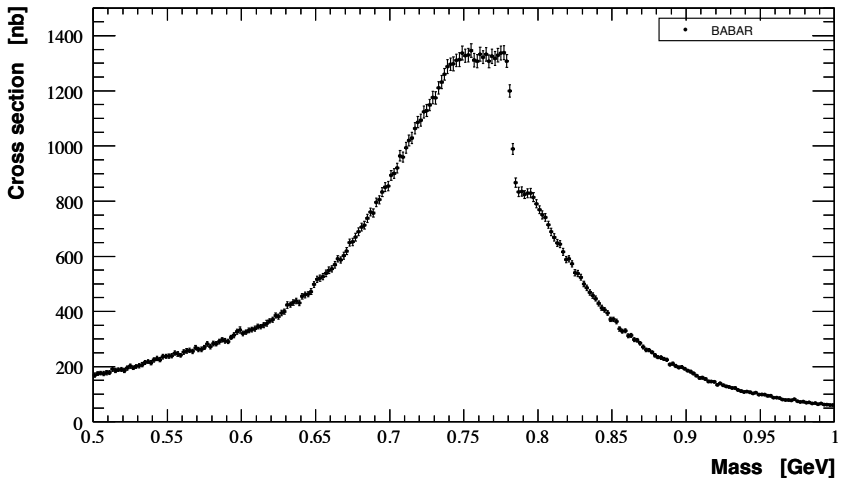

Figure 16.4: The measured cross section for $e^+e^- \to \pi^+\pi^-(\gamma)$ in the central ρ region. Systematic and statistical uncertainties are shown, but only the diagonal elements of the covariance matrix.

16.5 Comparison to other e^+e^- results

The measured form factor can be compared to published data from the CMD-2 [49] and SND [50] experiments in Novosibirsk, KLOE in Frascati, in the mass range between 0.5 and 1 GeV. We use the new KLOE [52] data released in Dec. 2008 which are claimed to supersede the older published ones [51]. The comparisons are shown in Figs. 16.5, 16.6, and 16.9 as the relative difference to *BABAR* of the form factor squared in the other experiments. For this comparison the data of the other experiments is compared with the interpolation of the *BABAR* cross sections in the nearest two 2-MeV bins. This introduces some statistical fluctuations, however mitigated by the smoothing effect of the unfolding procedure, but still clearly visible when the comparison is made with high statistics data, such as KLOE. The *BABAR* data appear as a band to which the data points from others can be compared.

The agreement looks reasonable at first sight, but overall the BaBar results lie generally above the Novosibirsk results, especially on the lower side of the ρ resonance. This discrepancy will be better quantified when computing the dispersion integral. The discrepancy is larger with KLOE above the ρ peak, it is

much reduced compared to the previous published KLOE results.

The region of the $\rho - \omega$ interference is examined in more detail in Figs. 16.7 and 16.8. No evidence is found for a significant variation in the steep part of the interference pattern around the ω mass, showing that the *BABAR* mass calibration is not shifted with respect to Novosibirsk by more than 0.2 MeV.

The comparison for the form factor squared in the low mass region is made in Fig. 16.10 (older results) and 16.11 (recent results from Novosibirsk). The agreement is reasonable, except with the NA47 experiment at CERN.

A direct cross section comparison is made in the large mass region in Fig. 16.12. The *BABAR* results agree with CMD-2 up to 1.4 GeV, while the DM2 cross section [53] appears larger by about 30-40%. The dip region near 1.6 GeV, usually interpreted as resulting from interference between the ρ' and ρ'' amplitudes, is clearly mapped with much increased precision. There is also an indication for more structure in the 2.2-2.2 GeV region which could be due to a still higher-mass ρ''' vector meson.

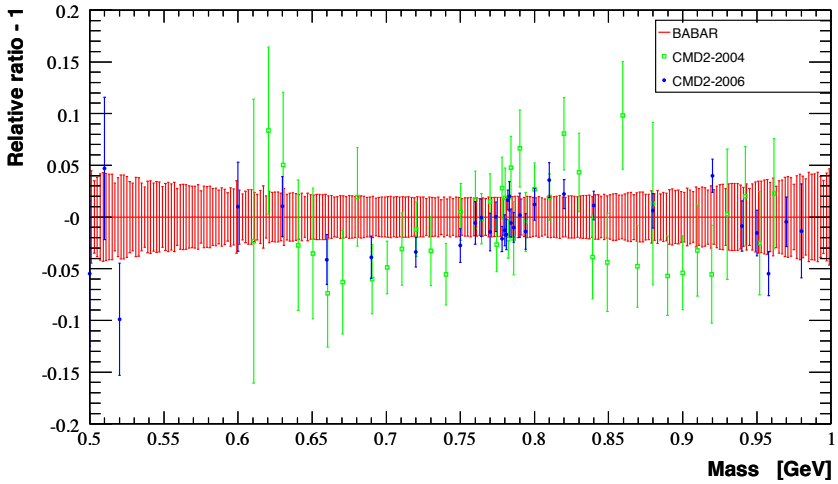

Figure 16.5: The relative difference of form factor squared from the $e^+e^- \to \pi^+\pi^-$ between *BABAR* and CMD-2 in the 0.5-1 GeV mass region. Systematic and statistical uncertainties are included for both results, with the diagonal elements of the *BABAR* covariance matrix.

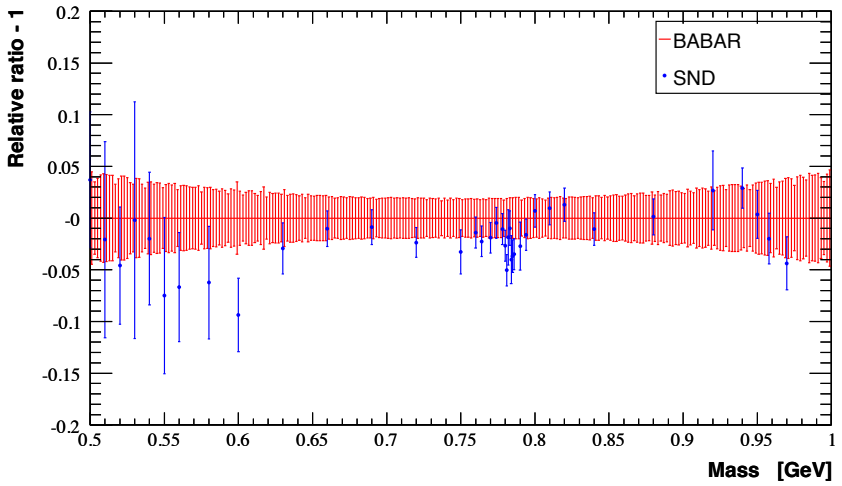

Figure 16.6: The relative difference of form factor squared from the $e^+e^- \to \pi^+\pi^-$ between *BABAR* and SND in the 0.5-1 GeV mass region. Systematic and statistical uncertainties are included for both results, with the diagonal elements of the *BABAR* covariance matrix.

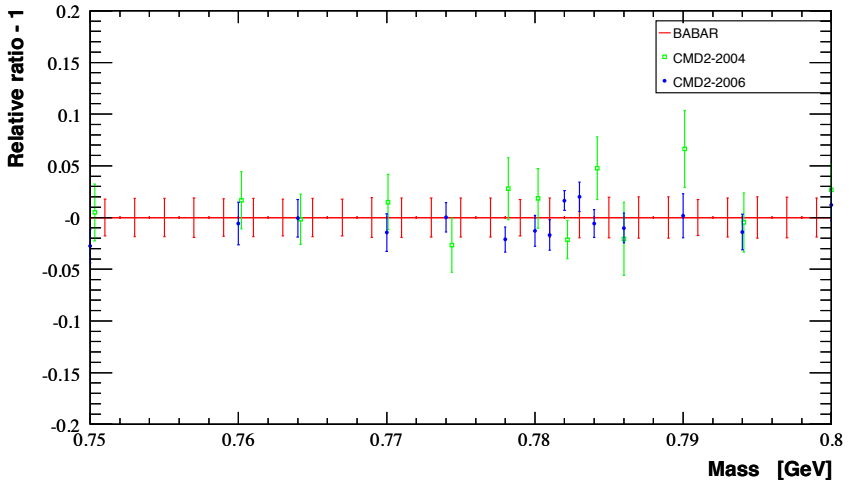

Figure 16.7: The relative difference of form factor squared from the $e^+e^- \to \pi^+\pi^-$ between *BABAR* and CMD-2 in the $\rho-\omega$ mass region. Systematic and statistical uncertainties are included for both results, with the diagonal elements of the *BABAR* covariance matrix.

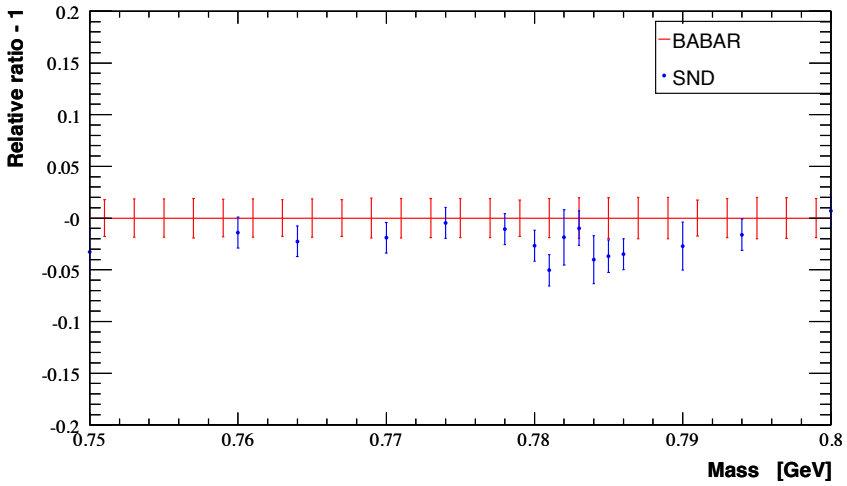

Figure 16.8: The relative difference of form factor squared from the $e^+e^- \to \pi^+\pi^-$ between *BABAR* and SND in the $\rho-\omega$ mass region. Systematic and statistical uncertainties are included for both results, with the diagonal elements of the *BABAR* covariance matrix.

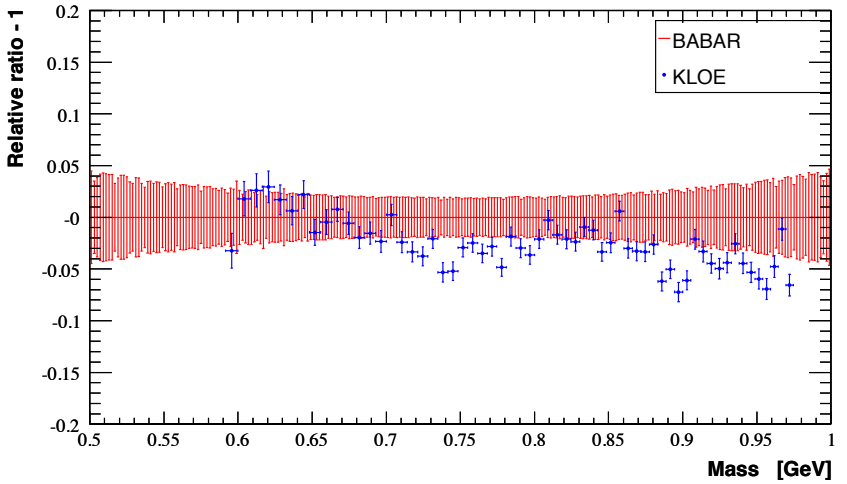

Figure 16.9: The relative difference of form factor squared from the $e^+e^- \to \pi^+\pi^-$ between *BABAR* and KLOE in the 0.5-1 GeV mass region. Systematic and statistical uncertainties are included for both results, with the diagonal elements of the *BABAR* covariance matrix.

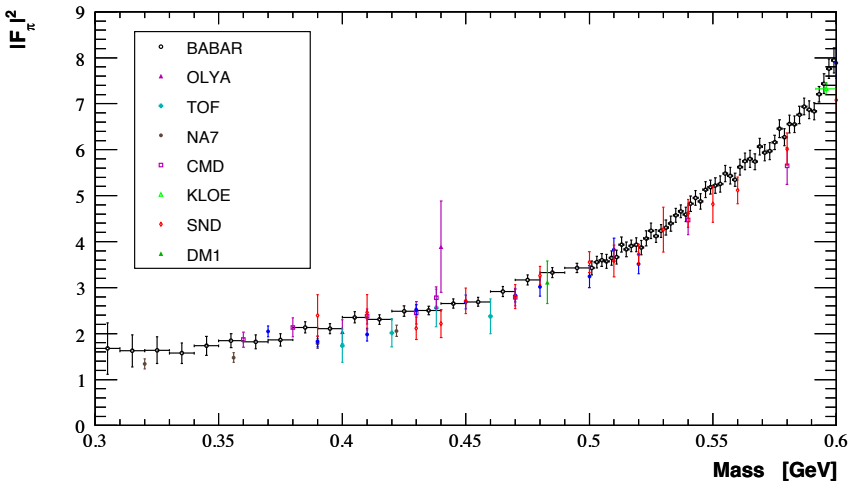

Figure 16.10: The measured pion form factor squared compared to published results from older experiments. Systematic and statistical uncertainties are shown for all results, with the diagonal elements of the *BABAR* covariance matrix.

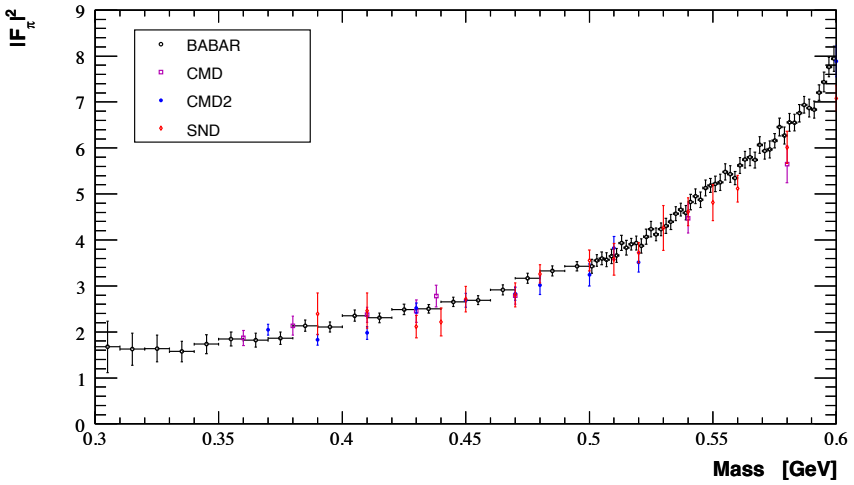

Figure 16.11: The measured pion form factor squared compared to published results from recent experiments. Systematic and statistical uncertainties are shown for all results, with the diagonal elements of the *BABAR* covariance matrix.

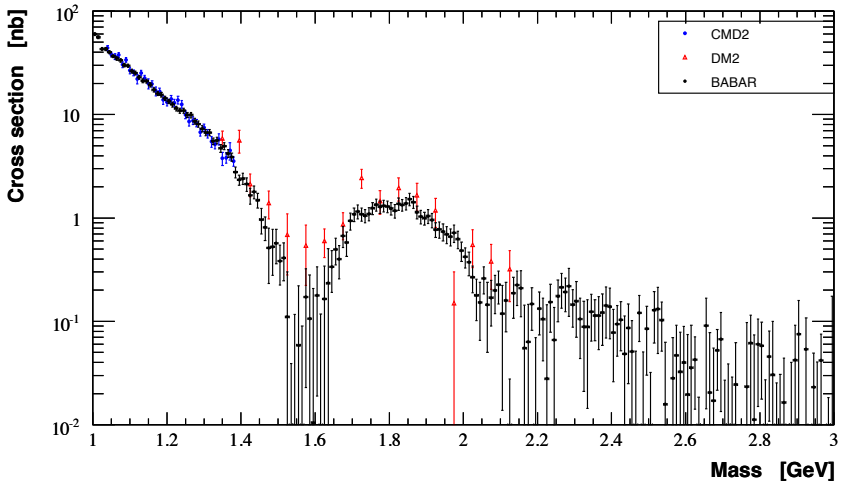

Figure 16.12: The measured cross section for $e^+e^- \to \pi^+\pi^-(\gamma)$ compared to published results from CMD-2 up to 1.4 GeV and DM2 above. Systematic and statistical uncertainties are shown for all results, with the diagonal elements of the *BABAR* covariance matrix.

16.6 Comparison to $\tau \to \nu_\tau \pi^- \pi^0$ results

It is also appropriate to compare the present results to the $\tau \to \nu_\tau \pi\pi^0$ spectral function. Taking isospin-breaking (IB) into account the CVC relation between the $e^+e^- \to \pi^+\pi^-(\gamma)$ bare cross section with FSR and the normalized hadronic invariant mass distribution in $\tau \to \nu_\tau \pi\pi^0$ decays is modified [54, 55] as following

$$\sigma^0_{\pi^+\pi^-(\gamma)} = \frac{1}{D(s)} \frac{B_{\pi\pi}}{B_e} \left(\frac{1}{N_{\pi\pi}} \frac{dN_{\pi\pi}}{ds} \right) \frac{R_{IB}}{S_{EW}} \left(1 + \frac{\alpha(0)}{\pi} \eta(s) \right) , \tag{16.3}$$

where

$$D(s) = \frac{3|V_{ud}|^2\, s}{2\pi\alpha^2(0) m_\tau^2} \left(1 - \frac{s}{m_\tau^2} \right)^2 \left(1 + \frac{2s}{m_\tau^2} \right) \tag{16.4}$$

and

$$R_{IB}(s) = \frac{1}{G_{EM}(s)} \left(\frac{\beta_0}{\beta_-} \right)^3 \frac{|F_0(s)|^2}{|F_-(s)|^2} . \tag{16.5}$$

$B_{\pi\pi}$ and B_e are the branching fractions for τ decay into the $\nu_\tau \pi\pi^0$ and $\nu_\tau e \overline{\nu_e}$ final states. $G_{EM}(s)$ is the long-distance QED radiative correction and S_{EW} the short-distance electroweak radiative correction. $F_0(s)$ and $F_-(s)$ are the

electromagnetic and weak form factors, while β_0 and β_- are the pion velocities in the $\pi^+\pi^-$ and $\pi\pi^0$ center-of-mass systems, respectively.

Taking into account $\rho - \omega$ interference in the G_{EM} factor, and including a charged/neutral ρ width difference from radiative decays and $m_{\pi^\pm}/m_{\pi^0}$ mass difference in the form factor [56], one can compare directly the τ and *BABAR* data. This is done in Figs. 16.13, 16.14, and 16.15 for the ALEPH [57], CLEO [58], and Belle [59] experiments, in a manner similar to the e^+e^- comparisons. Here, of course there is another uncertainty resulting from the IB theoretical corrections, corresponding roughly to a scale uncertainty of 0.5%. A new analysis of τ data, including the Belle results and revisited IB corrections is in progress [60] and will update the previous results [61].

The comparison with ALEPH shows a slope at the limit of the quoted errors, while a similar trend is observed with CLEO, although much smaller. In fact both ALEPH and CLEO are consistent with each other within errors and their results were combined in Ref. [61]). The *BABAR* data compares well with the recent high statistics Belle result, which though it displays similar trends as ALEPH and CLEO, generally agrees with *BABAR* over the 0.5-1 GeV range.

The comparison of the *BABAR* results with the τ data is also made in the threshold region up to 0.5 GeV in Figs. 16.16, 16.17, and 16.18. The accuracy of the τ data is much poorer in this region, and the agreement with *BABAR* is reasonable.

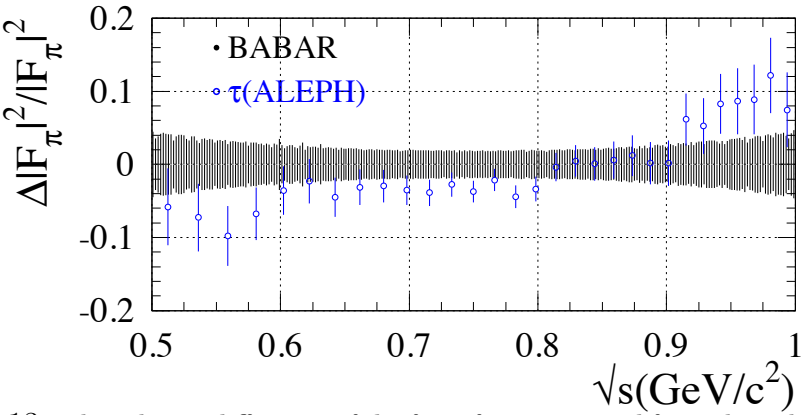

Figure 16.13: The relative difference of the form factor squared from the τ data of ALEPH with respect to the $e^+e^- \to \pi^+\pi^-$ *BABAR* measurements in the 0.5-1 GeV mass region. Systematic and statistical uncertainties are included for both results, with the diagonal elements of the *BABAR* covariance matrix.

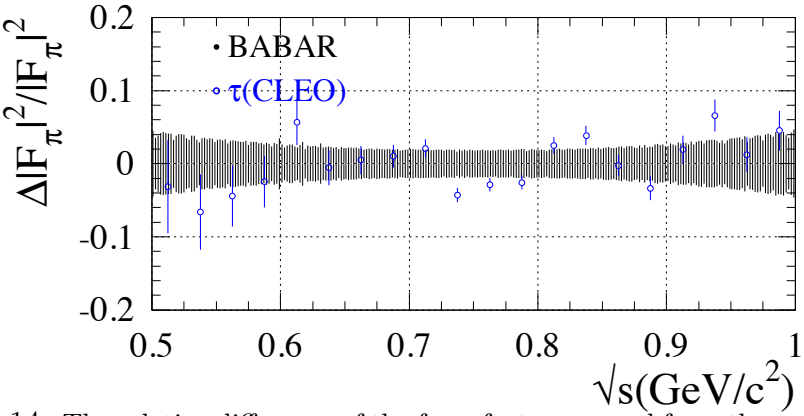

Figure 16.14: The relative difference of the form factor squared from the τ data of CLEO with respect to the $e^+e^- \to \pi^+\pi^-$ *BABAR* measurements in the 0.5-1 GeV mass region. Systematic and statistical uncertainties are included for both results, with the diagonal elements of the *BABAR* covariance matrix.

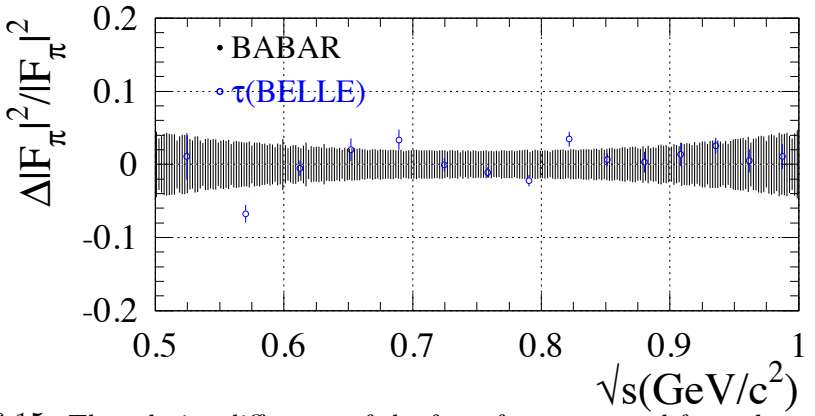

Figure 16.15: The relative difference of the form factor squared from the τ data of Belle with respect to the $e^+e^- \to \pi^+\pi^-$ *BABAR* measurements in the 0.5-1 GeV mass region. Systematic and statistical uncertainties are included for both results, with the diagonal elements of the *BABAR* covariance matrix.

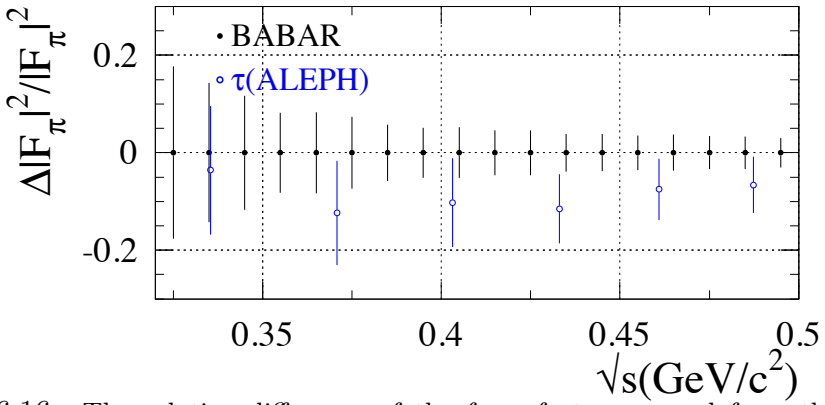

Figure 16.16: The relative difference of the form factor squared from the τ data of ALEPH with respect to the $e^+e^- \to \pi^+\pi^-$ *BABAR* measurements in the threshold region. Systematic and statistical uncertainties are included for both results, with the diagonal elements of the *BABAR* covariance matrix.

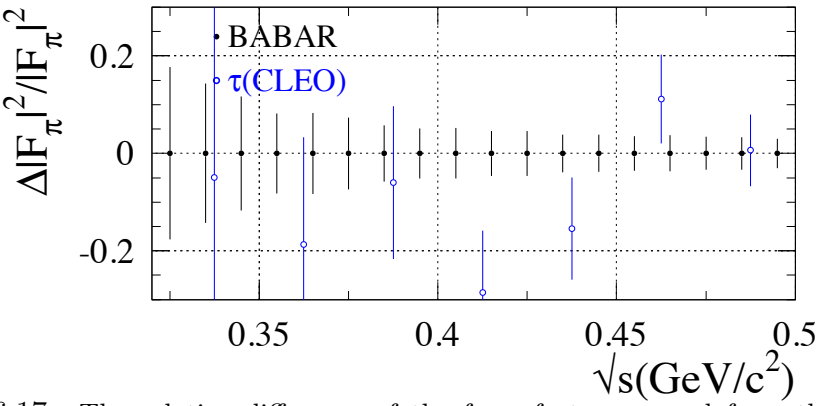

Figure 16.17: The relative difference of the form factor squared from the τ data of CLEO with respect to the $e^+e^- \to \pi^+\pi^-$ *BABAR* measurements in the threshold region. Systematic and statistical uncertainties are included for both results, with the diagonal elements of the *BABAR* covariance matrix.

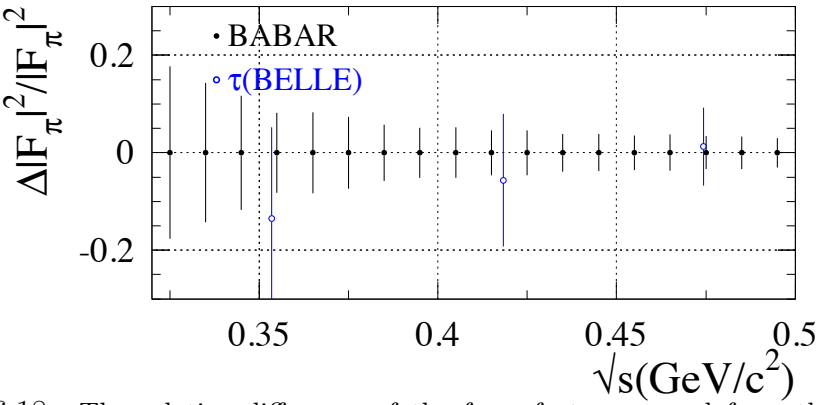

Figure 16.18: The relative difference of the form factor squared from the τ data of Belle with respect to the $e^+e^- \to \pi^+\pi^-$ *BABAR* measurements in the threshold region. Systematic and statistical uncertainties are included for both results, with the diagonal elements of the *BABAR* covariance matrix.

Chapter 17

The $\pi\pi$ contribution to the anomalous muon magnetic moment

The lowest-order loop contribution of the $\pi\pi(\gamma)$ intermediate state to the muon magnetic anomaly is given by

$$a_\mu^{\pi\pi(\gamma),LO} = \frac{1}{4\pi^3}\int_{4m_\pi^2}^{\infty} ds\, K(s)\, \sigma^0_{\pi\pi(\gamma)}(s)\ , \tag{17.1}$$

where $K(s)$ is the QED kernel (see Eq. 1.7).

The integration is carried out over the measured cross section and the statistical error is computed using the covariance matrix from the unfolding. The systematic uncertainty is evaluated using the components given in Table 16.1, taken fully correlated in all mass regions.

Several tests are possible since two analyses can be performed in the central region, using the 'ρ central' and the 'ρ tails' conditions. The main difference is the χ^2 cut, which affects the background level, the χ^2 efficiency, the mass resolution, hence the performance of the unfolding. For the range 0.5-1.0 GeV the result with the 'central' conditions is 447.0 10^{-10} in 2-MeV bins, and 447.7 10^{-10} in 10-MeV bins with the 'tails' conditions. Thus the effect of different resolution and efficiencies has little effect on the integral. The difference of 0.7 10^{-10} between the two analyses is consistent with their estimated uncommon systematic error of 3.5 10^{-3} and uncommon statistical error of 0.9 10^{-3}, giving an uncertainty on the integral of 1.6 10^{-10}.

The evaluation of the integral in the threshold region was made in previous estimates using a polynomial expansion in s' for the pion form factor, incorporating the constraint of the normalization of $F_\pi(0) = 1$ and the known slope in s' given by the quadratic charge radius of the pion. This procedure also compensated for the relatively poorer quality of data in this region. The *BABAR*

continuous low-mass data permit a direct evaluation, consistent with the constrained method. The very small contribution ($(0.55 \pm 0.01)\ 10^{-10}$) between the 2π threshold and 0.3 GeV is evaluated using the constrained fit between 0.3-0.5 GeV.

The *BABAR* results are given in Table 17.1 in the different mass ranges where they can be compared to previous evaluations. They are compared with previous evaluations using e^+e^- data [48] and τ data [61]. Both of these results are in the process of being updated with the more recent data from KLOE and Belle. The new IB corrections are expected to lower the τ result quoted here.

The comparison shows some level of discrepancy, which should be re-evaluated however after inclusion of the new data and IB corrections. Considering the fact that all four inputs (CMD-2/SND, KLOE, *BABAR*, τ) have completely independent systematic uncertainties, it is very important to take into account all data.

A more direct comparison to individual experiments can be made over a restricted mass range where CMD-2, SND, and KLOE data overlap between 0.630 and 0.958 GeV: the results (in 10^{-10}) are $362.1 \pm 2.4 \pm 2.2$ (CMD-2 94-95 data), $361.5 \pm 1.7 \pm 2.9$ (CMD-2 98 data), $361.0 \pm 1.2 \pm 4.7$ (SND) (all 3 results quoted in Ref. [49]), $356.8 \pm 0.4 \pm 3.1$ (KLOE new data) and $366.2 \pm 2.3 \pm 2.0$ (*BABAR*). In all of the four values, the first error is statistical and the second systematic. This direct comparison, involving about 71% of the total 2π contribution, is shown in Fig. 17.1. The disagreement between KLOE and *BABAR* is in contrast with the overconsistency of CMD-2 and SND, but overall the picture is acceptable: $\chi^2/DF = 4.8/4$, ignoring the correlations between the two CMD-2 results, and also between CMD-2 and SND for radiative corrections. The corresponding value for the average of the τ data with updated IB corrections [60] is $367.0 \pm 1.6 \pm 1.6_{IB}$, in good agreement with the *BABAR* result and somewhat higher than the other e^+e^- results.

Including the *BABAR* results will reduce the observed discrepancy between the BNL measurement [13] of the muon magnetic anomaly and the SM prediction which was estimated [48] to be $(27.5 \pm 8.4)\ 10^{-10}$.

Table 17.1: Evaluation of $a_\mu^{\pi\pi(\gamma),LO}$ using the *BABAR* data (in units of 10^{-10}). The first error is statistical and the second systematic. Previous evaluations using published e^+e^- data [48], dominated by the CMD-2 and SND results (first error statistical and systematic second error from radiative corrections) or using the $\tau \to \pi\pi^0\nu_\tau$ spectral function [60] from ALEPH-Belle-CLEO-OPAL (A-B-C-O) (first error statistical and systematic, second error from isospin-breaking corrections) are given for comparison.

$m_{\pi\pi}$ (GeV)	*BABAR*	previous e^+e^-	τ (A-B-C-O)
0.28−0.5 (direct)	$57.9 \pm 1.0 \pm 0.6$	–	–
0.28−0.5 (fit)	$57.7 \pm 0.9 \pm 0.6$	$55.6 \pm 0.8 \pm 0.1$	$56.0 \pm 1.6 \pm 0.3$
0.5−1.8	$456.9 \pm 2.5 \pm 2.8$	$449.0 \pm 3.0 \pm 0.9$	$464.0 \pm 3.2 \pm 2.3$
0.28−1.8	$514.7 \pm 2.6 \pm 3.4$	$504.6 \pm 3.1 \pm 1.0$	$520.1 \pm 3.6 \pm 2.6$

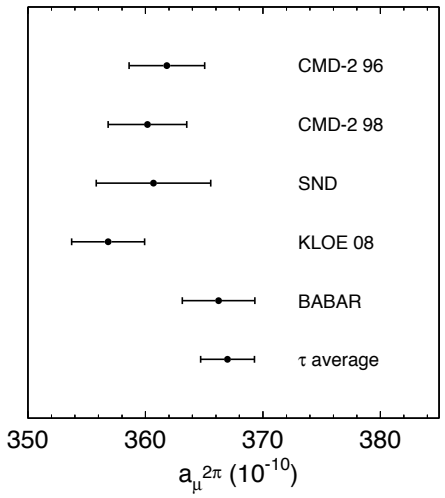

Figure 17.1: The LO hadronic VP 2π contributions to the muon magnetic anomaly, evaluated in the 0.630-0.958 GeV mass range where CMD-2, SND, and KLOE data overlap, are compared to the *BABAR* result and the average τ result from ALEPH, Belle, CLEO, and OPAL.

Chapter 18

Conclusions

The cross sections for the processes $e^+e^- \to \mu^+\mu^-(\gamma)$ and $e^+e^- \to \pi^+\pi^-(\gamma)$ has been measured from threshold to 3.5 GeV and 3.0 GeV respectively with the ISR method at *BABAR*. Efficiencies for trigger, tracking, PID and kinematic fits (χ^2-cut) are obtained in data in the same environment. Additional ISR and FSR radiation is studied, the latter one being included in the measurement. Corrections are determined in order to take into account NLO radiation which is simplified in the AfkQed generator.

The muons results agree with QED with a precision of 1.1%, dominated by the standard *BABAR* luminosity determination. The measurement of $e^+e^- \to \mu^+\mu^-\gamma(\gamma)$ provides a precise determination of the effective ISR luminosity needed for obtaining cross sections for $\pi^+\pi^-(\gamma)$ and other ISR-produced hadronic processes.

Benefiting not only from the careful studies for $\pi\pi\gamma(\gamma)$ events, but also from the effective ISR luminosity well determined in $e^+e^- \to \mu^+\mu^-(\gamma)$ channel, the precision measurement of the cross section for the process $e^+e^- \to \pi^+\pi^-(\gamma)$ is achieved. The systematic uncertainty in the main ρ resonance region of 5.4×10^{-3} permits a precise evaluation of the hadronic vacuum polarization contribution to the muon magnetic anomaly. Comparisons are made with existing determinations, both from e^+e^- annihilation experiments and τ decays. The overall agreement is fair with CMD-2/SND, poor with KLOE, and good with τ decays (ALEPH, CLEO, Belle).

The *BABAR* result on the dominant $\pi\pi$ hadronic contribution to the muon anomaly will reduce the previously estimated deviation between the direct measurement and the SM prediction. The deviation decreases from $(275 \pm 84) \times 10^{-11}$ (3.3 σ) to $(174 \pm 88) \times 10^{-11}$ (2.0 σ) , if only the *BABAR* result is used for the 2π

contribution.

Bibliography

[1] T. Kinoshita and M. Nio, Phys. Rev. **D73**, 013003 (2006);
T. Aoyama *et al.*, Phys. Rev. Lett. **99**, 110406 (2007);
T. Kinoshita and M. Nio, Phys. Rev. **D70**, 113001 (2004);
T. Kinoshita, Nucl. Phys. **B144**, 206 (2005)(Proc. Supp.);
T. Kinoshita and M. Nio, Phys. Rev. **D73**, 053007 (2006);
A.L. Kataev, arXiv:hep-ph/0602098;
M. Passera, J. Phys. **G31**, 75 (2005).

[2] R. Jackiw and S. Weinberg, Phys. Rev. **D5**, 2396 (1972);
G. Altarelli *et al.*, Phys. Lett. **B40**, 415 (1972);
I. Bars and M. Yoshimura, Phys. Rev. **D6**, 374 (1972).

[3] A. Czarnecki *et al.*, Phys. Rev. **D67**, 073006 (2003);
S. Heinemeyer, D. Stockinger, and G. Weiglein, Nucl. Phys. **B699**, 103 (2004);
T. Gribouk and A. Czarnecki, Phys. Rev. **D72**, 053016 (2005).

[4] M. Davier and W.J. Marciano, Ann. Rev. Nucl. and Part. Sci. **54**, 115 (2004).

[5] M. Davier, Nucl. Phys. (Proc. Suppl.), **169**, 288 (2007).

[6] M. Davier *et al.*, Eur. Phys. J. **C31**, 503 (2003);
M. Davier *et al.*, Eur. Phys. J. **C27**, 497 (2003).

[7] K. Hagiwara *et al.*, Phys. Lett. **B649**, 173 (2007).

[8] C. Bouchiat and L. Michel, J. Phys. Radium **22**, 121 (1961);
M. Gourdin and E. de Rafael, Nucl. Phys. **B10**, 667 (1969).

[9] S.J. Brodsky, E. de Rafael, Phys. Rev. **168**, 1620 (1968)

[10] B. Krause, Phys. Lett. **B390**, 392 (1997);
R. Alemany, M. Davier, A. Höcker, Eur.Phys.J. **C2**, 123 (1998).

[11] J. Bijnens, E. Pallante, J. Prades, Nucl.Phys. **B626**, 410 (2002);
M. Knecht and A. Nyffeler, Phys. Rev. **D65**, 073034 (2002);
M. Knecht *et al.*, Phys. Rev. Lett. **88**, 071802 (2002);
J. Hayakawa and T. Kinoshita, Erratum Phys. Rev. **D66**, 019902 (2002);
K. Melnikov and A. Vainshtein, Phys. Rev. **D70**, 113006 (2004);
J. Bijnens and J. Prades, Mod. Phys. Lett. **A22**, 767 (2007);
J. Prades, E. de Rafael, A. Vainshtein, arXiv:0901.0306 (Jan, 2009).

[12] J. Bailey *et al.*, Phys. Lett. **B68**, 191 (1977);
J. Bailey et al., Nucl. Phys. **B150**, 1 (1979);
F.J.M. Farley, E. Picasso, "The muon $(g-2)$ Experiments", Advanced Series on Directions in High Energy Physics - Vol. 7 Quantum Electrodynamics, ed. T. Kinoshita, World Scientific 1990.

[13] G.W. Bennett *et al.* (Muon g-2 Collaboration), Phys. Rev. Lett. **89**, 101804 (2002);
Erratum ibid. Phys. Rev. Lett. **89**, 129903 (2002);
G.W. Bennett *et al.* (Muon g-2 Collaboration), Phys. Rev. Lett. **92**, 161802 (2004);
G.W. Bennett *et al.* (Muon g-2 Collaboration), Phys. Rev. **D73**, 072003 (2006).

[14] R. R. Akhmetshin *et al.*, Phys. Lett. **B527**, 161-172 (2002);
R. R. Akhmetshin *et al.*, Phys. Lett. **B578**, 285-289 (2004);
R. R. Akhmetshin *et al.*, JETP Lett. **84**, 413, (2006);
R. R. Akhmetshin et al., arXiv:hep-ex/0610021;
V. M. Aulchenko *et al.*, JETP Lett. **82**, 743, (2005).

[15] J. Z. Bai *et al.*, Phys. Rev. Lett. **84**, 594 (2000);
J. Z. Bai *et al.*, Phys. Rev. Lett. **88**, 101802 (2002);
M. Ablikim et al., Phys. Lett. **B641**, 145 (2006).

[16] V.N. Baier and V.S. Fadin, Phys.Lett. **B27**, 223 (1968).

[17] A. B. Arbuzov, E. A. Kuraev, N. P. Merenkov, L. Trentadue JHEP **9812**, 009 (1998).

[18] S. Binner, J. H. Kühn and K. Melnikov, Phys. Lett. **B459**, 279 (1999).

[19] B. Aubert *et al.* (*BABAR* collaboration), Phys. Rev. **D70**, 072004 (2004).

[20] B. Aubert *et al.* (*BABAR* collaboration), Phys. Rev. **D71**, 052001 (2005).

[21] B. Aubert *et al.* (*BABAR* collaboration), Phys. Rev. **D73**, 012005 (2006).

[22] B. Aubert *et al.* (*BABAR* collaboration), Phys. Rev. **D73**, 052003 (2006).

[23] B. Aubert *et al.* (*BABAR* collaboration), Phys. Rev. **D76**, 012008 (2007).

[24] B. Aubert *et al.* (*BABAR* collaboration), Phys. Rev. **D76**, 092005 (2007).

[25] B. Aubert *et al.* (*BABAR* collaboration), Phys. Rev. **D76**, 092006 (2007).

[26] B. Aubert *et al.* (*BABAR* collaboration), Phys. Rev. **D77**, 092002 (2008).

[27] PEP-II Conceptual Design Report, SLAC-418 (1993).

[28] B. Aubert, *et al.* (*BABAR* collaboration), Nucl. Instrum. Meth. **A479**, 1-116 (2002).

[29] *BABAR* , Harrison, P. F., e. and Quinn, Helen R., e., The *BABAR* physics book: Physics at an Asymmetric B Factory Papers from Workshops on Physics at an Asymmetric B Factory (*BABAR* Collaboration Meetings), Rome, Italy, 11-14 Nov 1996, Princeton, NJ, 17-20 Mar 1997, Orsay, France, 16-19 Jun 1997 and Pasadena, CA, 22-24 Sep 1997.

[30] Benelli, G., *et al.*, *The BABAR LST detector high voltage system: Design and implementation*, IEEE Nucl. Sci. Symp. Conf. Rec. **2**, 1145 – 1148 (2006).

[31] M. Davier, A.M. Lutz, and W.F. Wang, *BABAR* Analysis Document #1605 (2009)

[32] M. Davier, A.M. Lutz, S. Rodier and W.F. Wang, *BABAR* Analysis Document #1775 (2007)

[33] M. Davier and W.F. Wang, *BABAR* Analysis Document #1773 (2009)

[34] D. Azzopardi *et al.*, *BABAR* Analysis Document #60 (2000).

[35] M. Davier and W.F. Wang, *BABAR* Analysis Document #1774 (2008)

[36] N. Arnaud, M. Davier, P. Lukin, and W.F. Wang, *BABAR* Analysis Document #1880 and #1504 (2007)

[37] M. Davier, L.L. Wang, and W.F. Wang, *BABAR* Analysis Document #1987 (2008)

[38] N. Berger and S. Dong, *BABAR* Analysis Document #1122 (2006)

[39] R. Gamet and C. Touramanis, *BABAR* Analysis Document #1312 (2005)

[40] R. Gamet and C. Touramanis, *BABAR* Analysis Document #1850 (2007)

[41] Yu.M. Bystritskiy *et al.*, hep-ph/0505236 (2005).

[42] H. Czyż *et al.*, Eur. Phys.J. **C39** 411 (2005).

[43] B. Malaescu, to be published.

[44] M. Davier, A. Höcker, and Z. Zhang, routine for computing $\Delta\alpha(s)$.

[45] ISR lumi functions provided by Genia Solodov at solodov/ISRtex/pawplaynew/lum-isr-novp-20deg.kumac .

[46] M. Davier, B. Malaescu, E.P. Solodov et al., in preparation.

[47] Review of Particle Physics, Y.M. Yao *et al*, J.Phys. G 33 (2006) 1.

[48] M. Davier, Nucl.Phys. B (Proc.Suppl.) **169** 288 (2007).

[49] V.M. Aulchenko *et al.* (CMD-2 Collaboration, JETP Lett. 82 743 (2005); JETP Lett. 84 413 (2006); R.R. Akhmetshin *et al.* (CMD-2 Collaboration), Phys. Lett. B648 28 (2007).

[50] M.N. Achasov *et al.* (SND Collaboration), JETP 101 1053 (2005); JETP 103 380 (2006).

[51] A. Aloisio *et al.* (KLOE Collaboration), Phys. Lett. B606 12 (2005).

[52] F. Ambrosino *et al.* (KLOE Collaboration), Phys. Lett. B670 285 (2009).

[53] D. Bisello *et al.* (DM2 Collaboration), Phys. Lett. B220 321 (1989).

[54] V. Cirigliano, G. Ecker, and H. Neufeld, Phys. Lett. B513 361 (2001); J. High Energy Phys. 08 002 (2002).

[55] A. Flores-Talpa *et al.*, Phys. Rev. D74 071301 (2006); Nucl. Phys. Proc. Suppl. 169 250 (2007).

[56] A. Flores-Talpa, G. Lopez Castro, and G. Toledo Sanchez, Phys. Rev. D76 096010 (2007).

[57] S. Schael *et al.* (ALEPH Collaboration), Phys. Rep. 421 191 (2005).

[58] S. Anderson *et al.* (CLEO Collaboration), Phys. Rev. D61 112002 (2000).

[59] M. Fujikawa et al., arXiv:0805.3773v1 [hep-exp] (May 2008).

[60] M. Davier *et al.* to be published.

[61] M. Davier, S. Eidelman, A. Höcker, and Z. Zhang, Eur.Phys.J. C 27 497 (2003).

Acknowledgments

First of all, I want to express my gratitude to my China-France joint Ph.D thesis advisors Professor Michel DAVIER from LAL (Orsay) and Professor Chang-Zheng YUAN from IHEP (Beijing) for their valuable, inspiring and patient guidance. I'm very grateful to have a such opportunity to work on a hard physics topic using real data collected by *BABAR* to complete my training to be professional physicist in the field of particle physics.

I wish to thank Professor Wei-Dong LI and Professor Zhe-Pu MAO from IHEP (Beijing) for their circumspective instructions that helped me to begin the software work for BESIII, which really gave me a good starting to understand the entire chain of the scientific process in experimental particle physics, from the basic software work to detectors, physics, and the scientific collaboration.

I want to say many thanks to Dr. Wen-Feng WANG, his wife Madam Meng YU, Professor Anne-Marie LUTZ and Professor Zhi-Qing ZHANG. When the first time I went to Orsay to begin my thesis work, they gave me much help to get familiar to the new life and the new working environment. And then in the last three years they also gave me really many good suggestions on both work and life.

Schoolmates are indispensable in one's life. They are my friends, companions and sometimes teachers. I'm pretty appreciate that we ever studied, worked and lived together. Many thanks to Heng-Ne LI, Shu-Xian DU, Hai-XUAN CHENG, Jin LIU, Bogdan MALAESCU, and many other friends.

Finally, I want to send my best wishes and thankfulness to my parents far away in the hometown, who always support me, understand me, encourage me and care about me.